



CARDIFF UNIVERSITY

SCHOOL OF ENGINEERING

The Performance of a Tidal Stream Turbine under Wave and Current Interaction

Catherine Lloyd

A Thesis submitted to Cardiff University for the degree of Doctor of
Philosophy

Submission Date: 06 March 2020

ACKNOWLEDGEMENTS

The author acknowledges support from SuperGen UK Centre for Marine Energy (EPSRC: EP/N020782/1) as well as Cardiff University for providing funding. The experimental testing carried out at IFREMER was funded by EPSRC Impact Acceleration Account (IAA) funding and supported by the staff at IFREMER. The author would like to thank the University of Liverpool for providing experimental data which was used to aid the numerical work carried out in this thesis.

In addition, this research was performed using the supercomputing facilities at Cardiff University operated by Advanced Research Computing at Cardiff (ARCCA) on behalf of the Cardiff Supercomputing Facility and the HPC Wales and Supercomputing Wales (SCW) projects. We acknowledge the support of the latter, which is part-funded by the European Regional Development Fund (ERDF) via the Welsh Government.

The author would like to thank her PhD supervisors Prof. Tim O’Doherty and Dr. Allan Mason-Jones for their continued guidance and support throughout her studies at Cardiff University; Dr. Matt Allmark for his assistance in using Matlab software and carrying out experimental data processing; Dr. Roger Grosvenor for his advice in the final stages of assembling the thesis; and friends and family for all their optimism, patience and encouragement.

ABSTRACT

This thesis examines the performance of a tidal stream turbine when operating under wave and current conditions. This was accomplished by investigating the loadings imparted on a 1/20th scale, 0.9m diameter tidal turbine, under multiple wave and current conditions. Experimental testing was undertaken as well as numerical modelling, achieved using the commercial CFD software package ANSYS CFX.

Initial investigations analysed the performance and loadings on the turbine under uniform and profiled current only conditions. Experimentally, some of the velocity data sets were not normally distributed and therefore modal values were found to present a more accurate method of calculating the predominant flow conditions at each water depth. Average performance characteristics were found to be unaffected by the presence of a profiled current velocity. However, transient loadings such as the out of plane bending moment, thrust and torque, experienced greater variations in the data sets due to stanchion interaction. The amplitude of fluctuation in the loadings were heightened with increasing shear in the velocity profile, while the maximum and minimum turbine loadings coincided with the rotational frequency of the turbine. CFD simulation results showed good agreement with those observed experimentally.

Further analysis explored the addition of waves which intensified the complexity of the flow conditions experienced by the turbine. The introduction of waves was found to have an insignificant effect on the average current velocity at each water depth and the average performance characteristics. However, the presence of an oscillatory flow effect induced by the waves greatly affects the transient turbine loadings. With the addition of waves, the fluctuation in the total turbine thrust and torque increased by roughly 35 times that of the current only cases. Peaks in the loadings were found to be aligned with those in the wave surface elevation. This indicates the importance of minimising large loading fluctuations to increase the fatigue life of a tidal stream turbine operating in these conditions.

A CFD model was developed to simulate combined wave and current interaction with a turbine. Optimisation of the model geometry, mesh and setup are detailed in this thesis for simulations using regular waves within the limits of Stokes 2nd order theory. Comparisons to experimental data highlight the homogeneity between the data sets, justifying the use of CFD to accurately replicate experimentally generated flow conditions.

TABLE OF CONTENTS

List of figures	ix
List of tables	xvii
Nomenclature	xxi
Alphabetical.....	xxi
Greek symbols.....	xxiii
Acronyms	xxiv
1 Introduction	1
1.1 The need for renewable energy	1
1.2 Marine renewable energy	6
1.2.1 Wave energy.....	6
1.2.2 Tidal energy	6
1.3 Thesis aims and objectives	8
1.4 Thesis layout.....	9
2 Literature review	11
2.1 Tidal stream technology and devices.....	11
2.1.1 Horizontal Axis Tidal Turbines	14
2.1.2 Vertical Axis Tidal Turbines (VATTs).....	17
2.1.3 Other tidal devices	18
2.2 Experimental testing.....	19
2.2.1 Full-scale ocean device testing	20
2.2.2 Model-scale laboratory device testing.....	21
2.3 Numerical modelling.....	34
2.3.1 Blade Element Momentum Theory.....	35
2.3.2 Computational Fluid Dynamics	36
2.4 Summary of literature review.....	50
3 Theory.....	52

3.1	Wave theory	52
3.1.1	Linear Wave Theory	52
3.1.2	Stokes 2 nd Order Theory	58
3.1.3	Wave properties	60
3.2	Computational Fluid Dynamics.....	61
3.2.1	Governing fluid flow equations	61
3.2.2	Turbulent flow conditions	63
3.2.3	Reynolds Averaged Navier-Stokes equations.....	63
3.2.4	Turbulence modelling	64
3.2.5	Multiphase modelling	67
3.3	Non-dimensional performance characteristics	69
3.3.1	Coefficient of torque.....	70
3.3.2	Coefficient of power	70
3.3.3	Coefficient of thrust.....	70
3.3.4	Tip Speed Ratio	70
3.3.5	Volumetrically averaged streamwise velocity.....	71
3.4	Summary	73
4	Experimental testing methodology.....	75
4.1	Turbine description.....	75
4.1.1	Instrumentation and data recording	76
4.1.2	Instrumentation calibration	77
4.1.3	Uncertainty analysis.....	78
4.2	University of Liverpool recirculating water channel.....	80
4.3	IFREMER wave-current flume tank.....	82
4.3.1	IFREMER Experimental set up	82
4.3.2	Flow measurement instrumentation calibration.....	86
4.3.3	Flow measurement uncertainty analysis	87
4.4	Experimental test matrices	87

4.5	Summary	89
5	Numerical modelling methodology	90
5.1	Software	90
5.2	Main domain modelling	91
5.2.1	Geometry.....	91
5.2.2	Mesh development	94
5.3	Turbine modelling.....	96
5.3.1	Geometry.....	96
5.3.2	Mesh development.....	97
5.4	Pre-processing setup.....	100
5.4.1	Analysis type	100
5.4.2	Domain properties and fluid models	101
5.4.3	Boundary conditions	104
5.4.4	Domain interfaces.....	107
5.4.5	Solver control.....	108
5.4.6	Output control and convergence monitoring criteria.....	109
5.5	Solver.....	112
5.5.1	Parallel processing	112
5.6	Post-processing.....	113
5.6.1	Extracting force, torque and out of plane bending moment	113
5.6.2	Calculating torque, power and thrust coefficients	114
5.7	CFD test matrix	114
5.8	Summary	116
6	CFD model optimisation	117
6.1	Mesh optimisation study.....	118
6.1.1	Simulating regular waves	118
6.1.2	Turbine model.....	122
6.2	Time step study.....	127

6.2.1	Wave-current CFD simulations.....	127
6.2.2	Turbine CFD simulations	129
6.2.3	Combined wave-current, turbine CFD simulations.....	130
6.3	CFD model setup configurations	130
6.3.1	'Free slip' CFD model	131
6.3.2	'Free surface' CFD model	133
6.3.3	'Free slip' and 'free surface' CFD model comparison	135
6.4	Summary	145
7	Turbine performance under current-only conditions: uniform and profiled velocity gradients	146
7.1	Experimental results	146
7.1.1	Turbine characterisation: uniform current flow.....	146
7.1.2	Turbine characterisation: profiled current flow	150
7.1.3	Uniform and profiled comparison	154
7.2	CFD model validation.....	161
7.2.1	Uniform flow CFD models	161
7.2.2	Profiled flow CFD models.....	165
7.3	Transient turbine loadings	176
7.4	Summary	179
8	Development of wave-current numerical model using CFD: regular waves with uniform current conditions	181
8.1	Experimental results	181
8.2	CFD results	185
8.2.1	Geometry, mesh, setup summary	185
8.2.2	Verification of reduced width domain	187
8.2.3	Deep-water wave conditions.....	189
8.2.4	Intermediate water wave condition	192
8.2.5	Deep and intermediate water wave numerical comparison.....	194

8.3	NWT validation using experimental data	197
8.4	Summary	200
9	Turbine performance under wave-current flow conditions: regular waves with profiled velocity gradients.....	201
9.1	Experimental results	201
9.1.1	Turbine characterisation: regular waves and profiled current flow	201
9.2	CFD model validation	209
9.2.1	Geometry, mesh, setup summary.....	209
9.2.2	Regular wave and profiled flow CFD model validation	211
9.2.3	Transient turbine loadings.....	226
9.3	Summary	230
10	Conclusions and future work	232
10.1	Conclusions.....	232
10.1.1	Turbine performance under uniform current conditions.....	232
10.1.2	Turbine performance under profiled current conditions.....	232
10.1.3	Turbine performance under regular wave and profiled current conditions 233	
10.1.4	Development of a wave-current CFD model	234
10.1.5	Validation of numerical models using experimental data.....	235
10.2	Future work	236
	References	237
	Appendix.....	I
A.	CFX Expression Language (CEL) expressions	I
	CEL for <i>CFD_UC3_Turb</i>	I
	CEL for <i>CFD_PC1_Turb</i>	II
	CEL for <i>CFD_UC1_W1_Int</i>	III
	CEL for <i>CFD_PC1_W4_Turb</i>	V
B.	Matlab: results processing scripts	VII

Matlab scripts used for CFD data processing:.....	VII
Matlab scripts used for experimental data processing:	XXV
C. Publications.....	XXXV
Journal publications.....	XXXV
Conference publications	XXXV

LIST OF FIGURES

Figure 1.1. Global average land-sea temperature anomaly relative to the average temperature in 1961-1990, figure reproduced from [3] using data from [173].	2
Figure 1.2. Global atmospheric carbon dioxide levels for the previous 800 000 years, figure reproduced from [6].	2
Figure 1.3. UK electricity generation by technology type from 2010 – 2018, figure reproduced from [2].	3
Figure 1.4. UK electricity generation by main renewable sources 2010 – 2018, figure reproduced from [9].	4
Figure 1.5. UK electricity generated in Q1 2018 and Q1 2019, figure reproduced from [11].	5
Figure 1.6. UK breakdown of renewable electricity generation, figure reproduced from [11].	5
Figure 2.1. The A) AR1500 and; B) AR2000 tidal stream turbines developed by SIMEC Atlantis Energy, figure reproduced from [30].	15
Figure 2.2. The SeaGen tidal energy system developed by Marine Current Turbines, figure reproduced from [31].	16
Figure 2.3. The A) PLAT-I and; B) PLAT-O tidal energy platforms developed by Sustainable Marine Energy, figures reproduced from [35] and [37].	17
Figure 2.4. The A) Darrieus and; B) Gorlov VATT, figure reproduced from [39].	18
Figure 2.5. The flexible membrane device developed by EEL Energy, figure reproduced from [41].	19
Figure 2.6. The DeepGreen ‘kite’ device developed by Minesto, figure reproduced from [43].	19
Figure 2.7. The different complex flow features present that can interact with turbine performance; (L-R) turbulence, velocity profiles and wave recirculation, figure reproduced from [85].	22
Figure 2.8. The Kelvin Hydrodynamic Laboratory (KHL) tow tank located at the University of Strathclyde.	23
Figure 2.9. The IFREMER wave-current flume located in Boulogne-Sur-Mer, France.	24
Figure 2.10. The FloWave ocean energy research facility located at the University of Edinburgh, figure reproduced from [183].	25

Figure 2.11. A plan view of the array spacing for: A) single row [$A=0.5\phi$, 1.0ϕ , 1.5ϕ] and; B) offset dual row [$A=1.5\phi$, $B=3.0\phi$]	29
Figure 2.12. The blade positions at: A) Top Dead Centre and; B) Bottom Dead Centre. ...	32
Figure 2.13. The normalised streamwise velocity results yielded by 3 models with the same boundary conditions: A) instantaneous DES, B) time averaged DES, and; C) RANS, reproduced from [184]. (For this case, D = diameter).	44
Figure 2.14. A schematic of a piston type wave maker, figure reproduced from [120]	46
Figure 2.15. A schematic of a flap type wave maker, figure reproduced from [120].	47
Figure 3.1. Applicability of wave theories, reproduced from [141].	53
Figure 3.2. Wave motion definition.	53
Figure 3.3. Subdivisions of the near-wall region, figure reproduced from [106]	66
Figure 3.4. Visual description of how to define the volume fractions of each fluid phase.	68
Figure 3.5. The defined pressure field as a result of using volume fractions for each fluid phase.	69
Figure 3.6. An example of the swept area being split up into horizontal sections which are used to calculate the flowrate for each horizontal section area.	71
Figure 3.7. Descriptors used for parts of a circle.	72
Figure 3.8. The process of dividing the turbine swept area up into horizontal sections.	73
Figure 4.1. Diagram of: A) the full turbine and; B) the new blade design.	75
Figure 4.2. Recirculating water channel layout, figure reproduced from [84].	81
Figure 4.3. Wave maker schematic, figure reproduced from [84].	81
Figure 4.4. IFREMER flume tank schematic, figure reproduced from [69].	82
Figure 4.5. A plan view of the IFREMER experimental setup of flow measurement equipment and the turbine positioning for: (a) when the turbine is present and; (b) when the turbine has been removed.	84
Figure 4.6. IFREMER experimental setup of wave maker when at position: A) NOWM (no wave maker), B) WM00 (fully submerged) and; C) WM20 (raised by 20cm)	85
Figure 4.7. IFREMER experimental setup.	86
Figure 5.1. Description of the different model domains.	91
Figure 5.2. General geometry setup guide for: A) 'free slip' model and; B) 'free surface' model.	92
Figure 5.3. General mesh layout for: A) HEXA meshing and; B) TETRA meshing.	95
Figure 5.4. Mesh description definitions.	96

Figure 5.5. 3-bladed HATT geometry from: A) the front, B) the side and; C) the side showing the MFR cylinder around the turbine.....	97
Figure 5.6. Primary features in turbine numerical model.....	97
Figure 5.7. Different mesh sections over model.	98
Figure 5.8. Meshes showing the integration of: A) 'ogrid' mesh around MFR cylinder; B) with TETRA mesh inside MFR cylinder.	99
Figure 5.9. Final mesh for section 2 encompassing the turbine support structure and MFR cylinder showing the integration of: A) 'ogrid' mesh around MFR cylinder; B) with TETRA mesh inside MFR cylinder.....	100
Figure 5.10. Location of the local coordinate frames 'TurbRotAxis' and 'RotAxis_BM' as well as the global coordinate frame.	103
Figure 5.11. Boundary conditions imposed for: A) 'free surface' and; B) 'free slip' models.	104
Figure 5.12. Typical location of monitor points in all numerical models.....	110
Figure 5.13. An example of monitoring the: A) force and; B) torque, on each turbine blade and the hub over time (per accumulated time step) to monitor convergence of the simulation.	111
Figure 6.1. Normalised results for the CFD, theory and experimental maximum and minimum wave-induced: A) streamwise and; B) vertical velocities. Experimental data supplied by the University of Liverpool [84].....	119
Figure 6.2. Computational speed of numerical model with different mesh sizes.	121
Figure 6.3. Final mesh selection using 120 cells per wavelength and 10 cells over the wave height: A) in the XY plane; B) in the YZ plane.	122
Figure 6.4. Explanation of inflation layer mesh descriptors.	123
Figure 6.5. Mesh comparison between CFD and experimental results for: A) C_p , B) C_t and; C) C_q . Experimental data supplied by the University of Liverpool [84].	124
Figure 6.6. Computational time comparison for 60s of run time for meshes 1-7.....	125
Figure 6.7. Final turbine mesh selection for section 3, the rotating turbine subdomain, using inflation layers and TETRA meshing viewed from the: A) front, and from the; B) side.	126
Figure 6.8. Normalised results for the CFD, theoretical and experimental maximum and minimum wave-induced: A) streamwise and; B) vertical velocities for different time steps. Experimental data supplied by the University of Liverpool [84].	128
Figure 6.9. Computational speed of numerical model with different time steps.	129

Figure 6.10. The mesh for the ‘free slip’ model as viewed from: A) the front and; B) the side.....	131
Figure 6.11. The mesh for the ‘free surface’ model as viewed from: A) the front and; B) the side.....	133
Figure 6.12. The streamwise velocity when the turbine is operating at a TSR of 4 for the: A) the ‘free surface’ and; B) the ‘free slip’ CFD models.....	136
Figure 6.13. The streamwise velocity when the turbine is operating at a TSR of 0 to 7 at a location 2.5m downstream of the inlet for the: A) the ‘free surface’ and; B) the ‘free slip’ CFD models.....	136
Figure 6.14. The A) C_q , B) C_t and C) C_p over a range of TSRs for the ‘free surface’ and ‘free slip’ CFD models in uniform flow conditions.....	138
Figure 6.15. Numerical CFD comparison between the 'free surface' and 'free slip' models, for A) thrust and B) torque results on each blade over 5s of converged run time for: i) TSR 3, ii) TSR 4 and; iii) TSR 5.....	139
Figure 6.16. Numerical CFD comparison between the 'free surface' and 'free slip' models, for A) thrust and B) torque results at a TSR of 4 relating to: i) blade 1, ii) the hub and; iii) the turbine total (all blades and hub).	141
Figure 6.17. FFT analysis for the 'free surface' and 'free slip' CFD models, for A) thrust and B) torque results at a TSR of 4 for: i) blade 1 and; ii) the turbine total (all blades and hub).	143
Figure 6.18. The orientation of the turbine when at Top Dead Centre, Bottom Dead Centre, and horizontal.	144
Figure 7.1. The A) streamwise and; B) vertical experimental velocity results through the water depth in uniform flow conditions. Bars show +/- 1 standard deviation.	148
Figure 7.2. The experimental A) C_q , B) C_t and C) C_p over a range of TSRs for the turbine in uniform flow conditions. Bars show +/- 1 standard deviation.	149
Figure 7.3. The A) streamwise and; B) vertical experimental velocity results through the water depth in 2 different profiled flow conditions. Bars show +/- 1 standard deviation. .	151
Figure 7.4. The experimental C_q over a range of TSRs for the turbine in flow conditions corresponding to: A) profile 1 and; B) profile 2. Bars show +/- 1 standard deviation.....	153
Figure 7.5. The experimental C_t over a range of TSRs for the turbine in flow conditions corresponding to: A) profile 1 and; B) profile 2. Bars show +/- 1 standard deviation.....	153
Figure 7.6. The experimental C_p over a range of TSRs for the turbine in flow conditions corresponding to: A) profile 1 and; B) profile 2. Bars show +/- 1 standard deviation.....	154

Figure 7.7. The A) C_q , B) C_t and C) C_p for the experimental results in uniform and profiled flow conditions. Bars show +/- 1 standard deviation.	155
Figure 7.8. Histograms showing the mean and mode of each experimental data set for A) uniform, B) profile 1 and C) profile 2 flow conditions. From i) to iv), each histogram corresponds to LDA data taken at a specific water depth as shown in Table 7.9.	157
Figure 7.9. Examples of normally distributed and skewed distributions.....	158
Figure 7.10. The A) C_q , B) C_t and C) C_p for the experimental results in uniform and profiled flow conditions, recalculated using the mode instead of the mean for the W_{vol} . Bars show +/- 1 standard deviation.	160
Figure 7.11. The A) C_q , B) C_t and C) C_p over a range of TSRs for the experimental and 'free surface' CFD model results in uniform flow conditions. Bars show +/- 1 standard deviation.....	164
Figure 7.12. The A) streamwise and; B) vertical, CFD and experimental velocity results through the water depth for different flow conditions. Bars show +/- 1 standard deviation.	167
Figure 7.13. The streamwise velocity when the turbine is operating at a TSR of 4 for the inlet current conditions representative of: A) uniform, B) Profile 1, and C) Profile 2.	168
Figure 7.14. The Ai) C_q , Bi) C_t and Ci) C_p for the experimental and CFD results in different flow conditions, with a zoomed in version of TSR 4 in ii). Bars show +/- 1 standard deviation.	171
Figure 7.15. The experimental results for the out of plane bending moment on a single blade in uniform, Profile 1 and Profile 2 current conditions.	172
Figure 7.16. The CFD results for the out of plane bending moment on a single blade in uniform, Profile 1 and Profile 2 current conditions.	172
Figure 7.17. The average experimental out of plane bending moment fluctuation on a single blade calculated using TSA for A) uniform, B) Profile 1, and C) Profile 2 current conditions.	175
Figure 7.18. Numerical CFD comparison between the uniform, profile 1 and profile 2 models, for A) thrust and B) torque results at a TSR of 4 relating to: i) a single blade, ii) the hub and; iii) the turbine total (all blades and hub).	178
Figure 8.1. Average streamwise velocity at points through the water depth for both Wave 1 and 2. Experimental data taken using an ADV had an estimated error of <1% in the mean velocity and an uncertainty of +/-1%. Data supplied by the University of Liverpool [84]. ...	182

Figure 8.2. Experimental results for Wave 1 and 2 of the normalised A) streamwise and; B) vertical velocities at points through the water depth. Experimental data taken using an ADV had an uncertainty of +/-1%. Data supplied by the University of Liverpool [84].	184
Figure 8.3. Average: A) streamwise and; B) vertical velocities for current-only flow through the water depth over 60s of converged run time.	188
Figure 8.4. Average: A) streamwise and; B) vertical velocities for current-only flow through the water depth at 6 different locations downstream of the inlet on the centreline at t=80s.	188
Figure 8.5. A comparison of the CFD and S2OT surface elevation for Wave 1, 2 and 3 in deep-water conditions at a location 4m downstream of the inlet.	189
Figure 8.6. The normalised A) streamwise and; B) vertical velocities at monitor points through the water depth at a location 4m downstream of the inlet for numerical results and S2OT.	191
Figure 8.7. A comparison of the CFD and S2OT surface elevation for Wave 1, 2 and 3 in intermediate water conditions at a location 4m downstream of the inlet.	192
Figure 8.8. The normalised A) streamwise and; B) vertical velocities at monitor points through the water depth at a location 4m downstream of the inlet for numerical results and S2OT.	193
Figure 8.9. The normalised maximum and minimum, streamwise and vertical velocities plotted for the normalised water depth, where the SWL is at 0 and the seabed at -1, to give an idea of the shape and magnitude of the velocity orbitals for A) deep and; B) intermediate water wave conditions for Wave 1.	196
Figure 8.10. Experimental and numerical comparison of Wave 1 and 2 results for the normalised a) streamwise and; b) vertical velocities at points through the water depth.	199
Figure 9.1. The A) streamwise and; B) vertical experimental velocity results through the water depth for conditions representative of Profile 1 (P1), and Profile 1 with Wave 4 (P1W4). Bars show +/- 1 standard deviation.	204
Figure 9.2. The A) streamwise and; B) vertical experimental velocity results through the water depth for conditions representative of Profile 2 (P2), and Profile 2 with Wave 5 (P2W5). Bars show +/- 1 standard deviation.	204
Figure 9.3. The mean and wave orbital components to the A) streamwise and; B) vertical experimental velocity results through the water depth for Profile 1 Wave 4 (P1W4). Bars show +/- 1 standard deviation. [<i>W</i> or <i>V</i> = average velocity, <i>W_{wave}</i> or <i>V_{wave}</i> = wave orbital velocity component]	205

Figure 9.4. The mean and wave orbital components to the A) streamwise and; B) vertical experimental velocity results through the water depth for Profile 2 Wave 5 (P2W5). Bars show +/- 1 standard deviation. [W or V = average velocity, W_{wave} or V_{wave} = wave orbital velocity component]	205
Figure 9.5. The experimental surface elevation results for P1W4 and P2W5.	206
Figure 9.6. The A) C_q , B) C_t and C) C_p for the experimental results in wave and profiled flow conditions - P1W4 and P2W5. Bars show +/- 1 standard deviation.....	208
Figure 9.7. The mean A) streamwise and; B) vertical, CFD and experimental velocity results through the water depth for P1W4 and P2W5. Bars show +/- 1 standard deviation.	212
Figure 9.8. A timeseries of the CFD model streamwise velocities taken at 19 positions through the water depth (-0.1 to -1.9m from the SWL) for the conditions given by A) P1W4 and; B) P2W5.	213
Figure 9.9. A timeseries of the CFD model vertical velocities taken at 19 positions through the water depth (-0.1 to -1.9m from the SWL) for the conditions given by A) P1W4 and; B) P2W5.	214
Figure 9.10. The mean and wave orbital components to the A) streamwise and; B) vertical, CFD and experimental velocity results through the water depth for P1W4. Bars show +/- 1 standard deviation. [W or V = average velocity, W_{wave} or V_{wave} = wave orbital velocity component]	215
Figure 9.11. The mean and wave orbital components to the A) streamwise and; B) vertical, CFD and experimental velocity results through the water depth for P2W5. Bars show +/- 1 standard deviation. [W or V = average velocity, W_{wave} or V_{wave} = wave orbital velocity component]	215
Figure 9.12. The wave orbital components for the A) streamwise and; B) vertical, CFD and experimental velocity results through the water depth for P1W4. Bars show +/- 1 standard deviation. [W_{wave} or V_{wave} = wave orbital velocity component].....	216
Figure 9.13. The wave orbital components for the A) streamwise and; B) vertical, CFD and experimental velocity results through the water depth for P2W5. Bars show +/- 1 standard deviation. [W_{wave} or V_{wave} = wave orbital velocity component].....	217
Figure 9.14. The experimental and CFD surface elevation for the conditions given by P1W4.....	218
Figure 9.15. The experimental and CFD surface elevation for the conditions given by P2W5.....	218

Figure 9.16. The instantaneous streamwise velocity when the turbine is operating at a TSR of 4 for the inlet wave and current conditions representative of: A) P1W4; and B) P2W5.....	219
Figure 9.17. The Ai) C_q , Bi) C_t and Ci) C_p for the experimental and CFD results in wave-current conditions, with a zoomed in version of TSR 4 in ii). Bars show +/- 1 standard deviation.	220
Figure 9.18. The CFD results for the out of plane bending moment on a single blade in wave-current conditions representative of A) P1W4; and B) P2W5.	222
Figure 9.19. The average out of plane bending moment fluctuation on a single blade calculated using TSA for A) P1W4, and B) P2W5 using i) experimental, and ii) CFD results.	223
Figure 9.20. FFT analysis for the A) experimental and B) CFD results at a TSR of 4 for: i) P1W4 and; ii) P2W5.	225
Figure 9.21. Numerical CFD comparison between the uniform, Profile 1, Profile 2, P1W4 and P2W5 models, for A) thrust and B) torque results at a TSR of 4 relating to: i) a single blade, ii) the hub and; iii) the turbine total (all blades and hub). The surface elevation of the waves at the turbine location for P1W4 and P2W5 are shown in iv) in order to compare to the corresponding thrust and torque loadings.	228

LIST OF TABLES

Table 2.1. A summary of recent active tidal technology.	12
Table 2.2. A summary of recent decommissioned tidal technology.	13
Table 3.1. Relative depth conditions for deep, intermediate and shallow water waves. ...	60
Table 3.2. The various regions for given wave steepness.....	61
Table 4.1. Blade geometry details.	76
Table 4.2. Main turbine characteristics summary.	76
Table 4.3. A summary of the turbine instrumentation used and the sample rates.	77
Table 4.4. Summary of calibration results for the thrust and torque transducers, undertaken by Applied measurements Ltd, figure reproduced from [156]......	77
Table 4.5. Summary of calibration results for the out of plane bending moment transducer for blade 2, figure reproduced from [156].	78
Table 4.6. Summary of the bias and precision uncertainties for the variables used in calculation of the turbine performance characteristics.....	79
Table 4.7. A summary of the instrumentation used, their sample rates and estimated uncertainty.	80
Table 4.8. Key features of each test facility.	81
Table 4.9. Angular velocities used to control turbine rotation.	83
Table 4.10. A summary of the instrumentation used, their sample rates and estimated uncertainty.	86
Table 4.11. Summary of calibration results for the wave probe.	87
Table 4.12. Summary of the uncertainties for the flow velocity and surface elevation measurements.....	87
Table 4.13. Experimental test matrix for testing conducted at the university of Liverpool recirculating water channel.....	88
Table 4.14. Experimental test matrix for testing conducted at the IFREMER wave-current flume.	88
Table 5.1. Fluid models and properties for the main domain of the 'free slip' model.	101
Table 5.2. Fluid models and properties for the main domain of the 'free surface' model.	102
Table 5.3. Fluid models and properties for the turbine subdomain.	103
Table 5.4. Boundary condition details for each model type.	104
Table 5.5. Solver control settings for transient analysis simulations.	109

Table 5.6. All possible variables used for each identifier in general CEL expressions.....	113
Table 5.7. CFD test matrix for numerical simulations conducted throughout this thesis.	115
Table 6.1. A summary of the different mesh setups.	118
Table 6.2. Recommended mesh settings for free surface modelling.....	120
Table 6.3. A summary of each mesh setup for the turbine subdomain.	122
Table 6.4. Angular velocities used to control turbine rotation.	132
Table 6.5. Summary of the geometry, mesh and setup for a 'free slip' uniform flow CFD model.	132
Table 6.6. Summary of the geometry, mesh and setup for a 'free surface' uniform flow CFD model.	134
Table 6.7. Volumetrically averaged streamwise velocity over the turbine swept area for the 'free surface' and 'free slip' CFD models.	137
Table 7.1. Angular velocities used to control turbine rotation.	147
Table 7.2. Values for the experimental streamwise and vertical velocities under uniform flow conditions.	147
Table 7.3. Values for the experimental peak performance characteristics under uniform flow conditions.	148
Table 7.4. Summary of experimental wave maker settings and the respective profile name.	150
Table 7.5. Values for the experimental streamwise and vertical velocities under profiled flow conditions.	151
Table 7.6. The difference between depth averaged and volumetrically averaged streamwise velocities.....	152
Table 7.7. Values for the experimental peak performance characteristics under profiled flow conditions.	154
Table 7.8. Average parameters used to calculate the C_p and C_q at TSR 4.	156
Table 7.9. Corresponding LDA water depth for each histogram.....	158
Table 7.10. The mean, mode and difference of each histogram displayed in Figure 7.9.	158
Table 7.11. The volumetrically averaged streamwise velocity calculated using the mean and mode.	159
Table 7.12. Summary of the geometry, mesh and setup for a 'free surface' uniform flow CFD model.	162
Table 7.13. results for the 'free surface' uniform flow CFD models and experimental data at TSR 4.....	163

Table 7.14. Summary of the geometry, mesh and setup for the 'free surface' profiled flow CFD model.	166
Table 7.15. Volumetrically averaged streamwise velocity in profiled flow conditions for the experimental and CFD model results.	167
Table 7.16. The experimental results, CFD model results, and the difference between them for C_q , C_t and C_p , in profiled flow conditions.	170
Table 7.17. The average CFD and experimental out of plane bending moment results in uniform and profiled flow conditions.	172
Table 7.18. The amplitude of fluctuation in the CFD and experimental out of plane bending moment results calculated using different methods.	174
Table 7.19. The individual and total component loadings on the turbine when subjected to uniform and profiled flow conditions.	176
Table 8.1. Wave and current characteristics used in the experimental testing.....	182
Table 8.2. Mesh sizing parameters.....	186
Table 8.3. A summary of the wave characteristics used.....	186
Table 8.4. Summary of the geometry, mesh and setup for a 'free surface' wave-current CFD model.	187
Table 8.5. A summary of the wave height from experimental testing and numerical CFD results.....	197
Table 9.1. A summary of the wave characteristics.....	202
Table 9.2. Velocity fluctuations induced by the surface wave for the points measured nearest the top, middle and bottom of the flume.....	203
Table 9.3. A summary of the target and experimentally obtained wave frequencies and wave heights.....	206
Table 9.4. The volumetrically averaged streamwise velocity calculated using the mean and mode.....	207
Table 9.5. Values for the experimental performance characteristics at a TSR of 4.	207
Table 9.6. Summary of the geometry, mesh and setup for 'free surface' regular wave, profiled flow CFD models using 2 different wave characteristics.....	210
Table 9.7. Volumetrically averaged streamwise velocity for the experimental and CFD model results.	211
Table 9.8. A summary of the experimental and CFD model wave frequencies and wave heights.....	218
Table 9.9. The experimental results, CFD model results, and the difference between them for C_q , C_t and C_p , in profiled flow conditions.	221

Table 9.10. The average CFD and experimental out of plane bending moment results for wave-current conditions.	224
Table 9.11. The amplitude of fluctuation in the CFD and experimental out of plane bending moment results.	226
Table 9.12. The individual component and total average thrust loadings on the turbine when subjected to current-only and wave-current conditions.	226
Table 9.13. The individual component and total average torque loadings on the turbine when subjected to current-only and wave-current conditions.	227
Table 9.14. The amplitude of fluctuation in the thrust loading on the turbine when subjected to current-only and wave-current conditions.	229
Table 9.15. The amplitude of fluctuation in the torque loading on the turbine when subjected to current-only and wave-current conditions.	230

NOMENCLATURE

ALPHABETICAL

Symbol	Definition	Units
a	Wave amplitude	m
A_{horiz}	Area of horizontal circle section	m^2
A_{sec}	Area of circle sector	m^2
A_{seg}	Area of circle segment	m^2
A_{tri}	Area of a triangle	m^2
A_{turb}	Swept area of the turbine	m^2
b	Base of triangle	m
BM_x	Out of plane Bending Moment	Nm
c	Chord length	m
C_a	Apparent wave celerity, stationary ref. frame	m/s
C_p	Coefficient of power	-
C_q	Coefficient of torque	-
C_r	Relative wave celerity, moving ref. frame	m/s
C_t	Coefficient of thrust	-
D	Characteristic linear dimension	m
F_α	Buoyancy force	N
g	Gravitational acceleration	m/s^2
h	Water depth	m
h_{seg}	Height of a circle segment	m
h_{tri}	Height of triangle	m
H	Wave height	m
k	Wave number	rad/m
k_t	Turbulent kinetic energy	J
L	Wavelength	m
p	Pressure	Pa
p_η	Gauge pressure at the free surface	Pa
P	Power	W
Q	Torque	Nm
Q_{flow}	Volumetric flow rate	m^3/s
r_α	Volume fraction of fluid α	-
R	Turbine radius	m
Re	Reynolds number	-
S	Water surface	m
S_M	Body force source term per unit volume per unit time	$N/m^3/s$

NOMENCLATURE

t	Time	s
Δt	Time step	s
Δt_{turb}	Optimum time step for turbine models	s
Δt_{wave}	Optimum time step for wave models	s
T	Thrust	N
T_a	Apparent wave period, stationary ref. frame	s
T_r	Relative wave period, moving ref. frame	s
u	Cartesian coordinate of velocity in x direction	m/s
v	Cartesian coordinate of velocity in y direction	m/s
v_a	Vertical velocity component under a wave, stationary ref. frame	m/s
v_{2a}	Vertical velocity component under a wave for S2OT, stationary ref. frame	m/s
v_r	Vertical velocity component under a wave, moving ref. frame	m/s
V	Volume	m^3
V_α	Volume occupied by fluid α	m^3
w	Cartesian coordinate of velocity in z direction	m/s
w_a	Horizontal velocity component under a wave, stationary ref. frame	m/s
w_{2a}	Horizontal velocity component under a wave for S2OT, stationary ref. frame	m/s
w_r	Horizontal velocity component under a wave, moving ref. frame	m/s
W	Current velocity in z direction	m/s
W_{wave}	Wave orbital velocity	m/s
W'	Velocity fluctuation	m/s
\bar{W}	Average current velocity in z direction	m/s
\bar{W}_{vol}	Volumetrically averaged streamwise velocity	m/s
x	Cartesian coordinate reference	m
y	Cartesian coordinate reference	m
y^+	Near wall flow resolution factor	-
z	Cartesian coordinate reference	m

GREEK SYMBOLS

Symbol	Definition	Units
ε	Turbulence eddy dissipation	J/s
η	Surface elevation	m
η_2	Surface elevation for S2OT	m
θ	Angle	$^\circ$
θ_{centre}	Central angle in circle	$^\circ$
λ	Tip speed ratio	-
μ	Dynamic viscosity	$Pa \cdot s$
μ_b	Bias error	-
μ_p	Precision error	-
μ_{tot}	Total uncertainty	-
ρ	Density	kg/m^3
τ	Viscous stress	Pa
\varnothing	Diameter	m
ϕ	Velocity potential	m^2/s
ϕ_2	Velocity potential for S2OT	m^2/s
ω	Angular velocity of the turbine	rad/s
ω_a	Apparent angular velocity of wave, stationary ref. frame	rad/s
ω_r	Relative angular velocity of wave, moving ref. frame	rad/s
ω_t	Turbulence frequency	Hz

ACRONYMS

Acronym	Definition
ADCP	Acoustic Doppler Current Profiler
ADM	Actuator Disc Method
ADV	Acoustic Doppler Velocimetry
AHH	Andritz Hydro Hammerfest
ALM	Actuator Line Model
ARCCA	Advanced Research Computing at Cardiff
BDC	Bottom Dead Centre
BEMT	Blade Element Momentum Theory
BET	Blade Element Theory
CEL	CFX Expression Language
CFD	Computational Fluid Dynamics
CMERG	Cardiff Marine Energy Research Group
CNR-INM	Consiglio Nazionale delle Ricerche Istituto di Ingegneria del Mare
DES	Detached Eddy Simulation
DFSBC	Dynamic Free Surface Boundary Condition
EC	European Commission
EMEC	European Marine Energy Centre
EVM	Eddy Viscosity Models
FAWT	Finite Amplitude Wave Theory
FFT	Fast Fourier Transform
FS	Full Scale
FVM	Finite Volume Method
GHG	Green House Gases
HATT	Horizontal Axis Tidal Turbine
HOBEM	Higher Order Boundary Element Method
HPC	High Performance Computing
IFREMER	French Research Institute for Exploitation of the Sea
INSEAN	Istituto Nazionale Per Studi Ed Esperienze Di Architettura Navale
IPCC	Intergovernmental Panel on Climate Change
KFSBC	Kinematic Free Surface Boundary Condition
KHL	Kelvin Hydrodynamic Laboratory
LDA	Laser Doppler Anemometry
LES	Large Eddy Simulation
low- <i>Re</i>	Low-Reynolds-Number
LWT	Linear Wave Theory
MFR	Multiple Frames of Reference

MRF	Moving Reference Frame
NWT	Numerical Wave Tank
PMSM	Permanent Magnet Synchronous Machine
ppm	parts per million
PV	Photo Voltaic
RANS	Reynolds Averaged Navier-Stokes
RITE	Roosevelt Island Tidal Energy
RMS	Root Mean Square
RSM	Reynolds Stress Models
SAWT	Small Amplitude Wave Theory
SCW	Supercomputing Wales
SST	Shear Stress Transport
SWL	Still Water Level
S2OT	Stokes 2nd Order Theory
TDC	Top Dead Centre
TI	Turbulence Intensity
TIGER	Tidal Stream Industry Energiser Project
THAWT	Transverse Horizontal Axis Water Turbine
TRL	Technology Readiness Level
TSA	Time Synchronous Averaging
TSR	Tip Speed Ratio
TST	Tidal Stream Turbine
VATT	Vertical Axis Tidal Turbine
VBM	Virtual Blade Model
VOF	Volume of Fluid
WMT	Wave Maker Theory
WM00	Wave maker position: fully submerged
WM20	Wave maker position: raised by 20cm

1 INTRODUCTION

1.1 THE NEED FOR RENEWABLE ENERGY

Global warming is causing significant changes to both land and marine ecosystems, and the potential future impact of climate change is a challenge to humanity that is unprecedented in scale [1]. “Climate change is the defining issue of our time” [1] and without immediate social and political action, disruption to the world we live in will only increase.

Global warming reached a temperature of 1°C above pre-industrial levels in 2017 [2], [3], as shown in Figure 1.1. The Intergovernmental Panel on Climate Change (IPCC) have predicted that an increase of 1.5°C is likely to be reached in the next 10-20 years [4]. The global mean surface temperature is rising with anthropogenic warming and is estimated to be increasing by 0.17°C per decade [4]. However, the main driver of global warming is reported to be directly related to the concentration of Green House Gases (GHG) in the atmosphere. These consist of water vapour (H_2O), ozone (O_3), carbon emissions (carbon dioxide CO_2 , methane CH_4) as well as nitrous oxides (NO_x). GHG underlie the rapid rise in global temperature since the beginning of the industrial revolution, however; without GHG the average temperature of the Earth’s surface would be around -18°C [5]. The atmospheric CO_2 concentration levels today are higher than any point in the past 800 000 years [4], [6], as shown in Figure 1.2. The global average atmospheric carbon dioxide concentration in 2019 was 409.1 parts per million (ppm) [7] with the highest previous concentration reaching 300 ppm, over 300 000 years ago [6].

Other indicators of climate change, such as an increase in the ocean heat content, rising sea levels and increasing acidity of the oceans, are linked to the rise in global atmospheric temperature. Over the previous century (1901-2010), the global average sea level has risen by 19cm and is estimated to continue rising to a level of 24-30 cm by 2065 [3]. This increase is mainly due to ocean warming and melting of the arctic sea ice, which has decreased by 1.07 million km^2 successively each decade since 1979 [3]. Global warming is transforming the world in which we live, and a global shift to reduce carbon emissions is necessary to ameliorate climate change and the degradation of our land and marine ecosystems.

1 INTRODUCTION

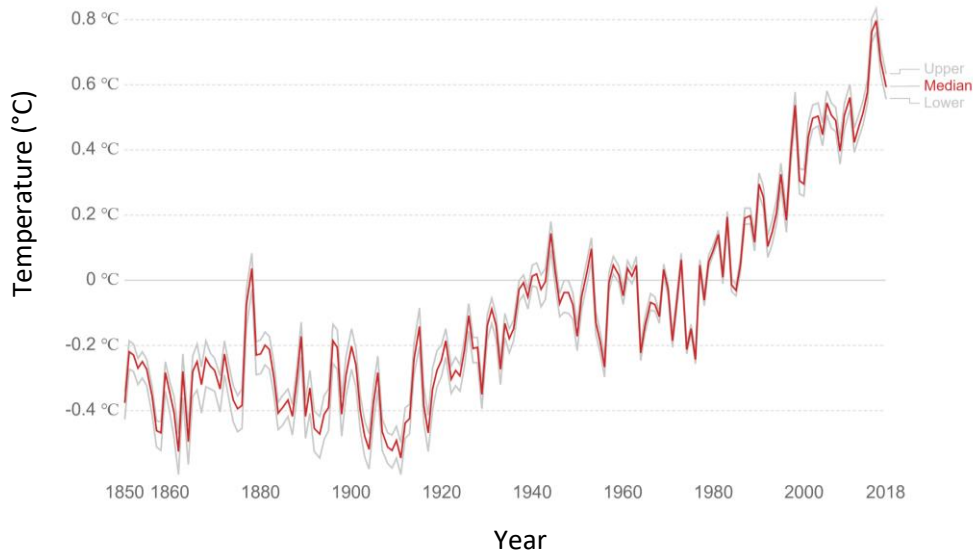


Figure 1.1. Global average land-sea temperature anomaly relative to the average temperature in 1961-1990, figure reproduced from [3] using data from [173].

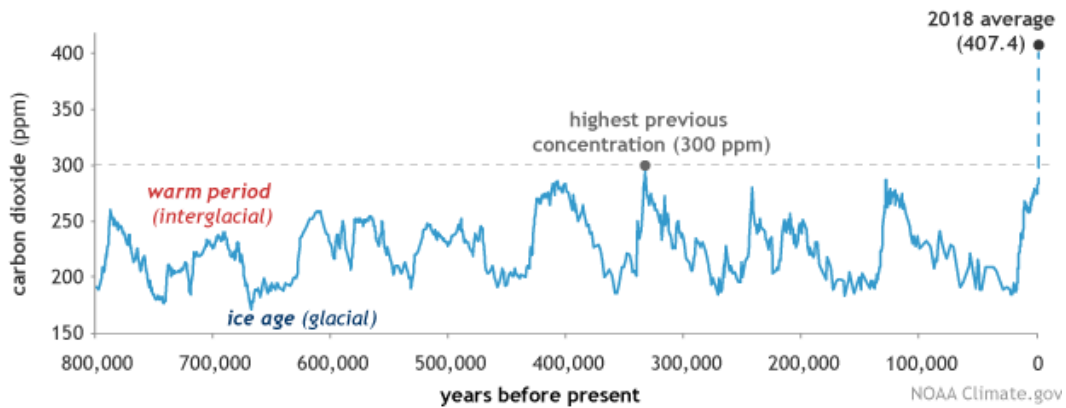
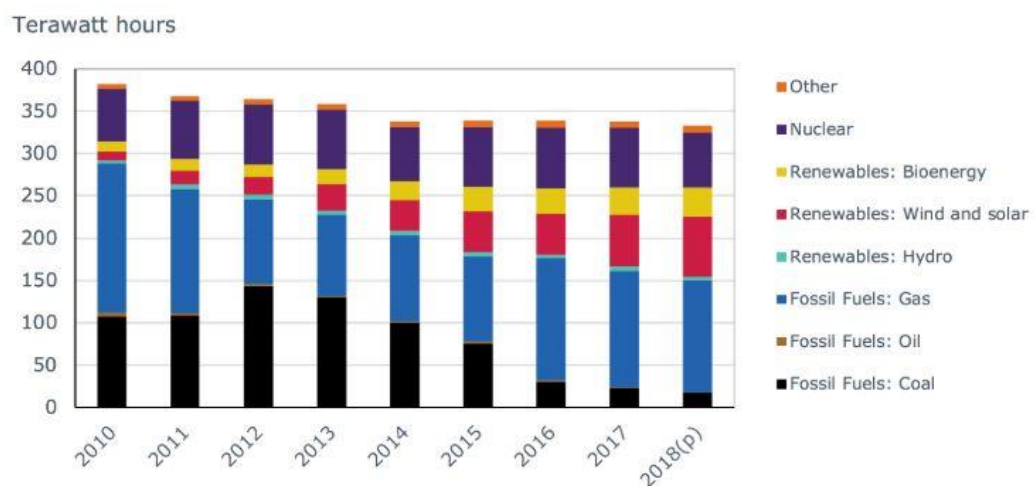


Figure 1.2. Global atmospheric carbon dioxide levels for the previous 800 000 years, figure reproduced from [6].

As the population increases and energy consumption per person rises, carbon emissions are getting larger and larger. World energy consumption is predicted to increase by 28% from 2015 to 2040 [8], leading to finite supplies of fossil fuels (such as coal, oil and natural gas) being consumed at an unsustainable rate. Therefore, the need for cleaner, alternative sources of energy is becoming more urgent, not only for sustainability of the economy but in order to minimise the effect of further climate change. This increasing demand for energy, coupled with environmental concerns, has sparked an interest into sources of renewable energy. Renewables do not contribute to the emission of GHG and are not depleted when used. Renewable energy can come from a number of sources, including

solar, wind, tidal, wave, biomass and geothermal. Some of these renewable energy sources are already being used commercially, while others are in the process of resource assessment and development of the technology for commercial viability.

The current state of the UK energy market is shown in Figure 1.3 which shows a growing contribution from renewable energy sources and a decreasing dependency on fossil fuels [2]. Since 2012 it is clear to see a decline in coal usage, working towards the government target of ceasing unabated coal power generation (the use of coal without any treatment to substantially reduce the emission of CO_2) by 2025 [2], as well as a large increase in the proportion of electricity generation from renewables.



Note: 2018 is a provisional estimate. Other includes pumped storage and other fuels.

Figure 1.3. UK electricity generation by technology type from 2010 – 2018, figure reproduced from [2].

The increase in electricity generated from renewable sources can be seen more clearly in Figure 1.4 which shows the long term trend over the past 18 years. This figure shows the small contribution that renewables had in the early 2000's (<10 TWh) compared to the generation of 110 TWh of electricity in 2018 [9]. In 2008, the European Commission (EC) published the 'EC package' detailing how Europe could meet the '20:20:20' targets set out in 2007. These targets were to reduce GHG emissions by 20%, improve energy efficiency by 20%, and to secure 20% of Europe's energy from renewable sources – all by 2020 [10]. For Europe to meet the target of a 20% share of final energy consumption from renewable sources by 2020, each member country was given an individual target with the UK's being 15%. In 2018 the UK achieved a final energy consumption from renewables of 11% as measured against the target under the 2009 EU renewable directive [11]. More recently, in

1 INTRODUCTION

June 2019 the UK government became the first major economy to pass a law committing to reduce GHG emissions to net zero by 2050 [12]. Therefore, progression in the renewable sector over the last 10 years has been positive, gathering public interest as well as governmental support.

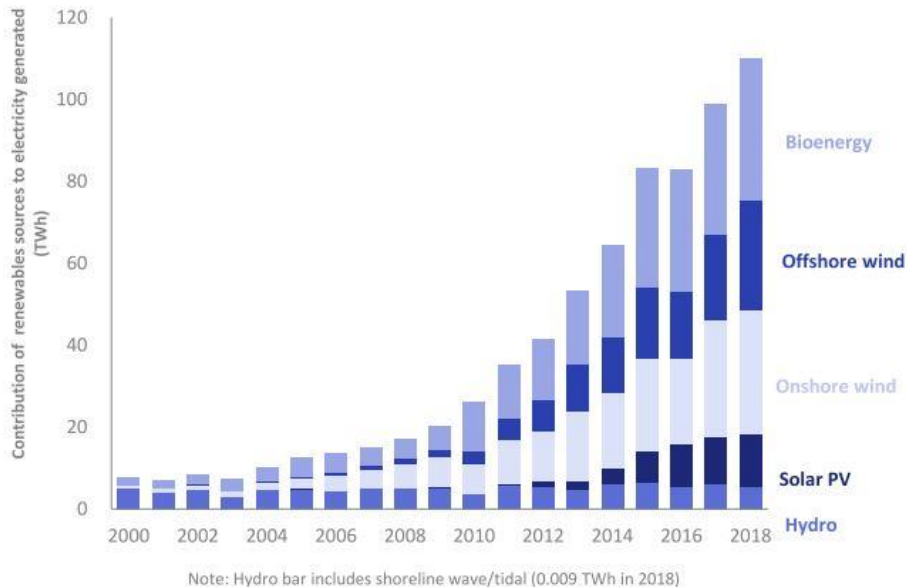


Figure 1.4. UK electricity generation by main renewable sources 2010 – 2018, figure reproduced from [9].

Figure 1.5 shows a comparison of the electricity generated by different technologies from Q1 2018 to Q1 2019. The renewable share of electrical generation increased to a record high of 35.8% for Q1 2019 in comparison to 30.5% in Q1 2018, while coal use reduced by 5.8%, from 9.3% to just 3.5% of UK power generation [11]. Of the 35.8% of electricity generated by renewables, Figure 1.6 shows the breakdown of each renewable technology, giving a total of 31.1 TWh generated by renewable sources for Q1 2019.

Solar Photo Voltaic (PV) and wind energy technologies are largely developed, with a recorded electricity generation of 13 TWh for solar PV, and 57 TWh for wind (30 TWh onshore, 27 TWh offshore) in 2018 [9]. Wind energy offers one of the cheapest generated electricity methods in the UK [13] and represents just under 50% of the UK's renewable installed capacity as well as having a 50% share of the total electricity generation by renewable energy sources [9]. There is an increase in electricity generation from both onshore and offshore wind in Q1 and Q4 each year when compared to Q2 and Q3. This is due to increased wind speeds in the winter months in comparison to the summer, proving the seasonal variations associated with electricity generation using the wind. Solar PV shows the opposite pattern with increased electricity generation during the summer

months when the percentage of sunny days is higher. The use of Solar PV equates to almost 30% of the UK renewable installed capacity although only produces a 12% share of the total electricity generation by renewable energy sources due to the significant influence of changeable seasonal weather [9].

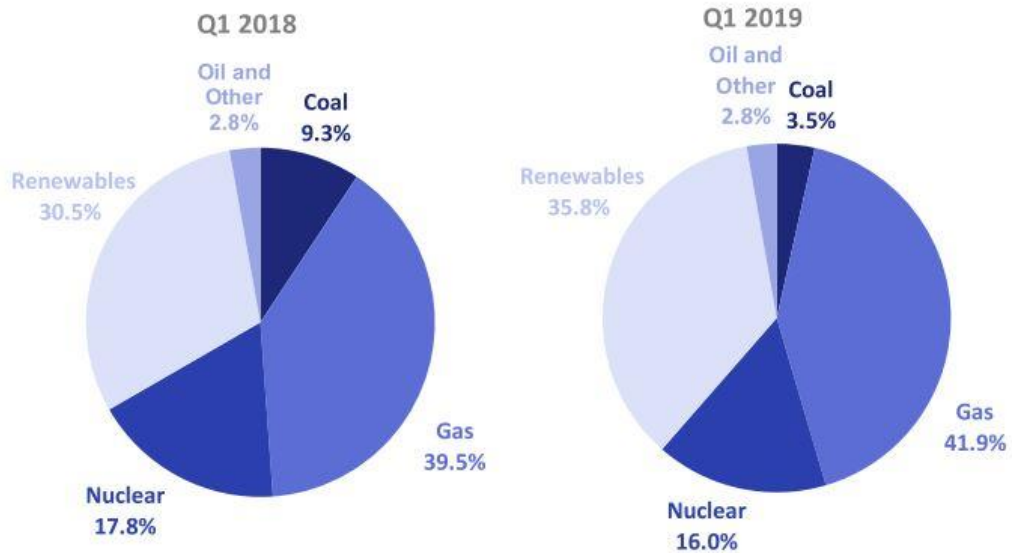


Figure 1.5. UK electricity generated in Q1 2018 and Q1 2019, figure reproduced from [11].

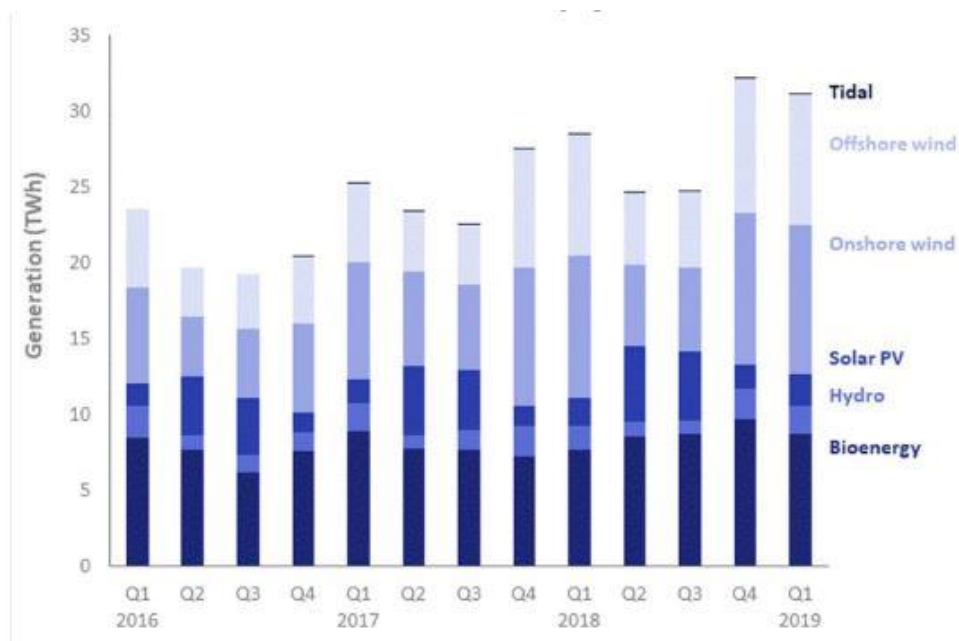


Figure 1.6. UK breakdown of renewable electricity generation, figure reproduced from [11].

Tidal and wave technologies generate the smallest amount of electricity from renewable resources at present, with just 9 GWh produced in 2018 from 20 MW of installed capacity [9]. However, these technologies mainly exist as pre-commercial devices and have great potential for increasing installed capacity and therefore electricity generation, imminently.

In contrast to the intermittency of both solar PV and wind power, tidal energy offers a predictable and potentially dependable source of renewable energy. However, the difficulty associated with production of these marine devices is apparent, with 15 MW of tidal capacity decommissioned since 2010 [14].

1.2 MARINE RENEWABLE ENERGY

Marine renewable energy involves exploiting the oceans' vast resource, in the form of wave and tidal energy sources, to generate electricity. The oceans cover around 70% of the earth's surface and is therefore an extensive renewable energy source which can be used to yield energy of a high quality [15]. The oceans also represent a highly predictable source of energy, unlike solar PV and wind which could never fully replace the use of fossil fuels due to their unreliability [16]. Europe is reported to hold 20-30% of the global tidal resource, of which 80% is located in and around the coastlines of the UK and France. If fully utilised using current technology, wave and tidal power could supply at least 10% of the UK's electricity [17].

1.2.1 Wave energy

Wave energy devices can generate electricity using the movement of the waves and can be designed to operate in deep/shallow, shoreline or coastal regions [18]. The amount of energy extracted depends on the height and wavelength of the wave. 5 MW of wave energy capacity has been deployed over the past 5 years with further projects in construction and another 15 MW of wave energy capacity permitted [18]. However, the wave industry remains relatively young with wave energy technology still being very diversified, with 8 main types of wave energy convertor widely identified [19]. The most advanced device types are 'oscillating water columns' and 'point absorbers' [20]. The biggest problem is the complex and diverse environment involved in wave energy extraction, with technological convergence and further progress needed to make it a commercially viable option.

1.2.2 Tidal energy

Tidal energy is progressing ahead of wave energy with current developments proving very successful. Gravitational forces of the moon and the sun cause the oceans to move, creating the tides. The flow of water between high and low tides creates currents which tidal devices can exploit to generate electricity [18]. Most locations experience semidiurnal tides which means they experience two tides per day. Significant differences in the tidal

range occur between spring and neap tides. Tidal ranges vary between locations along the coast, with the maximum UK tidal range being on the Severn Estuary where a range of 14m occurs at spring tides [21]. Tidal energy therefore has the potential to be the most predictable and dependable source of renewable energy, providing a base upon which future energy production estimations can be made.

Tidal energy can be divided into two main types of technology: tidal range and tidal stream. Tidal range technology, such as tidal barrages or tidal lagoons, has an estimated resource of 1000 GW in the world [22]. It uses the difference in height between water inside and outside an impounded area to drive turbines housed in the wall of the structure to generate electricity [23]. Tidal range is a proven technology which has been producing energy since the 1960s. The first major tidal range project was at the La Rance estuary in France with an installed capacity of 240 MW. This was the largest tidal power plant producing 500 GWh/year [24] until Sihwa Lake Tidal Lagoon was built in South Korea in 2011 with a capacity of 254 MW [22], [23]. Tidal lagoons use the same technology as tidal barrages, however they don't need to span an estuary, unlike tidal barrages, as they use a ring-shaped harbour wall which has less of an impact on the environment and uses less marine space.

Tidal stream technology, also known as hydrokinetic technology, uses the movement of water in tidal currents to extract kinetic energy and generate electricity. Horizontal Axis Tidal Turbines (HATT) are the main type of technology used with over 75% of companies developing full-scaled HATT devices over other Tidal Stream Turbine (TST) devices [14], [20]. This occurs in a similar manner to that of wind turbines extracting energy from the moving air. However, due to the slower flow speeds of water in comparison to air, the turbine blades can rotate slower and still extract a substantial amount of energy using smaller blades due to the increased density of water. A full review of the technologies used to exploit the tidal stream resource are discussed in Chapter 2.

The estimated total technical resource for tidal stream in the UK is 20.9 TWh using 8.3 GW of installed capacity [25]. The Crown estate has leased 26 suitable sites for tidal stream arrays, and if all these projects are realised, installed tidal stream capacity in the UK could reach 1200 MW [26]. Currently the UK has only 10 MW of operational tidal stream capacity [27] showing that the potential for progression in the tidal stream sector is significant. To rely on the contribution of tidal stream electricity production into the renewable energy mix, devices would need to have the ability to operate in deep water (>50m) and to exploit

slow moving currents (<2m/s), neither of which are currently economically or technologically possible. This would reduce the competition between developers for the most attractive tidal sites and increase the accessibility of many other potential tidal areas [26]. Currently, TSTs are generally mounted on, or moored to, the seabed which again limits the number of deployment sites. Floating platform technologies are being investigated by developers, such as Sustainable Marine Energy [28], and involves mounting tidal turbines onto a platform positioned near the water surface, allowing easier inspection and maintenance of the turbines, as well as reducing installation costs. However, different problems exist with this technology, such as the flow effects from surface waves and interference with shipping routes.

2016 saw the first tidal energy farms installed and connected to the grid [18]. The MeyGen project, located off the north coast of Scotland, is currently the biggest tidal stream demonstration project in the world with an installed capacity of 6 MW which generated 8 GWh in 2018 alone [14] and has exported a total of 17 GWh to the grid (up to June 2019) [29]. The MeyGen team claim that the project will be ‘transformational’ for the tidal stream industry giving confidence in the technology while securing a low carbon, affordable energy future.

This thesis looks to investigate the extraction of energy from the tidal flow using HATT technology, and to examine the impact of complex flow conditions, particularly due to wave-current interaction, on the loadings and performance of the turbine.

1.3 THESIS AIMS AND OBJECTIVES

The aim of this work was to investigate the loading imparted onto a HATT when subjected to wave and current flow conditions, using numerical modelling and experimental validation. This was achieved using the following objectives:

1. Investigation of the effects and significance, on turbine loadings and performance, of profiled current-only conditions in comparison to uniform current-only conditions
2. Development of a wave-current numerical model, using CFD, that is representative of experimental test facility flow conditions
3. To examine the turbine performance and transient loadings under regular waves and profiled current conditions
4. Validation of numerical CFD models using lab-scale experimental data

1.4 THESIS LAYOUT

Chapter 1: Introduction

Examines the drivers for this research into tidal energy as well as setting out the main aims and objectives of this thesis.

Chapter 2: Literature review

Reviews the relevant literature, outlining the status of experimental and numerical research in the marine energy sector, to identify gaps in the knowledge of the industry.

Chapter 3: Theory

Presents the applicable theory used to numerically model regular waves superimposed upon a current flow, as well as outlining the calculations in assessing the turbine performance characteristics.

Chapter 4: Experimental testing methodology

Explains the experimental methodology used to obtain data for the validation of Computational Fluid Dynamics (CFD) models.

Chapter 5: Numerical modelling methodology

Describes the numerical methodology used in creating CFD models, by applying the theory presented in Chapter 3.

Chapter 6: CFD model optimisation

Presents and discusses the methodology used in optimisation of the CFD models.

Chapter 7: Turbine performance under current-only conditions: uniform and profiled velocity gradients

Discusses the impact of different flow conditions on the performance of the TST.

Chapter 8: Development of wave-current numerical model using CFD: regular waves with uniform current conditions

Explains the development process of the wave-current CFD model.

Chapter 9: Turbine performance under wave-current flow conditions: regular waves with profiled velocity gradients

1 INTRODUCTION

Presents the results of the most complex flow conditions examined in this thesis and how they impact the turbine loadings and performance.

Chapter 10: Conclusions and future work

Summarises the main conclusions of the work presented in this thesis as well as the implications this has on the industry. Recommendations for future work are also considered.

Appendices: A. includes the expressions used to setup the CFD models

B. details the Matlab scripts used in the post processing of data

C. presents a list of the publications written by the author related to the work in this thesis

2 LITERATURE REVIEW

This chapter introduces and outlines relevant work that has been previously performed in the field of tidal stream energy research. This literature review presents the different approaches used in extracting energy from the tidal flow, detailing the types of device currently under development. An analysis of full-scale projects is then carried out to investigate the challenges with deployment and operation of tidal devices in the marine environment. Smaller, model-scale laboratory testing is also reviewed to examine how useful this type of turbine testing can be when considering the scalability of the results. Numerical modelling is a widely used tool which allows tidal stream research to be carried out at a considerably reduced cost. The modelling techniques used are investigated, as well as examining the methods used to calculate the loadings and performance of the numerical results output. This chapter generally outlines the areas in which research is being undertaken to move the tidal stream sector to commercial viability and contribute towards the energy targets outlined in Chapter 1.

2.1 TIDAL STREAM TECHNOLOGY AND DEVICES

Tidal stream devices are designed to exploit the movement of the tidal currents and convert kinetic energy into electrical energy. The main device technology being used by current developers is the Horizontal Axis Tidal Turbines (HATT), with over 75% of companies researching the design and manufacture of full-scale HATT devices [14], [20]. Although this thesis focusses on the HATT, Vertical Axis Tidal Turbines (VATT) and alternative device types will also be highlighted in the following section. Examples of some of the active and decommissioned tidal technologies are given in Table 2.1 and Table 2.2.

TABLE 2.1. A SUMMARY OF RECENT ACTIVE TIDAL TECHNOLOGY.

Developer name	Device name	Technology type	Size	Rated capacity	No. devices	Status
ACTIVE						
SIMEC Atlantis [30]	AR15000	3-bladed HATT	D = 18m	1.5 MW	1	Grid connected: 2016
Andritz Hydro Hammerfest [174]	AR2000	3-bladed HATT	D = 20-24m	2 MW	-	In construction: 2019
	HS1000	HATT		1 MW	3	Grid connected: 2016
Verdant Power [50]	Gen4 Free Flow	3-bladed HATT	D = 5m	35 kW	6	Grid connected: 2006 – 2009
Sabella [175]	Gen5 Free Flow Triframe	3-bladed HATT	D = 5m	105 kW (3 x 35 kW)	1	Prototype testing at EMEC: 2020
	D03-30	6-bladed HATT	D = 3m	30 kW	1	Deployed: 2008 (12 months)
	D10-1000	6-bladed HATT	D = 10m	1 MW	1	Grid connected: 2015 (removed: 2016)
	ICE D10-1000	6-bladed HATT	D = 10m	1 MW	1	3 year test started Oct 2019
	PHARES D12-500	5-bladed HATT	D = 12m	1 MW (2 x 500 kW)	1	In construction: 2019
Magallanes Renovables [176]	ATIR Ocean_2G	Floating Platform	D = 19m	2 MW (2 x 1 MW)	1	Prototype testing at EMEC: 2019
Sustainable Marine Energy [37]	PLAT-I: SIT250 instream turbines	Floating platform with 3-bladed HATT	D = 4/6.3m	280 kW (4 x 70 kW)	1	Deployed: 2018
	PLAT-O: SIT250 instream turbines	Submerged buoyant platform with 3-bladed HATT	D = 4/6.3m	280 kW (4 x 70 kW)	1	Prototype testing at EMEC: 2016
Minesto [43]	DeepGreen	Tidal kite	D = 1.5m Wingspan = 12m	0.5 MW	1	Deployed: 2018
Nautricity [177]	CoRMaT	Contra-rotating turbine (3-bladed clockwise HATT, 4-bladed anticlockwise HATT)	D = 10m	500 kW	1	Deployed: 2017 Recovered: 2018 for further development
Orbital Marine Power Ltd [178]	SR2000	Floating platform with 2 x 2-bladed HATT	D = 16m	2 MW (2 x 1 MW)	1	Grid connected: 2017 (Removed: 2018 to make way for Orbital O2)
	Orbital O2	Floating platform with 2 x 2-bladed HATT	D = 20m	2 MW (2 x 1 MW)	1	To be deployed at EMEC: 2020
EEL Energy [41]	-	Flexible membrane	-	1 MW	-	Scheduled production: 2020

TABLE 2.2. A SUMMARY OF RECENT DECOMMISSIONED TIDAL TECHNOLOGY.

Developer name	Device name	Technology type	Size	Rated capacity	No. devices	Status
DECOMMISSIONED						
OpenHydro [179]	-	Open centre HATT	D = 16m	2 MW	1	Grid connected: 2018 Decommissioned: 2018
Marine Current Turbines [31]	SeaGen	2-bladed HATT	D = 16m	1.2 MW (2 x 600 kW)	1	Grid connected: 2009 Decommissioned: 2017
Alstom (previously Tidal Generation Ltd) [180]	Deepgen	3-bladed HATT 3-bladed HATT		500 kW (1st Gen.) 1 MW (2nd Gen.)	1	Grid connected: 2010 – 2012 Deployed: 2013 Decommissioned: 2016
Tocardo [181]	T2 Turbine	3-bladed HATT	D = 18m	250 kW	1	Deployed at EMEC: 2017 Decommissioned: 2019
Voith Hydro [182]	HyTide 1000	3-bladed HATT	D = 13m	1 MW		Deployed: 2013 Decommissioned: 2015

2.1.1 Horizontal Axis Tidal Turbines

HATTs extract energy from the tidal currents in much the same way as wind turbines extract energy from the moving air. Water is much denser than air, so HATTs can generate equivalent amounts of electricity but by using a much smaller rotor diameter (\emptyset) than used for wind turbines [30]. Consequently, HATTs can be deployed closer together. There are many different designs of HATT, varying in the number of turbine blades present and how the blades are secured and controlled, yet the rotational axis of a HATT is always parallel to the flow. A Transverse Horizontal Axis Water Turbine (THAWT) is also classed as a horizontal axis turbine, but the rotational axis is perpendicular to the flow instead. A selection of the main developers and their device designs using HATT technologies are given below.

2.1.1.1 SIMEC Atlantis Energy: AR1500/AR2000

The Atlantis turbine division of SIMEC Atlantis Energy is a union between Marine Current Turbines SeaGen team and the Atlantis Turbine and Engineering Services team, which were brought together in 2015. The Atlantis turbine technological development has predominantly been through 3-bladed HATTs which are the most conventional type of Tidal Stream Turbine (TST)¹. SIMEC Atlantis Energy developed the AR1500 turbine which has an 18m rotor diameter, rated power of 1.5 MW and a design life of 25 years with a quarterly maintenance cycle [30]. One AR1500 turbine has been deployed in the Pentland Firth region, between Scotland's north coast and the island of Stroma, along with three similar Andritz Hydro Hammerfest (AHH) turbines totalling 6 MW capacity as phase 1 of the MeyGen project [14]. 17 GWh has been exported to the grid since initial installation in 2018 (up to June 2019) [29]. Development of the AR2000 turbine has been undertaken by SIMEC Atlantis Energy in collaboration with GE, to build upon the successes of the AR1500. This turbine has a rotor diameter of 20-24m with a cut-in speed of <1 m/s, rated power of 2 MW and features a new mechanical pitch and yaw system with an upgraded health monitoring system [30]. The main improvement of this latest model is the evolution of a subsea hub that allows for multiple devices to be connected, reducing the impact of cabling so that only one power export cable is required. SIMEC Atlantis Energy describes this turbine as a 'record breaking system' with expected installation in the future MeyGen project phases as

¹ Other developers using 3-bladed HATTs are AHH and Verdant Power, as shown in Table 2.1. Alstom, Voith Hydro and Tocardo previously developed 3-bladed HATTs but have recently been decommissioned, as shown in Table 2.2. Nautricity have developed a contra rotating device with a 3 and 4-bladed rotor called CoRMaT, while Sabella have developed a 6-bladed HATT.

well as being on sale to commercial developers from late 2019. Figure 2.1 shows the AR1500 and AR2000 SIMEC Atlantis Energy tidal turbines.

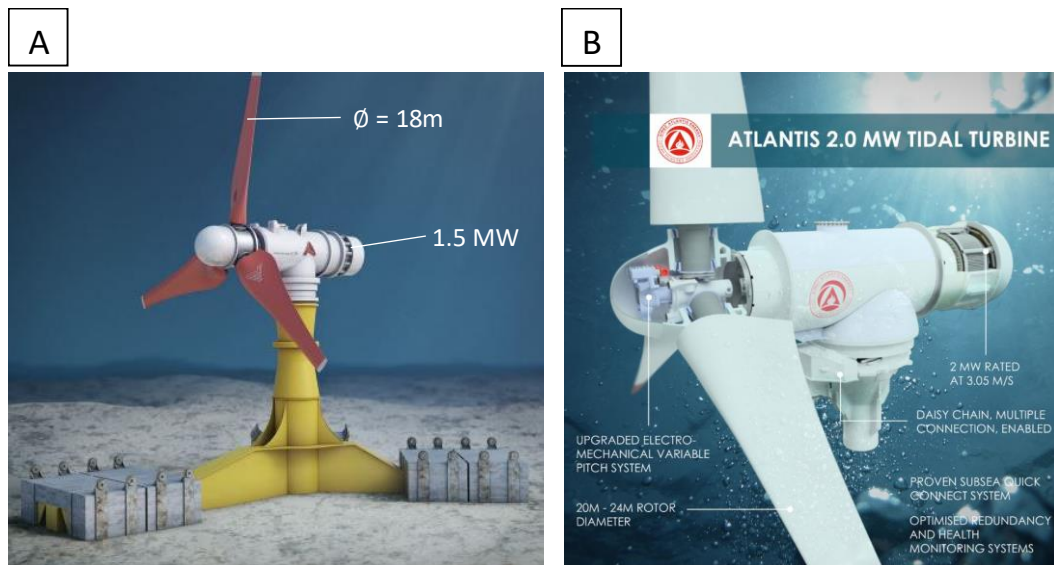


Figure 2.1. The A) AR1500 and; B) AR2000 tidal stream turbines developed by SIMEC Atlantis Energy, figure reproduced from [30].

2.1.1.2 Marine Current Turbines: SeaGen

The SeaGen tidal stream system was installed by Marine Current Turbines in Strangford Lough, Northern Ireland in 2008. The concept combines two 600 kW, 2-bladed, 16m diameter turbines mounted on a single, surface piercing monopile support [31], as shown in Figure 2.2. The two turbines were secured to a crossbeam that could be moved up and down the monopile structure. This design allowed the turbines to be brought above the water surface to ease inspection and maintenance procedures [32]. The 1.2 MW prototype was the first tidal stream device to be connected to the national grid with 15 GWh of electrical generation exported to the grid from 2009 – 2016 [33], [34]. After being extremely successful in the research and development of tidal devices, the SeaGen system was the first commercial scale turbine development to be decommissioned, beginning in 2017. The developer of SeaGen, Marine Current Turbines, merged with Atlantis Resources (now SIMEC Atlantis Energy) in 2015 to consolidate two established tidal technologies and create “one of the largest portfolios of tidal current power projects in the UK” [30].

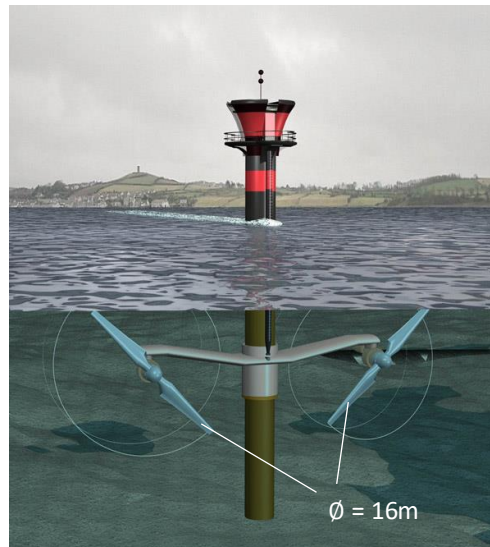


Figure 2.2. The SeaGen tidal energy system developed by Marine Current Turbines, figure reproduced from [31].

2.1.1.3 Sustainable Marine Energy: PLAT-I/PLAT-O

Sustainable Marine Energy are a UK turbine platform developer who merged with the tidal energy business of Schottel Hydro in 2018 to produce inshore (PLAT-I) and offshore (PLAT-O) energy platforms, shown in Figure 2.3. PLAT-I has been developed for sheltered inshore locations and is the first platform in a commercial deployment, currently installed at Grand Passage, Nova Scotia [35]. The 280 kW trimaran platform is fitted with four 70 kW SIT250 in-stream turbines developed by Schottel hydro [36]. The platform has a modular design with 'swing up' turbines which makes shipping to site and maintenance much easier. The platform uses a turret mooring which allows the platform to align with the flow in any direction for maximum power extraction. PLAT-O has been designed for offshore deployment and is the world's first submerged tidal energy platform. PLAT-O sits just below the water surface in the optimum position to give an enhanced energy yield. The platform is taut moored to the seabed using an anchoring system and uses the same previously mentioned SIT250 Schottel hydro turbines. The first prototype was tested in the south of England and at the European Marine Energy Centre (EMEC) in Orkney in 2016 [37]. Since then, Sustainable Marine Energy have focused on the development and testing of the PLAT-I tidal energy platform.

Other developers researching floating platform technologies include Magallanes Renovables and Orbital Mariner Power Ltd as shown in Table 2.1.

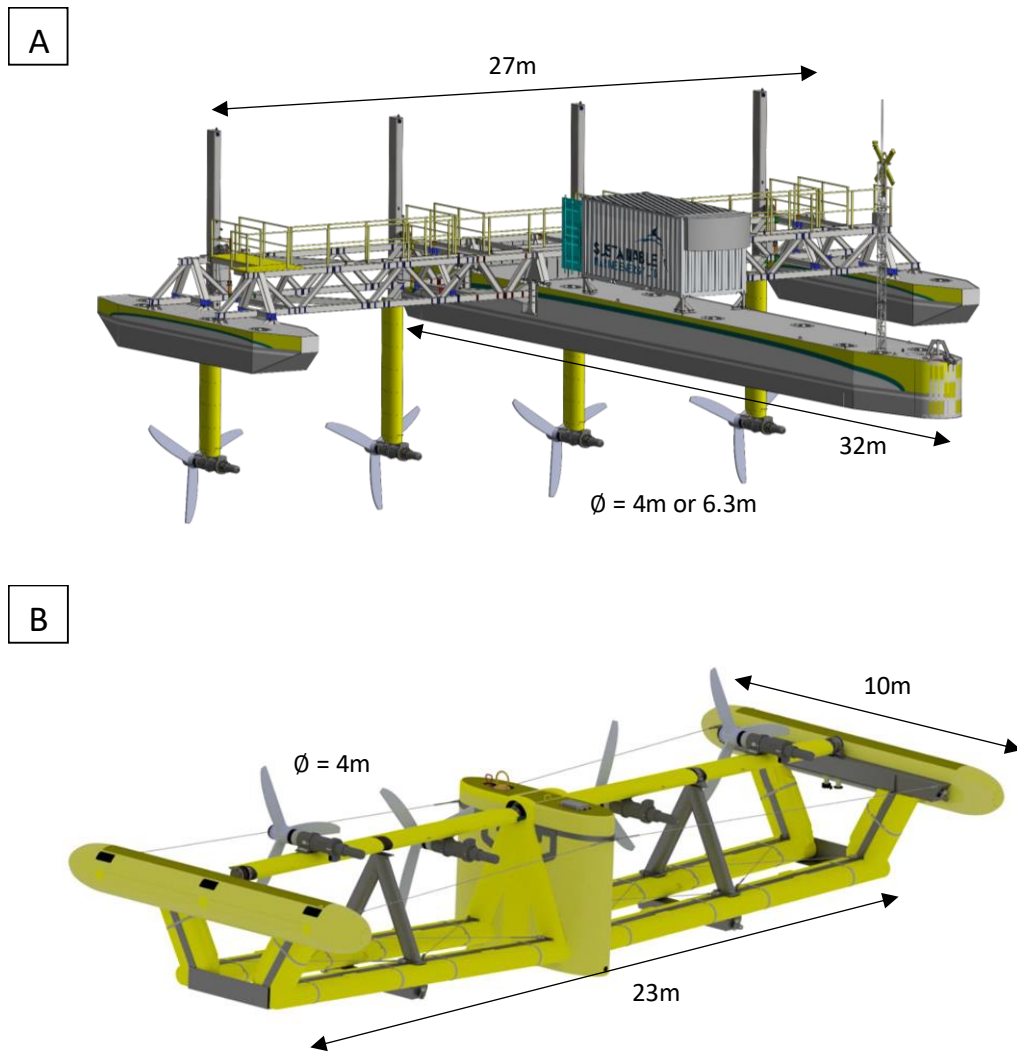


Figure 2.3. The A) PLAT-I and; B) PLAT-O tidal energy platforms developed by Sustainable Marine Energy, figures reproduced from [35] and [37].

2.1.2 Vertical Axis Tidal Turbines (VATTs)

VATTs extract energy from the tidal currents with their rotational axis perpendicular to the tidal flow and the seabed. The main advantage of a VATT is that they can operate regardless of the tidal flow direction and without pitch or yaw mechanisms [38]. However, VATTs tend to have a lower efficiency than HATT devices and require a starting mechanism, as unlike many HATTs they do not self-start [39]. There are currently very few VATT devices in development in comparison to HATTs [40]. There are two main types of VATT categorised depending on the design of the turbine blades, straight bladed VATTs, eg. the Darrieus turbine, and helical shaped blades, eg. the Gorlov turbine [39]. Figure 2.4 shows the arrangement of a typical straight and helical bladed, Darrieus and Gorlov VATT.

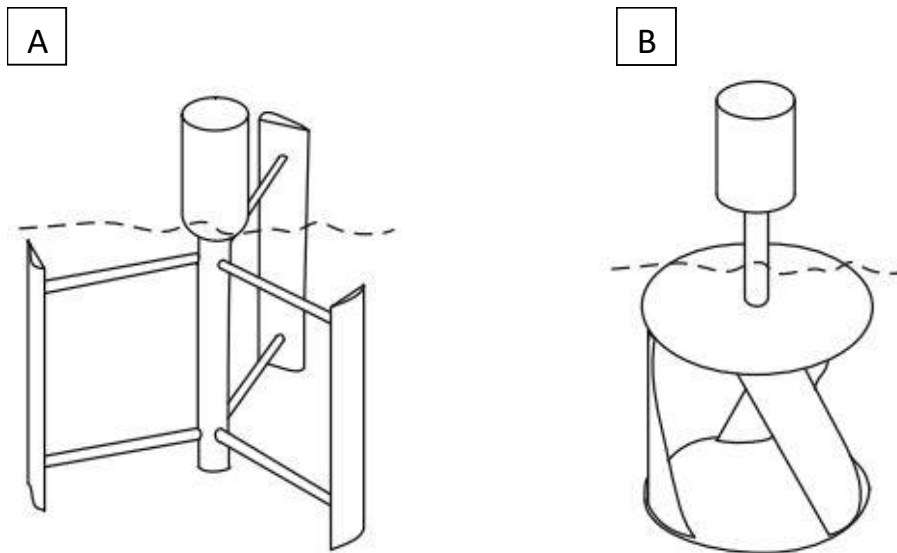


Figure 2.4. The A) Darrieus and; B) Gorlov VATT, figure reproduced from [39].

2.1.3 Other tidal devices

With developers predominantly choosing to design and manufacture HATT and VATT devices, there are only a small number of companies developing alternative devices. An example is the use of oscillating devices which can use a flexible membrane design to allow undulation of the membrane under moving fluid pressure to generate electricity. Flexible membranes have few moving parts so are relatively easy to manufacture, however, care must be taken over selection of the material to minimise fatigue. EEL Energy are a French developer who have successfully tested the first commercial flexible membrane prototype in open sea trials, reaching an average power of >4 kW [41]. Their objective is to develop a 225m² (15x15m) device capable of producing 1 MW at 2.5 m/s, scheduled for industrial production in 2020 [42]. Figure 2.5 shows the flexible membrane EEL Energy device.

Another example of an alternative device is the DeepGreen device developed by Minesto [43]. The DeepGreen technology consists of a turbine attached on the underside of a wing and moves through the water in a figure of 8 shape, similar to the movement of a kite. Hydrodynamic lift, created by the flow of water over the wing, pushes the device upwards reaching speeds up to 10 times the current velocity. This allows operation at low flow speeds (1.2 - 2.4 m/s) as the relative flow over the turbine is actually much greater. Deployment must be at depths of 60-120m as the device is tethered to the seabed using an 80-120m tether. Currently DeepGreen is the only tidal technology which can utilise the tidal resource at this depth. However as a consequence, this will dictate the size of the figure of 8 sweep which gives each device a relatively big footprint. In June 2018, Minesto installed a

0.5 MW demonstrator device in Holyhead Deep, North Wales. This device has a turbine diameter of 1.5m and wingspan of 12m as shown in Figure 2.6. Following successful deployment, further DeepGreen devices will be installed to reach a commercial demonstration array capacity of 10 MW [44].

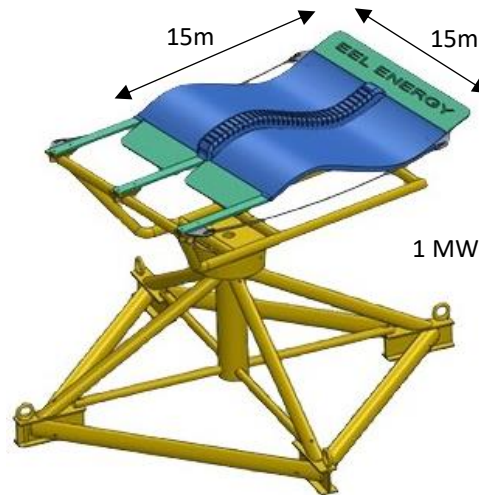


Figure 2.5. The flexible membrane device developed by EEL Energy, figure reproduced from [41].

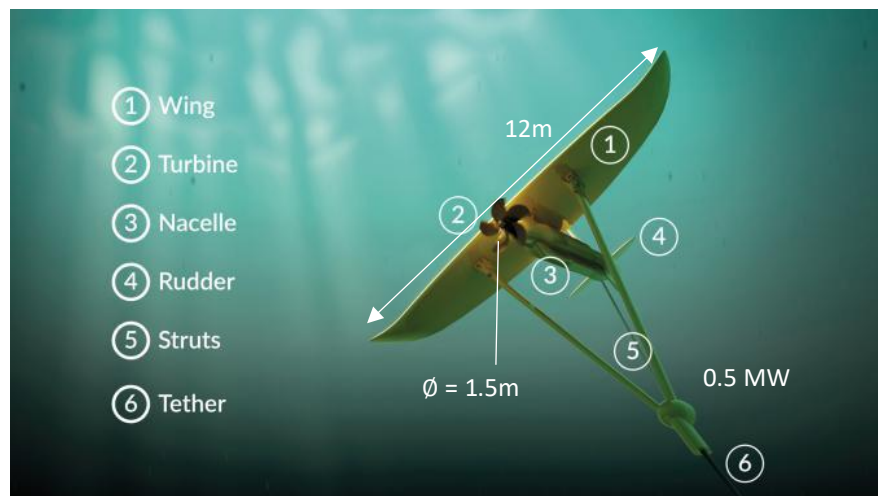


Figure 2.6. The DeepGreen 'kite' device developed by Minesto, figure reproduced from [43].

2.2 EXPERIMENTAL TESTING

Currently, the biggest problem with energy extraction in the marine environment, is the complex and diverse flow conditions, as detailed by [45]. Device components must be able to withstand substantial, spatial and temporal sub-surface forces generated by tidal

currents, surface waves and turbulence. It is therefore important to quantify the magnitude of these forces prior to the full-scale design, manufacture and testing of a device.

Experimental testing is carried out to evaluate tidal stream devices at various stages of their development. These development stages are measured using Technology Readiness Levels (TRLs) on a scale of 1 – 9, with concept formulation at TRL 1-3 and testing a commercial demonstrator for an extended period at TRL 9 [46]. Physical testing can be conducted at custom-built laboratory facilities as well as in coastal locations. Model-scale testing is usually a precursor to full-scale testing due to the costs involved with the design and manufacture of tidal energy devices. In order to directly compare between model-scale and full-scale testing, the geometric and dynamic scalability needs to be considered. Provided that at model-scale and full-scale, the same Reynolds number (Re) and Tip Speed Ratio (TSR) are used, the non-dimensional performance characteristics measured in model-scale testing will be representative of the turbine at full-scale. Once the flow conditions become independent of Re , the scaling process is significantly simplified [47]. Model-scale testing in a laboratory provides a controlled environment in which various flow conditions can be generated. Changes between tests can then be isolated to identify the subsequent effects on the tidal device. The two main types of testing facility used are tow tanks or recirculating flumes. Coastal device testing gives a more realistic insight into device performance in flow conditions featuring interactions between velocity profiles, turbulence and waves. An assessment of existing experimental testing using HATT devices is detailed in the following sections, divided into full-scale ocean device testing and model-scale laboratory device testing.

2.2.1 Full-scale ocean device testing

Full scale ocean device testing provides realistic flow conditions and performance results in comparison to the controlled, idealised conditions generated in experimental facilities. Model-scale laboratory testing is necessary in the evolution of TST technologies but full-scale prototype testing in coastal surroundings is the only way to fully experience the complex operating conditions presented by the ocean environment at specific tidal sites.

The first HATT array in the UK was installed and connected to the grid in 2016 [18]. 6MW (4 x 1.5 MW) of tidal capacity was deployed as part of the MeyGen project, by developer SIMEC Atlantis Energy [29]. MeyGen is currently the largest planned tidal stream project in the world, with the ability to develop up to 398 MW (< 256 turbines) of tidal stream capacity [29].

The launch of a €46.8 million project named Tidal Stream Industry Energiser Project (TIGER) was announced on October 16th 2019 [48]. The project, comprising 19 partners, aims to reduce the generating costs of tidal stream energy from the existing 300€ MW/h to 150€ MW/h by 2025, with an EU target to reach 100€ MW/h by 2030 [49]. TIGER aims to deploy 8 MW of new tidal capacity using the technology developed by SIMEC Atlantis Energy, amongst other developers, although a total of 4 GW of exploitable tidal energy resource is present in the Channel regions of the UK and France [49].

Another developer, Verdant Power, has installed four 5m diameter turbines in the East river, New York City, as part of the Roosevelt Island Tidal Energy (RITE) project [50]; this equates to a capacity of 140 kW, with future plans to install up to 30 turbines totalling approximately 1 MW. Each of these projects are reported as being extremely promising and suggest tidal stream energy extraction is progressing into the realms of being a commercially viable technology. However, because these are all commercial installations, figures relating to cost and energy production are confidential to each company and very little information is released into the public domain. For this reason, research must advance in alternative ways, such as using model-scale laboratory testing which is cheaper yet still informative.

2.2.2 Model-scale laboratory device testing

As stated previously, there are two types of laboratory testing facilities that are widely used to test tidal energy devices: tow tanks and recirculating flumes. These facilities are used to examine the response of a tidal device when exposed to various flow conditions. Common characteristics investigated include turbine performance and downstream wake generation as a result of different flow features [51]–[53]. These features are shown in Figure 2.7, comprising upstream turbulence, uniform/profiled current velocities, and regular/irregular waves. The following section details relevant studies carried out in tow tanks and recirculating flumes using a HATT.

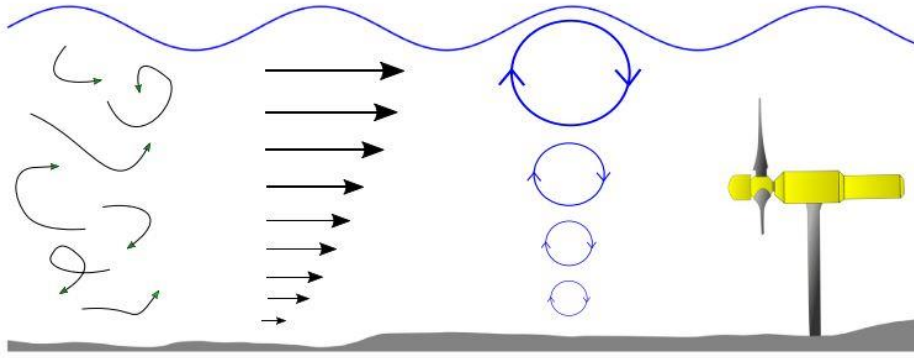


Figure 2.7. The different complex flow features present that can interact with turbine performance; (L-R) turbulence, velocity profiles and wave recirculation, figure reproduced from [85].

2.2.2.1 Experimental facilities

2.2.2.1.1 Tow tank

A tow tank consists of a large body of water enclosed in a basin and uses a carriage spanning the basin to mount and tow a device through the water. Test times are therefore limited by the length of the tank and the speed of the carriage. Figure 2.8 shows an example of a tow tank at the Kelvin Hydrodynamic Laboratory (KHL) at the University of Strathclyde. The uniformity of the water provides idealised conditions for uniform current flow testing as there is no turbulence present. This creates a very controlled environment but lacks the ability to reproduce highly turbulent, more realistic flow conditions [54]. Using wave paddles installed at one end of the tow tank and a beach region at the opposite end, it is possible to study the effects of wave generation. The beach region helps to dissipate waves, preventing reflection once the waves reach the end of the tank. This methodology does not fully represent wave-current interaction as there is no change in the angular frequency of the waves as a result of the Doppler shift. This is because there is no current present limiting the ability of tow tanks to simulate wave-current interaction [55]. Often, it is required to wait for the water to settle in between tests to ensure the replication of flow conditions each time; this is especially true between tests involving waves.



Figure 2.8. The Kelvin Hydrodynamic Laboratory (KHL) tow tank located at the University of Strathclyde.

2.2.2.1.2 *Recirculating flume*

Recirculating flumes are usually shorter in length than a tow tank as they have a working section within the flume generating the desired flow conditions. Figure 2.9 shows an example of a recirculating flume at the French Research Institute for Exploitation of the Sea (IFREMER), Boulogne-Sur-Mer. An advantage of this type of setup is that the flume can maintain the set flow conditions for long periods of time, not restricting the length of each test. The inlet velocity can be controlled to introduce velocity profiles or by using flow straighteners to generate a uniform flow [56]. Turbulence can also be generated at the inlet with most flumes possessing a base turbulence level of around 3-5% with the capability to

increase this level [54], [56], [57]. Many flumes are also capable of producing waves, allowing wave-current interaction which is more representative of ocean conditions than those generated in a tow tank. Recirculating flumes often have a restricted cross-sectional area which must be accounted for. Otherwise, this can increase the blockage ratio between the cross-section of the flume and that of the turbine being tested, leading to an increase in the value of the turbine performance characteristics [58]. An example of a flume that can generate a much wider range of flow conditions is a facility at the University of Edinburgh called FloWave, as shown in Figure 2.10. FloWave is a unique, circular testing facility which can generate different combinations of waves and currents in any relative direction across the central test volume [59].

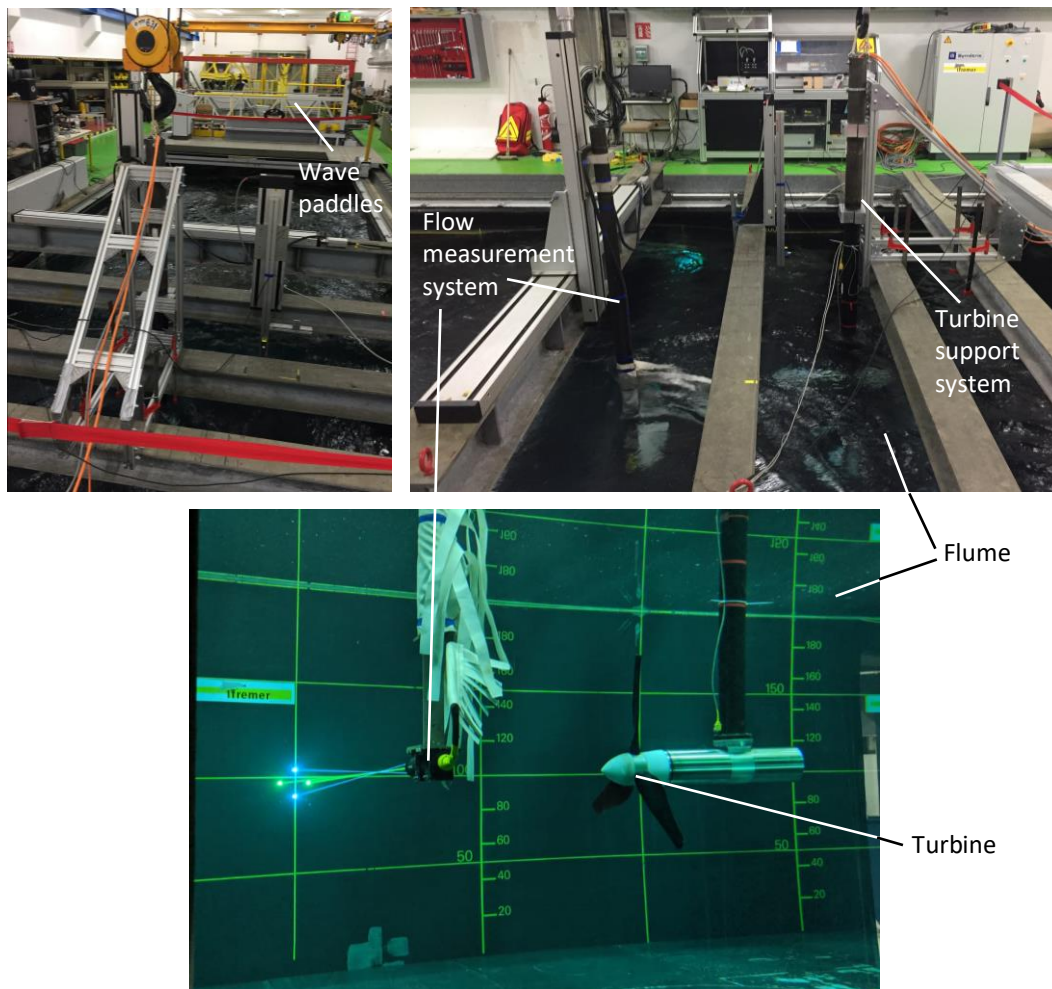


Figure 2.9. The IFREMER wave-current flume located in Boulogne-Sur-Mer, France.



Figure 2.10. The FloWave ocean energy research facility located at the University of Edinburgh, figure reproduced from [183].

2.2.2.2 Turbine testing

2.2.2.2.1 Current flow conditions

Experiments performed under uniform flow conditions allow researchers to fully characterise a TST in both a tow tank and flume facility. A comparison between tow tank and recirculating flume experimental facilities was carried out in a series of round-robin tests by Gaurier et al. [54]. The same 3-bladed, 0.7m diameter model-scale tidal turbine was tested in four different facilities to explore the sensitivity of the results to the choice of facility. Two tow tanks (Consiglio Nazionale delle Ricerche Istituto di Ingegneria del Mare (CNR-INM²): 220m long and KHL at the University of Strathclyde: 76m long) and two recirculating flumes (IFREMER and CNR-INM) were used. The torque, drag and inflow water velocity all showed very similar results in all facilities. However, greater differences were observed in the fluctuation of the results between testing in a tow tank and flume. The greatest variations were observed in the time-varying fluctuation in the power and thrust coefficients as a result of the turbulent inflow present in a recirculating flume. A study by Allmark et al. [60] shows agreement with these findings as results were found to be highly repeatable when using a tow tank due to the consistent conditions provided. A 0.9m diameter HATT was used by [60] and was tested in the CNR-INM, Rome tow tank to investigate the average turbine performance characteristics.

The immersion depth of the turbine is an important characteristic as faster flow velocities are usually present in the upper 50% of the water depth [61]. It would therefore be

² Previously known as Istituto Nazionale Per Studi Ed Esperienze Di Architettura Navale (INSEAN).

preferable to place a device near the water surface, yet interaction between the turbine and the water surface must be investigated. Bahaj et al. [62] performed experiments using a 3-bladed, 0.8m diameter HATT in the Southampton Institute, 60m tow tank. The performance of the turbine was investigated under various flow conditions (0.8-1.5 m/s), yaw angles (0-30°) and tip immersion depths (shallow: 0.19 ϕ and deep: 0.55 ϕ). Maganga et al. [63] carried out a similar set of experiments to [62] using a 0.7m diameter, 3-bladed HATT but instead using the IFREMER flume. This study examined the effect of yaw angle (-10 to 20°) as well as the effect of depth of the turbine hub beneath the free surface (0.94 ϕ , 1.57 ϕ and 2.04 ϕ). [62] found that the power extracted by the turbine when operating at shallow tip immersion (0.19 ϕ) was reduced by 10-15% while the thrust results also decreased by 5% in comparison to deep tip immersion (0.55 ϕ). The proximity of the free surface is significant as it can prevent full expansion of the wake which reduces the pressure difference across the turbine. This effect is what causes the decrease in the production of power and thrust at shallow tip immersion. Conversely, [63] saw that there was no significant difference in results between each of the different hub depth settings investigated (0.94 ϕ , 1.57 ϕ and 2.04 ϕ). Converting these hub depth settings into tip immersion depths (0.44 ϕ , 0.93 ϕ and 1.54 ϕ), it can be seen that [62] investigated a shallower setting and so it could be that the specified tip immersion depths in this current study [63] were not shallow enough to see an interaction with the free surface.

In reality, the magnitude and direction of tidal currents is dictated by headlands, tidal channels and seabed bathymetry, which can lead to strong tidal asymmetry in certain locations [64]. Therefore, an analysis on the impact of flow misalignment also needs to be performed, to determine if yaw systems on TSTs are necessary. [63] found that increasing the yaw angle (-10 to 20°) decreases turbine performance, as also found by [62] at 0 to 30° yaw. Both studies found that increasing the yaw angle gave a reduction in power and thrust yet only the average performance characteristics were analysed to examine the turbine performance in various operating conditions. Further investigation into the fluctuation in the loading cycle and a breakdown of the individual component loadings would improve operational knowledge and increase the reliability of predictions for the fatigue life.

A study by Tedds et al. [56] investigated the effect of pitch angle and solidity (number of blades) of a 0.5m diameter, HATT using the recirculating water channel at the University of Liverpool. The benefit of using a flume to carry out experimental testing is the unlimited operational time period as well as the inclusion of free stream turbulence and velocity profiles. It was found that the peak coefficient of power (C_p) was unaffected by solidity,

however, the coefficient of thrust (C_t) showed a big increase as the number of blades increased. This is contrary to the findings of Allmark et al. [65] and Hau [66] who found that peak C_p increased as the solidity increased, for tidal and wind turbines respectively.

2.2.2.2.2 *Turbulence and wake studies*

Researchers often try to reproduce controlled but realistic test conditions which involves adding different complexities into the flow regime [67], [68]. Waves and turbulence can introduce unsteady, fluctuating characteristics into the flow, which can be detrimental to the fatigue life of the turbine [69]. Due to the absence of any current flow in a tow tank, it is possible to produce unsteady upstream conditions as described by [70], but not the turbulence that is representative of an ocean environment. Therefore, turbulence testing is usually carried out in a flume environment.

The level of Turbulence Intensity (TI) is of great interest in marine turbine studies, as many identified potential deployment sites are highly turbulent with site specific conditions varying throughout the water column [67]. Interaction of waves will increase the turbulence towards the water surface, while turbulence levels at the seabed depend on the seabed topography upstream of the site [68]. Knowledge of the complex nature of unsteady loading on individual turbine components is necessary to design and manufacture a cost effective and sustainable tidal device.

Payne et al. [51] assessed the effect that onset turbulence has on the variation and frequency of the thrust and torque on the turbine rotor, blades and support structure. A 3-bladed, 1.2m diameter HATT was tested in this study at the wave-current flume in IFREMER. They found that at low turbulence levels (3%), the blade loading frequencies were clearly observed at the rotational frequency due to shadow effect from the support structure. Higher levels of turbulence (12%) led to blade loading at the rotational frequency as well as the first 2 harmonics but with much greater variation. A study, carried out by Blackmore et al. [67], also examined the effect of turbulence on the performance and loadings of a 3-bladed, slightly smaller 0.8m diameter turbine. They present a methodology for generating flows with different turbulence characteristics in a flume using static grids. The turbulence decays downstream of the grid and so different turbulence characteristics can be generated by changing the downstream distance of the turbine and the size of the grid. Peak C_p and C_t variations of >10% were observed showing the impact of turbulence on turbine performance. They found that rotor fluctuations were directly linked to the fluctuations experienced by the turbine blades, and therefore proposed that fatigue loads

on the blades could be estimated by monitoring the fluctuations in power to carry out real time fatigue load monitoring.

Maganga et al. [63] also investigated the effect of inflow TI (8 to 25%) on the performance of the turbine as this can be altered when using an experimental flume facility. They found that as the ambient TI increased, the C_p and C_t saw a 9% reduction due to high loading fluctuations on the blades. The TI also had an effect on the wake, showing that wake recovery is faster when a greater ambient TI exists, due to a narrower wake being formed. A numerical study by Ebdon [71] also found that a higher TI caused the wake width to decrease, which aids wake recovery due to an increase in the flow mixing between the wake and the free stream, due to turbulent fluctuations. However, contrary to Maganga et al., Ebdon found that increasing TI produced an increase in all the turbine performance characteristics due to the fluctuations in C_p , C_t and the coefficient of torque (C_q) having a greater magnitude.

Tedds et al. [72] carried out a detailed investigation into the near wake (<7D downstream) of a 0.5m diameter HATT using the experimental flume at the University of Liverpool. They reported that the near wake turbulence was highly anisotropic, induced by the blade rotation, and suggested that isotropic turbulence models should not be used to numerically model near wake dynamics. The rate of decay of the turbulent kinetic energy was also found to differ significantly to that observed when using grids or perforated discs. These methods neglect swirl effects and therefore over predict the turbulent kinetic energy decay rate of HATT wakes.

The wake of one turbine can have a significant effect on the performance of a second turbine placed downstream, due to the reduction in flow velocity along with high levels of swirl and unsteadiness in the downstream wake [52]. These characteristics are important when considering the placement of multiple devices in a tidal array, and are investigated in a study by Myers and Bahaj [52]. Their investigation into the array spacing of TSTs was carried out using actuator discs of 100 mm diameter at the University of Southampton flume. A comprehensive flow mapping exercise was performed using an Acoustic Doppler Velocimetry (ADV) device to fully characterise the flow around the mesh disc simulators. Different array spacings were examined to aid potential developers in understanding the concept of TST array spacing. Figure 2.11 shows a plan view of the array spacing for single and dual row arrays. For single row arrays, it was found that close lateral separation (0.5ϕ) increased the thrust force acting on the adjacent rotor discs while optimum lateral spacing

of 1.5ϕ led to accelerated flow passing between adjacent rotor discs with 22% more kinetic energy than the inflow. For two row arrays, the downstream discs encountered a greater thrust force than the upstream discs, as expected. The far wake region of the array had a higher velocity deficit than of a single disc on its own. The mesh rotor discs approach is useful where large scale flow characteristics are of interest and aids understanding of a simple tidal array. However, this approach has limitations and it was predicted that the downstream wake may be underestimated, having a lack of rotation in the flow simulated by the rotor disc wakes.

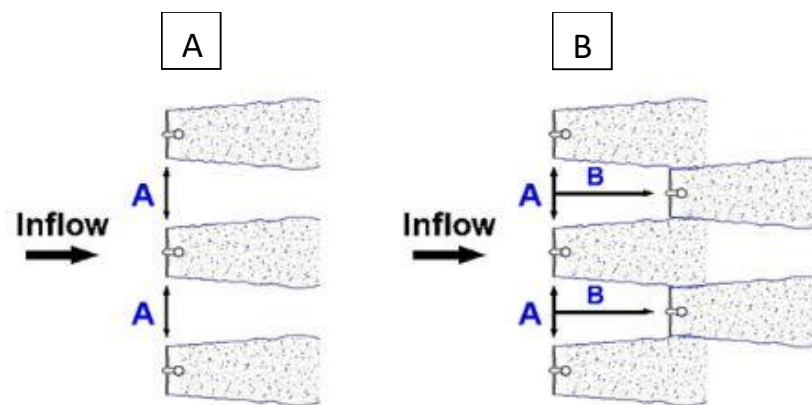


Figure 2.11. A plan view of the array spacing for: A) single row [$A=0.5\phi$, 1.0ϕ , 1.5ϕ] and; B) offset dual row [$A=1.5\phi$, $B=3.0\phi$].

2.2.2.2.3 Wave conditions

Waves induce a fluctuating, sub surface, horizontal and vertical velocity component which create oscillatory motions which can penetrate the water column by up to half the wavelength [73]. The fluctuations decay exponentially and so for engineering applications, the half wavelength estimation is considered satisfactory [74]. This implies that as the wavelength increases, so does the depth of impact of the oscillatory motions of the wave, although the maximum intensity of the disturbance is towards the surface of the water.

Acoustic Doppler Current Profiler (ADCP) data taken from the EMEC found that, in a body of water 45m deep, oscillatory wave velocities penetrated the water column down to 15m from the water surface and bottom boundary layer turbulence reached as far up as 17m [75]. This left a region of less than 1/3 of the water column where the water was less disturbed and turbulent. In storm conditions, the waves could affect the flow conditions to an even greater depth, leaving an even smaller region of optimal flow conditions. Faster flow velocities are found near the surface of the water with 75% of the available energy

being in the upper 50% of the water depth [61]. Therefore, greater energy extraction is possible nearer to the surface of the water, yet this is where the oscillatory effects induced by waves also have the greatest impact. As stated by [76], a compromise must be made between placing a tidal device near the water surface in the fastest flowing water, and minimising the load fluctuations induced by the waves.

A tidal turbine deployed in an ocean environment will never experience a perfect regular wave field as found in a tow tank or flume facility. However, analysis of a tidal turbine with regular waves, of relevant heights and wave periods, helps to quantify the extreme loading experienced by each of the turbine components [77].

Luznik et al. [78] performed tow tank experiments using a 3-bladed, 0.46m diameter HATT, while Lust et al. [76] used a 2-bladed, 0.8m diameter HATT. Both studies conducted tests with and without the presence of waves to examine the resulting effect on the respective turbines. [78] used waves which were scaled to match those found on the continental shelf of the United States eastern seaboard which categorised the surface waves as intermediate water waves. [76] also performed tests using conditions representative of intermediate water waves. Both studies, as well as others [53], [55], [79]–[81], found that the average performance characteristics were very similar for the cases with and without waves. However, oscillatory motions induced by the waves presented significant cyclic variations in the measured turbine thrust, torque and rotational speed. In particular, the fluctuation in torque appeared dependent on the vertical velocity which lags the horizontal velocity by 90 degrees of the wave phase. There was significant variability during the period of decreasing vertical velocity and this fluctuation therefore limited the lower range of TSRs at which the turbine could operate. This highlights the importance of the vertical positioning of the turbine in the water depth as a balance must be struck between maximising the flow velocity near the free surface and minimising the unsteady velocity variations caused by the surface waves [76].

To investigate the positional depth dependency of the turbine, Lust et al. [76] investigated testing the turbine at two different tip immersion depths (0.8ϕ and 1.75ϕ), while a comparative study by Sos et al. [80] tested a 2-bladed, 0.5m diameter HATT in five different tip immersion depths (0.11ϕ , 0.32ϕ , 0.53ϕ , 1.02ϕ , 1.22ϕ). [76] examined the effect of regular waves while [80] extended experimental testing to also include irregular waves. Both studies found that close proximity to the free surface had a detrimental effect on the turbine performance, with [80] finding that C_p decreased by 3-10% over the range of

TSRs tested between tip immersion depths of 0.11ϕ and 0.53ϕ . This agreed with the previously mentioned findings of current-only testing carried out by Bahaj et al. [62] and Maganga [63]. The average performance characteristics were unaffected by the presence of waves; however, there were significant fluctuations in instantaneous performance over each wave period. The maximum values of C_p and C_t coincided with a wave peak passing over the turbine. For the biggest wave cases tested, fluctuations in C_p and C_t were found to be 36% and 17% respectively; this agrees with the study by Barltrop et al. [79] who found that the effect of increasing the wave height resulted in the torque and thrust variation also increasing, especially for the lower frequency waves. Sos et al. [80] also found that the irregular waves tested had a greater impact on the frequency variation of C_p and C_t over a wave period in comparison to the regular waves tested.

A study by Galloway et al. [55] used a 3-bladed, 1.0 m diameter TST to investigate the effect of waves on TST loadings at Southampton Solent's 60m tow tank. As previous literature found [78], [79], the loadings imposed by waves is not a significant problem in terms of average thrust and power output, but instead the main issue is the cyclic loading induced by the waves. The thrust and torque fluctuations were found to be in excess of 35% of the mean rotor load which can result in accelerated fatigue of the individual turbine components. Galloway et al. [82] then extended this testing by introducing the effect of yaw (7.5° , 15° , 22.5°) as well as waves on a 0.8m diameter turbine at the same facility. When exposed to regular waves with zero yaw, the out of plane and in plane bending moments were 175% and 100% of the mean values, respectively. It was found that the cyclic loadings were significant; however, the yaw loading on an individual blade was found to be negligible in comparison to the loading imparted by wave action.

Ordonez et al. [53] analysed the effect of extreme wave-current interaction on a 3-bladed, 0.5m diameter tidal turbine. Again, average performance characteristics showed good agreement between current-only and wave-current conditions. However, a significant increase in the standard deviation was observed for the results obtained under wave-current conditions. The presence of waves with a current velocity was also found to increase the torque range on the rotor, while increasing the wave height also had the same effect. The blade root forces fluctuate depending on the position of the blade in the water column. Larger loadings were experienced when the blade was at Top Dead Centre (TDC) due to the higher wave induced velocities near the water surface, and smaller loadings were observed when the blade was at Bottom Dead Centre (BDC). These definitions are illustrated in Figure 2.12. The loading fluctuations were also considerably reduced when the

wave trough coincided with a blade at BDC as the blade is lower in the water column, away from where the maximum inflow velocity occurs. These observations highlight the importance of identifying possible control mechanisms which could be used to monitor the incoming waves and position the turbine blades accordingly to reduce the loadings experienced by the turbine.

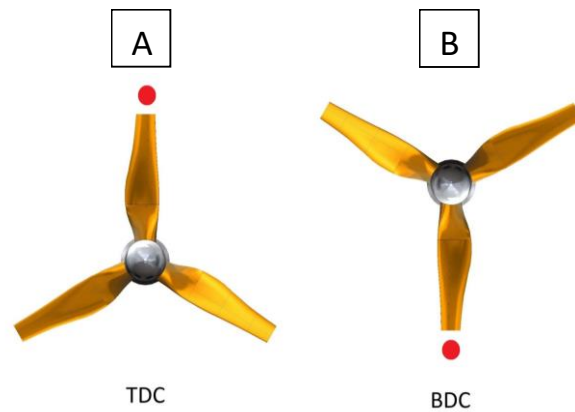


Figure 2.12. The blade positions at: A) Top Dead Centre and; B) Bottom Dead Centre.

These aforementioned studies were all carried out in tow tanks which limits the interaction between the waves and current as mentioned previously [55]. However, one benefit is that tow tanks can produce idealised waves, isolating the flow conditions and allow exact interpretation of the resulting effect on a tidal device. A comparison between the wave-current conditions generated by tow tanks and recirculating flumes was investigated in a second series of round-robin tests by Gaurier et al. [83]. This study was an extension of the previous round-robin tests in current-only conditions [54]. The first two of four facilities, the CNR-INM tow tank and the IFREMER flume, are detailed in this study. Differences in the velocity inflow conditions exist due to variations in the wave generation methods between facilities. The performance characteristics, between facilities, are comparable, but there are some small differences related to turbulence and wave-current interaction due to the intrinsic characteristics of the different type of tanks, ie. tow tank vs flume.

The study by Gaurier et al. [69] investigated the influence of waves and current interaction on a 3-bladed, 0.9m diameter HATT at the IFREMER flume. The generation of waves alone increases the turbulence intensity in the flow from around 5% to 30%, especially in the upper part of the water column. The mean performance characteristics remained the same in wave-current and current-only conditions; however, the standard

deviation of the performance characteristics was much greater in the combined wave and current conditions, as similarly found by [53]. This testing emphasised how much the contribution of waves increases the loading on turbine blades, with fatigue performance being dominated by the wave contribution. A detailed knowledge of both wave and current conditions is therefore necessary to inform turbine rotor and blade design decisions.

As mentioned by [53], the loading on the turbine blades is directly related to their position and the relative position of the wave. A study by Henriques et al. [84] investigated the effect of varying the pitch angle from optimum conditions to attenuate unsteady loadings caused by wave-current interaction without a major loss of power. Increasing the blade pitch angle away from the optimum settings caused a reduction in both mean thrust and power with greater decrease in the mean thrust than in mean power. The fluctuation in power and thrust also decreased showing that this can be used as a mechanism to reduce excessive loading on a HATT when operating with significant wave-induced loading while still being able to extract available power from the tidal stream.

Tidal currents are typically semidiurnal, which means that a flood and ebb occurs twice per day. If a tidal turbine is installed in a coastal location then it will experience a shift of approximately 180° in the predominant tidal flow direction, four times per day. Surface waves are generated by the wind and therefore have no dependency on the direction of the tidal current. Therefore, research must investigate more common ocean flow environments, using following/opposing wave and current scenarios as well as looking at the interaction of oblique waves and current.

Draycott et al. [85] investigated the power and thrust response of a 1.2m diameter, 3-bladed TST under a wide range of regular wave conditions with a following and opposing uniform current. Wave action induces large variations in the flow, which were found to increase with wave amplitude and decrease with wave frequency. Following wave-current conditions also exhibited greater variations than opposing wave-current conditions with the same wave height and frequency due to the lower associated wavenumbers. Peak values of thrust and power in wave-current conditions were found to exceed that of current-only conditions by 7-65% and 13-160% respectively. The study showed the significant effect that wave and current interaction can have on a TST. Therefore, model-scale testing as described in that study [85], is important in allowing the loading and power fluctuations of the turbine to be analysed and understood in a controlled and repeatable environment.

The FloWave facility at the University of Edinburgh is a unique, circular testing facility which can generate waves and currents in any combination and in any relative direction across the central test volume [59]. Martinez et al. [57] presents a test campaign under combined oblique wave and current conditions at FloWave. The experimental testing used a 3-bladed, 1.2m diameter HATT, and is known to be the first experimental investigation of a TST subjected to oblique waves and current [57]. The flow was initially characterised using three different flow directions of 0° , -10° and -20° . It was found that the flow at -10° had the highest C_p values, as also found by [86], hypothesised to be due to the significant velocity fluctuations in the onset flow. Four different regular waves with different propagation angles of 0° , 45° , -45° and 135° were then superimposed on the three different current flow directions. The introduction of waves at 0° with flow at different yaw angles was found to increase the C_p and C_t in comparison to current-only conditions. Waves at an angle of 45° , -45° and 135° were found to decrease the C_p and C_t due to the rotor experiencing a component of the wave force and not the whole force magnitude. Waves also resulted in the standard deviation of the rotor torque and thrust to increase considerably, being almost double that observed in the current-only flow.

2.3 NUMERICAL MODELLING

Model-scale laboratory testing can be carried out to reproduce ocean flow conditions and examine the performance of a prototype TST. However, the expenditure involved with the design evolution of a device, from concept, to model-scale prototype, to full-scale device, as well as the operational costs from using an experimental facility, can make the whole process very expensive. With advances in technology, quicker processing times and the reduced cost in comparison to physical testing, numerical modelling has become a widely adopted tool to provide researchers and developers with estimates of the loadings and performance of tidal devices in various flow conditions. These numerical models still require initial validation via the use of experimental data; however, the number of experiments is far less than required for a full experimental design campaign. There are a variety of techniques used in numerical modelling, generally dependent on the users requirements as compromises must be made between solution accuracy, the level of detail in the model, and computational expense [71]. The most common methods used to create numerical models are Blade Element Momentum Theory (BEMT) ie. [77], [79], [82], [87]–[89] and Computational Fluid Dynamics (CFD) ie. [71], [90]–[94].

2.3.1 Blade Element Momentum Theory

BEMT provides a first stage, 'quick' design approach to developing and assessing 2D turbine blade and rotor geometric characteristics [89], [95]. The methodology does not fully resolve 3D characteristics and so detailed hydrodynamic results are not provided. BEMT is based on a combination of momentum theory and blade element theory. Momentum theory uses a disc to extract kinetic energy from a moving fluid flow in place of a HATT. This disc is then divided up into infinitesimally small width annular rings where axial and tangential induction factors are expressed following the laws for conservation of mass and momentum. It is assumed that there is no interaction between neighbouring annular rings, which are partially occupied by a blade element. These elements are assigned a chord length and twist angle specified as a function of the radius [95]. These values, as well as the flow velocity and rotational velocity, are then used to calculate the resultant velocity and therefore find the lift and drag forces on each blade section. This enables the total torque and thrust to be calculated. A detailed description on BEMT can be found in [96].

Malki et al. [97] developed a coupled BEMT-CFD model to evaluate the model's ability to simulate TST performance in the ocean environment. The relative simplicity of the model allows the use of momentum sources from the BEMT to be used in a Reynolds Averaged Navier-Stokes (RANS)-CFD model; this leads to shorter run times, a relatively quick achievement of model convergence, and lower computational demand. The numerical model was compared to experimental data obtained by [62] where high variations in the C_p were observed. These variations were attributed to the inability of the model to capture the transient features within the flow, particularly in the immediate vicinity of the blades. BEMT is based on the assumption that water flow is 2D and inviscid when actually the flow around a TST blade can be 3D and turbulent which is much more complex than these assumptions [95].

Mason-Jones [89] used a basic BEMT as a quick and easy method to find the optimum pitch angle for custom designed TST blades. It was estimated by BEMT that the optimum setting was at 7° , however, subsequent investigations using the fully resolved CFD methodology found that it was 6° . Su et al. [95] also found flow patterns in the wake were underestimated by the steady 2D assumptions of BEMT, requiring the use of CFD to check and validate turbine design carried out initially with BEMT.

More complex flow characteristics have been modelled using BEMT, such as regular wave-current interaction [77], [79], [87], [88], [98], [99] as well as yaw effects [82]. Barltrop

et al. [79] used a BEMT model incorporating Linear Wave Theory (LWT) to predict the resulting rotor torque and thrust of a 3-bladed, 0.4m diameter turbine when subjected to surface waves. It was found that BEMT predictions were comparable to the baseline performance characteristics obtained from the tow tank testing. Faudot et al. [88] carried out a similar study using a combined BEMT and LWT model with a 2-bladed, 1.475m diameter turbine. Again, they found good agreement between the BEMT model and the experimental testing in terms of the mean loads and load variations. However, extreme loads are of importance for the design of any blade and they therefore concluded that this method was not suitable in low relative current numbers. The current number describes the importance of the wave loading in comparison to the current loads [88]. Faudot et al. stated that a low relative current number indicates there are large variations in the particle velocity and therefore the inclusion of additional dynamic effects are necessary to estimate the loads when using BEMT. Guo et al. [98] also investigated the effect of surface waves on TSTs in uniform current flow using a BEMT numerical model. Numerical inaccuracies were again encountered as this BEMT analysis was based on assumptions for steady, non-turbulent flow and did not account for tip losses [100].

Galloway et al. [82] investigated yaw and wave effects by comparing a BEMT numerical model with experimental results. The study similarly concluded that the BEMT numerical model must include a dynamic inflow in the calculation of TST loads otherwise loading amplitudes can be significantly under predicted. Gravitational and buoyancy components must also be incorporated in the BEMT model as neglecting these forces also results in under prediction of the loadings.

BEMT remains an important tool for blade design and simple flow applications [101] with the requirement of quick simulation time and minimal computational expense. However, CFD can be used as an alternative numerical modelling tool to more accurately analyse the hydrodynamic forces and give estimates for the loadings over all the blades in a rotor [95].

2.3.2 Computational Fluid Dynamics

CFD is a computer-based simulation technique used to fully resolve 3D hydrodynamic features. It can be used as a substitute for experimental tank testing due to the flexibility in modelling. There are many different CFD codes and software which have been used for TST modelling, some commercial eg. ANSYS-CFX, FLUENT, STAR-CCM⁺, and others open source eg. OpenFOAM, REEF 3D, HOBEM, Code_Saturne, PimpleDym-Foam. In terms of TST modelling, there are also multiple ways in which the rotation of a turbine can be simulated,

specification of the boundary conditions selected, and also the methods used for wave and current generation. The following section presents some of the possible methods used to simulate turbine performance in various flow conditions.

2.3.2.1 *Turbine representation*

The representation of the TST can be achieved in predominantly four ways, as detailed below.

2.3.2.1.1 *Actuator Disc Method*

The Actuator Disc Method (ADM) comprises a disc region, the same swept area as the turbine, where forces are applied to the flow as they would be imposed by a turbine. This method is computationally much less expensive than a fully resolved model; however, simulations are usually steady-state leading to time-averaged results. Experimentally, as the turbine rotates, tip vortices are shed from the blades and swirl is introduced to the flow. Neither of these features are replicated in the ADM, therefore this method is mainly applied to models for investigating large-scale flow effects simulating multi-turbine arrays [58].

Harrison et al. [91] carried out a comparison between CFD simulations generated using the commercial software ANSYS CFX and experimental data to predict the far wake of HATTs. Porous discs were used in the experiments to replicate the use of the ADM in the CFD. It was found that the RANS-CFD simulation, using the Shear Stress Transport (SST) turbulence model, predicts wake recovery to occur further downstream of the turbine than in the experiments. This is because of disparities in the near wake and the ambient turbulence levels. The ADM assumes resistance is isotropic but [91] concluded that further investigation is needed to ascertain whether this accurately replicates the characteristics of a porous disc or not.

2.3.2.1.2 *Actuator Line Model*

The Actuator Line Model (ALM) consists of actuator lines which represent each turbine blade. These lines are divided into a number of equally spaced segments whereby the body forces are imposed on the flow, equal and opposite to the lift and drag forces experienced by the turbine. Churchfield et al. [102] used the ALM method to model arrays of multiple tidal turbines, while Creech et al. [103] investigated the impact of a support structure on the performance of two contra-rotating turbines. The study by [102] used OpenFoam to test the use of a Large Eddy Simulation (LES) turbulence models, to simulate the flow through turbine arrays. LES requires very small grid spacing to be able to resolve the

turbulent fluctuations in the flow [90]. In this instance, a fully resolved turbine could not be achieved as it would require such fine grid spacing near the surface of the turbine as to render the computation infeasible. Therefore, the ALM provided a level of detail in the simulation that otherwise couldn't be achieved. Two 8m diameter contra-rotating turbines mounted on a central support structure were modelled by [103], to study the interaction of the two turbines with the support structure. Commonly, the ADM has been used in this type of application, however it has not been able to capture the fluctuations in power output from blade-structure interaction due to the use of a disc to represent the turbine. It was found that the ALM, in this instance, is better for examining transient features produced by the turbine-structure interaction. Results from this study found that there is a noticeable effect on the turbine performance due to the presence of the structure, causing regular fluctuations in both power output and flow speed. These are features that the ADM would not be able to estimate.

2.3.2.1.3 *Virtual Blade Model*

In the Virtual Blade Model (VBM), the blades are 'virtual' and representation of the turbine is achieved by adding body forces in the x , y and z directions using Blade Element Theory (BET) [104]. The rotor is simulated inside a rotor disc across which the virtual blades swipe [93]. Li et al. [93] and Sufian et al. [105] both detail simulations using the VBM to investigate the interaction of TSTs and surface waves. [105] found that the VBM was able to replicate the rotational movement of the rotor with reasonable computational cost. The actual blades were not represented but instead the motion of the fluid surrounding the blades was simulated. This method provides a useful compromise in achieving a reasonable accuracy in results when assessing turbine performance and capturing near-wake processes. However, both studies acknowledged limitations when compared to a fully resolved model. The tip and hub vortices, as well as the trailing edge wake, cause turbulence. These transient features are not accounted for in the VBM, leading to an under prediction of the turbulence downstream of the turbine [105]. The lift and drag on each blade element is averaged over a full rotation which could lead to turbine loadings due to wave action being missed as it is possible for the waves to have a higher frequency than the blade passing frequency [93]. However, both studies investigated the effect of the turbine on the surface waves instead of the other way around, so the coefficients used could be validated against measured data. Despite this, it is necessary to have a fully resolved model to realistically estimate the blade loadings under wave conditions, as explained in the following section.

2.3.2.1.4 Fully resolved model

A fully resolved model is achieved by creating a cylindrical subdomain which encapsulates the full turbine rotor geometry and surrounding computational mesh. The flow field around the specific geometry is resolved and the use of a sliding mesh between the stationary domain and rotating subdomain accounts for the transient interaction effects across the domain interface. Use of the fully resolved model allows simulations to be carried out as a steady state or transient analysis. Steady state analyses are used to model flows that do not change over time, while transient analyses are time-dependent [106]. Hafeez et al. [107] conducted a study to compare the use of a steady state and transient set up to model the performance of a 3-bladed, 0.28m diameter HATT. The performance characteristics differed from the compared published data by 3% for the steady state model and 1.2% for the transient model. The transient model accounted for the transient flow features providing results of a higher resolution than the previous methods discussed. However, the transient simulation required a greater computational effort in comparison to steady state analyses.

O'Doherty et al. [108] and Frost et al. [92] both compared fully resolved CFD models of 3-bladed turbines at 0.5m and 10m respectively. [108] compared their CFD results to experimental data using the same size TST, whilst [92] scaled these experimental results for a 10m diameter turbine. The Moving Reference Frame (MRF) approach was used to apply a sliding mesh at the stationary/rotating domain interface for both studies, and found that the numerical turbine performance characteristics displayed good agreement with the comparable experimental data. The interaction of a stanchion with the full-scale TST was also investigated by [92] for bidirectional current flows. The study found that the further away the stanchion was from the rotor plane, the smaller the cyclic loadings experienced by the turbine. At 2.5 stanchion diameters separation, the stanchion effect on the turbine was negligible [92], which is significant for power conditioning and increasing the fatigue life of the device. It was also found that a yaw mechanism would be beneficial for the turbine fatigue life, because if the stanchion remained static while the current ebbed and flowed, the turbine could experience up to 10 times the average moment when compared to normal operation $<10^\circ$. An open source CFD solver, PimpleDym-Foam, was similarly used by Su et al. [95] to analyse the effect of yawing currents on the turbine performance. The study also found that the yaw angle had no effect on the efficiency of the turbine below 10° , and therefore above this, yaw mechanisms would be recommended.

The water depth at the tidal site as well as the interaction with seabed topography can introduce velocity profiles into the tidal current flow [68]. The profiles can be highly

variable, depending on the location of the tidal site, and therefore it is important to evaluate the impact of high/low shearing velocity profiles as well as idealised uniform current velocities on the performance of TSTs. If a TST takes up a significant area of the water column then the difference in water velocity between the tip of a blade positioned at TDC and BDC can be substantial [53]. This difference complicates the calculation of turbine performance characteristics which use the average inflow velocity to the turbine. Ebdon [71] found that this calculation, commonly used in uniform current flow conditions, can equally be used in high shearing velocity profile circumstances as long as the volumetrically averaged velocity over the turbine swept area was used [47].

O'Doherty et al. [68] evaluated the performance of a 10m diameter, 3-bladed HATT in uniform and profiled flow conditions based on identified tidal sites located off the Welsh coastline. The study identified that the calculation of the performance characteristics using velocity profiles is highly dependent on the inflow velocity used. It was recommended that the monitored velocity should be taken 5D upstream of the turbine at the same depth as its hub. However, the extracted power and torque were analysed to directly compare between the different flow conditions and it was found that velocity profiles have a significant effect on power attenuation, reducing the extracted power to 30-40% of the peak power. This was given as an average power reduction as the individual blade loading was not investigated in that study. Similar findings were shown by Hafeez et al. [107] and Mason-Jones [89] who observed a 12% and 30% reduction in the power under a velocity shear in comparison to uniform flow conditions, respectively.

Mason-Jones et al. [109] investigated turbine performance and individual blade loadings on a 10m diameter, 3-bladed HATT within a high shear velocity profiled environment. To investigate the individual blade loadings, it was necessary to use a fully resolved model. ADCP measurements from the Severn estuary were used as the inflow for the CFD model created using ANSYS FLUENT. The inclusion of a stanchion downstream of the turbine resulted in reduced performance characteristics over a complete rotation. The further incorporation of a high shear velocity profile, increased the cyclic torque, thrust and power when compared to uniform flow conditions. The point of peak power extraction through the rotational cycle was not at TDC as expected due to the blade being in the maximum velocity region at TDC. Instead, the peak power showed a lag of 72° from TDC due to an interaction of the downstream wake vortex with the velocity field.

2.3.2.2 Upper surface boundary condition

As well as having multiple methods for modelling the turbine, the water/air surface boundary can also be represented in different ways. The main two methods used are the ‘free slip’ and ‘free surface’ upper surface boundary conditions. The ‘free slip’ upper surface boundary condition gives the velocity component of the water parallel to the boundary a finite value. This type of numerical model has been widely used to compare average turbine performance characteristics to experimental data.

Li et al. [93] used ANSYS FLUENT to create a ‘free slip’ simulation to investigate the average power and torque generated by a 0.5m diameter HATT. A comparative study was found to provide excellent agreement with experimental results, as found by [108] and [92] who performed complementary studies. Similarly, McSherry et al. [110] developed a free slip, uniform flow CFD model which incorporated a lab-scale 0.8m diameter, 3-bladed TST. Good agreement was found between experimental and numerical data for the turbines’ average C_p and C_t values, giving confidence in the ability of the CFD model. This type of numerical model could then be used to predict the hydrodynamic loading conditions experienced by a larger turbine in full-scale tidal flows.

Alternatively, the ‘free surface’ model can be used to represent the upper surface boundary using a two-fluid, multiphase approach which has a distinct interface between the two phases used. Yan et al. [111] used the level-set method to track the air-water interface of the uniform flow, ‘free surface’ model. The performance of a 0.8m diameter, 3-bladed TST was investigated when submerged to deep tip immersion ($0.55\emptyset$) ie. blade tip at TDC, and shallow tip immersion ($0.19\emptyset$) ie. blade tip at BDC. This ‘free surface’ model was compared to a purely hydrodynamic simulation, without the free surface, to investigate the free surface effects on the turbine performance characteristics, C_p and C_t . The pure hydrodynamic model showed good agreement for C_p and C_t with the free surface deep tip immersion case, while the shallow tip immersion gave lower C_p and C_t values. Shallow tip immersion resulted in bigger changes to the free surface and greater deformation which explained the more pronounced free surface effect on the C_p and C_t . These simulations were able to capture the effect of the free surface on the hydro-dynamic loading of the rotor. Further testing of the free surface model was carried out using Linear wave conditions showing the same trend with the C_p and C_t , ie. decreasing as the turbine moved closer to the free surface. The ‘free surface’ type of model enables more complex conditions, such as waves, to be modelled at the water surface which is not possible when using a ‘free slip’ type of model.

An in house code, CgLes [112], developed by Bai et al. [94] implemented two different free surface schemes: the 'height function' method and the 'level set' method. It was noted that the existence of the free surface, in comparison to the 'free slip' approximation, caused an increase in the C_p , predicting that locating the turbine closer to the free surface or in the presence of surface waves, the C_p could increase even more. Sun et al. [113] used the Volume of Fluid (VOF) method to create a multiphase, 'free surface' model. The effect of varying the turbine thrust on the free surface was investigated and it was found that the extraction of energy from tidal currents resulted in a free surface drop behind the turbine, which is not seen in a 'free slip' arrangement of the model.

2.3.2.3 Turbulence modelling

The use of a sliding mesh in the fully resolved numerical model allows the transient interaction effects to be modelled across the stationary/rotating domain interface. However, depending on the model used to simulate the turbulence, varying degrees of accuracy can be achieved.

The normal CFD approach to simulating turbulent flows is by using the RANS equations which solve for time averaged quantities [106]. Different turbulence models can then be used to solve these RANS equations, using the k_t - ε model, k_t - ω_t model or the SST model [114]. However, turbulence from the inlet has been found to dissipate considerably using these RANS turbulence models [89]. Therefore, further complexity in the flow field can be simulated using LES which involves solving the time dependent equations for the turbulent motion by filtering the equations to remove very fine time and length scales based on the eddy sizes [106]. This approach requires a very fine mesh and time step selection but gives details on the structure of turbulent flows which cannot be obtained in a RANS simulation [106].

Ahmed et al. [90] carried out a numerical study using an open source solver, Code_Saturne, to investigate the performance and loadings on a 3-bladed, 18m diameter turbine when subjected to flow turbulence and velocity shear. SST-RANS and LES turbulence models were used to numerically model the loadings on the rotor and the blades. They found that fluctuations in the thrust, power and blade bending moment arose cyclically from the onset mean velocity shear and the shadowing effect from the stanchion. Mean blade loadings under low turbulence inflow conditions were found to be similar between RANS and LES, and yielded mean power coefficients comparable with site data from device deployment at EMEC. Therefore, the less computationally demanding RANS

approach was favoured to determine the mean loading characteristics as computation times for a single turbine rotation using RANS took a day while LES took a week. To simulate the effect of turbulence on the turbine loadings, LES with synthetic turbulence prescribed at the inlet was employed using inflow profiles of mean velocity, Reynolds stresses and length scales determined from a precursor flow-only simulation. The study established that LES could resolve blade generated turbulence and so reproduced the spectral distribution of blade bending moments with good agreement to the site data. Kang et al. [115] details a study which used LES to model 3D flow past a 3-bladed, 5m diameter turbine. The 3D wake structures are shown to be accurately modelled, revealing three distinct regions: the outer layer, the counter rotating inner layer, and the core layer. However, the wake recovery data obtained using LES by [90] was under-estimated and so simulations using multiple devices in an array would not be accurately represented using this method.

Detached Eddy Simulation (DES) is a hybrid LES/RANS turbulence model which is designed to represent the boundary layer using the RANS model but switches to LES in detached regions [106]. This method can save a large amount of computing power as it does not use the more complex LES model in regions of the flow where it is not necessary. The turbulent length scale is compared to the local cell size to determine whether the RANS approach should be used to model the turbulence or whether the fluctuations can be resolved using LES [116].

Ebdon et al. [116] compared the ability of two different turbulence models, DES and SST-RANS, to simulate a 3-bladed, 10m HATT under various ambient turbulence conditions. The results show that the SST-RANS model can produce accurate estimations for performance characteristics. However, this type of model underestimates the length and character of the wake which is better predicted by the DES model, as shown in Figure 2.13. This study was extended to assess the ability of a DES model to accurately reproduce the wake and performance of a 0.5m turbine when compared to experimental testing carried out at IFREMER [116]. The DES model showed very good agreement for the mean centreline velocities measured in the wake, as well as the averaged swept area velocities in the wake. These wake velocities, produced using the DES model, show a significant improvement on the RANS model results as the mixing process between the free stream and wake region of the flow could be reproduced, which affects the rate of wake recovery. However, neither CFD models showed good agreement with the experimental results for the turbine performance characteristics, overpredicting C_p and C_q by 13%. However, these results are similar to previously reported values for this turbine blade geometry [16] using the SST-

RANS model. Therefore, there is no negative effect of using DES instead of RANS in estimating the performance characteristics, yet DES produces much better estimations than RANS in the wake region of the flow. RANS simulations are much quicker to run, taking a half to a third of the time of an equivalent DES simulation [116]. DES does however provide instantaneous results which are vital for developers placing devices in tidal flows affected by upstream turbines in tidal arrays.

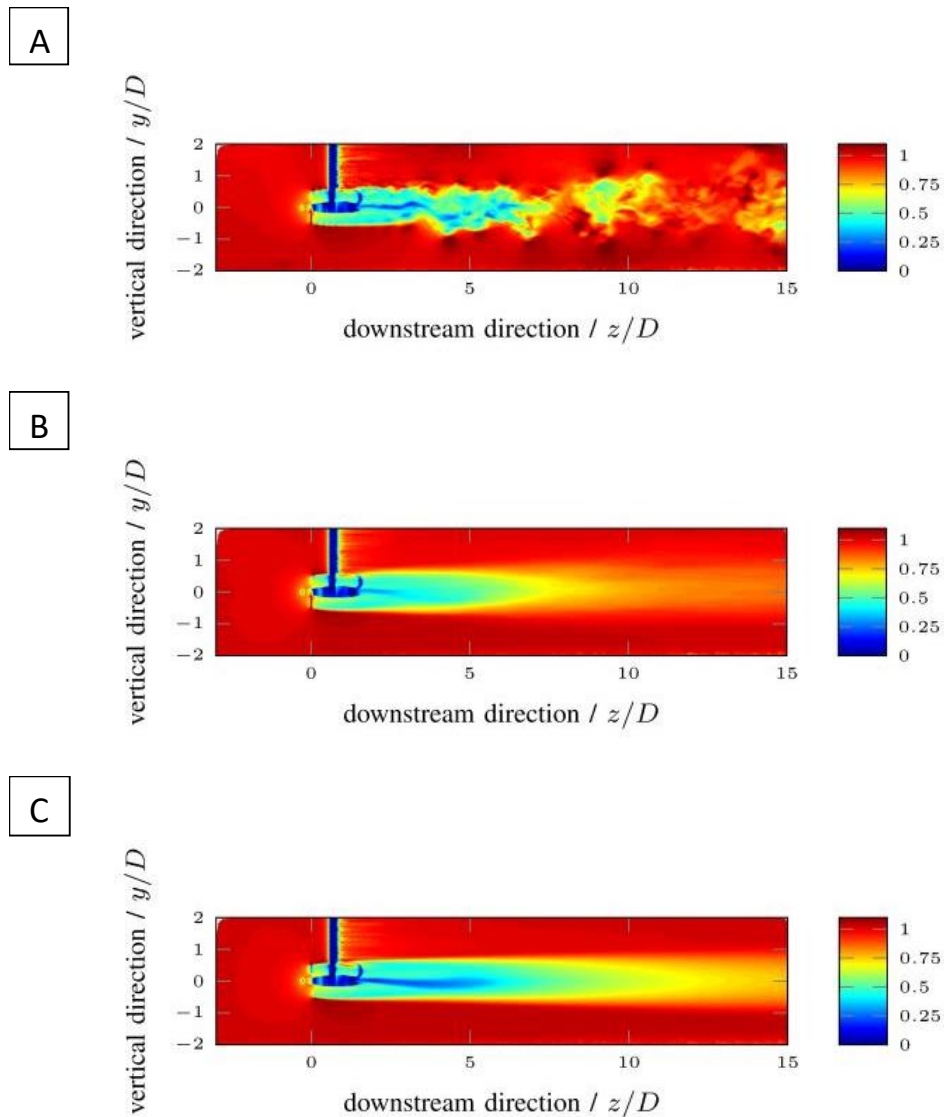


Figure 2.13. The normalised streamwise velocity results yielded by 3 models with the same boundary conditions: A) instantaneous DES, B) time averaged DES, and; C) RANS, reproduced from [184]. (For this case, D = diameter).

A fully resolved, transient model using LES represents a computationally expensive, high-resolution simulation [90], while a steady state, SST-RANS model is much simpler but also provides a less detailed, time averaged solution [106]. The aforementioned studies describe

a single turbine modelled in various flow conditions and present the problems associated with modelling complex flow conditions at a high resolution [90], [115], [116]. The concept of simulating multi-turbine interaction in tidal arrays is therefore much more challenging and a compromise between computational run time and solution detail must be reached. The ADM and ALM methods are therefore commonly used to simulate multiple turbines and array simulations [58], [102], as the detail required in the mesh for modelling arrays >10 turbines using SST-RANS or LES would not be feasible due to the computational effort required [91].

McCann et al. [117] investigated the effect of flow turbulence and wave action on TST fatigue loading. A high level, macro-scale numerical model was created using GH Tidal Bladed to model a 2MW, 3-bladed tidal turbine with a rotor diameter of 22.8m in a water depth of 50m. These dimensions were realistic to the planned deployment of the AR2000 turbines in the MeyGen project [29]. A strong correlation was observed between turbine fatigue loading with both turbulence and wave action. Therefore, the potential damage that unsteady flows generated by wave action and turbulence can cause, suggests that fatigue loading mitigation mechanisms, such as individual blade pitch control [84] or passively adaptive blades [118], [119], can be beneficial.

2.3.2.4 *Wave generation*

Waves are an important flow feature that induce fluctuating velocity components into the flow and must be examined in order to realistically predict TST performance. It has been shown that wave motion can penetrate the water column by up to half the wavelength [73], hence distorting the water column profile in both magnitude and transience. This can have consequences on the TST transient characteristics of power, thrust and torque. The introduction of waves into numerical CFD models can be conducted in three main ways: using a piston type wave maker, a flap type wave maker or by numerical generation. These types of numerical models are sometimes referred to as a Numerical Wave Tank (NWT) as they are a numerical representation of a physical testing facility or ocean environment.

2.3.2.4.1 *Piston type wave maker*

A piston type wave maker displaces water by moving axially, in the direction of the waves, as shown in Figure 2.14. It is normally used for generating waves for modelling coastal structures, harbours and shore mounted devices [120]. There is usually significant

orbital particle motion near the bottom of the tank as motion from the piston type wave maker tends to compress the particle motion into an ellipse.

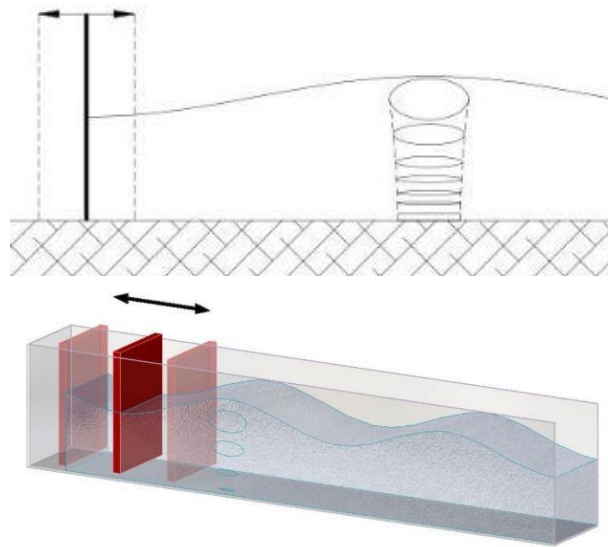


Figure 2.14. A schematic of a piston type wave maker, figure reproduced from [120].

Liang et al. [121] and Higuera et al. [122] both developed numerical models using a piston type wave maker to generate wave motion. ANSYS FLUENT was used by [121] to generate an irregular wave train, validating the model using experimental data. It was found that good agreement existed between both data sets for the wave elevation results in terms of wave height, crest height and period of the individual waves. Numerically reproducing waves using a piston type wave maker is advantageous as it allows a direct replication with laboratory tests as piston type wave makers are often used in experimental facilities [69]. OpenFoam was used by [122] to consider the coastal application of simultaneous wave generation and active wave absorption, covering the full spectrum of water waves with both first and second order wave generation. Active wave absorption was found to increase the stability of the system in OpenFoam and correct the problem of an increasing water level when run for long simulations. Both studies were only interested in the wave shape and therefore only the surface elevation of the wave. They did not investigate the sub surface flow conditions generated by the piston type wave maker in either model.

2.3.2.4.2 Flap type wave maker

A flap type wave maker is fixed at the bottom and oscillates forwards and backwards on a hinge to produce wave motion, as shown in Figure 2.15. This type of wave maker is

normally used to produce deep-water waves where the orbital motion decays with depth and is negligible at the bottom of the tank [120].

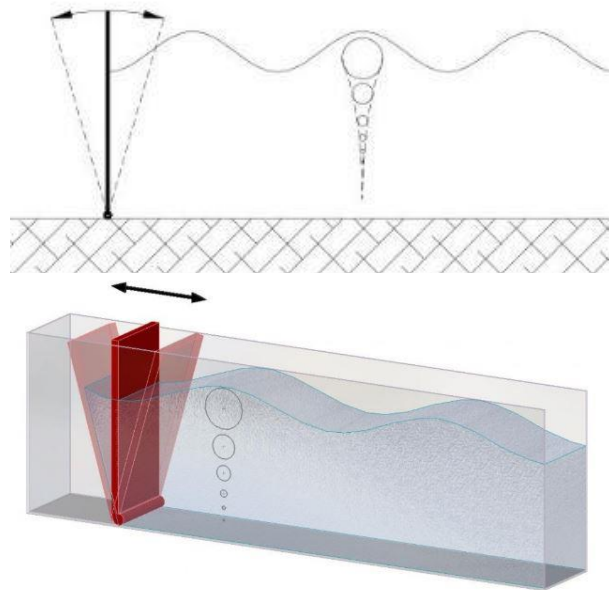


Figure 2.15. A schematic of a flap type wave maker, figure reproduced from [120].

Lal and Elangovan [123] developed a CFD model to simulate a flap type wave maker with validation against Wave Maker Theory (WMT). Only shallow water waves were investigated, which exist at sites unsuitable for tidal energy development. Typical sea gravity waves are 1.5 – 150m in wavelength [124] and would therefore have a water depth of <6m based on shallow water wave requirements, as shown later in Table 3.1. This is currently too shallow for HATT deployment as a water depth of 25 - 50m is the operational depth range for seabed mounted tidal devices [125]. Computed results for the wave elevation were in good agreement with wave maker theory; however, the sub surface particle velocities induced by the wave were not investigated and would be necessary to investigate the loadings imparted on a tidal turbine under wave action.

Linear deep and finite depth water waves were simulated using a flap type wave maker, in a study by Finnegan and Goggins [126], representative of suitable water depths for TST deployment. A methodology for optimising the NWT is presented, similar to [127], analysing the model dimensions, mesh size, time step and damping technique to dissipate the wave energy. The model also investigated wave-structure interaction with a truncated vertical cylinder and was validated against LWT and WMT. There were limitations in using WMT for the deep-water wave cases, as wave generation in ANSYS CFX was restricted to low normalised wave numbers.

Both previous studies focus only on wave generation; however, both wave and current conditions must be generated to replicate realistic ocean conditions. A study by Silva et al. [128] examined the ability of a CFD model, using ANSYS CFX, to reproduce the wave-current conditions generated by the LabOceano ocean technology laboratory, Brazil. Current-only (0.1, 0.3, 0.5 m/s), wave-only (wave height = 0.08m, period = 1.8s, wavelength = 5.06m), and wave-current conditions were simulated by the numerical model and compared to the experimental data. The wave-current conditions were examined at a locally constant location and it was found to reproduce the same wavelength as the waves used in the experimental testing. Although, only the wavelength was compared to experimental results and not the sub surface velocities which would add confidence in the ability of the model.

2.3.2.4.3 Numerical wave generation

Numerical generation of waves is implemented by specifying the vertical and horizontal wave velocity components as well as the surface elevation of the wave at the inlet.

Machado et al. [129] used Stokes 2nd Order Theory (S2OT) to model regular, intermediate water waves with different wave generation methods. The mesh, time step, damping method, domain length and inlet conditions were all investigated using ANSYS CFX to give an optimised NWT model. A numerical inlet velocity method and a piston type wave maker were both investigated. It was concluded that implementation of the piston type wavemaker gave better agreement with theory than when using the velocity inlet method, mainly because the velocity inlet method specified the free surface elevation at $t = 0s$ across the whole domain and so reflection was a problem from the beginning of the simulation, causing the beach to be ineffective. The piston type wavemaker therefore generates regular waves but without the addition of any current flow.

Jacobsen et al. [130] created a wave generation toolbox through the open source code, OpenFoam. It was found that it is possible to model surface waves using this framework, using wave relaxation methods to prevent reflection of the waves from the end of the model domain. The method is limited to shallow water theory, which would not be suitable for the waves present in tidal sites due to the depth requirements [125]. It was found that induced early wave breaking occurs when the aspect ratio of the computational mesh does not equal 1. Lambert [127] also used OpenFoam, but to model regular waves in intermediate and deep-water depths. It was found that the simulation of regular deep-water waves, with a steepness of > 0.05 , experienced damping throughout the domain and

were susceptible to early wave breaking, as mentioned by [130]. Neither study investigated the effect of simultaneous wave and current generation.

A series of studies have detailed the methodologies used for investigating the effect of wave-structure interaction, placing various structures within the flow. Tian et al. [131] used ANSYS FLUENT to investigate the effect of wave-structure interaction under three different regular, intermediate water waves with various wave heights and wave periods. The model was initially validated using S2OT before investigating the effect of waves interacting with a vertical cylinder. It was concluded that the maximum wave height decreased in the presence of the structure, but the wave phase remained equal, showing good agreement between experimental and numerical results. Bihs et al. [132] used REEF 3D to investigate wave-structure interaction with a rectangular abutment, vertical circular cylinder, submerged bar and a sloping bed. The study found the numerical model accurately modelled the surface elevation of the wave and structure interaction, but the sub surface interactions were not investigated. Both these studies provide a methodology for the development of a NWT; however, neither considers wave and current interaction. Realistically waves in the ocean environment will always exist superimposed upon tidal currents so it would be more representative to incorporate this into the numerical model.

ANSYS FLUENT was used by Kim et al. [133] to generate regular waves superimposed on a uniform current velocity to investigate wave-current and structure interaction in offshore environments. A detailed investigation into the damping domain was provided alongside a study to optimise the mesh sizing. The model enabled a calculation of the wave loads present on offshore structures under wave and current interaction, similar to the methodology required when investigating the loadings on a TST due to wave-current interaction. However, a turbine is a moving body rather than a stationary offshore structure and is therefore an added complication to the simulation.

Higher Order Boundary Element Method (HOBEM) was used by Ning and Teng [134] to model linear and non-linear, regular and irregular waves. Excellent agreement was achieved between the wave elevation for second order theory and the numerical results for the regular and irregular simulations. Linear irregular waves were also modelled by Finnegan and Goggins [135], expanding upon their previous study [126], to compare against real ocean data from the Atlantic Marine Energy Test Site (AMETS). This study showed that real ocean conditions can be modelled accurately, proving beneficial to researchers in the industry as it's relatively inexpensive in comparison to physical model testing.

A number of studies have investigated the complexity of numerical wave generation [127], [129]–[132]; however, Tatum et al. [136] present a study which investigated the challenge of numerical wave and current generation, while investigating the induced loadings on a rotating TST. This CFD investigation analysed the effect of a uniform current velocity (3.086 m/s) and surface waves (wave height = 6.0m, period = 4.38s, wavelength = 30m) on the performance characteristics of a 10m, 3-bladed TST. It was found that the wave-induced flow conditions had no effect on the average thrust and power, as found experimentally by [53], [55], [76], [78]–[81]. However, [136] also examined the individual turbine component loadings, finding that wave action increased the fluctuation in the thrust and power by 10 and 16 times the current-only loadings respectively. The resultant shaft bending moment for current-only conditions resulted in fluctuations of ± 12 kNm around a mean value of 26 kNm due to interaction with the support structure. The introduction of waves increased this fluctuation to ± 19.5 kNm, causing the amplitude of fluctuation to almost double while the mean value remained the same. These variations in the shaft bending moment due to wave motion directly affect areas of the drivetrain and can induce additional wear on components such as bearings and seals. In addition to the surface waves, a velocity profile was then incorporated to investigate the effects of in/out of phase wave loadings on the performance of the TST. A combination of the wave with the longest period and in-phase turbine rotation was found to have the most significant effect on the power fluctuations. The wave effect was dominant over blade shadowing, and the addition of a velocity profile had a significant effect on the bending moment of the turbine blades. These results emphasise how important it is to include waves in the numerical modelling of marine devices, provided the devices are positioned at a water depth within half the wavelength of the wave [73].

2.4 SUMMARY OF LITERATURE REVIEW

There are many different types of tidal stream devices currently available and under development in the tidal energy industry. This review has detailed a few of the approaches used in extracting tidal energy; however, the HATT is the leading type of tidal technology and hence is the focus of the work carried out in this thesis. Experimental and numerical methods for investigating the performance, loadings and wakes of a HATT under uniform/profiled current velocities, turbulence and surface waves have been discussed.

Many studies report the characterisation of a HATT under uniform flow conditions, demonstrating these aspects are well-studied. However, experimental testing campaigns

have identified the importance of investigating unsteady flows on the individual turbine component loadings. Turbulence has a big effect on turbine loading, while the loadings induced by waves produce greater fluctuations in the power and thrust than offset flow conditions or interaction with a turbine support structure. Many studies report that waves have a negligible effect on the mean performance characteristics; yet, investigating the significance of individual blade loadings using fully instrumented model tidal turbines remains in its infancy.

Numerical modelling is being used to develop various methods of wave generation; however, multiple studies examine wave-structure interaction with stationary objects and not wave-current interaction with a rotating tidal turbine. This thesis will therefore focus on the development of a wave-current CFD model for the sole purpose of investigating the loadings imparted on a TST. This research will help inform developers making decisions about the turbine rotor and blade design by presenting the individual component loadings imparted by wave and current conditions.

The literature demonstrates the benefits of using a CFD approach to numerically model 3D flow fields around a turbine. The fully resolved, SST-RANS modelling method is therefore used in this thesis as it is important to analyse the individual rotor and blade loadings induced by unsteady flow conditions. The ADM would not provide enough detail, while the use of DES or LES would be computationally infeasible with excessive simulation run times, especially given the mesh requirements for both wave and current models including a TST. The research methods adopted in this thesis will include the use of numerical CFD modelling, as well as validation using experimental testing at recirculating flume facilities.

3 THEORY

This chapter presents the key theory used throughout this thesis. Two types of wave theory are presented, and details of the relationships used in the classification of surface waves. The underlying equations used in the CFD models are shown, specifically for multiphase, free surface numerical modelling. The non-dimensional parameters used to estimate the loadings and performance imparted on a TST are given in the final section of the chapter.

3.1 WAVE THEORY

Waves are caused by disturbances to a body of water, such as the wind blowing across the surface of the ocean. These waves do not actually move the water but instead transmit energy across the ocean. There are many different types of wave that can be generated and to accurately estimate the elevation, celerity and water particle kinematics, various theories have been developed. This thesis focusses on two of these theories: Linear Wave Theory (LWT) and Stokes 2nd Order Theory (S2OT). LWT was developed by Airy in 1845 [137], and provides a description of a progressive wave but is only applicable for waves with a small amplitude. S2OT was established by Stokes [138] and includes 2nd order terms making it applicable for a wider range of waves.

3.1.1 Linear Wave Theory

LWT, often referred to as Airy Wave Theory or Small Amplitude Wave Theory (SAWT), was first published by Airy in 1845 [137] and provides a reasonable description of progressive wave motion in all water depths. LWT relies on the assumption that the wave amplitude is very small in comparison to the wavelength and therefore higher order terms are ignored allowing the free surface boundary condition to be linearised. If the amplitude of the wave is large then the higher order terms must be retained to get a more accurate representation of wave motion [139]. These higher order theories were first developed by Stokes [138] in 1847 and are detailed in Section 3.1.2. Figure 3.1 shows the distinct regions of applicability for LWT and S2OT.

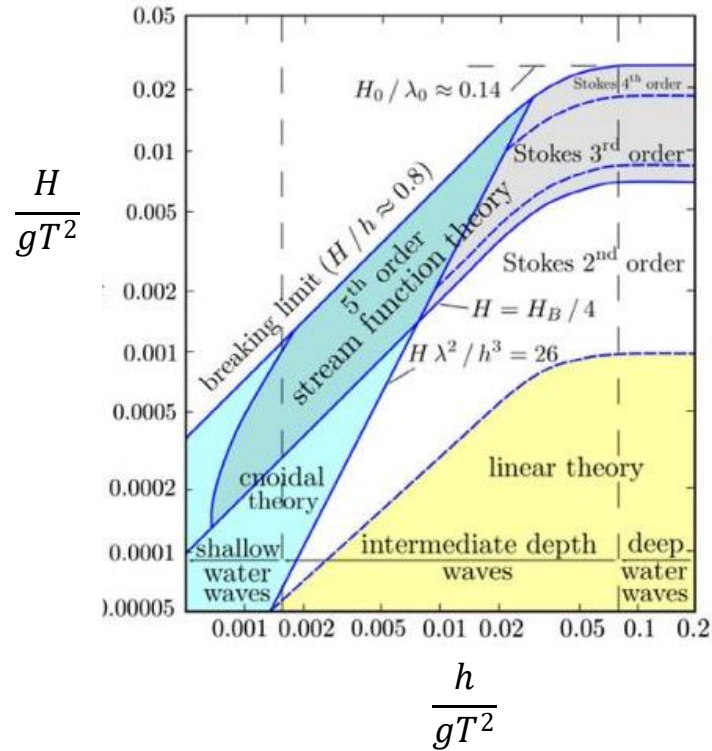


Figure 3.1. Applicability of wave theories, reproduced from [141].

Figure 3.2 shows the variables assigned to each wave property. The coordinate frame is set with the z -axis in the direction of wave travel, y -axis in the gravity direction and x -axis perpendicular to the YZ plane. The positional depth is referred to as ' y ' with the Still Water Level (SWL) at $y = 0$ and the seabed at $y = -h$, where h is the depth of the water. The surface elevation (η) of the wave fluctuates around the SWL by a set amount known as the amplitude (a) of the wave.

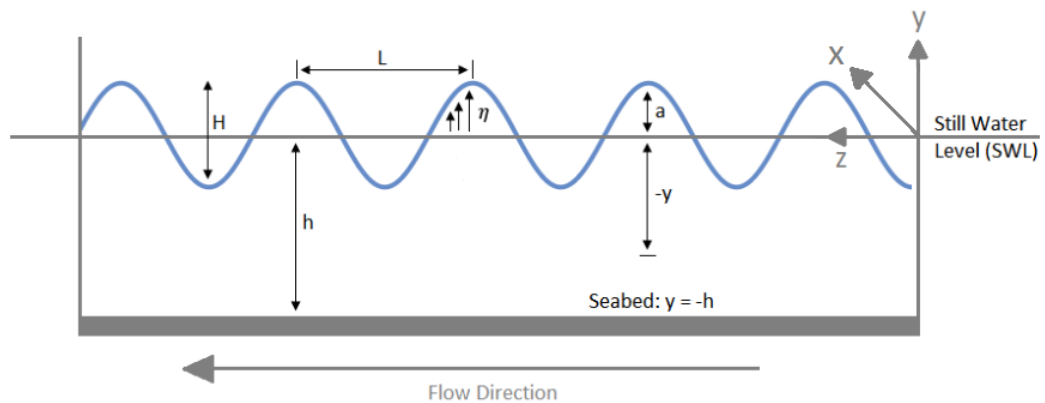


Figure 3.2. Wave motion definition.

It is assumed that the fluid under consideration is incompressible, inviscid and irrotational [140]. Due to these assumptions, the theory of potential flow is applicable and therefore a velocity potential (ϕ) is used to describe the flow. The velocity components in the x , y and z directions are assigned the variables u , v and w , respectively. These velocity components for the flow field can be derived from the velocity potential as shown by Equations (3.1a), b and c [139].

$$u = \frac{d\phi}{dx} = \frac{dx}{dt} \quad (3.1a)$$

$$v = \frac{d\phi}{dy} = \frac{dy}{dt} \quad (b)$$

$$w = \frac{d\phi}{dz} = \frac{dz}{dt} \quad (c)$$

When substituted into the continuity equation (Equation (3.31)), appropriate boundary conditions can be used to find a solution to give a representation of the flow field [141].

3.1.1.1 Boundary conditions

A free surface exists as an interface between two fluids and therefore specific boundary conditions must be applied to account for the motion of this free surface. Specifically, the variations in the water surface elevation as well as the pressure distribution over the free surface. These boundary conditions are known as the Kinematic Free Surface Boundary Condition (KFSBC) and the Dynamic Free Surface Boundary Condition (DFSBC).

3.1.1.1.1 Kinematic Free Surface Boundary Condition

Variations in the free surface motion can be expressed as shown in Equation (3.2) [142].

$$S(x, y, z, t) = y - \eta(x, z, t) = 0 \quad (3.2)$$

Where S represents the surface and η is the surface elevation of the free surface around the SWL. The variation of y with respect to time (t) is shown by Equation (3.3) [141].

$$\frac{dy}{dt} = \frac{\partial \eta}{\partial t} + \frac{\partial \eta}{\partial x} \frac{dx}{dt} + \frac{\partial \eta}{\partial z} \frac{dz}{dt} \quad (3.3)$$

Substituting Equations (3.1a), b and c, the free surface equation becomes as seen in Equation (3.4) [142]. This is known as the KFSBC which imposes the condition of no flow across an interface and is imposed on the water particle kinematics [143]. A full derivation

of the KFSBC can be found in [4] and [5] which relates the vertical velocity component at the surface to the surface position. This implies that the wave surface variations with respect to time are equal to the vertical water velocity if $\frac{\partial \eta}{\partial x}$ and $\frac{\partial \eta}{\partial z}$ are negligible due to the assumption that the wave amplitude is small compared to the wavelength (Equation (3.5)) [142].

$$v = \left. \frac{\partial \eta}{\partial t} + u \frac{\partial \eta}{\partial x} + w \frac{\partial \eta}{\partial z} \right]_{y=\eta} \quad (3.4)$$

$$v = \left. \frac{\partial \eta}{\partial t} \right]_{y=\eta} \quad (3.5)$$

3.1.1.1.2 Dynamic Free Surface Boundary Condition

The Bernoulli Equation for unsteady, irrotational flow for an incompressible fluid is shown by Equation (3.6) [142].

$$\frac{\partial \phi}{\partial t} + \frac{1}{2}(u^2 + v^2 + w^2) + \frac{p_\eta}{\rho} + gy = 0 \quad (3.6)$$

This is known as the DFSBC and describes the pressure distribution on the free surface boundary. The gauge pressure at the free surface (p_η) when $y = \eta$ is considered constant ($p_\eta = 0$) as it is assumed there is negligible motion in the air [144]. When accounting for this and using Equations (3.1a), b and c, the DFSBC simplifies to Equation (3.7) which rearranges to Equation (3.8) [139].

$$\left. \frac{\partial \phi}{\partial t} + g\eta = 0 \right]_{y=\eta} \quad (3.7)$$

$$\eta = - \left. \frac{1}{g} \frac{\partial \phi}{\partial t} \right]_{y=\eta} \quad (3.8)$$

3.1.1.1.3 Bottom boundary condition

The bottom boundary condition is described as where $y = -h$. The flow here is parallel to the boundary and the vertical component of the velocity is zero. This boundary condition is given by Equation (3.9) [141] which satisfies the condition that no flow can pass through a solid boundary.

$$v = \left. \frac{\partial \phi}{\partial y} \right|_{y=-h} = 0 \quad (3.9)$$

3.1.1.2 Reference frames

To describe the properties of a wave travelling in the same direction as a uniform current, it is convenient to establish the use of two different reference frames. A regular wave travelling in the same direction as a uniform current (\bar{W}), in a reference frame moving at the same velocity as the current, uses the Lagrangian reference frame to describe the relative wave properties. For example, the wave would have a relative angular velocity (ω_r), relative wave period (T_r) and relative wave celerity (C_r). However, using a stationary frame of reference, the wave would have an apparent angular frequency (ω_a), apparent wave period (T_a) and apparent wave celerity (C_a) by using an Eulerian reference frame.

3.1.1.3 Fundamental wave equations

The KFSBC, DFSBC and the bottom boundary condition are all used to determine the solution to the Laplace Equation. This leads to the definition of the velocity potential for a progressive wave as shown by Equation (3.10) [139]. A full derivation is detailed by [3] and [5].

$$\phi = \frac{ag \cosh k(h+y)}{\omega_r \cosh kh} \sin(kz - \omega_r t) \quad (3.10)$$

When the velocity potential is substituted into the DFSBC (Equation (3.8)), an expression for the surface elevation of a wave is given, as shown in Equation (3.11) [142].

$$\eta = a \cos(kz - \omega_r t) \quad (3.11)$$

This equation represents the fluctuation of the free surface around the SWL where a is the amplitude of the wave, k is the wave number and ω_r is the relative angular velocity of the wave, as shown in Equation (3.12). The wave fluctuates above and below the SWL so can be positive or negative.

$$\omega_r = \frac{2\pi}{T_r} \quad (3.12)$$

The distance between the crest and trough of the wave is known as the wave height (H) (Equation (3.13)) while the distance between progressive crests of each individual wave is

known as the wavelength (L) (Equation (3.14)) [73]. The speed at which the wave is travelling at is known as the relative wave celerity (C_r) and is described by Equation (3.15) [139].

$$H = 2a \quad (3.13)$$

$$L = \frac{2\pi}{k} \quad (3.14)$$

$$C_r = \frac{L}{T_r} = \frac{\omega_r}{k} \quad (3.15)$$

The dispersion relation (Equation (3.16)) shows the relationship between the angular velocity of the wave and the wave number [145]. It has two solutions, $\pm\omega_r$, corresponding to the direction of propagation of the wave, and depends upon the effects due to gravity (g) as well as the depth of the water (h). The dispersion relation is a transcendental equation and therefore iterative techniques must be used to solve it.

$$\omega_r^2 = gk \tanh(hk) \quad (3.16)$$

As previously mentioned in Equation (3.1) c, ie. $w = \frac{d\phi}{dz}$, the water velocity components can be solved using the velocity potential given in Equation (3.10). The horizontal (w_r) and vertical (v_r) velocity components are therefore given by Equations (3.17) and (3.18) respectively [73]. These velocity components are composed of the surface deep-water particle speed, the velocity variation over the water column at a given location, and a phasing term dependent on position in the wave and time [142].

$$w_r = a\omega_r \frac{\cosh k(h+y)}{\sinh kh} \cos(kz - \omega_r t) \quad (3.17)$$

$$v_r = a\omega_r \frac{\sinh k(h+y)}{\sinh kh} \sin(kz - \omega_r t) \quad (3.18)$$

Both w_r and v_r are out of phase by 90° so when w_r is maximum, v_r is minimum and vice versa.

3.1.1.4 Wave-current interaction

When surface waves are superimposed upon a uniform current, there is an interaction between the two, whereby the effect of the current causes the angular frequency of the waves to change due to the Doppler shift [55]. These changes can be observed in Equation (3.19).

$$\omega_r = \omega_a - k\bar{W} \quad (3.19)$$

The relationship between the wave period and wave celerity in the two different reference frames are shown in Equations (3.20) and (3.21).

$$\frac{1}{T_a} = \frac{1}{T_r} + \frac{\bar{W}}{L} \quad (3.20)$$

$$C_a = C_r + \bar{W} \quad (3.21)$$

Similarly, to calculate the water velocity components considering the effect of the current, Equations (3.22) and (3.23) need to be used.

$$w_a = \bar{W} + a\omega_r \frac{\cosh k(h+y)}{\sinh kh} \cos(kz - \omega_a t) \quad (3.22)$$

$$v_a = a\omega_r \frac{\sinh k(h+y)}{\sinh kh} \sin(kz - \omega_a t) \quad (3.23)$$

3.1.2 Stokes 2nd Order Theory

S2OT is a type of Finite Amplitude Wave Theory (FAWT) which include the higher order terms that LWT excludes. S2OT was first developed by Stokes [138] in 1847, and uses equations that retain the second order terms to enable a more accurate representation of wave motion for waves with a larger amplitude [139]. Classification of FAWTs are based on parameters such as relative depth (h/L) and wave steepness (H/L), explained further in Section 3.1.3.

3.1.2.1 Boundary conditions

The S2OT boundary conditions for the KFSBC, DFSBC and the bottom boundary condition are mostly the same as for LWT although they contain the nonlinear, higher order terms. The following Sections provide the equations used to define the S2OT boundary conditions.

3.1.2.1.1 Kinematic Free Surface Boundary Condition

The KFSBC given using S2OT is shown by Equation (3.24) [143].

$$v = \left. \frac{\partial \phi}{\partial y} = \frac{\partial \eta}{\partial t} + \frac{\partial \phi}{\partial z} \frac{\partial \eta}{\partial z} \right]_{y=\eta} \quad (3.24)$$

3.1.2.1.2 Dynamic Free Surface Boundary Condition

The DFSBC, retaining second order terms, is shown in Equation (3.25), with a full derivation given by [146].

$$\frac{\partial^2 \phi}{\partial t^2} + g \frac{\partial \phi}{\partial y} = - \frac{\partial}{\partial t} \left[\left(\frac{\partial \phi}{\partial z} \right)^2 + \left(\frac{\partial \phi}{\partial y} \right)^2 \right] \quad (3.25)$$

3.1.2.1.3 Bottom boundary condition

The bottom boundary remains the same as for LWT, as shown in Equation (3.9).

3.1.2.2 Fundamental wave equations

For second order theory, the velocity potential (ϕ_2) and the surface elevation (η_2) are expressed in Equations (3.26) and (3.27) respectively. These equations are the same as for LWT but with additional higher order terms. A full derivation is detailed in [142].

$$\phi_2 = \frac{ag \cosh k(h+y)}{\omega_r \cosh kh} \sin(kz - \omega_r t) + \frac{3a^2 \omega_r \cosh 2k(h+y)}{8 \sinh^4 kh} \sin 2(kz - \omega_r t) \quad (3.26)$$

$$\eta_2 = a \cos(kz - \omega_r t) + \frac{\pi a^2 \cosh kh}{2L \sinh^3 kh} (2 + \cosh 2kh) \cos 2(kz - \omega_r t) \quad (3.27)$$

Second order expressions, in a stationary reference frame, for the horizontal (w_{2a}) and vertical (v_{2a}) velocity components are given by Equations (3.28) and (3.29) [139].

$$w_{2a} = \bar{W} + a\omega_r \frac{\cosh k(h+y)}{\sinh kh} \cos(kz - \omega_a t) + \frac{3}{4} \left[\frac{\pi H}{L} \right]^2 C_r \frac{\cosh 2k(h+y)}{\sinh^4(kh)} \cos(2kz - 2\omega_a t) \quad (3.28)$$

$$v_{2a} = a\omega_r \frac{\sinh k(h+y)}{\sinh kh} \sin(kz - \omega_a t) + \frac{3}{4} \left[\frac{\pi H}{L} \right]^2 C_r \frac{\sinh 2k(h+z)}{\sinh^4(kh)} \sin(2kz - 2\omega_a t) \quad (3.29)$$

3.1.3 Wave properties

The classification of a wave can be defined by using two characteristic ratios associated with the water depth (h), wavelength (L) and wave height (H). These ratios can be used to understand the nature of the wave induced orbital motions as well as identify when wave breaking will occur.

3.1.3.1 Relative depth, h/L

The relative depth is one of the main parameters used to dictate the behaviour of a wave and determine whether the wave is a deep, intermediate or shallow water wave. Each relative depth condition influences the shape and size of the velocity orbitals as they penetrate through the water depth (see Figure 2.14 and Figure 2.15). Table 3.1 shows the classification of a deep, intermediate and shallow water wave along with the corresponding relative depth [84].

TABLE 3.1. RELATIVE DEPTH CONDITIONS FOR DEEP, INTERMEDIATE AND SHALLOW WATER WAVES.

Relative Depth (h/L)	Type of water wave
$\frac{h}{L} > 0.5$	Deep
$0.04 \leq \frac{h}{L} \leq 0.5$	Intermediate
$\frac{h}{L} < 0.04$	Shallow

Surface waves induce orbital motions which introduce a horizontal and vertical velocity component to the flow. Circular velocity orbitals arise from having an equal horizontal and vertical velocity component and are found in deep-water waves. These sub surface velocity components decay exponentially through the water depth; however, they can penetrate the water column by up to half the wavelength [73]. Intermediate water waves possess circular velocity orbitals at the water surface but become elliptical towards the seabed. This is because at shallower water depths, the bottom surface has an interaction with the wave motion. The vertical velocity component decays from a maximum near the water surface, to zero at the seabed while the horizontal component decays at the same rate as previously

described. Shallow water waves have a constant horizontal velocity component throughout the water depth while the vertical velocity decays to zero at the seabed.

3.1.3.2 Wave steepness, H/L

The wave steepness defines the phenomenon of wave breaking as well as governing the suitability of various theories, as shown in Table 3.2 [147]. Wave breaking occurs when the particle velocity at the crest of the wave becomes larger than the wave velocity [141], and occurs at $\frac{H}{L} > 0.141$ for most deep and intermediate water waves. An expression for the limiting condition of wave breaking in any water depth was given by [148] as shown in Equation (3.30).

$$\frac{H}{L} = \frac{1}{7} \tanh(kh) \quad (3.30)$$

TABLE 3.2. THE VARIOUS REGIONS FOR GIVEN WAVE STEEPNESS.

Wave Steepness (H/L)	Region
$\frac{H}{L} > 0.141$	Wave breaking
$0.04 < \frac{H}{L} < 0.141$	Stokes Theory
$\frac{H}{L} < 0.04$	Linear Wave Theory

3.2 COMPUTATIONAL FLUID DYNAMICS

CFD is a computer-based simulation technique, used for the analysis of systems involving fluid flow, heat transfer and other associated physical processes. There are a number of different CFD codes available but ANSYS CFX 18.0 [149] was the software used for all numerical models discussed in this thesis. ANSYS CFX uses the Finite Volume Method (FVM) which functions by dividing the fluid region of interest into small sub-regions which can then be used to discretise and solve the governing equations iteratively over each smaller sub-region. This gives an approximation of each variable at points throughout the domain and so a picture of the full flow characteristics can be obtained [149].

3.2.1 Governing fluid flow equations

The governing equations of fluid flow are the mathematical expressions used to describe the conservation of mass, momentum and energy for a Newtonian flow field of a given control volume. These equations are derived by considering a finite volume of fluid and using the conservation laws to describe the behaviour of the fluid in terms of the velocity, pressure, density and temperature with respect to time. The continuity equation ensures

that the mass of fluid in the finite volume is conserved. Equation (3.31) shows the continuity equation for unsteady, incompressible flow, with a full derivation available in [114]. The incompressible flow equations given in the following section are used even though air is used in some of the numerical models. There is no pressure applied to the air region and thereby an insignificant pressure change exists over the volume of this region. There is a negligible density difference over the volume and therefore the incompressible flow equations give a good representation of the flow field.

$$\frac{\partial u}{\partial x} + \frac{\partial v}{\partial y} + \frac{\partial w}{\partial z} = \text{div } \mathbf{u} = 0 \quad (3.31)$$

Using Newton's second law, the rate of change of momentum equals the sum of the forces on a fluid particle. The two types of forces are surface and body forces which are calculated in the x , y and z directions. The surface forces are primarily comprised of the pressure (p) and viscous stresses (τ) over the area, with the body forces included as source terms per unit volume per unit time (S_M). Equations (3.32a), b and c describe the momentum equations in the x , y and z directions [114].

$$\rho \frac{Du}{Dt} = \frac{\partial(-p + \tau_{xx})}{\partial x} + \frac{\partial\tau_{yx}}{\partial y} + \frac{\partial\tau_{zx}}{\partial z} + S_{Mx} \quad (3.32a)$$

$$\rho \frac{Dv}{Dt} = \frac{\partial\tau_{xy}}{\partial x} + \frac{\partial(-p + \tau_{yy})}{\partial y} + \frac{\partial\tau_{zy}}{\partial z} + S_{My} \quad (b)$$

$$\rho \frac{Dw}{Dt} = \frac{\partial\tau_{xz}}{\partial x} + \frac{\partial\tau_{yz}}{\partial y} + \frac{\partial(-p + \tau_{zz})}{\partial z} + S_{Mz} \quad (c)$$

The viscous stress components are unknown variables, but these equations can be solved by introducing a suitable model for these unknown stresses. The dynamic viscosity (μ) can be used to relate these stresses to linear deformation, whereby the viscous stresses equate to twice the rate of linear deformation multiplied by the dynamic viscosity. It is this substitution into the momentum equations which lead to the generation of the Navier-Stokes equations shown by Equation (3.33a), b and c [114]. The Navier-Stokes equations were independently derived by Claude-Louis Navier and George Stokes in 1845.

$$\begin{aligned}\rho \frac{Du}{Dt} &= -\frac{\partial p}{\partial x} + \frac{\partial}{\partial x} \left[2\mu \frac{\partial u}{\partial x} \right] + \frac{\partial}{\partial y} \left[\mu \left(\frac{\partial u}{\partial y} + \frac{\partial v}{\partial x} \right) \right] + \frac{\partial}{\partial z} \left[\mu \left(\frac{\partial u}{\partial z} + \frac{\partial w}{\partial x} \right) \right] + S_{Mx} \\ &= -\frac{\partial p}{\partial x} + \mu \left[\frac{\partial^2 u}{\partial x^2} + \frac{\partial^2 u}{\partial y^2} + \frac{\partial^2 u}{\partial z^2} \right] + S_{Mx}\end{aligned}\quad (3.33a)$$

$$\begin{aligned}\rho \frac{Dv}{Dt} &= -\frac{\partial p}{\partial y} + \frac{\partial}{\partial x} \left[\mu \left(\frac{\partial u}{\partial y} + \frac{\partial v}{\partial x} \right) \right] + \frac{\partial}{\partial y} \left[2\mu \frac{\partial v}{\partial y} \right] + \frac{\partial}{\partial z} \left[\mu \left(\frac{\partial v}{\partial z} + \frac{\partial w}{\partial y} \right) \right] + S_{My} \\ &= -\frac{\partial p}{\partial y} + \mu \left[\frac{\partial^2 v}{\partial x^2} + \frac{\partial^2 v}{\partial y^2} + \frac{\partial^2 v}{\partial z^2} \right] + S_{My}\end{aligned}\quad (b)$$

$$\begin{aligned}\rho \frac{Dw}{Dt} &= -\frac{\partial p}{\partial z} + \frac{\partial}{\partial x} \left[\mu \left(\frac{\partial u}{\partial z} + \frac{\partial w}{\partial x} \right) \right] + \frac{\partial}{\partial y} \left[\mu \left(\frac{\partial v}{\partial z} + \frac{\partial w}{\partial y} \right) \right] + \frac{\partial}{\partial z} \left[2\mu \frac{\partial w}{\partial z} \right] + S_{Mz} \\ &= -\frac{\partial p}{\partial z} + \mu \left[\frac{\partial^2 w}{\partial x^2} + \frac{\partial^2 w}{\partial y^2} + \frac{\partial^2 w}{\partial z^2} \right] + S_{Mz}\end{aligned}\quad (c)$$

3.2.2 Turbulent flow conditions

The Reynolds number (Re) is an important parameter used to give an indication of the flow regime in different fluid flows. Above a critical value (Re_{crit}) the flow behaviour becomes unsteady and chaotic and is known as turbulent flow. The equation for calculating the Reynolds number is given by Equation (3.34), where ρ is the density of the fluid, w is the velocity of the fluid in the streamwise direction, D is a characteristic linear dimension, and μ is the dynamic viscosity.

$$Re = \frac{\rho w D}{\mu} \quad (3.34)$$

An instantaneous velocity, $w(t)$, at any given time, can be deconstructed into a steady, time-averaged mean value, \bar{w} , with a fluctuating component, $w'(t)$, superimposed on it. This is known as the process of Reynolds decomposition, as shown in Equation (3.35) [150].

$$w(t) = \bar{w} + w'(t) \quad (3.35)$$

3.2.3 Reynolds Averaged Navier-Stokes equations

The RANS equations are a time-averaged form of the instantaneous Navier-Stokes equations. The RANS equations arise from the process of Reynolds decomposition, whereby the flow variable is decomposed into a fluctuating and mean component, as shown in Equation (3.35). These decomposed variables are substituted into the continuity and

Navier-Stokes equations, and then time-averaged. The continuity equation remains unchanged as the mean of the fluctuating quantity is zero ($\overline{u'} = 0$). However, the process of time-averaging produces new terms in the Navier-Stokes equations due to the interaction of various turbulent fluctuations. These new terms are known as the Reynolds stresses ($-\rho\overline{u'^2}$, $-\rho\overline{v'^2}$, $-\rho\overline{w'^2}$, $-\rho\overline{u'v'}$, $-\rho\overline{u'w'}$, $-\rho\overline{v'w'}$). They are non-zero as they contain squared velocity fluctuations. These time-averaged Navier-Stokes equations are now known as the RANS equations [114]. Turbulence models are used to predict the Reynolds stresses in order to close the system of mean flow equations.

3.2.4 Turbulence modelling

To enable the effects of turbulence to be numerically modelled without requiring unjustifiable amounts of computational power, statistical turbulence models have been developed to model turbulence effects without needing to resolve the turbulent fluctuations. Various turbulence models are used to close the RANS equations by providing models to compute the Reynolds stresses. There are two main types of approach used to close the RANS equations, Eddy Viscosity Models (EVM) or Reynolds Stress Models (RSM) [150]. The EVM methods rely on the assumption that the Reynolds stresses are proportional to the mean rates of deformation. This was proposed by Boussinesq and assumes that the turbulence present is isotropic, therefore the ratio between Reynolds stress and mean rate of deformation is the same in all directions. The RSM approach evaluates the individual stress components rather than assuming isotropic turbulence. This model is better suited for modelling flows with high levels of rotation but at the cost of large increases in computational power and time, as well as greater sensitivity to initial conditions and fine mesh requirements [150].

This thesis looks at the EVM methods and specifically the two-equation turbulence models. These are classified by the number of extra transport equations needed to be solved along with the RANS equations. They offer a good compromise between computational effort and numerical accuracy, solving separate transport equations for the velocity and length scale. Details on the k_t - ε , k_t - ω_t and SST turbulence models are given in the following sections.

3.2.4.1 The k_t - ε model

The k_t - ε turbulence model uses the turbulent kinetic energy (k_t) and the turbulence eddy dissipation (ε) to define the velocity and length scale for large scale turbulence. The model is based on the best understanding of the relevant processes presenting a set of

equations that can be applied to a large number of turbulent applications. The k_t - ε turbulence model uses a scalable wall function approach to increase the accuracy on very fine near-wall meshes. This model provides a good prediction for many engineering applications; however, certain uses are not suitable. Specifically, the model predicts excessive levels of turbulent shear stress particularly in the presence of adverse pressure gradients leading to flow separation on curved surfaces. It is also not recommended for flows in rotating fluids or flows with boundary layer separation. A full derivation of the k_t - ε turbulence equations can be found in [114].

3.2.4.2 *The k_t - ω_t model*

Wilcox [151] developed the k_t - ω_t turbulence model which solves two transport equations for the turbulent kinetic energy (k_t) and the turbulent frequency (ω_t). The main advantage of the k_t - ω_t turbulence model over the k_t - ε model is that a new near-wall treatment method was developed to allow better predictions of the near-wall interactions. The prediction of flow separation from a surface is often one of the main problems with turbulence modelling, yet this is very important when examining the effect of air flow over an aeroplane wing, or water flow over a TST blade. The k_t - ω_t model accounts for low Re effects in the boundary layer but is not as good at modelling free stream flows. Further details on the Wilcox k_t - ω_t turbulence model can be found in [151] while [150] details its implementation by ANSYS CFX.

3.2.4.3 *The Shear Stress Transport model*

The SST model was developed by Menter [152] and combines the previously mentioned k_t - ε and k_t - ω_t turbulence models. This hybrid turbulence model addresses the problems demonstrated by the k_t - ε model, which shows limitations in modelling near-wall flow fields, while the k_t - ω_t model shows problems modelling the turbulence in free stream flows. Therefore, the SST model couples the use of the k_t - ε model in the free stream regions and the k_t - ω_t model in the near-wall regions, using a blending function, based on wall distance, to allow a smooth transition between the two models. This gives a more accurate and reliable prediction for various flow types and is therefore recommended by [106] due to its improved performance under adverse pressure gradients and more accurate boundary layer simulations.

3.2.4.4 Near-wall treatment

An important feature of turbulence modelling is an accurate and robust near-wall treatment. The near-wall can be divided into three regions, the viscous sublayer, the buffer layer, and the logarithmic layer, as shown in Figure 3.3.

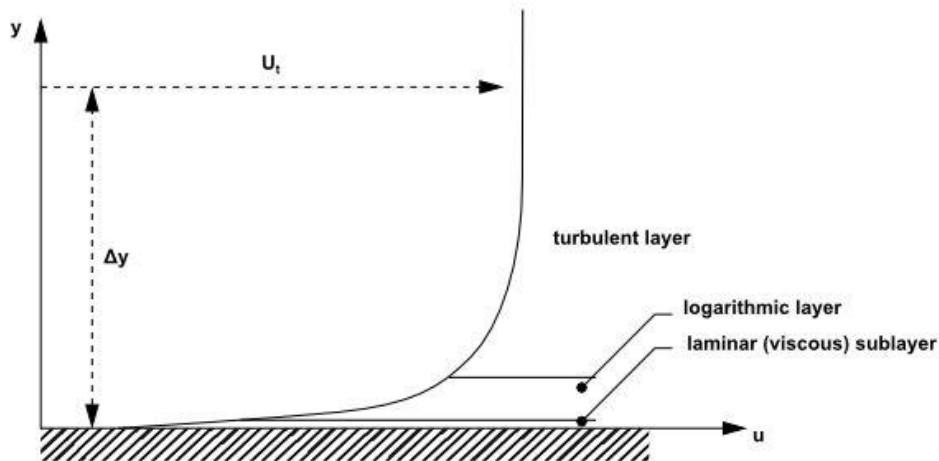


Figure 3.3. Subdivisions of the near-wall region, figure reproduced from [106].

There are two main ways to model the flow in the near-wall region, using wall functions or a Low-Reynolds-Number (Low- Re) method. The wall function method uses estimations to impose suitable conditions near the wall, reducing the computational expense required. If the logarithmic profile predicts the velocity distribution near the wall reasonably well then it enables the computation of the shear stress as a function of the velocity at a given distance from the wall. The main advantage of this approach is that it can work with a relatively course mesh near the wall with an upper y^+ limit of 500 [89]. However, the predictions deteriorate when the mesh becomes too fine and instead a low- Re method can be used. The low- Re method uses very small mesh inflation layers normal to the wall to resolve the boundary layer profile. This requires a fine mesh in the near-wall zone and can dramatically increase computational run times and increase memory provisions.

A new near-wall treatment method was developed to allow automatic switching from wall functions to the low- Re near-wall formulation, based on the refinement of the mesh [153]. This allows models with various different sized meshes to all use the same near-wall treatment. A study by Menter [153], using automatic near-wall treatment, shows that the prediction of the wall shear stress varies by less than 2% for grids using a y^+ of between 0.2 and 100. All solutions follow the logarithmic profile and therefore this shows that the new wall treatment method dramatically increases the accuracy of near-wall modelling while

being less user-dependent for the mesh generation. Automatic near-wall treatment is the default method used for all ω_t -based turbulence models.

3.2.5 Multiphase modelling

Multiphase modelling exists where there is more than one fluid present in the numerical model. The two or more fluids are mixed on a macroscopic scale with an easily distinguished interface between the fluids. Each fluid variable is solved individually, however, the fluids may interact with each other across the phase interface. Homogeneous multiphase flow is a limiting case of the Eulerian-Eulerian multiphase model used, where all fluids share the same field variables. The homogeneous model is used when the interface is well defined throughout the model, present in applications such as open channel flows [106]. Therefore, all ‘free surface’ models described in this thesis use homogeneous, multiphase, free surface flow modelling techniques, as recommended by [106].

3.2.5.1 Volume fractions

Volume fractions are used to specify the fraction of the control volume that a fluid phase occupies. All volume fractions assigned for each fluid in the same control volume must sum to 1. All multiphase models in this thesis use water and air as the two fluid phases present. The volume fractions of a fluid is described by Equation (3.36):

$$V_\alpha = r_\alpha V \quad (3.36)$$

Where r_α is the volume fraction of fluid α , and V_α is the volume occupied by fluid α in an overall volume, V [150].

To accurately model free surface flow problems, the initial conditions for the model must be clearly defined. The volume fraction and relative pressure field of each fluid phase can be defined using CFX Expression Language (CEL) step functions. The pressure field in the water phase must be hydrostatic, while the air phase has a uniform pressure field. The water depth is defined by Equation (3.37), while Figure 3.4 shows the setup of the problem that will be addressed later in Chapter 5.

$$h = 2[m] \quad (3.37)$$

A step function is then used to define the volume fraction of air and water present in the model in comparison to the specified water depth. If the argument in the step function is positive, a value of 1 is returned, negative and a value of 0 is returned, or equal to zero and

3 THEORY

a value of 0.5 is returned. For the step function to work it must be dimensionless, hence the division of the equation by 1[m]. This is shown in Equations (3.38) and (3.39) for the air and water respectively.

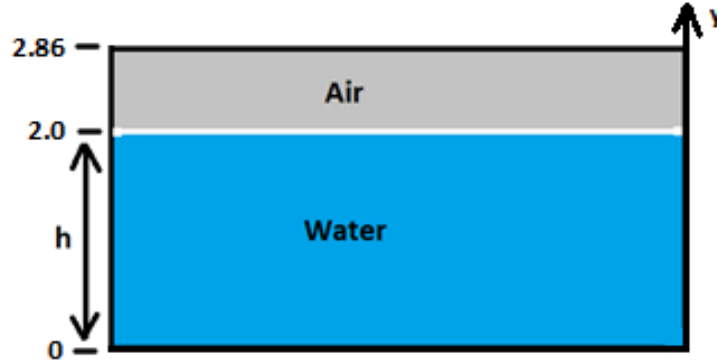


Figure 3.4. Visual description of how to define the volume fractions of each fluid phase.

$$UpStreamVolFractAir = step((y - h)/1[m]) \quad (3.38)$$

$$UpStreamVolFractWater = 1 - UpStreamVolFractAir \quad (3.39)$$

Therefore,

- 0 - 2m: $UpStreamVolFractWater = 1$ and $UpStreamVolFractAir = 0$
- 2 - 2.86m: $UpStreamVolFractAir = 1$ and $UpStreamVolFractWater = 0$

The pressure field is then defined as shown in Equation (3.40). Due to the inclusion of the volume fraction term for the water phase, the hydrostatic pressure is only applied in the water region between 0 and 2m. The pressure field can be observed in Figure 3.5.

$$UpStreamPressure = ((\rho_{water} - \rho_{air}) \cdot g \cdot (h - y)) \cdot UpStreamVolFractWater \quad (3.40)$$

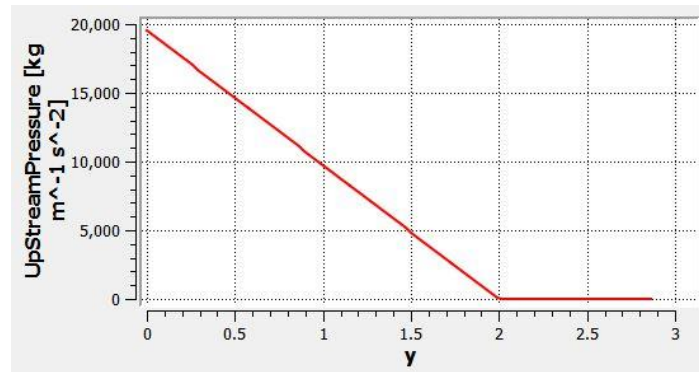


Figure 3.5. The defined pressure field as a result of using volume fractions for each fluid phase.

3.2.5.2 Free surface flow

Free surface flow is a specific type of multiphase modelling where the phases used are separated by a distinct interface.

3.2.5.2.1 Interface compression

The interface compression level controls the volume fraction advection scheme for free surface flows [106]. This in turn controls the interface sharpness and is set at a setting of 2 for ‘aggressive compression’ which is the default.

3.2.5.3 Buoyancy

Buoyancy forces can be modelled by ANSYS CFX by the inclusion of buoyancy source terms. In multiphase flows, the density difference between the phases results in a buoyancy force. The buoyancy reference density is chosen to be the density of the lighter fluid, in this case, air. This gives a constant pressure in the lighter fluid phase and a hydrostatic pressure in the heavier phase.

The density difference fluid buoyancy model is used as recommended for all multiphase flows [106]. The buoyancy force (F_α) is calculated as shown in Equation (3.41).

$$F_\alpha = (\rho_\alpha - \rho_{ref})g \quad (3.41)$$

3.3 NON-DIMENSIONAL PERFORMANCE CHARACTERISTICS

The torque (Q), power (P) and thrust (T) are used to characterise the performance of a TST in different flow conditions. The power specifies the rate at which the turbine rotor extracts energy; the thrust describes the axial force of the fluid on the turbine; and the torque is the measure of rotational force imparted on the turbine [96]. These variables can

be turned into non-dimensional performance characteristics which are more useful for comparing different tidal turbines in varying flow conditions. These performance characteristics are based on linear momentum theory for an actuator disc model [154], and consist of three main performance indicators: the coefficient of torque (C_q), the coefficient of power (C_p) and the coefficient of thrust (C_t).

3.3.1 Coefficient of torque

The C_q is the ratio of torque generated by the turbine to the maximum theoretical torque, as shown in Equation (3.42), where ρ is the water density, A_{turb} is the swept area of the turbine ($A_{turb} = \pi R^2$), R is the radius of the turbine, and \bar{W}_{vol} is the volumetrically averaged velocity over the turbine swept area in the streamwise direction normal to the turbine. A volumetrically averaged flow velocity, taken 1m upstream of the turbine, is used to define the flow conditions at the inflow to the turbine. The calculation of this variable is explained in Section 3.3.5.

$$C_q = \frac{Q}{\frac{1}{2}\rho A_{turb} \bar{W}_{vol}^2 R} \quad (3.42)$$

3.3.2 Coefficient of power

The C_p is the ratio of the energy extracted by the rotor to the available energy in the moving water over the turbine swept area. The output power is calculated by multiplying the torque and the angular velocity of the turbine (ω) as shown by Equation (3.43) [96].

$$C_p = \frac{Q\omega}{\frac{1}{2}\rho A_{turb} \bar{W}_{vol}^3} \quad (3.43)$$

3.3.3 Coefficient of thrust

The C_t is the ratio of the axial load on the turbine compared to the available axial load over the swept area of the turbine and is given by Equation (3.44) [96].

$$C_t = \frac{T}{\frac{1}{2}\rho A_{turb} \bar{W}_{vol}^2} \quad (3.44)$$

3.3.4 Tip Speed Ratio

The TSR, defined by the symbol λ , describes the ratio of the blade tip speed to the average upstream velocity, as shown in Equation (3.45) [96]. Most performance curves,

using each of the three performance coefficients, are plotted against TSR as it enables different tidal turbines to be compared regardless of its turbine diameter or the upstream flow conditions.

$$\lambda = \frac{\omega R}{\bar{W}_{vol}} \quad (3.45)$$

3.3.5 Volumetrically averaged streamwise velocity

The volumetrically averaged streamwise velocity over the turbine swept area (\bar{W}_{vol}) is used to provide an estimation of the flow conditions upstream of the turbine. When there is a profiled velocity acting over the water depth, the depth averaged velocity over the swept area of the turbine is not equally distributed. The velocity at the top/bottom of the turbine swept area is acting over a much smaller area of the turbine than in the central section of the turbine swept area. Therefore, the volumetrically averaged flowrate over different horizontal sections of the turbine swept area need to be calculated to provide a good estimate of the average streamwise velocity. To do this the swept area is split up into horizontal sections as shown in Figure 3.6.

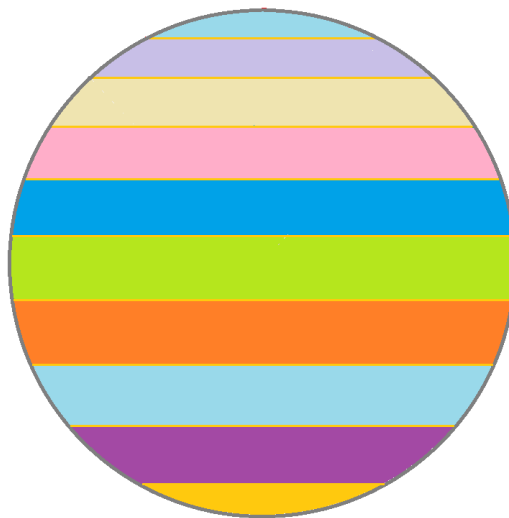


Figure 3.6. An example of the swept area being split up into horizontal sections which are used to calculate the flowrate for each horizontal section area.

The relationship between the swept area circle radius (or turbine radius) (R), the height of the segment (h_{seg}) and the chord length (c) is represented by Equation (3.46) [155]. A diagram of these circle descriptors are shown in Figure 3.7.

$$R = \frac{h_{seg}}{2} + \frac{c^2}{8h_{seg}} \quad (3.46)$$

The height of the segment and radius are predetermined and therefore the chord length can be found. The area of the segment (A_{seg}) can then be found, as shown in Equation (3.47), using the area of the sector (A_{sec}) (Equation (3.48)) and also the area of the triangle (A_{tri}) (Equation (3.50)). The central angle (θ_{centre}) can be found using trigonometry using half the chord length (b) (Equation (3.49)) and the triangle height (h_{tri}).

$$A_{seg} = A_{sec} - A_{tri} \quad (3.47)$$

$$A_{sec} = \frac{\theta_{centre}}{360} \pi R^2 \quad (3.48)$$

$$b = \frac{1}{2} c \quad (3.49)$$

$$A_{tri} = \frac{1}{2} b h_{tri} \quad (3.50)$$

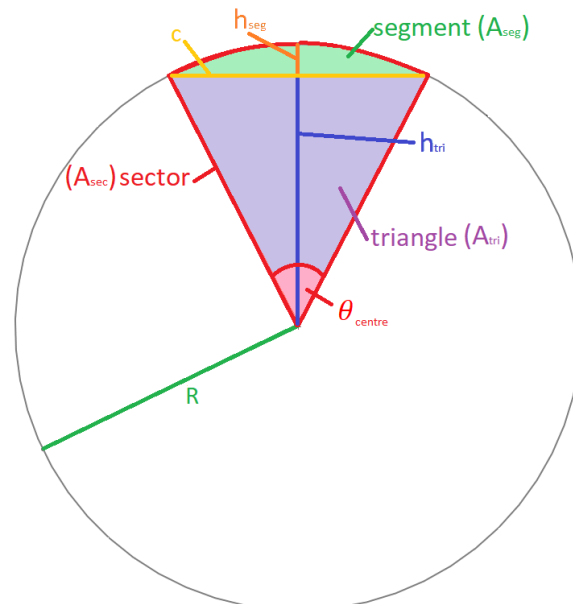


Figure 3.7. Descriptors used for parts of a circle.

The first horizontal area section is found using the equations stated previously to find the area of the top segment labelled segment 1/horizontal section 1, as shown in Figure 3.8. After this, a larger segment is found, segment 2, and the previous segment area, horizontal section 1, is taken away from it leaving the next horizontal section area 2. The volumetric flow rate (Q_{flow}) over the swept area is found using Equation (3.51), where A_{horiz} is the area of each horizontal section and \bar{W} is the average streamwise velocity at that specific water depth. Once the total flow rate is calculated, this can be divided by the total swept area of the turbine to give an estimation of the volumetrically averaged streamwise velocity over the turbine swept area. This is shown by Equation (3.52). It is assumed that the velocity profile through the water depth is constant across the flow.

$$Q_{flow} = \sum_{n=1}^N (A_{horiz_n} \bar{W}_n + A_{horiz_{n+1}} \bar{W}_{n+1} + \dots) \quad (3.51)$$

$$\bar{W}_{vol} = \frac{Q_{flow}}{A_{turb}} \quad (3.52)$$

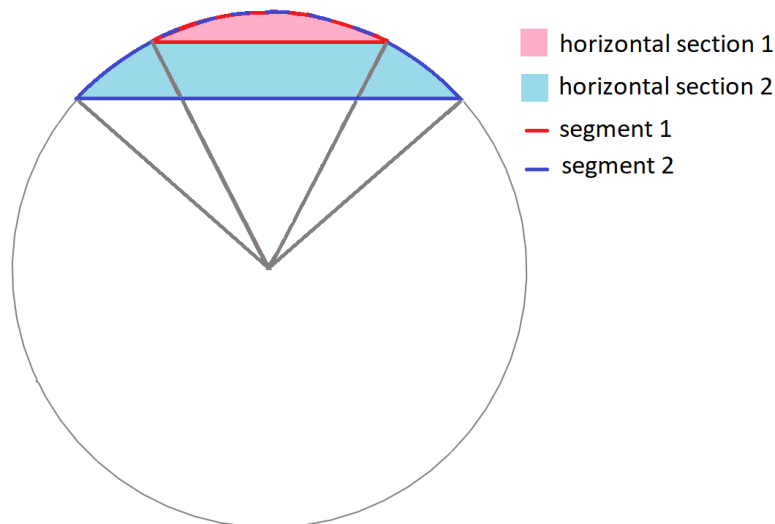


Figure 3.8. The process of dividing the turbine swept area up into horizontal sections.

3.4 SUMMARY

This chapter provides a description of the relevant theory used in this thesis. The fundamental wave equations used in LWT and S2OT are presented, along with definitions of the relative depth and wave steepness which are used to describe the behaviour of

3 THEORY

surface waves. The underlying equations used in CFD modelling are shown, specifically for multiphase, free surface, RANS-SST numerical simulations. The non-dimensional performance characteristics used to estimate the performance of a TST are given in the final section of the chapter, along with the method used in calculating the volumetrically averaged streamwise velocity.

4 EXPERIMENTAL TESTING METHODOLOGY

Experimental testing was carried out at the University of Liverpool's recirculating water channel and the IFREMER wave-current flume, to allow validation of the CFD models developed, as described later in Chapter 5. This chapter describes the experimental procedure for each test facility, detailing the measurement equipment employed and the corresponding setup used. Experimental flow data obtained from the recirculating water channel at the University of Liverpool was provided by an independent testing campaign conducted by the University of Liverpool. All testing carried out at IFREMER was conducted by Cardiff (including the author) and Strathclyde Universities. This chapter provides information on the design and manufacture of a model scale tidal turbine developed by the Cardiff Marine Energy Research Group (CMERG). This turbine built upon previous iterations of turbine design from Cardiff University [89], [156].

4.1 TURBINE DESCRIPTION

The 3-bladed, HATT used in this thesis was designed and manufactured by CMERG [156], with a diameter of 0.9m making it approximately 1:20 scale, as shown in Figure 4.1A.

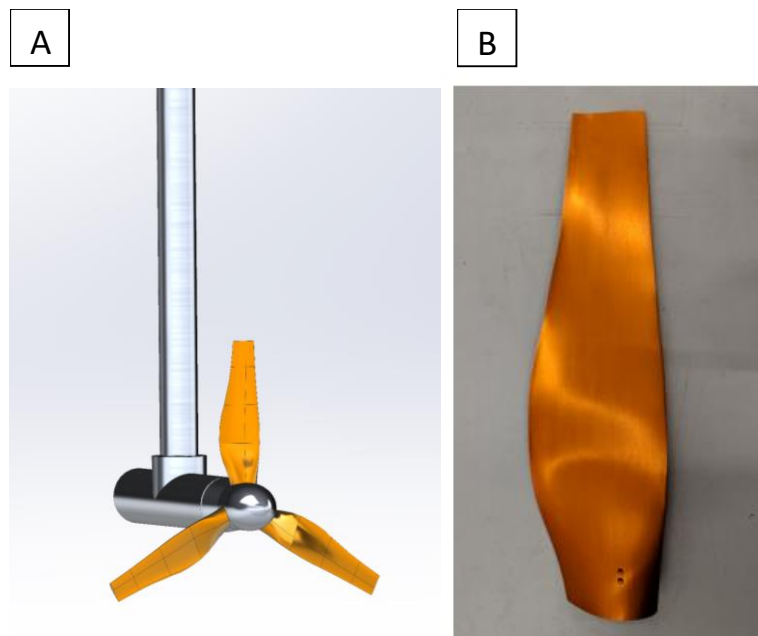


Figure 4.1. Diagram of: A) the full turbine and; B) the new blade design.

The blade design was based upon the Wortmann FX63-137 aerofoil, as detailed by [101], with a pitch angle of 6.24° and a twist distribution of 19° . These settings were found to be

the optimum for this design and are shown in Figure 4.1B. Table 4.1 presents the details for the blade geometry while Table 4.2 provides a summary of the main turbine characteristics. More information on the turbine design and manufacture can be found detailed in [101], [156].

TABLE 4.1. BLADE GEOMETRY DETAILS.

r/R	Blade chord (mm)
0.146	72.5
0.229	87.8
0.305	103.1
0.382	1.906
0.459	109.5
0.536	105.1
0.615	93.1
0.692	83.6
0.768	73.6
0.845	67.6
0.922	62.8
1.0	58.9

TABLE 4.2. MAIN TURBINE CHARACTERISTICS SUMMARY.

Characteristic	Description
No. Blades	3
Blade length	384.5 mm
Pitch angle	8°
Twist distribution	19°
Turbine diameter	900 mm
Hub diameter	130 mm

4.1.1 Instrumentation and data recording

The turbine had a direct drive and used a Permanent Magnet Synchronous Machine (PMSM) for the turbine control and power take-off. The turbine was fully instrumented in order to quantify the dynamic loadings on the turbine under various fluid flow conditions. Data acquisition was undertaken using a National Instruments Compact Rio. Table 4.3 provides a summary of the turbine instrumentation used and the sample rates. Further information on the turbine instrumentation can be found in [156], but a basic overview of the instrumentation consists of:

- Integrated rotor thrust/torque transducer
- Instrumented rotor to measure the in-plane and out-of-plane blade root bending moments for each turbine blade
- Optical encoder to determine the turbine position

- Instrumented stanchion to measure the bending moment and two accelerometers used to measure vibration through the support structure
- Moisture sensor for leakage detection

TABLE 4.3. A SUMMARY OF THE TURBINE INSTRUMENTATION USED AND THE SAMPLE RATES.

Measurement type	Device used	Sample rate
Thrust	Applied measurements transducer	200 Hz
Torque	Applied measurements transducer	200 Hz
Out of plane bending moment	Full bridge strain gauge	200 Hz
Turbine position	Heidenhain Optical encoder	45 Hz
Stanchion vibration	Single axis accelerometer	10000 Hz

4.1.2 Instrumentation calibration

Calibration of the model scale turbine instrumentation was carried out as detailed in the following section.

4.1.2.1 Rotor thrust and torque transducers

The rotor thrust and torque transducers were calibrated by Applied Measurements Ltd. Table 4.4 reports any non-linearity, hysteresis and cross-axis sensitivity. Non-linearity is the maximum amount that the actual data deviates from the line of best fit. It is given as a percentage of the full-scale output (FS). Hysteresis is the maximum difference between measurement values when approaching a specified point upon loading and then unloading of the system. It is specified as a positive or negative percentage of the measurement range. Cross-axis sensitivity is the resulting effect of loading in one direction in response to the other direction, also given as a percentage. More information on the discussed calibration parameters can be found in [157].

TABLE 4.4. SUMMARY OF CALIBRATION RESULTS FOR THE THRUST AND TORQUE TRANSDUCERS, UNDERTAKEN BY APPLIED MEASUREMENTS LTD, FIGURE REPRODUCED FROM [156].

Characteristic	Quantity	Value
Thrust (T)	Gradient (A/N)	0.005349
	Non linearity	$\pm 0.056\%$ FS
	Hysteresis	$< 0.098\%$ FS
	Cross sensitivity	0.45% FS
Torque (Q)	Gradient (A/Nm)	0.00801
	Non linearity	$\pm 0.031\%$ FS
	Hysteresis	$< 0.062\%$ FS
	Cross sensitivity	0.18% FS

4.1.2.2 Out of plane bending moment transducer

The out of plane bending moment transducers for each blade were calibrated according to the British Standards Institution – BS 8422:2003 [158]. The out of plane bending moment

was only measured around the x -axis, as shown in Figure 5.10. Hanging masses were used to gradually load and unload the transducers, recording the output current. Only blade 2 was instrumented during the IFREMER testing described in this thesis, and therefore only that single blade calibration data is included here, in Table 4.5. From here on, all experimental blade results discussed in this thesis refer to the experimental results obtained by blade 2.

TABLE 4.5. SUMMARY OF CALIBRATION RESULTS FOR THE OUT OF PLANE BENDING MOMENT TRANSDUCER FOR BLADE 2, FIGURE REPRODUCED FROM [156].

Characteristic	Quantity	Value
Out of plane bending moment (BM_x)	Gradient (mA/Nm)	0.163

4.1.3 Uncertainty analysis

This section describes the methodology used to calculate the total uncertainties of measured variables in the experimental testing, as outlined by [159] and [6]. The total uncertainty associated with measurements is a combination of precision error (μ_p) and bias error (μ_b). Precision error relates to how repeatable the measurement is while bias error indicates the true accuracy of the measurement and remains constant in repeat measurements [71]. Manufacturers often provide information on the bias error with their physical measurement equipment. This source has been used in estimation of the bias error as well as methods used in the instrumentation calibration. The precision uncertainties have been calculated using the standard deviation of the average values for each parameter. The physical experimental testing has both precision and bias errors which can be combined to calculate the total uncertainty (μ_{tot}) using Equation (4.1):

$$\mu_{tot} = \sqrt{\mu_p^2 + \mu_b^2} \quad (4.1)$$

The turbine loadings can be used to calculate the performance characteristics of the turbine, as previously discussed in Section 3.3. The uncertainties on these turbine loadings as well as the variables used in the calculation of the performance characteristics are detailed in Table 4.6.

The sources for the bias uncertainties are detailed below:

- **thrust and torque transducers:** traceable to National Standards Certificate No: TD0242 and were calculated from the methods used in the instrumentation calibration

- **out of plane bending moment:** calculated using the calibration results
- **angular velocity:** calculated using the encoder position accuracy and the clock time stamp frequency
- **water density:** taken using the difference between the densities of water between 10°C and 25°C
- **turbine radius:** takes into account the blade manufacturing processes as well as inaccuracies in assembling the blades onto the hub

The sources for the precision uncertainties were taken under uniform current-only conditions at a TSR of 4.

TABLE 4.6. SUMMARY OF THE BIAS AND PRECISION UNCERTAINTIES FOR THE VARIABLES USED IN CALCULATION OF THE TURBINE PERFORMANCE CHARACTERISTICS.

Characteristic	Mean value	Bias uncert. (μ_b)	Precision uncert. (μ_p)	Total uncert. (μ_{tot})	μ_{tot} as a percentage of mean value (%)
Thrust transducer, T (Nm)	301.64	7.11	5.90	9.24	3.06
Torque transducer, Q (Nm)	16.36	0.20	0.61	0.64	3.91
Out of plane bending moment, BM_x (Nm)	24.01	0.12	0.60	0.61	2.54
Angular velocity, ω (rad/s)	8.89	0.0001	0.028	0.028	0.31
Water density, ρ (kg/m ³)	998.6	2.0	-	2.0	0.2
Turbine radius, R (m)	0.45	0.005	-	0.005	1.11

The total uncertainties as a percentage of the mean value were <4% for all the turbine parameters, demonstrating the small magnitude of uncertainty in each variable. To calculate the total uncertainty for each of the performance characteristics, the individual component uncertainties must be used with the uncertainty function. For example, calculation of the uncertainty propagation for C_p , as shown in Equation (4.2), uses the uncertainty function for each of the components given in Section 3.3. Equations (4.3) and (4.4) show the equivalent calculations for C_t and C_q .

$$\mu_{C_p} = \bar{C}_p \sqrt{\left(\frac{\mu_Q}{\bar{Q}}\right)^2 + \left(\frac{\mu_\omega}{\bar{\omega}}\right)^2 + \left(\frac{\mu_\rho}{\bar{\rho}}\right)^2 + \left(\frac{2\mu_R}{\bar{R}}\right)^2 + \left(\frac{3\mu_w}{\bar{w}}\right)^2} \quad (4.2)$$

$$\mu_{C_t} = \bar{C}_t \sqrt{\left(\frac{\mu_T}{\bar{T}}\right)^2 + \left(\frac{\mu_\rho}{\bar{\rho}}\right)^2 + \left(\frac{2\mu_R}{\bar{R}}\right)^2 + \left(\frac{2\mu_w}{\bar{w}}\right)^2} \quad (4.3)$$

$$\mu_{C_q} = \overline{C_q} \sqrt{\left(\frac{\mu_Q}{\overline{Q}}\right)^2 + \left(\frac{\mu_\rho}{\overline{\rho}}\right)^2 + \left(\frac{3\mu_R}{\overline{R}}\right)^2 + \left(\frac{2\mu_w}{\overline{w}}\right)^2} \quad (4.4)$$

4.2 UNIVERSITY OF LIVERPOOL RECIRCULATING WATER CHANNEL

The experimental data later referred to in Chapter 8 was carried out independently by the University of Liverpool at their recirculating water channel facility, as detailed by [84], [160]. These flow-only results were used for validation of the numerical wave and current flow model. The recirculating water channel, shown by the schematic in Figure 4.2, is 1.4m wide, 0.76m deep and 3.7m long with a capacity of 90 000L. An electric motor drives an axial flow impeller capable of providing flow velocities of up to 6m/s with a TI of $\approx 2\%$. The water channel was designed so that the main current flow had a uniform velocity profile to within 1% except near the walls and base of the channel where normal boundary layer effects were present. The generation of regular waves was carried out using a hinged paddle type wave maker, as shown in Figure 4.3.

Flow velocity measurements were obtained using a Nortek Vectrino+ ADV at a sampling rate of 200Hz. The ADV had 4 receiving transducers with a sample volume of 0.2cm³ located 50cm below the probe. The estimated error was < 1% in the mean velocity. A resistance wave probe was used to measure the water surface elevation at a sampling rate of 200Hz. Data was collected for a minimum of 200s. Table 4.7 provides a summary of the flow measurement data along with their sample rate and estimated uncertainty values.

TABLE 4.7. A SUMMARY OF THE INSTRUMENTATION USED, THEIR SAMPLE RATES AND ESTIMATED UNCERTAINTY.

Measurement type	Device used	Sample rate	Estimated uncertainty
Flow velocity	Nortek Vectrino+ ADV	200 Hz	$\pm 1\%$
Water surface elevation	Resistance wave probe	200 Hz	-

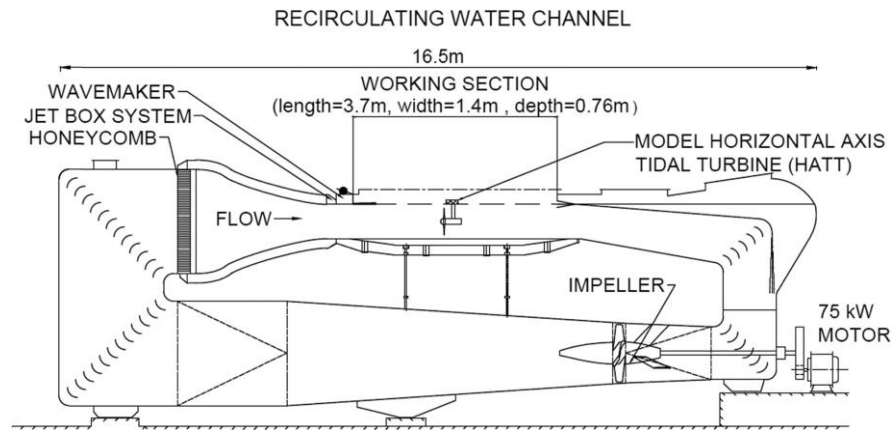


Figure 4.2. Recirculating water channel layout, figure reproduced from [84].

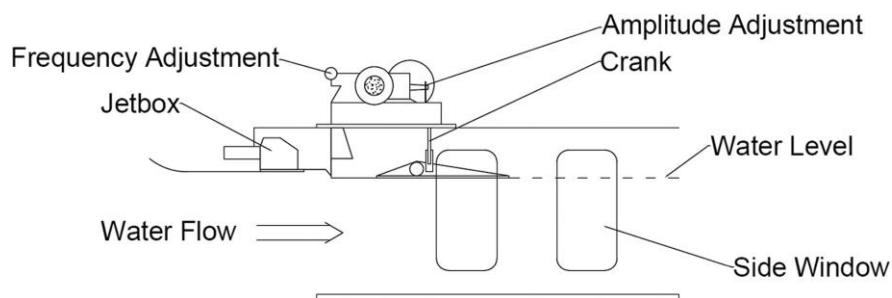


Figure 4.3. Wave maker schematic, figure reproduced from [84].

The test campaign was performed using a target uniform streamwise velocity of 0.93 m/s and by superimposing two different wave profiles on top of the current flow to investigate the wave-current interaction. Details of these wave characteristics can be found in Table 4.13. The experimental results obtained by the University of Liverpool were collected over 250 wave cycles and averaged to determine the mean wave profiles. The flow velocities were measured using the ADV which covered a depth range from $y = -0.12\text{m}$ to $y = -0.445\text{m}$ with $y = 0\text{m}$ being at the SWL [84]. Table 4.8 gives a summary of the key features for the University of Liverpool recirculating water channel.

TABLE 4.8. KEY FEATURES OF EACH TEST FACILITY.

	University of Liverpool Recirculating Water channel (LVP)	IFREMER wave-current flume (IFR)
Facility type	Flume	Flume
Facility dimensions	1.4 x 0.76 x 3.7 m	4 x 2 x 18 m
Testing date	2015	2018
Length of measured data	200 s	100 – 200 s
Turbine depth	-	1 m
Blockage ratio	-	7.95%
Pitch angle	-	6.2 +/- 0.5deg
Flow velocities tested	0.93 m/s	1.00 m/s
$Re_{0.7chord}$		6.48×10^4

4.3 IFREMER WAVE-CURRENT FLUME TANK

Experimental testing was carried out by Cardiff and Strathclyde Universities using the wave-current flume at IFREMER. The dimensions of the flume are 4m wide, 2m deep and 18m long, as shown in Figure 4.4, with a general flow turbulence of $\approx 3\%$ [69]. It was possible to produce streamwise velocities of between 0.1 – 2.2m/s, while results detailed in this thesis are all conducted at a streamwise velocity of 1.0 m/s. Wave generation can also be achieved using eight displacement paddles which are 0.5m wide and sit 0.5m into the top of the water column, spanning the entire width of the flume as shown in Figure 4.5. The wave maker could produce regular waves between $f=0.5\text{-}2\text{Hz}$. A physical beach was located at the opposite end of the tank to the wave maker to dampen the waves and prevent reflection from the end of the tank. Table 4.8 gives an overview of the key features for each test facility.

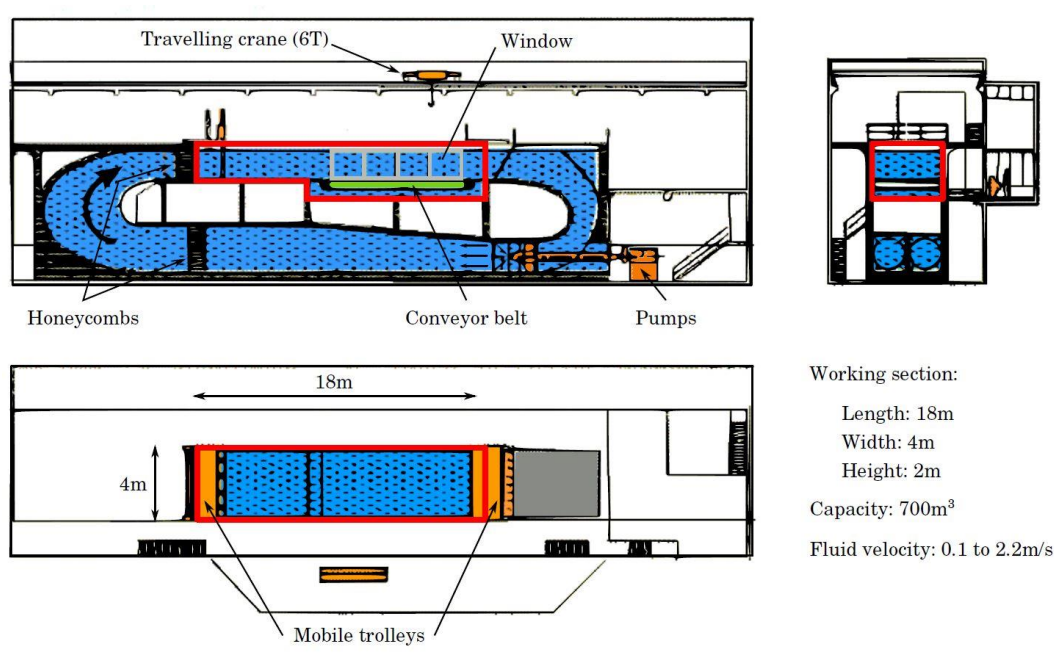


Figure 4.4. IFREMER flume tank schematic, figure reproduced from [69].

4.3.1 IFREMER Experimental set up

The turbine was installed at a depth of 1m for all tests, giving a clearance in still water of 0.61ϕ , and centralised in the cross-stream direction. The turbine was supported by a 0.09m diameter stanchion which held the turbine stationary within the flume. The pitch angle for each blade was set to $6^\circ \pm 0.5^\circ$. All testing was conducted using speed control, whereby the angular velocity of the turbine was controlled so that it remained constant. The angular velocities and corresponding TSRs used are specified in Table 4.9. There was a blockage

ratio of 7.95% while the turbine was submerged in the IFREMER wave-current flume. This ratio was low enough not to interfere with the flow characteristics [161].

TABLE 4.9. ANGULAR VELOCITIES USED TO CONTROL TURBINE ROTATION.

Turbine Angular Velocity, ω (rad/s)	Approximate TSR, λ
0.00	0
2.22	1
4.44	2
6.67	3
8.89	4
11.11	5
13.33	6
15.55	7

Figure 4.5 provides a schematic of the experimental facility at IFREMER and the instrumentation setup for when the turbine is present and also when the turbine had been removed to enable flow measurements to be taken at the turbine location. 2D Laser Doppler Anemometry (LDA) was used to measure the flow velocity in the streamwise and vertical directions at multiple points through the water depth. The measurement volume was initially aligned 1m upstream of the centre of the turbine nose cone. From this location, the LDA was then positioned at multiple locations through the water depth at ± 0.6 m from the centre of the turbine nose cone. The streamwise velocity was set to induce a current flow of 1.0 m/s which equated to a chord based Reynolds number of $Re_{0.7chord} = 6.48 \times 10^4$ [156], as defined by Equation (4.5).

$$Re_{0.7chord} = \frac{\rho c_{0.7} W}{\mu} \quad (4.5)$$

$c_{0.7}$ is the chord length at 70% of the radius. Previous experimental testing confirmed that Reynolds effects become negligible, with a variation $< 1\%$, for Reynold's numbers above $Re_{0.7chord} = 6.48 \times 10^4$ [156].

4 EXPERIMENTAL TESTING METHODOLOGY

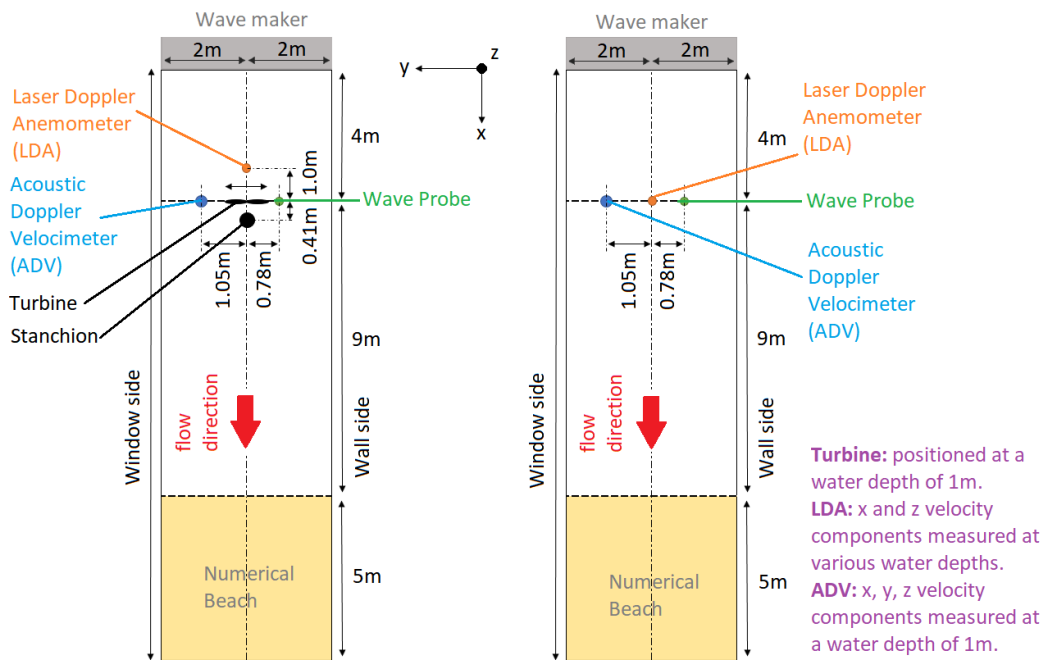
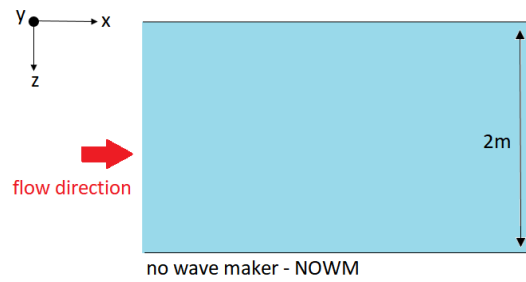


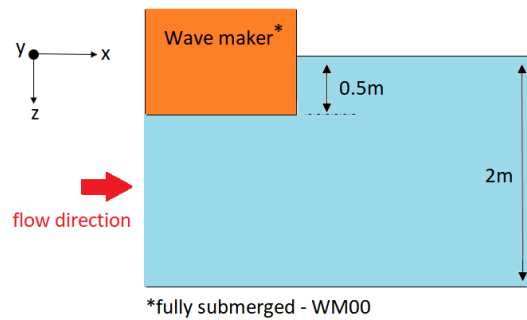
Figure 4.5. A plan view of the IFREMER experimental setup of flow measurement equipment and the turbine positioning for: (a) when the turbine is present and; (b) when the turbine has been removed.

Flow straighteners placed in the upstream area of the flume aided the generation of uniform current conditions. However, profiled current conditions could also be generated by positioning the wave maker paddles to create a blockage in the upper section of the water column. The wave maker could be positioned in two different locations, WM00 or WM20, creating two different velocity profiles. The blockage that the wave maker presents to the flow, extends across the full width of the flume, and therefore also produces profiled flow conditions across the full width of the flume. Unsteadiness in the flow is also introduced due to the unsteady wake behind the wave maker paddles. WM00 refers to the wave maker being fully submerged to a water depth 50cm below the water surface, therefore raised by 0cm. WM20 refers to the wave maker being raised by 20cm so it was only submerged in the top of the water column to a depth of 30cm. Figure 4.6 describes these two different positions that the wave maker can adopt. Experimental testing was carried out in both uniform and profiled conditions, as detailed in Table 4.14. Even though the presence of the wave maker induced the velocity profiles, it was not operational in profiled current-only testing. Figure 4.7 shows the setup of the TST and the LDA, 1m upstream.

A



B



C

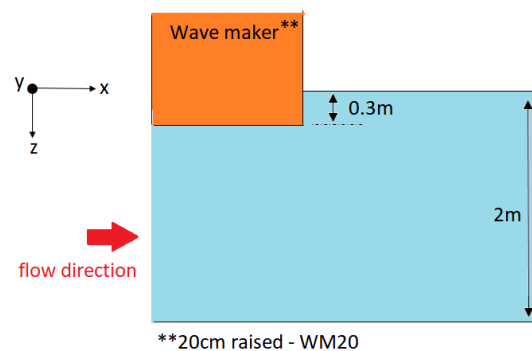


Figure 4.6. IFREMER experimental setup of wave maker when at position: A) NOWM (no wave maker), B) WM00 (fully submerged) and; C) WM20 (raised by 20cm).

As well as current-only conditions, wave and current interaction with the TST were also tested. However, due to the addition of the wave maker blockage, there was always an induced velocity profile present when testing in wave and current conditions. Two different regular waves, combined with current conditions, were used to test the performance of the model TST in more complex conditions, as shown in Table 4.14. A capacitance type wave probe was used to measure the surface elevation of the water surface. A summary of the

instrumentation used to measure the flow velocity and surface elevation is given in Table 4.10. Measurements for each test were taken for between 100-200 seconds.

TABLE 4.10. A SUMMARY OF THE INSTRUMENTATION USED, THEIR SAMPLE RATES AND ESTIMATED UNCERTAINTY.

Measurement type	Device used	Sample rate
Flow velocity	DANTEC 2D LDA	200 Hz
Water surface elevation	Churchill controls wave probe	100 Hz

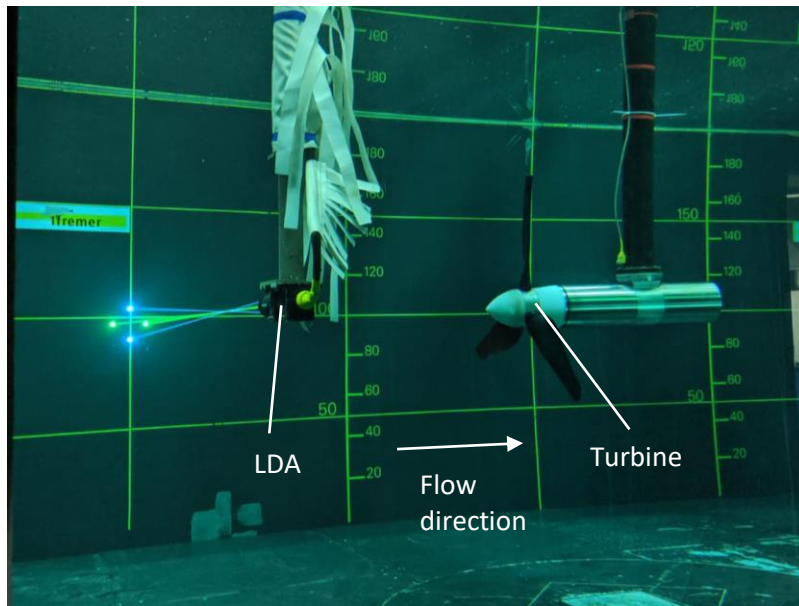


Figure 4.7. IFREMER experimental setup.

4.3.2 Flow measurement instrumentation calibration

A methodology for the calibration of the instrumentation used to measure the water level and velocity is detailed in the following section.

4.3.2.1 LDA

A 2D LDA manufactured by DANTEC was used to measure the instantaneous flow velocities in the streamwise and vertical directions. Calibration of the 2D LDA was carried out by the manufacturer and provides only the calibration uncertainties, as detailed in Section 4.3.3.

4.3.2.2 Wave probe

The wave probe was manufactured by Churchill Controls and consisted of 2 x 3mm diameter stainless steel rods, 500mm in length. There was an ‘in-situ’ calibration setting allowing the probe to be moved vertically in steps of 10mm through the water. Table 4.11 presents the calibration data used for the wave probe. It is important to note that the

calibration takes place while the water in the flume is stationary and so deflection of the wave probe when the flume is active is not accounted for.

TABLE 4.11. SUMMARY OF CALIBRATION RESULTS FOR THE WAVE PROBE.

Characteristic	Quantity	Value
Wave Probe	Gradient (mm)	1.0215
	Non linearity	$\pm 0.335\%$

4.3.3 Flow measurement uncertainty analysis

Instantaneous LDA velocity measurements are used to calculate the time averaged velocities used in the performance characteristic expressions, while the wave probe is used to give information on the surface elevation when conducting experiments using surface waves. The uniform current-only flow case has been used as a baseline of the uncertainties present for the flow measurement parameters. A summary of the uncertainties for the flow velocity and surface elevation measurements are given in Table 4.12.

TABLE 4.12. SUMMARY OF THE UNCERTAINTIES FOR THE FLOW VELOCITY AND SURFACE ELEVATION MEASUREMENTS.

Characteristic	Mean value	Bias uncert. (μ_b)	Precision uncert. (μ_p)	Total uncert. (μ_{tot})	μ_{tot} as a percentage of mean value (%)
Flow velocity (m/s)	1.01	0.001	0.02	0.02	1.98
Surface elevation, η (m)	-	0.54	4.89	4.92	-

The sources for the bias uncertainties are detailed below:

- **flow velocity:** manufacturer calibration
- **surface elevation:** 'in situ' calibration carried out in the specified flow conditions

The precision uncertainty of the wave probe is highly dependent on the flow conditions that it is exposed to. The value given here is in uniform flow conditions, however, it is extremely difficult to measure the deflection of the wave probe which will only increase in more complex flow conditions. When subjected to surface waves, this deflection could vary cyclically.

4.4 EXPERIMENTAL TEST MATRICES

All the experimental data used in this thesis is shown in Table 4.13 and Table 4.14. Two sets of wave-current data from the testing carried out by the University of Liverpool were used in this thesis, as detailed by Table 4.13, while a mixture of current-only and wave-current testing was conducted at the IFREMER wave-current flume, as shown in Table 4.14.

TABLE 4.13. EXPERIMENTAL TEST MATRIX FOR TESTING CONDUCTED AT THE UNIVERSITY OF LIVERPOOL RECIRCULATING WATER CHANNEL.

Case Name	Water Depth, h (m)	Current Description		Wave Description					
		Type of flow	Target \bar{W} (m/s)	Depth Condition	H (m)	Tr (s)	L (m)	Steepness H/L	Relative Depth h/L
LVP_UC1_W1_Int	0.76	Uniform	0.93	Intermediate	0.058	1.218	2.250	0.026	0.338
LVP_UC1_W2_Int	0.76	Uniform	0.93	Intermediate	0.082	1.147	2.020	0.041	0.377

TABLE 4.14. EXPERIMENTAL TEST MATRIX FOR TESTING CONDUCTED AT THE IFREMER WAVE-CURRENT FLUME.

Case Name	Water Depth, h (m)	Current Description		Wave Description						Turbine Settings		
		Type of flow	Target \bar{W} (m/s)	Wave maker position	Depth Condition	H (m)	Tr (s)	L (m)	Steepness H/L	Relative Depth h/L	Angular Velocity, ω (rad/s)	Approximate TSR, λ
IFR_UC3_Turb	2.0	Uniform	1.00	NOWM	-	-	-	-	-	-	See Table 4.9	0-7
IFR_PC1_Turb	2.0	Profile 1	1.00	WM00	-	-	-	-	-	-	See Table 4.9	2-5, 7
IFR_PC2_Turb	2.0	Profile 2	1.00	WM20	-	-	-	-	-	-	See Table 4.9	2-5, 7
IFR_PC1_W4_Turb	2.0	Profile 1	1.00	WM00	Intermediate	0.082	2.566	9.07	0.009	0.221	See Table 4.9	2-5, 7
IFR_PC2_W5_Turb	2.0	Profile 2	1.00	WM20	Intermediate	0.12	1.917	5.61	0.021	0.357	See Table 4.9	2-5, 7

4.5 SUMMARY

This chapter has provided a summary of the experimental methodology used in the testing carried out at two different facilities. Flow data was used from the University of Liverpool's recirculating water channel while the testing conducted at the IFREMER wave-current flume analysed the performance of a 0.9m diameter HATT, developed by CMERG, in different flow conditions. The calibration techniques used for each piece of instrumentation has been detailed, as well as information of the uncertainties present while using this equipment. This experimental testing assisted the development and validation of CFD models discussed next in Chapter 5.

5 NUMERICAL MODELLING METHODOLOGY

The use of numerical modelling to investigate TST performance in different flow conditions has become much more accessible due to the advances in computational power and available software. The need to find an alternative method to investigate these types of problems has been driven by the costs and complexities associated with the design, manufacture and testing of model scale devices, as mentioned by [57] and [69]. Numerical models provide a cheaper analysis of model scale devices than physical testing while also being more versatile as it is relatively easy to make changes to the flow conditions or tank dimensions. This chapter describes the different types of numerical models that have been used in this thesis to enable the analysis of multiple flow conditions, and to investigate the effect these conditions have on the turbine performance and loadings.

Initially, the use of a 'free slip' model for the main domain is detailed and presents the simplest model type used in this thesis. A 'free surface' model is then described which is capable of modelling more complex flow conditions such as surface waves due to the ability of the free surface interface to deflect. Finally, the turbine subdomain parameters are provided which give details on the inclusion of the TST within the main fluid domain. Each type of model is split up into three main sections: geometry, mesh development and pre-processing setup. All models use similar settings for the solver and post-processing methods and therefore are included together at the end of the chapter. This chapter provides a general overview of the CFD model design with the specific details described later in each individual results chapter.

5.1 SOFTWARE

All the numerical modelling was carried out using the commercial CFD software ANSYS CFX 18.0 which uses the FVM to discretise and solve the governing equations iteratively for small sub-divisions of the region of interest. This procedure gives an approximation of each variable at points throughout the domain and so a picture of the full flow characteristics can be obtained [106]. Further information on the CFD software can be found in Section 3.2.

The model geometry and mesh were created using ANSYS ICEM 18.0 while ANSYS CFX 18.0 was then used for the simulation setup, solver and post processing. As specified previously, the turbine sub domain settings are detailed separately to the main domain

model settings due to significant differences between the two processes. For those models that include both domains, the two processes were combined into one model.

5.2 MAIN DOMAIN MODELLING

The main domain represents the overall domain which contains the main fluid flow, while the subdomain, if present, encloses the rotating turbine, as shown in Figure 5.1. This section provides the details for the geometry and meshing for the main domain only.

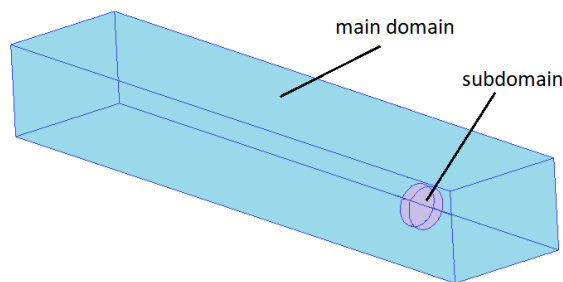


Figure 5.1. Description of the different model domains.

5.2.1 Geometry

Each numerical model was developed to compare directly against experimental data taken from a variety of testing facilities. These facilities were all different sizes and so a general set of guidelines were created to allow a standardised way of creating the model geometry for different flow conditions and different test facilities. Experimental data was taken from the University of Liverpool's recirculating water channel as well as at the IFREMER wave-current flume. Therefore, models of the turbine and fluid flow of these facilities were developed to replicate these experimental conditions. However, a CFD model generates the current flow and surface waves numerically, unlike the experimental facilities which use a wave maker or flow impeller. Therefore, in general the geometry of the CFD model domain is adapted to be different to that of the experimental facility dimensions. This is necessary to reproduce the flow conditions in the working section of the experimental facility at a known location in the CFD model.

There were two main types of model used in the main domain, a 'free slip' model and a 'free surface' model. The 'free slip' model is a single-phase, incompressible flow model with the 'top' boundary at the SWL using the 'free slip' boundary condition. The 'free surface' model is a homogenous, multiphase model with a distinct free surface interface between the water and air phases. Another simpler model was also used, referred to as the 'thin'

domain model as detailed in Section 5.2.1.3, which had a reduced width and therefore domain size, leading to a simplified model geometry without a turbine, and was used to replicate experimental current-only conditions.

Details for each of these types of model are presented in the following section. ANSYS ICEM 18.0 was the software used to create the geometry.

5.2.1.1 'Free slip' model

The 'free slip' model geometry presents the simplest geometry and is used to model current-only flow, with or without a turbine. The model is single phase and therefore water is the only fluid present in the model. The height and width of the domain was the same as the water depth and width of the channel at the experimental facility. The length of the domain is dependent on what is being examined in the model, in this case turbine performance characteristics, and therefore the length of the domain downstream of the turbine was chosen to be suitably long so not to interfere with the turbine characteristics. A domain length of 20m was used after reviewing other similar studies [71], [89], [101]. If the wake propagation from the turbine was being investigated then a study of different length domains would need to be considered, however, this is not of interest in this thesis. Figure 5.2A shows a summary of the general geometry conditions for the 'free slip' model.

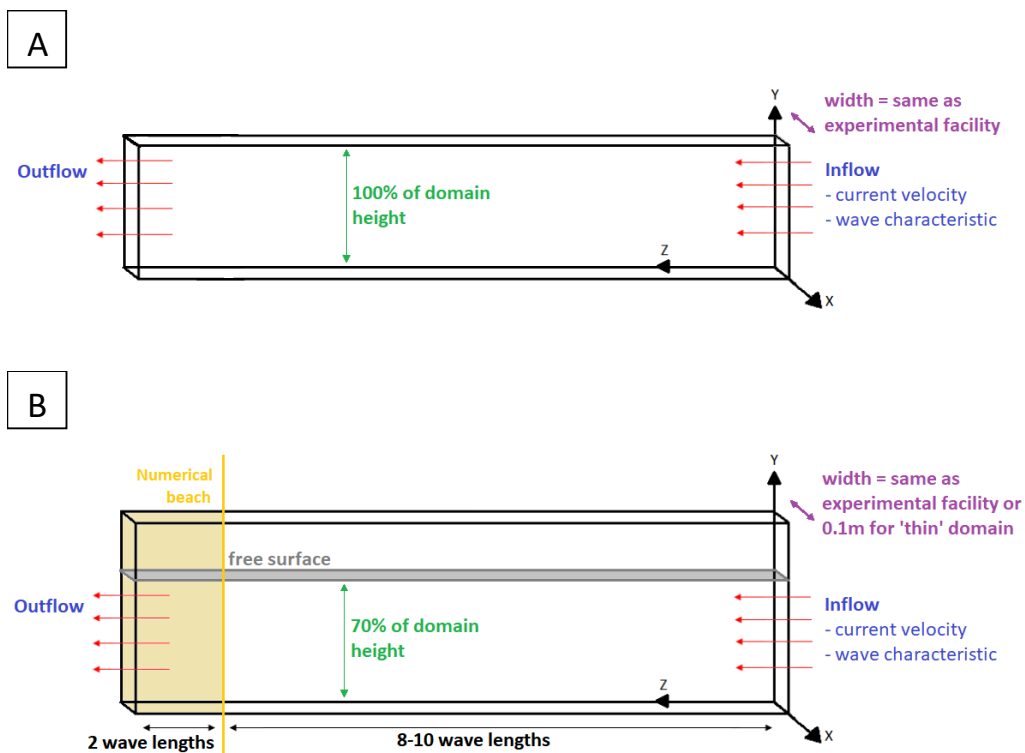


Figure 5.2. General geometry setup guide for: A) 'free slip' model and; B) 'free surface' model.

5.2.1.2 'Free surface' model

The 'free surface' model is a 2-phase multiphase model where both water and air phases are present in the model, allowing the air-water interface to deflect depending on the specified inlet conditions. The geometry of the main domain is dependent upon the type of flow conditions input to the model, eg. current-only or wave-current conditions. Figure 5.2B shows the general geometry for a 'free surface' model, identifying changes to certain parameters for different inflow characteristics as detailed in the following sections.

5.2.1.2.1 Current-only flow conditions

For current-only conditions, the geometry of the main domain is as specified in Section 5.2.1.1 with the only difference being to the overall height of the model due to the inclusion of an air region above the water surface. The overall domain height (D) increases, as recommended by [126], so that the SWL is at 70% of the overall domain height ($h_{water} = 0.7D$) leaving the remaining 30% for the air region above the water surface ($h_{air} = 0.3D$). The overall domain height and the region of air above the water surface can be calculated once the desired water depth is set. This is a general condition specifically set to work for all water depths.

5.2.1.2.2 Wave-current flow conditions

To allow the incorporation of wave action into a current-driven flow model, a free surface interface is necessary to allow deflection of the water surface in order to model the propagation of waves through the domain. These conditions also require changes to the dimensions of the fluid domain, such as the domain length, due to computational requirements. The model dimensions are given as general terms in order to optimise the model geometry so that it can be adapted for facilities with different water depths as well as being dependent upon the wave characteristic and current conditions chosen.

The overall height of the model and the air-water ratio are as described in Section 5.2.1.2.1. The length of the domain is dependent on the wavelength of the chosen wave characteristic as it was found that allowing the propagation of 8-10 waves before reaching the end of the model was optimum. This enabled a numerical beach of twice the wavelength ($2L$) to be incorporated, which was necessary to prevent any reflection of the waves from the end of the domain, as recommended by [162].

The width of the domain was kept the same as the experimental facilities modelled, unless using the 'thin' domain model (see Section 5.2.1.3), to ensure the blockage ratio of the turbine was the same between experimental and numerical testing. These general

dimensions are for a 'free surface' model, with specific details provided later in each results chapter.

5.2.1.3 *'Thin' domain model*

For wave-current simulations without a turbine, the 'free surface' numerical model was simplified to have a reduced width of 0.1m reducing the overall model size and therefore the computational time taken to run the simulations. This type of model was used to analyse the flow conditions at different points in the flow before incorporating the turbine and increasing the complexity of the model.

5.2.1.4 *University of Liverpool's recirculating water channel*

Chapters 6 and 8 use CFD models based on the working section of the University of Liverpool's recirculating water channel which is 1.4m wide, 0.76m deep and 3.7m long [84]. More details on this testing facility can be found in Chapter 4.

5.2.1.5 *IFREMER wave-current flume*

Chapters 6, 7 and 9 use CFD models based on the wave-current flume at IFREMER which is 4m wide, 2m deep and 18m long [69]. Further details about the IFREMER wave-current flume facility can be found in Chapter 4.

5.2.2 Mesh development

A mesh is required to divide the flow field of the numerical model into smaller sub-divisions of the region of interest. These smaller sub-divisions can then be used to analyse the fluid flow by discretising and solving the governing equations iteratively over each of the smaller sections using the FVM. This method provides an approximation of each variable at points throughout the domain so a picture of the full flow characteristics can be obtained [106]. This section details the specifics of the mesh for the 'free surface' model. However, the exact same mesh was used for the 'free slip' model up to the surface of the water, as the 'free slip' model does not include the air region. Similarly with the 'thin' domain model, the same mesh was used as the 'free surface' mesh but only for 0.1m wide instead of the full width.

ANSYS ICEM 18.0 was used to develop the mesh using a variety of tools and methods. A HEXA mesh was developed for the main fluid domain using a 'top down' blocking strategy to create a structured mesh [106]. A HEXA mesh encompasses a surface and volume mesh comprising of hexahedral shapes and volumes. This type of meshing is highly space-efficient and has many advantages in comparison to an unstructured TETRA mesh. In particular,

fewer computational points are needed, a higher spatial resolution is observed, and the mesh has a better aspect ratio, all of which contribute towards increasing the accuracy of the simulation [163]. HEXA meshing also allows refinement of the mesh in one direction without causing distortion in the other directions, which is an important factor when looking to reduce computational run time without reducing the accuracy of the simulation. Figure 5.3 shows the differences between HEXA and TETRA meshing.

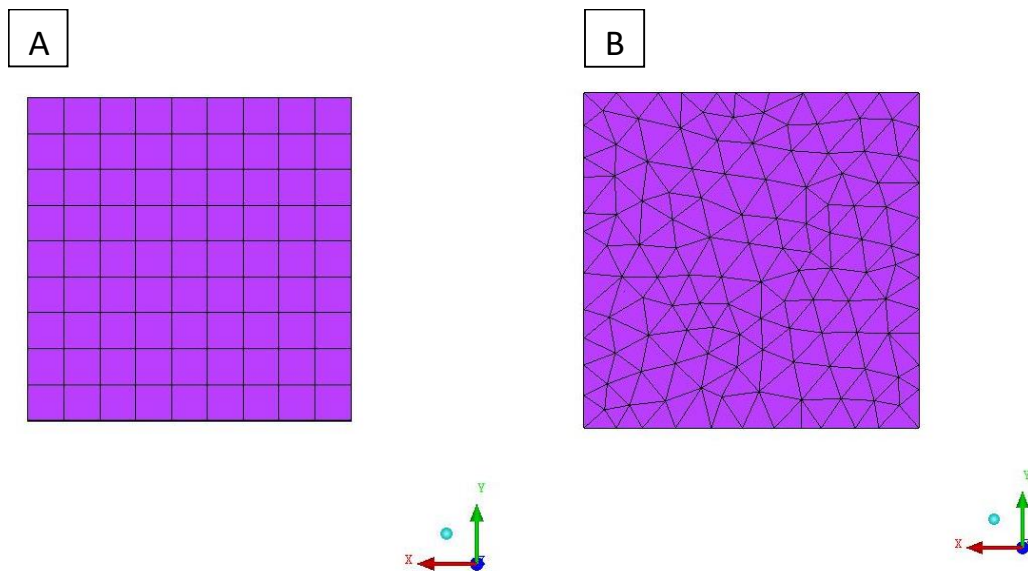


Figure 5.3. General mesh layout for: A) HEXA meshing and; B) TETRA meshing.

For free surface modelling, it is particularly important to have a region of increased mesh resolution around the air-water interface to accurately capture the interface motion and enhance the results. For wave modelling, this region must capture the entire wave height to maintain the desired surface resolution at all points along the wavelength. The types of mesh used in the following sections are specified in terms of the number of cells over the wave height and the number of cells per wavelength in order to develop a standardised setting for the grid spacing dependent on the wave characteristic. Figure 5.4 provides more detail on these mesh definitions.

A mesh independence study was carried out, using the ‘thin’ wave domain, to compare different meshing techniques based on the recommendations by [126], [128], [162], [163]. Finnegan and Goggins [126] reported restrictions in the mesh size and model geometry as the numerical analysis was performed using an ANSYS academic license. The work presented in this thesis used ANSYS research licenses and therefore was not limited. Results from this study and a final mesh summary can be found in Chapter 6.

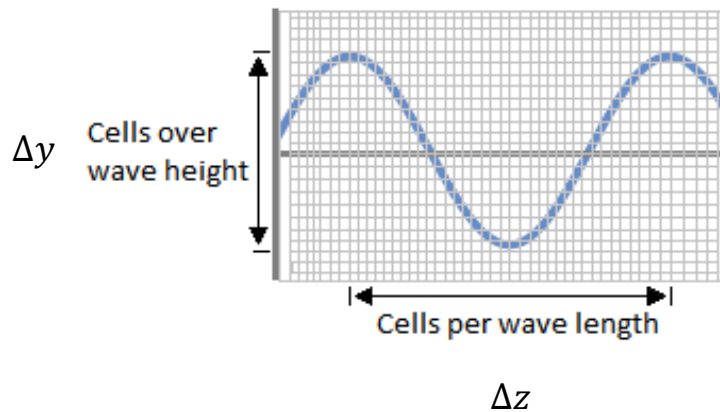


Figure 5.4. Mesh description definitions.

5.3 TURBINE MODELLING

Once the overall main fluid domain was established, the supporting structure and the subdomain enclosing the rotating turbine could be incorporated into the numerical model. This section provides a description of the geometry and meshing methods used for modelling the TST.

5.3.1 Geometry

The turbine geometry was developed using Solidworks 2016, as shown in Figure 5.5. It was then imported into ANSYS ICEM 18.0 where the overall geometry was assembled. The 3-bladed model scale turbine had a diameter of 0.9m. More detail on the turbine design can be found in Chapter 4.

To enable rotation of the turbine in the numerical model, a cylindrical subdomain was created to enclose the turbine blades and hub, as shown in Figure 5.5C. This cylinder was 1.3m in diameter and 0.4m wide, as recommended by [101], as it was found that a smaller diameter would influence the turbine results yet a bigger diameter had no effect. This created two separate domains, a rotating subdomain within the stationary main fluid domain, as shown in Figure 5.6. The rotating Multiple Frames of Reference (MFR) technique could then be used to allow a domain to rotate around a given axis at a specified angular velocity, simulating the turbine rotation. This method uses a sliding mesh interface between the stationary and rotating domains. More information about the MFR technique can be found in Section 5.4.4.1.

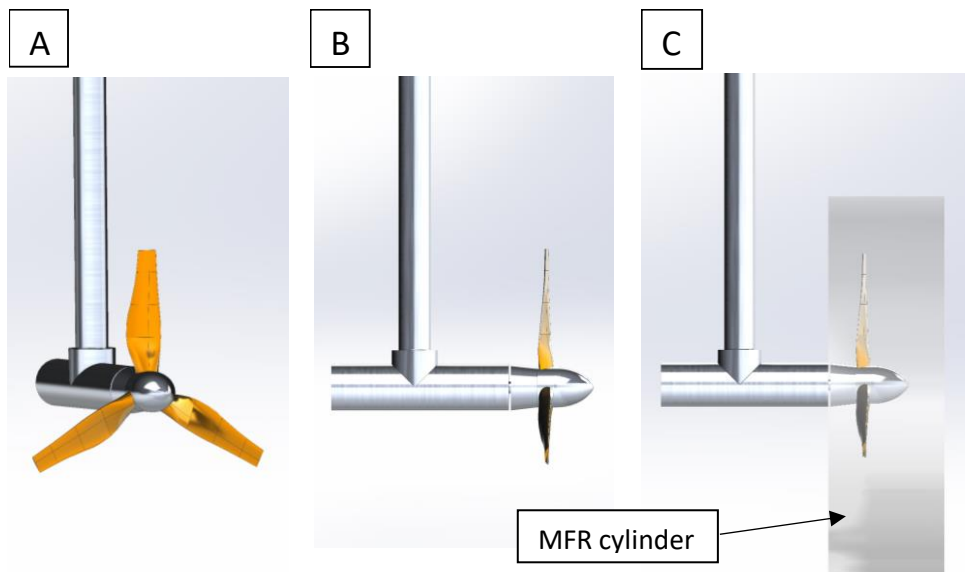


Figure 5.5. 3-bladed HATT geometry from: A) the front, B) the side and; C) the side showing the MFR cylinder around the turbine.

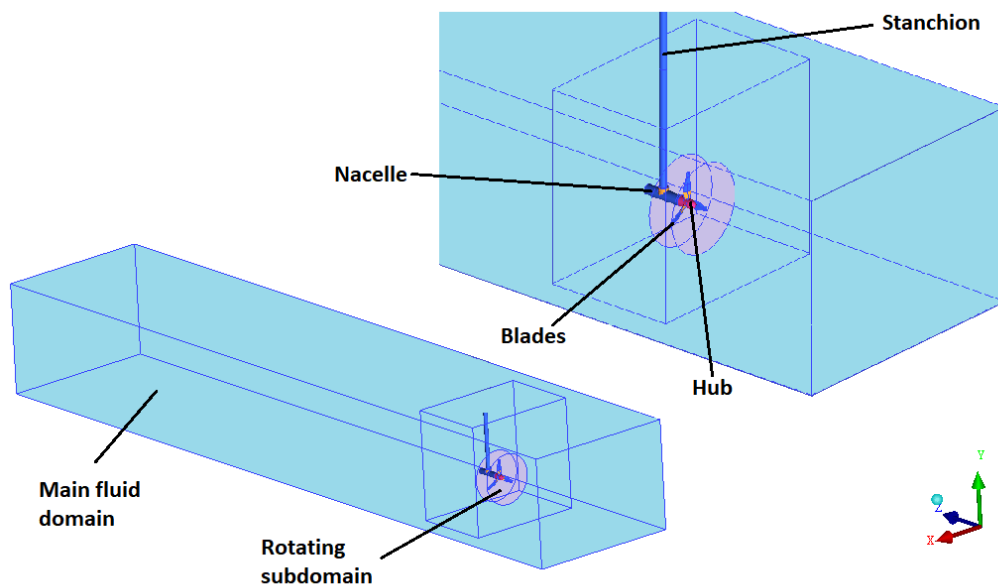


Figure 5.6. Primary features in turbine numerical model.

5.3.2 Mesh development

The mesh around the turbine and supporting structure was much more challenging to create due to the complex nature of the geometry. Therefore, the geometry was split up into sections to ease the process of mesh generation. Section 1 contained the MFR cylinder surrounding the turbine, section 2 encompassed the turbine support structure as well as

the MFR cylinder, and section 3 included the rest of the main fluid domain, as shown in Figure 5.7. The meshing of section 3 is explained previously in Section 5.2.2.

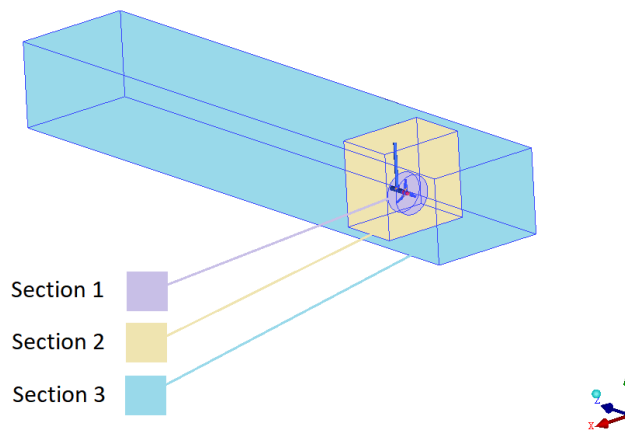


Figure 5.7. Different mesh sections over model.

The mesh for sections 1 and 2 were generated using a mixture of HEXA and TETRA meshing. As detailed in Section 5.2.2, HEXA meshing was developed using a ‘top down’ blocking strategy to create a structured mesh, while a TETRA mesh was achieved using a ‘bottom up’ meshing method by creating a surface mesh which was then refined to produce a finer volume mesh. Section 2 used HEXA meshing in a similar approach to the mesh developed for section 3. However, meshing around the supporting structure and MFR cylinder required the use of ‘ogrid’ blocking, as shown in Figure 5.8. ‘Ogrid’ blocking can be used when needing a circular shaped mesh to conform with HEXA meshing. An ‘ogrid’ was used around the MFR cylinder to reduce skew where an individual block corner lies on a curve. It also helped maintain a quality mesh and integrate the mesh between the MFR cylinder and the rest of the flume.

The mesh for section 1 was developed using a TETRA mesh instead of the HEXA mesh due to the complexity of the geometry. This TETRA mesh used the ‘Robust (Octree)’ approach which is a top-down meshing method which creates a TETRA mesh consisting of tetrahedra and prisms. Following this, the ‘Quick (Delaunay)’ technique was used, which is a bottom-up meshing method that builds upon the previous surface mesh to generate a finer volume mesh. Further information on these meshing methods is provided in [164]. To locally control certain areas of the mesh, ‘part mesh setup’ was used to limit the maximum mesh size allowed on specific parts. Prism layers were also added to the surface of the turbine blades and hub to increase the boundary layer resolution perpendicular to the wall of the

turbine surface. Problems using tetrahedral cells in the boundary layer are well known, as explained by [165].

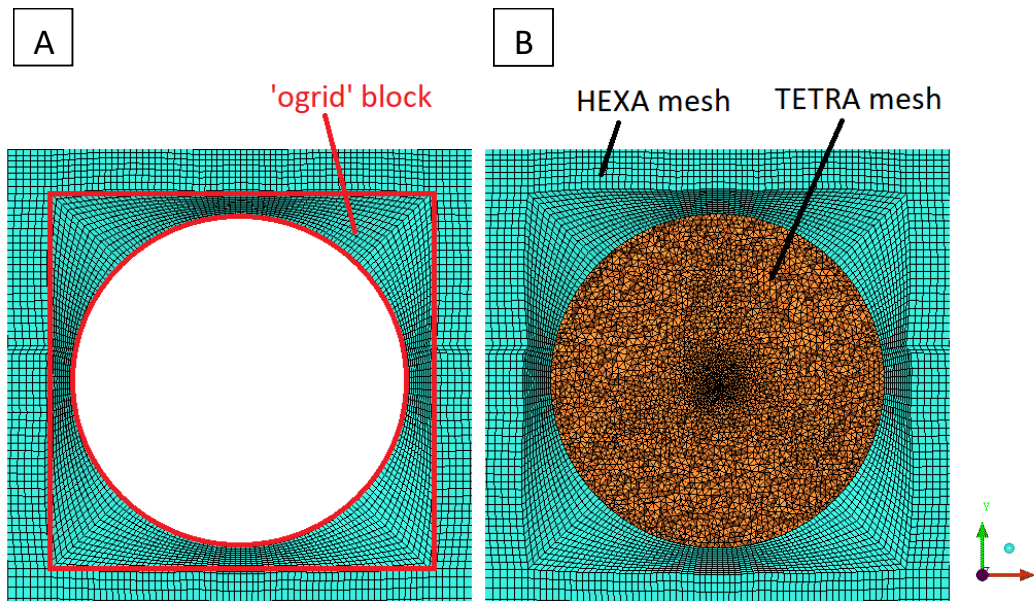


Figure 5.8. Meshes showing the integration of: A) 'ogrid' mesh around MFR cylinder; B) with TETRA mesh inside MFR cylinder.

A mesh independence study for the mesh inside the MFR cylinder, section 1, was carried out to ensure that mesh refinement was carried out to an acceptable level, while taking into consideration computational time and model accuracy. The mesh in sections 2 and 3 remained constant because the focus of the study was to investigate the mesh sizing on the turbine blades and hub, as well as the effect of prism layers over the turbine surface. Various numbers of layers and first thickness were investigated along with the mesh distribution along the blade root, middle and tip. Results from this mesh study can be found in Chapter 6 along with the final turbine mesh used in all numerical models.

5.3.2.1 Supporting structure mesh

The final mesh for section 2, encompassing the turbine support structure and MFR cylinder, was created using multiple 'ogrids'. The main structural layout for this mesh was taken from the requirements of the free surface wave domain mesh, to be discussed in Chapter 6. This mesh was not necessary for simple uniform current flow modelling as it was finer than it needed to be, and a much simpler mesh would have been adequate. However, in order to develop a single mesh that was suitable for simple as well as more complex flow modelling, the free surface wave-current mesh was used around the turbine and supporting structure. The final mesh for section 2 is shown in Figure 5.9.

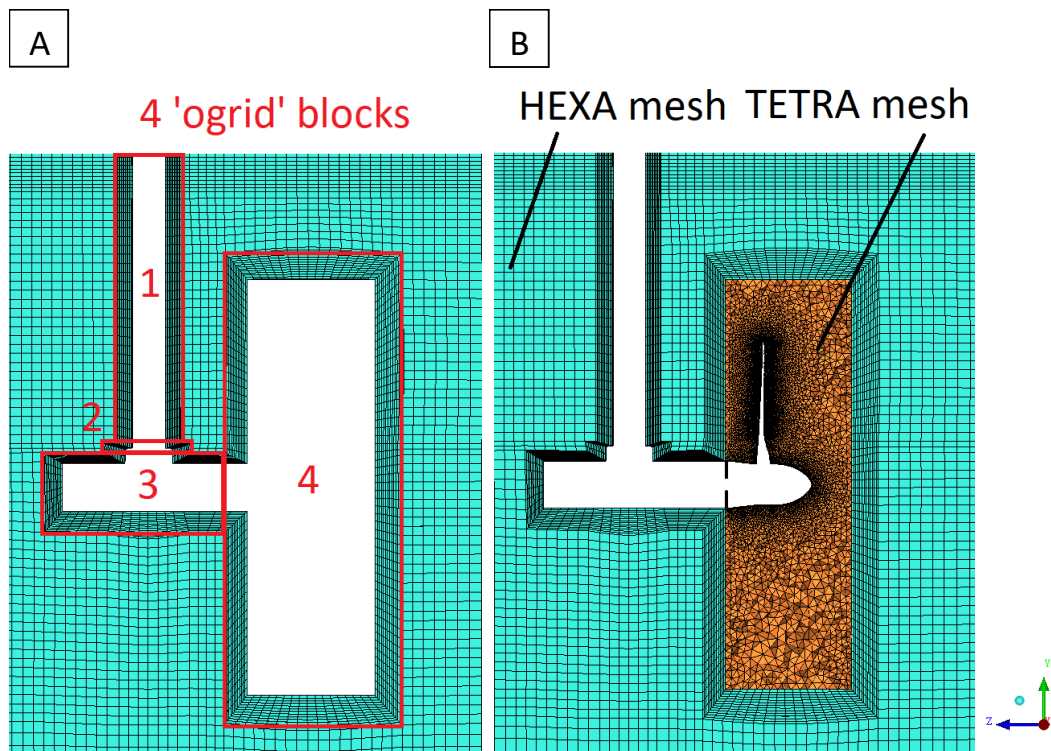


Figure 5.9. Final mesh for section 2 encompassing the turbine support structure and MFR cylinder showing the integration of: A) 'ogrid' mesh around MFR cylinder; B) with TETRA mesh inside MFR cylinder.

5.4 PRE-PROCESSING SETUP

To enable the numerical simulation to be solved, the physics of the problem needed to be defined using ANSYS CFX-Pre 18.0. This section explains how each type of model was created with details on the analysis type, domain properties and boundary conditions used.

5.4.1 Analysis type

In all simulations, the analysis was set up as a transient analysis to capture the time dependent nature of the flow and the dynamic loading on the turbine, when present. This type of analysis required real time information and therefore it was necessary to state the time intervals at which the CFX-Solver calculated the flow field. The ANSYS CFX-Solver uses an implicit solution method and so a physical time step (Δt) was used to control the simulation. The optimum time step for any free surface model simulating waves was Δt_{wave} , while models incorporating a turbine used a time step of Δt_{turb} which was defined by the angle (θ) through which the turbine turned per time step. For combined wave-current and turbine models, the smaller of the two time steps was used in order to

guarantee satisfying both criteria. Further details on this time step analysis can be found in Chapter 6.

Due to the increased data capture and therefore the increased resolution of the transient simulations, the CFD models take longer to run and require greater computational power while using more memory in the output of the results files. Therefore, the use of High Performance Computing (HPC) helped to increase the number of simulations that could be run, as well as reducing each job's individual run time. Further information on HPC is detailed in Section 5.5.1.2, later in this chapter.

5.4.2 Domain properties and fluid models

Both the stationary main fluid domain and the rotational turbine subdomain were set up with some common basic settings relating to the fluid models and properties. These settings differed between the 'free slip' and 'free surface' models as the 'free slip' model was single phase while the 'free surface' model was multiphase. Differences between the two types of main fluid domain are discussed in the following sections with details for the turbine subdomain given afterwards. The 'thin' domain model uses the same settings as the 'free surface' model.

5.4.2.1 'Free slip' model - main domain

The 'free slip' model was treated as single phase, incompressible flow using water as the single fluid. The buoyancy model was switched off as average loadings were not affected by buoyancy. The turbulence model used was the SST model, as described in Chapter 3. Table 5.1 provides an overview of the fluid models and properties used in the 'free slip' model.

TABLE 5.1. FLUID MODELS AND PROPERTIES FOR THE MAIN DOMAIN OF THE 'FREE SLIP' MODEL.

Basic setting	Definition	Property	Value	Units
Fluid definition	Water	Density	997	kg/m ³
		Molar mass	18.02	kg/kmol
		Reference temperature	25	°C
		Reference pressure	0	Pa
Domain models	Buoyancy	Option	Non-Buoyant	-
	Domain motion	Stationary	-	-
Fluid models	Turbulence	Shear Stress Transport	-	-

5.4.2.2 'Free surface' model - main domain

The 'free surface' model was a multiphase model using air and water, with a distinct interface between the two phases. More details on multiphase modelling can be found in Chapter 3. The buoyancy model was activated, acting in the vertical direction opposing

gravity. The buoyancy reference density is chosen to be that of the density of air, as described in Section 3.2.5.3. The SST turbulence model was used in all ‘free surface’ modelling, with further details given in Section 3.2.4.3. Specifically for models simulating wave motion, the influence of three different turbulence models (laminar, k-epsilon ($k_t - \epsilon$), SST) on the generation and propagation of regular waves was investigated by [123], [126], [135], [166]. These studies deduced that there was no significant difference between each case and hence the SST turbulence model was used. The SST turbulence model is required for more accurate boundary layer simulations necessary in general turbine modelling, as recommended by [167]. Therefore, even in CFD models simulating current-only or wave-current conditions, the SST turbulence model was still used with the foresight to incorporate a TST into these flow-only CFD models as the development of the simulations progressed. Table 5.2 provides an overview of the fluid models and properties used in the ‘free surface’ model.

TABLE 5.2. FLUID MODELS AND PROPERTIES FOR THE MAIN DOMAIN OF THE ‘FREE SURFACE’ MODEL.

Basic setting	Definition	Property	Value	Units
Fluid definition	Water	Density	997	kg/m ³
		Molar mass	18.02	kg/kmol
		Reference temperature	25	°C
		Reference pressure	1	atm
	Air	Density	1.185	kg/m ³
		Molar mass	28.96	kg/kmol
		Reference temperature	25	°C
Domain models	Buoyancy	Option	Buoyant	-
		Direction {x,y,z}	{0, -g, 0}	m/s ²
		Reference density	1.185	kg/m ³
	Domain motion	Stationary	-	-
	Fluid models	Multiphase	Homogenous model	On
Free surface model			Standard	-
Turbulence		Shear Stress Transport	-	-
Fluid pair models	Interphase transfer	Option	Free surface	-

5.4.2.3 Turbine subdomain

The turbine subdomain possessed the same properties for the fluid definitions, domain models and fluid models as specified in the ‘free slip’ and ‘free surface’ main domain settings, according to which model it was incorporated into. The only difference with the turbine subdomain was that the domain motion was set to ‘rotating’ at a specified rotor angular velocity (ω). A new local coordinate frame labelled ‘TurbRotAxis’ was also incorporated to align the local coordinate frames z-axis with the axis of rotation of the

turbine, as shown in Figure 5.10. Table 5.3 provides an overview of the fluid models and properties used in the turbine subdomain.

Another local coordinate frame labelled ‘RotAxis_BM’ was also incorporated to allow the out of plane bending moment around the x -axis (BM_x), for a single blade, to be calculated. ‘RotAxis_BM’ is orientated in the same way as ‘TurbRotAxis’ but is raised by 0.065m in the y -direction and by 3.89m in the z -direction so that the coordinate frame origin sits at the base of the blade and rotates with the cylindrical turbine subdomain as shown in Figure 5.10. The BM_x was only calculated for a single blade as only a single blade from the experimental data was available for comparison. The method used for extracting the BM_x data from the CFD model is described in Section 5.6.1.

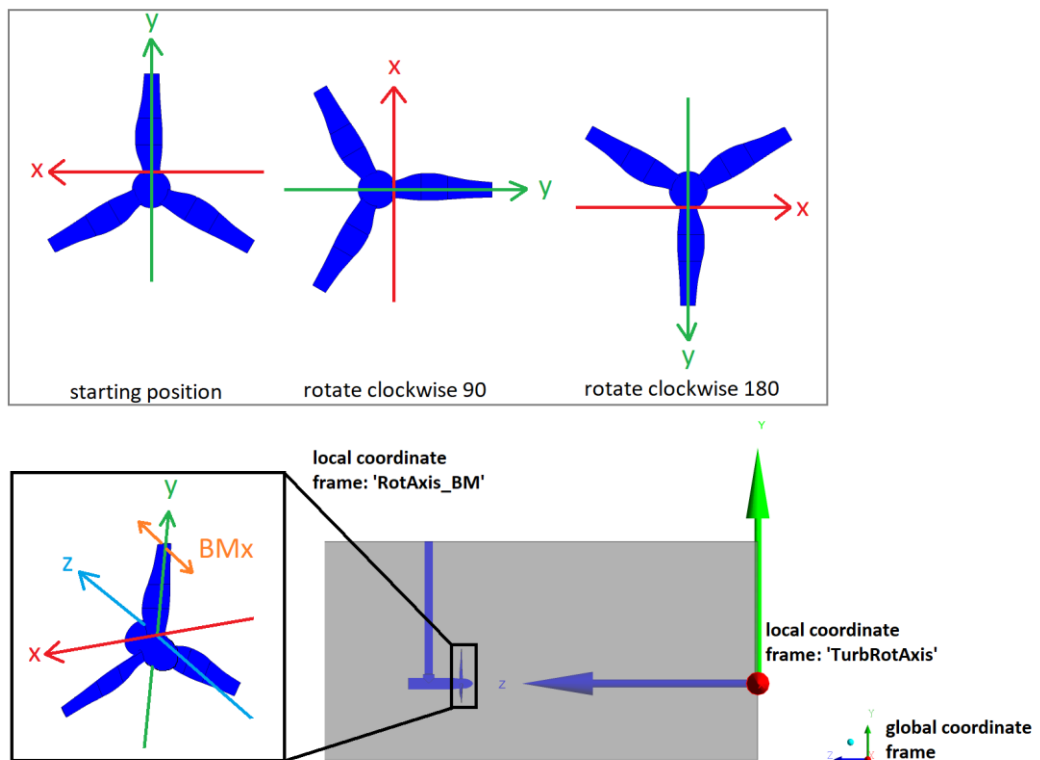


Figure 5.10. Location of the local coordinate frames ‘TurbRotAxis’ and ‘RotAxis_BM’ as well as the global coordinate frame.

TABLE 5.3. FLUID MODELS AND PROPERTIES FOR THE TURBINE SUBDOMAIN.

Basic setting	Definition	Property	Value	Units
Domain models	Domain motion	Rotating	ω	rad/s
	Axis definition	Coordinate axis	‘TurbRotAxis’	

5.4.3 Boundary conditions

The following section defines what boundary conditions were used in each type of model, with Table 5.4 providing a summary of the boundary conditions and Figure 5.11 showing the location of each boundary.

TABLE 5.4. BOUNDARY CONDITION DETAILS FOR EACH MODEL TYPE.

Boundary name	Boundary conditions			
	'Free surface' models			'Free slip' model
	Current-only	Waves and current	'Thin' domain model	Current-only
inlet	Velocity-inlet	Velocity-inlet (opening)	Velocity-inlet (opening)	Velocity-inlet
outlet	Pressure-outlet	Pressure-outlet (opening)	Pressure-outlet (opening)	Pressure-outlet
top	Pressure-opening	Pressure-opening	Pressure-opening	Free-slip wall
base	No-slip wall	No-slip wall	No-slip wall	No-slip wall
walls	No-slip wall	No-slip wall	Free-slip wall	No-slip wall
stanchion, hub, turbine blades	No-slip wall	No-slip wall	No-slip wall	No-slip wall

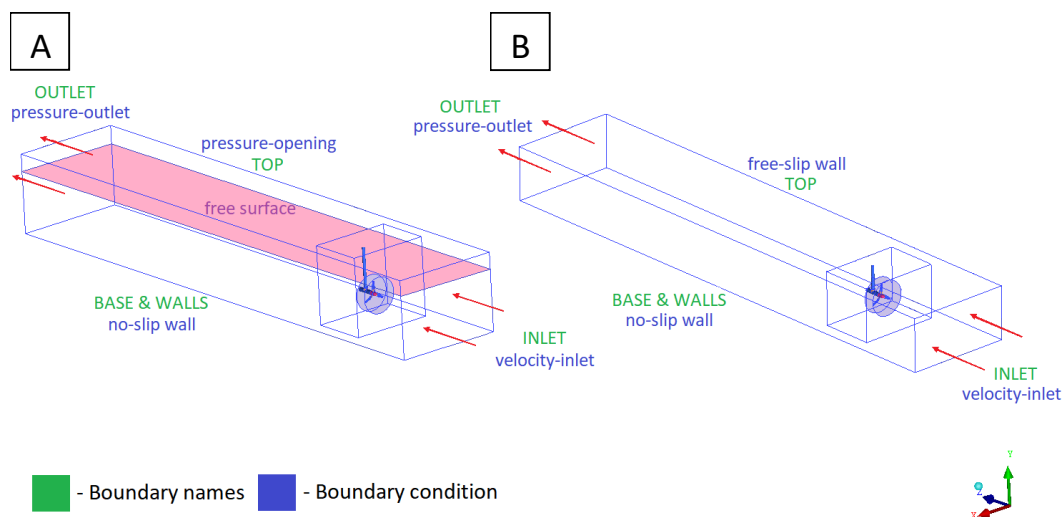


Figure 5.11. Boundary conditions imposed for: A) 'free surface' and; B) 'free slip' models.

5.4.3.1 Inlet

The fluid flow entered the model at the boundary named 'inlet', as shown in Figure 5.11. The boundary condition was set as a 'velocity-inlet' and directed flow into the main domain acting in a direction perpendicular to the front face of the domain. The inlet velocity was set using cartesian coordinates, where $\{u, v, w\}$ acts in the $\{x, y, z\}$ directions. These criteria were robust when modelling current-only conditions; however, for any models incorporating waves, the boundary conditions needed to be modified. The generation of

waves at the inlet produces horizontal and vertical velocities, which can produce back flow. Therefore, for wave models a ‘velocity-inlet’ was still achieved but by using an ‘opening’ at the boundary instead. This allows bidirectional flow at the inlet, into and out of the domain, and was necessary to prevent the model from crashing. The inlet velocity was applied to the water phase only and so in the 2-phase ‘free surface’ models, volume fractions were used, as described in Chapter 3, Section 3.2.5.1.

5.4.3.1.1 Implementation of uniform and profiled current conditions

As explained previously, the inlet conditions were added to the model mathematically using cartesian coordinates. For models using a uniform current flow, the streamwise velocity (W) was input using cartesian coordinates, where $\{u, v, w\}$ represent the velocity in the $\{x, y, z\}$ directions. For example,

$$U: \mathbf{u}(x, y, z) = 0 \text{ [ms}^{-1}\text{]}$$

$$V: \mathbf{v}(x, y, z) = 0 \text{ [ms}^{-1}\text{]}$$

$$W: \mathbf{w}(x, y, z) = 1.0 \text{ [ms}^{-1}\text{]}$$

would input a streamwise velocity of 1.0 m/s.

For models using a profiled current flow, average, steady state, experimental data was directly input to the model inlet to ensure the replication of the profiled velocities observed at the chosen test facility. The data was input by creating a boundary condition at the inlet using the ‘Profile Method’ in ANSYS CFX-Pre 18.0. This boundary condition used interpolated values from a data file containing the current flow profiles obtained during experimental testing. CEL expressions were then used to refer to the imported data using interpolation functions. For example,

$$U: \text{InletProf.Water.Velocity } \mathbf{u}(x, y, z)$$

$$V: \text{InletProf.Water.Velocity } \mathbf{v}(x, y, z)$$

$$W: \text{InletProf.Water.Velocity } \mathbf{w}(x, y, z)$$

would input the velocity profile specified in the data file called ‘InletProf’. This method ensured minimal changes were made when transferring experimental data across to be used in numerical models.

5.4.3.1.2 Generation of regular waves

Regular wave generation was achieved by defining CEL expressions for the velocity components and surface elevation of the wave. These CEL expressions are detailed in

Appendix A and define the main characteristics of the wave motion. These properties were superimposed upon a uniform or profiled current condition that was already established.

For example,

U: InletProf.Water.Velocity $\mathbf{u}(x,y,z)$

V: InletProf.Water.Velocity $\mathbf{v}(x,y,z)$ +VerticalParticleVelocity

W: InletProf.Water.Velocity $\mathbf{w}(x,y,z)$ +HorizontalParticleVelocity

would establish the average, steady state, velocity profile specified in the data file called 'InletProf, as well as superimposing the time-dependent wave characteristics on top of this current flow using the streamwise (HorizontalParticleVelocity) and vertical (VerticalParticleVelocity) velocity components. The free surface interface was controlled using an equation for the surface elevation of the wave. Volume fractions were used to stipulate the water and air regions of the model, as described in Section 3.2.5.1.

5.4.3.2 *Outlet*

The fluid flow exited the model at the boundary named 'outlet', which was identified as a 'pressure-outlet'. The 'free slip' model used a relative pressure of 0 Pa, which given that the reference pressure of this model was also 0 Pa, ensured the flow was driven by the velocity-inlet and nothing else. The 'free surface' model used 0 Pa in the air region of the model while a hydrostatic pressure was imposed over the depth of the water region of the model. Similarly to the inlet of the 'free surface' model, the outlet boundary was considered an 'opening' when modelling waves and volume fractions were used to distinguish between the two fluid phases.

5.4.3.3 *Side walls and base*

The side walls and base of the numerical model were set as 'no-slip' walls to model the frictional effects near the walls and base of the experimental flume. This boundary condition assumes the fluid immediately next to the wall has zero velocity by default. These settings were used for the 'free slip' and 'free surface' models; however, the 'thin' domain model used 'free-slip' side walls instead of 'no-slip'. 'Free-slip' conditions set the shear stress of the wall to zero and therefore the velocity of the fluid near the wall is not slowed by frictional effects [106]. The main aim of the 'thin' domain model was to reduce the complexity of the model and enable the generation of wave-current conditions in a simplified domain. There was no need to model the wall effects when using this model to trial different methods for the generation of waves.

5.4.3.4 Top

The top boundary condition was the main difference between the ‘free surface’ and ‘free slip’ models. The ‘free slip’ model used a ‘free-slip’ wall boundary condition which defined the velocity component parallel to the top boundary as a finite value while normal to the wall was zero [150]. The ‘free surface’ model used an ‘opening’ to represent the top boundary, allowing flow in and out of the boundary. This enabled the deflection of the free surface interface between the air and water phases, allowing the propagation of waves throughout the model domain.

5.4.3.5 Stanchion, hub and turbine blades

The stanchion, hub and turbine blades were set as ‘no-slip’ walls in order to model the frictional effects as described for the side walls and base of the numerical flume.

5.4.3.6 Numerical beach – wave modelling

A numerical beach was used to dampen out the surface waves and prevent any reflection from the end of the model. The numerical beach was applied using a ‘subdomain’ and by generating expressions using CEL [106] to target a region $2L$ upstream of the outlet. The numerical beach was created by using a general momentum source acting in the streamwise direction. In this application, it was used to force the velocity in the beach region to be the same as the current velocity, removing the oscillatory effects of the wave. This was achieved by using Equation (3.35).

$$S_z = -C(U_z - U_{z,spec}) \quad (5.1)$$

where S_z is the source term in the z -direction, $-C$ is the momentum source coefficient and should be set to a large number (eg. 10^5 kg/m³/s) in order to linearise the source, U_z is the measured velocity at a certain point and $U_{z,spec}$ is the target velocity [106]. The size of the mesh elements are also gradually increased in size, making it coarser, to help depress the wave motion towards the end of the domain as recommended by [162].

5.4.4 Domain interfaces

In simulations combining the main fluid domain and the turbine subdomain, an interface exists between them. Domain interfaces are used not only to connect multiple domains, but also to model changes between reference frames which occur between a stationary and rotating domain. Between the main fluid domain and the turbine subdomain was a ‘fluid-fluid’ type of interface which allows continuous fluid flow across the interface. The interface model between the domains is ‘general connection’ which is necessary when

there is a frame change at the interface. Following this selection, the frame change/mixing model must be selected and in all transient models, 'transient rotor-stator' is chosen with a pitch change of 'none'.

5.4.4.1 *Rotation of the turbine using the MFR technique*

The rotating turbine subdomain was set to rotate around the local coordinate frame 'TurbRotAxis' at a specified angular velocity. As discussed in Section 5.4.4, an interface exists between the main fluid domain and the turbine subdomain to account for interaction across the interface. A sliding interface is present which allows the rotating turbine subdomain to move relative to the stationary main fluid domain. The 'transient rotor stator' interface model was used to account for the transient interaction effects across the sliding interface, capturing the temporal features at every time step. The interface position is updated every time step as the relative position of the mesh on each side of the interface changes with time [106]. This is known as the MFR method and it provides a 'fully resolved' model which produces a more accurate solution. This method requires a greater computational capacity, increasing the time taken to complete each simulation, as well as the post processing of the data.

5.4.5 Solver control

The following settings are used to control the CFX-Solver during the solution stage. Advection schemes are the mechanisms used to transport a quantity, such as temperature or velocity, through the solution domain. The 'high resolution' advection scheme is used in all simulations as recommended by [106]. The transient scheme defines the discretization algorithm and is set to 'second order backward Euler' as again is recommended by [106].

For every time step that the solver performs, a number of coefficient iterations or loops are carried out. This ensures that the solution is converging for each time step and therefore the maximum and minimum number of coefficient loops must be set. For all transient simulations, a minimum number of 1 coefficient loop and a maximum of 15 coefficient loops were used. It is recommended for multiphase cases to use a maximum value of 10 or more coefficient loops [106]. If the residual target level is achieved first, then the maximum number of coefficient loops per time step may not be reached.

Residuals can be used to monitor the level of convergence in a simulation, and are a measure of the local imbalance of each conservative control volume equation [106]. The Root Mean Square (RMS) residual level was selected with a target of 1e-04, as

recommended by [106] to achieve a good level of convergence sufficient for most engineering applications.

Additional multiphase control is required to establish how the solver solves the equations for pressure, velocity and the volume fractions. The volume fraction coupling is set to ‘segregated’ to allow the solver to solve for pressure and velocity in a coupled manner before solving the phasic continuity equations for the volume fractions. Initial volume fraction smoothing is chosen as ‘volume-weighted’ as this improves the model start up robustness. Table 5.5 provides a summary of the chosen solver control settings.

TABLE 5.5. SOLVER CONTROL SETTINGS FOR TRANSIENT ANALYSIS SIMULATIONS.

Basic setting	Definition	Property	Value	Units	
Fluid definition	Advection scheme	Option	High resolution	-	
	Transient scheme	Option	Second order backward Euler	-	
	Fluid timescale control	Timescale control	Coefficient loops	-	
	Convergence control		Min. coefficient loops	1	-
			Max. coefficient loops	15	-
	Convergence criteria		Residual type	RMS	-
Residual target			1e-04	-	
Advanced options	Multiphase control	Option	On	-	
	Volume fraction coupling	Option	Segregated	-	
	Initial volume fraction smoothing	Option	Volume-weighted	-	

5.4.6 Output control and convergence monitoring criteria

The output control section of the pre-processing setup is used to manage the way files are written by the solver. All simulations are run as transient analyses and therefore it is possible to create transient results files. The variables contained in each transient results file can be set, as well as deciding how frequently they will be created.

Monitor points were added into the models and positioned in the main fluid domain to observe changes in the velocity over time. These points could be used to identify when the flow conditions had reached either stable conditions for current-only flow or repeating oscillatory conditions for wave and current flow. The exact position of the monitor points are detailed in each individual results section. Figure 5.12 shows the typical location of the monitor points placed in the main fluid domain, upstream of the TST device if present in the model.

For simulations where the TST is present, the torque and thrust, on each of the turbine blades and the hub, were monitored every time step to examine the change in transient loading effects for different angular velocities and upstream flow conditions. This was implemented using CEL expressions as shown in Equation (5.2):

$$\text{Torque}_z_{TurbRotAxis()}@Blade1 \quad (5.2)$$

Where '*Torque*' is the function being carried out, '*z*' specifies the rotational axis with '*TurbRotAxis*' being the name of the local coordinate frame, and '*Blade1*' referring to the surface on which the function is carried out. These functions could also be used to monitor the convergence of the simulation over time as shown in Figure 5.13. Convergence is reached when a steady or repeating pattern is sustained, exhibiting stability in the model at this specified location.

Depending on the complexity of the model, simulations were set to run for 100 seconds with stability in the simulation reached between 40-70 seconds of run time. Specific details for the convergence time of each model is detailed in the individual results sections.

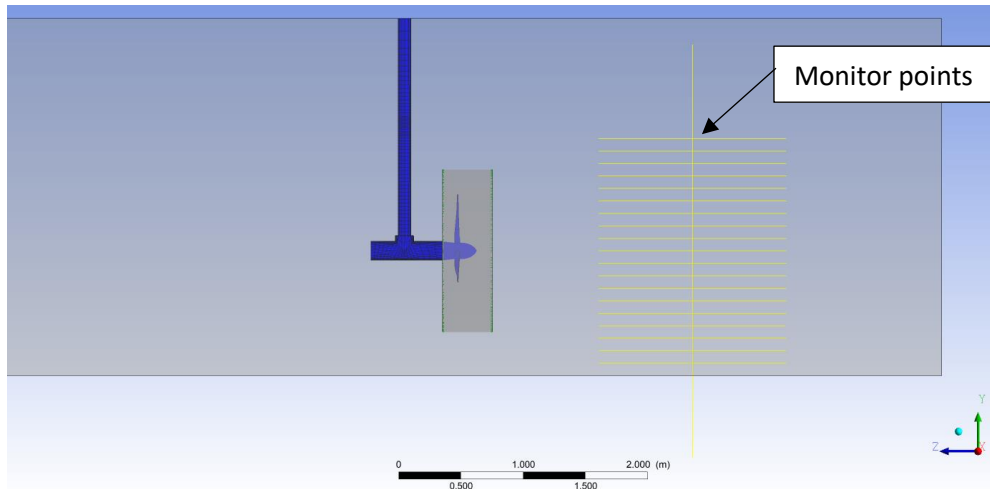


Figure 5.12. Typical location of monitor points in all numerical models.

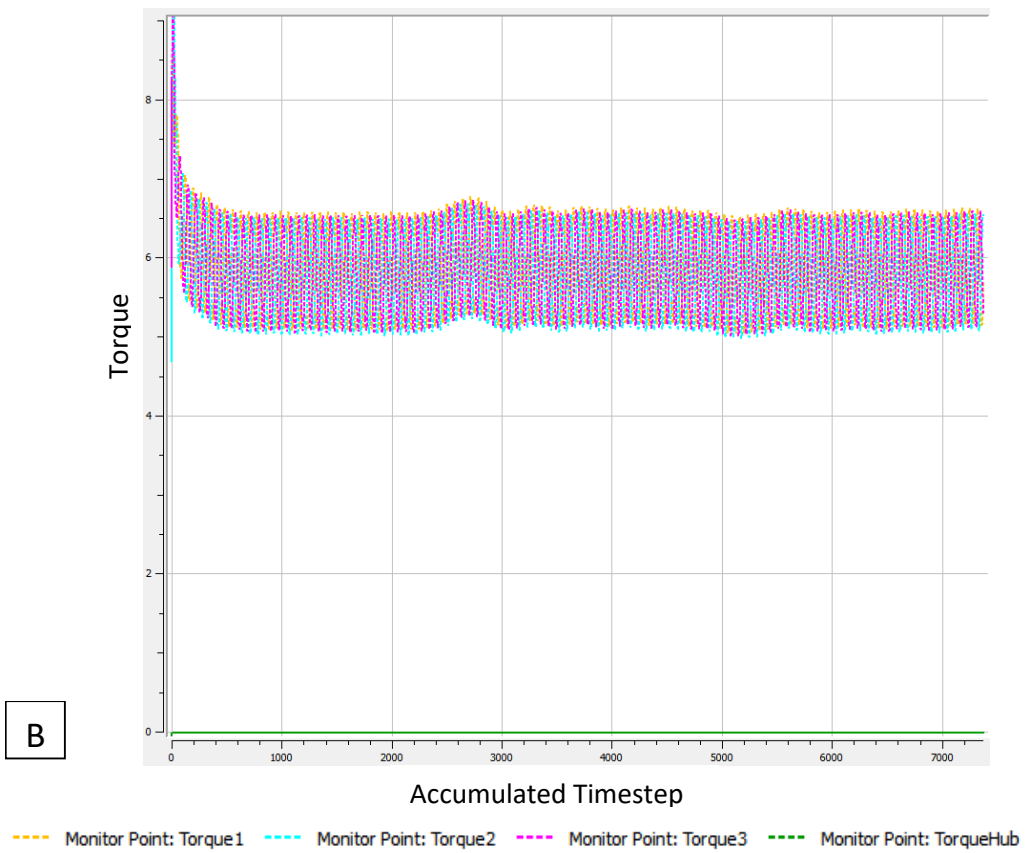
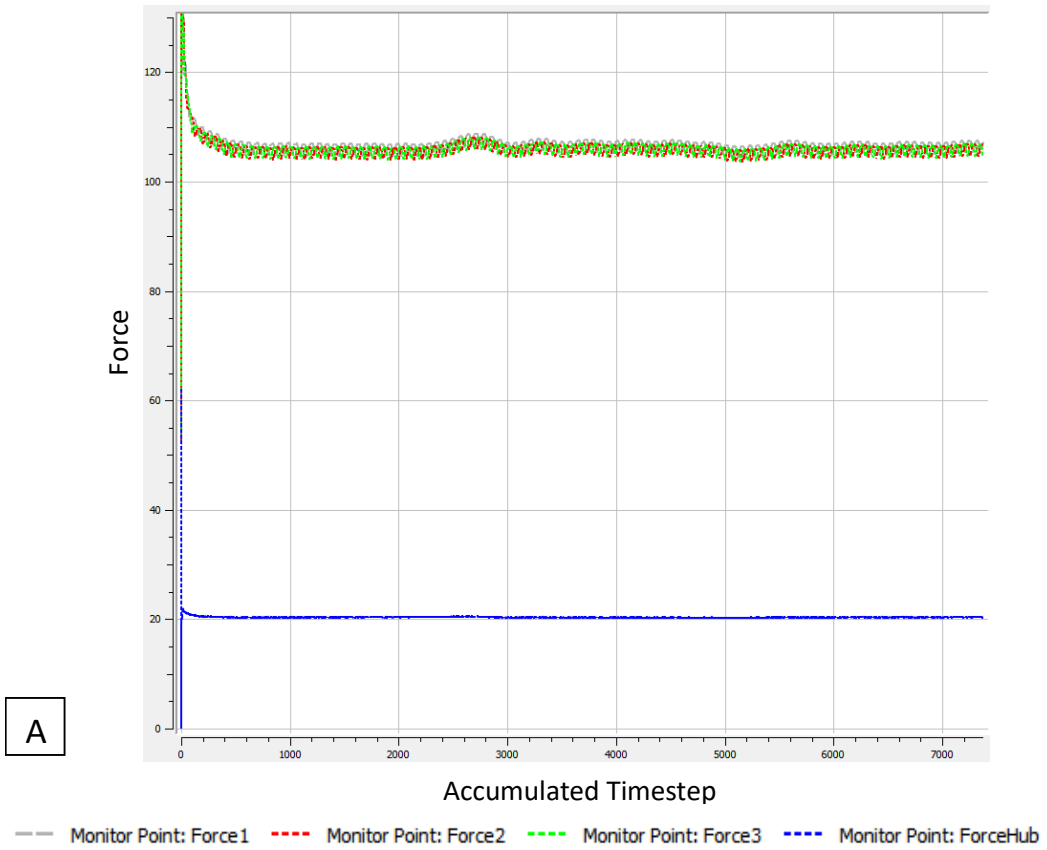


Figure 5.13. An example of monitoring the: A) force and; B) torque, on each turbine blade and the hub over time (per accumulated time step) to monitor convergence of the simulation.

5.5 SOLVER

ANSYS CFX 18.0 was used as the solver for all numerical modelling. The ‘double precision’ solver executable was activated when defining the run as this setting permits higher resolution numerical mathematical operations and can improve convergence significantly. Specifically, for the multiphase ‘free surface’ models, the ‘double precision’ setting was recommended [106]. ‘Double precision’ accuracy can be beneficial; however, it is another factor that increases the amount of computer memory necessary to run these simulations as well as increasing the overall run time of the models.

5.5.1 Parallel processing

Parallel processing was used to run all numerical simulations due to the speed increase observed in comparison to serial processing. The different facilities used are detailed in the following sections. When running ‘free surface’ simulations in parallel, it was important to restrict the partitioning direction used so that the free surface was not aligned with any partition boundaries. Failure to do so can result in the free surface interface not being robust which can cause the simulations to crash. Therefore, partitioning was restricted to the x and z directions only, and not in the y direction.

5.5.1.1 Z840 workstation

A HP Z840 workstation was used for initial running of simple simulations. The workstation had two Intel Xeon processors, using 28 cores and 256 GB of physical memory. Initially, models were run using between 12 and 24 cores, however the complexity of the models increased rapidly and the Z840 workstation did not possess the computational capability required.

5.5.1.2 High Performance Computing facilities

The research presented in this thesis used the supercomputing facilities at Cardiff University operated by Advanced Research Computing at Cardiff (ARCCA) on behalf of the Cardiff Supercomputing Facility and the HPC Wales and Supercomputing Wales (SCW) projects. Access to the HPC cluster, ‘Hawk’, which comprised of 201 nodes, each with 40 cores on each node, was facilitated through Cardiff University. ANSYS HPC research licenses were then needed in order to use the HPC facilities. For each simulation, the first 16 cores did not require an ANSYS HPC license, but for every core thereon, 1 ANSYS HPC license was needed per 1 core used. Therefore, the simulations were restricted by the number of ANSYS HPC licenses the University had and not the supercomputing facilities.

Simulations were typically run using between 80 and 200 cores per model. Further details on the exact run definition is given in the individual results sections.

5.6 POST-PROCESSING

Post processing of each simulation was carried out to extract the necessary flow and turbine properties to calculate performance related parameters. ANSYS CFD-Post software was used to obtain the necessary results and they were then extracted for further processing in Matlab.

5.6.1 Extracting force, torque and out of plane bending moment

The values for force (T), torque (Q) and out of plane bending moment (BM_x) on the turbine were obtained using CEL expressions, extracting these values from specific locations of the geometry as a function over time. As seen in Section 5.4.6, Equation (5.2) shows the use of CEL expressions to find the torque on Blade 1 for convergence monitoring. More generally, Equation (5.3) shows the generic expression used to calculate the force, torque and out of plane bending moment at different locations on the geometry.

$$Function_Axis_CoordinateFrame()@Location \quad (5.3)$$

Where '*Function*' is the function being carried out, '*Axis*' specifies the global axis around which the function is applied with '*CoordinateFrame*' being the name of the local coordinate frame used, as shown in Figure 5.10, and '*Location*' referring to the surface of the geometry on which the function is carried out. Table 5.6 shows the possible variables used for each different identifier in the expression.

TABLE 5.6. ALL POSSIBLE VARIABLES USED FOR EACH IDENTIFIER IN GENERAL CEL EXPRESSIONS.

Identifier			
<i>Function</i>	<i>Axis</i>	<i>CoordinateFrame</i>	<i>Location</i>
<i>Force</i>	<i>z</i>	<i>TurbRotAxis</i>	<i>Blade1</i>
<i>Torque</i>	<i>x</i>	<i>RotAxis_BM</i>	<i>Blade2</i>
			<i>Blade3</i>
			<i>Hub</i>

The force was calculated in the z -axis only using the coordinate frame 'TurbRotAxis', around which the turbine rotates. This was calculated for the locations of blades 1, 2 and 3 as well as the hub. The torque was also calculated around the z -axis using the coordinate frame 'TurbRotAxis' for blades 1, 2, 3 and the hub. Calculation of the torque around the x -axis using the coordinate frame 'RotAxis_BM' provides the out of plane bending moment

for a single blade. This was only calculated for blade 1 as only a single blade from the experimental data was available for comparison.

5.6.2 Calculating torque, power and thrust coefficients

Using the equations specified in Section 5.6.1, the force and torque were found for each individual component of the turbine. The total turbine torque and force were then found by summing the values acting on each blade and the hub. The power of the turbine was calculated by multiplying the total torque by the angular velocity of the turbine. The non-dimensional performance characteristics were then calculated using these total torque, force and power values as shown in Equations (3.43), (3.44), (3.45) in Section 3.3.

5.7 CFD TEST MATRIX

Multiple CFD models were created to investigate flow features such as regular wave propagation and combined wave-current flows, while also examining the effect of these flow features on the performance of a model scale TST. Table 5.7 shows all the different CFD models developed with the corresponding experimental data sets used in validation of the models.

TABLE 5.7. CFD TEST MATRIX FOR NUMERICAL SIMULATIONS CONDUCTED THROUGHOUT THIS THESIS.

Case Name	Water Depth, h (m)	Current Description		Wave Description							Turbine Settings		Equivalent experimental data
		Type of flow	Target \overline{W} (m/s)	Wave maker position	Depth Condition*	H (m)	Tr (s)	L (m)	Steepness H/L	Relative Depth h/L	Angular Velocity, ω (rad/s)	Approx. TSR, λ	
CFD_UC1_W1_Int	0.76	Uniform	0.93	-	Int	0.058	1.218	2.250	0.026	0.338	-	-	LVP_UC1_W1_Int
CFD_UC1_W2_Int	0.76	Uniform	0.93	-	Int	0.082	1.147	2.020	0.041	0.377	-	-	LVP_UC1_W2_Int
CFD_UC2_W3_Int	0.76	Uniform	0.10	-	Int	0.01	1.218	2.250	0.0044	0.338	-	-	No
CFD_UC1_W1_Deep	2.5	Uniform	0.93	-	Deep	0.058	1.218	2.315	0.025	1.080	-	-	No
CFD_UC1_W2_Deep	2.5	Uniform	0.93	-	Deep	0.082	1.147	2.052	0.040	1.220	-	-	No
CFD_UC2_W3_Deep	2.5	Uniform	0.10	-	Deep	0.01	1.218	2.315	0.0043	1.080	-	-	No
CFD_UC3_Turb	2.0	Uniform	1.00	NOWM	-	-	-	-	-	-	See Table 4.9	0-7	IFR_UC3_Turb
CFD_PC1_Turb	2.0	Profile 1	1.00	WM00	-	-	-	-	-	-	8.8874	4	IFR_PC1_Turb
CFD_PC2_Turb	2.0	Profile 2	1.00	WM20	-	-	-	-	-	-	8.7934	4	IFR_PC2_Turb
CFD_PC1_W4_Turb	2.0	Profile 1	1.00	WM00	Int	0.082	2.566	9.07	0.009	0.221	8.8874	4	IFR_PC1_W4_Turb
CFD_PC2_W5_Turb	2.0	Profile 2	1.00	WM20	Int	0.12	1.917	5.61	0.021	0.357	8.7934	4	IFR_PC2_W5_Turb

*Int - Intermediate

5.8 SUMMARY

This chapter has provided a general description of the methodology used to develop each type of CFD model used in this thesis. The model generation is broken down into development of the main fluid domain and the turbine subdomain. The description of a simplified 'thin' model domain is presented for use in investigating the model optimisation parameters, to be discussed in Chapter 6. Two different main fluid domain models, a 'free slip' and 'free surface' model, are also detailed in Chapter 6, but a general description of the model setup is provided in this chapter. These models were used to compare the main fluid domain setup features and to investigate how they affect the generated current flow conditions.

Different models use various types of flow conditions. The methods used to generate uniform and profiled current conditions were summarised in this chapter, while regular wave propagation from the domain inlet has also been detailed. The use of a subdomain to incorporate a HATT into the chosen flow conditions is carried out using the MFR technique. Specifically, only the general model geometry, mesh and physics setup parameters are described in this chapter. However, greater detail for each specific CFD model is given in each results chapter and is therefore not included here.

6 CFD MODEL OPTIMISATION

This chapter describes the methods adopted to optimise the CFD models used in this thesis. This optimisation consists of a mesh and time step study, with a comparison of two different CFD model setup configurations.

A mesh optimisation study was carried out for the mesh in the main fluid domain as well as in the turbine subdomain. This process was carried out to ensure the spatial features required to model the specified flow conditions were sufficiently captured. A final summary of the mesh requirements for the main fluid domain and turbine subdomain are presented in Section 6.1.

A method for setting the time step of the simulation is also described as is it dependent on the transient nature of the simulation, ie. wave-current flow, current flow with a TST, or combined wave-current flow with a TST. A description of the time step required for each different type of simulation is detailed in Section 6.2.

A comparison of CFD model setup configurations was carried out using the typical CFD model setups, as described by literature in Chapter 2, using the two different surface boundary conditions: the 'free slip' and 'free surface' model. Both types of model are widely used in the TST industry to analyse the effect of different flow conditions on turbine performance, as detailed in Chapter 2. The two different models are therefore compared to determine which model is better suited to capture the hydrodynamics and performance characteristics of the TST used in this thesis. The 'free slip' model is a single-phase, incompressible flow model with the 'top' boundary at the SWL specified as a 'free slip' boundary condition. The 'free surface' model is a homogenous, multiphase model with a distinct free surface interface between the water and air phases. The 'top' boundary is in the air region of the model and specified as an 'opening' allowing bidirectional flow across the boundary. The 'free slip' and 'free surface' CFD models are compared in order to investigate the differences in flow conditions and turbine performance using uniform current-only conditions.

6.1 MESH OPTIMISATION STUDY

6.1.1 Simulating regular waves

A mesh independence study was carried out using different HEXA meshes to ensure the mesh was optimised for the desired flow conditions without being too computationally expensive. Table 6.1 shows the settings used for comparing different meshing techniques, based upon the findings of [126], [128], [162], [163].

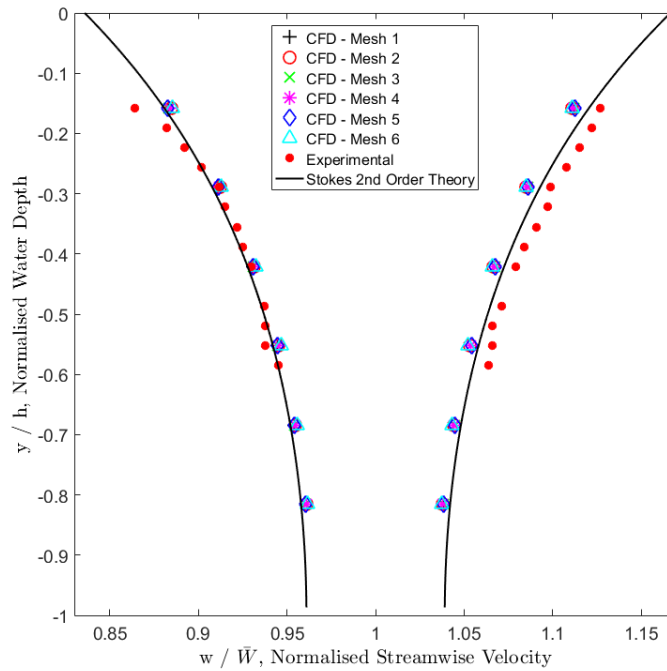
TABLE 6.1. A SUMMARY OF THE DIFFERENT MESH SETUPS.

Mesh Number	Cells over wave height ($H/\Delta y$)	Cells per wavelength ($L/\Delta z$)	Total Elements (thousands)
1	10	60	378
2	10	80	488
3	10	100	620
4	10	120	730
5	10	140	839
6	20	100	1140

The mesh study was carried out using a ‘thin’ domain model with uniform current conditions, $\bar{W} = 0.93m/s$, and a regular wave in intermediate water depth conditions with the following properties: $H = 0.058m$, $T_r = 1.218s$, $L = 2.25m$. The computational speed of the CFD models was examined while also comparing the velocity components through the water depth against theoretical data and experimental results. The experimental comparison was made against recirculating water channel results obtained by the University of Liverpool [84].

Initially the streamwise and vertical velocity components from the CFD models were compared to the S2OT results. Figure 6.1 shows the normalised streamwise and vertical velocities at points through the water depth for CFD, theory and experimental results. The maximum difference between the CFD model results and the equivalent theory was 1% for the streamwise velocities and 25% for the vertical velocities. The maximum difference between the vertical velocity components was 0.00367 m/s, and although the difference is small it results in a much bigger percentage difference as all the vertical velocity results are close to zero. The purpose of this mesh optimisation study was to see how comparable the numerical velocity results for each mesh were to the theoretical and experimental results. Therefore, the relative difference between each of the mesh results is what was important here.

A



B

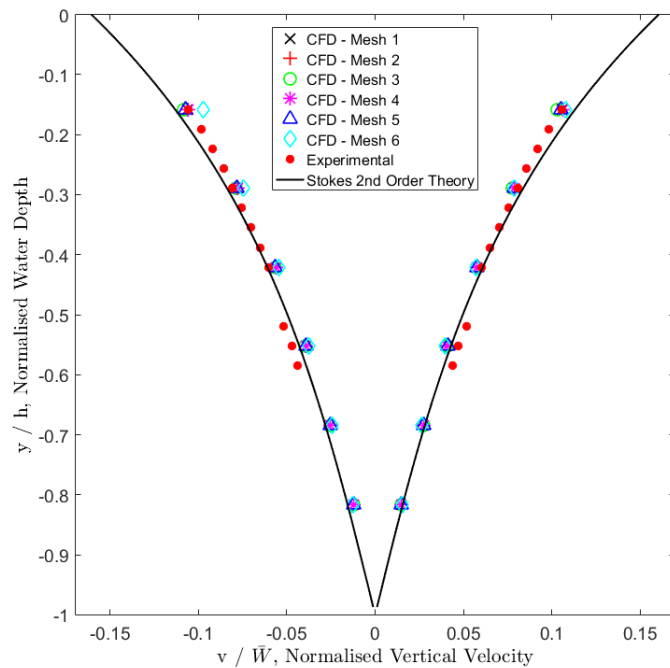


Figure 6.1. Normalised results for the CFD, theory and experimental maximum and minimum wave-induced: A) streamwise and; B) vertical velocities. Experimental data supplied by the University of Liverpool [84].

The numerical streamwise velocities shown in Figure 6.1A, display better agreement between the theory towards the base of the tank, with bigger divergence observed towards

the water surface. Mesh 4 showed the closest results to theory for the streamwise velocity, with a maximum difference of 0.7% between the CFD and theoretical results. Mesh 6 showed the biggest differences to theory with a maximum difference of up to 1%, while meshes 1 & 2 showed similar differences of 0.8% and 0.9%, respectively. The vertical velocity components in Figure 6.1B, show that mesh 3 gave the best agreement for all points through the water depth. Again, the CFD model results were more comparable to theory at the base of the tank, with greater differences towards the water surface. Meshes 4 and 5 gave similar results to mesh 3 for the vertical velocity component, all being within 2% of one another. Due to the minor differences of all mesh results being within 2% of one another, consideration of published literature as well as the computational run time of each simulation were taken into account.

It was recommended by [126], [128], [162], [163] to use between 10-20 cells over the wave height and ≥ 100 cells over the length of a single wave. Specifically, it was suggested by [162] to use >10 cells over the height of the wave and >100 cells over the length of a single wave, which agreed with the findings of [128]. It was proposed by [126] that an element size of $1/10$ th of the wave height was sufficient, while [163] stated that 16 cells over the wave height would produce mesh independent results. A summary of these results are shown in Table 6.2.

TABLE 6.2. RECOMMENDED MESH SETTINGS FOR FREE SURFACE MODELLING.

Author	Cells over wave height ($H/\Delta y$)	Cells per wavelength ($L/\Delta z$)
Finnegan & Goggins [126]	10	-
ANSYS Inc [162]	10-20	>100
Silva et al. [128]	10	145
Raval [163]	16	100

After examining the recommendations in the literature, meshes 1 and 2 would not be used as they had < 100 cells over the length of a single wave. Equally, after analysing all the velocity results, meshes 1, 2 and 6 were narrowly outperformed by meshes 3, 4 and 5. Figure 6.2 shows the total time for the simulations using each of the different meshes to reach convergence and complete 80s of run time. Mesh 6 took the longest to complete the simulation, taking $>30\%$ longer than mesh 5 which was the next slowest. Therefore, mesh 6 would also not be used. Of the remaining meshes, mesh 3 showed good agreement with theory for the vertical velocity results but performed less well with the horizontal velocity results. Meshes 4 and 5 both gave the best agreement with the streamwise and vertical theoretical velocity components. Mesh 4 was computationally faster than mesh 5 by about

10% and considering this ‘thin’ domain model was 1/14th to 1/40th of the size of the full-sized domains used in this thesis, this speed difference could make a big difference in more computationally demanding models. Therefore, considering the marginal differences in accuracy while also recognising the computational run speeds, mesh 4 was chosen as the optimum mesh arrangement.

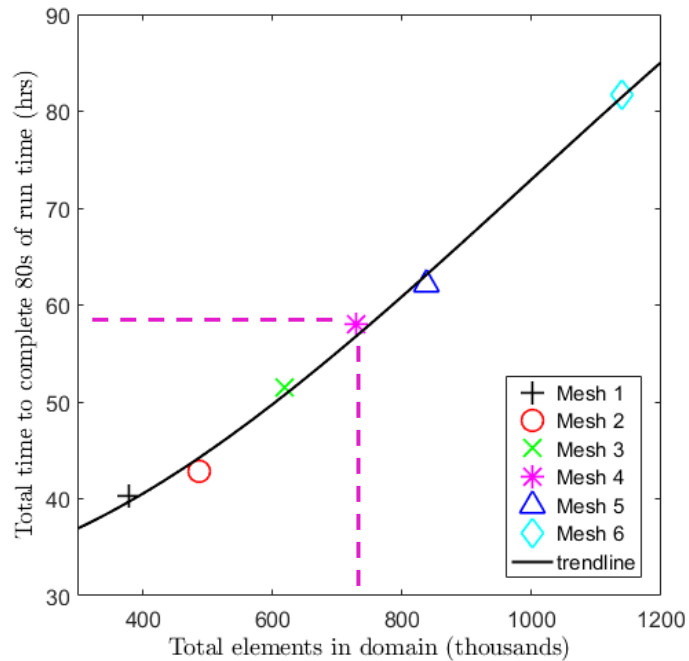


Figure 6.2. Computational speed of numerical model with different mesh sizes.

6.1.1.1 Mesh summary

All CFD models simulating wave-current flow conditions have the same generalised mesh as shown in Figure 6.3. As a result of the mesh study detailed in the previous section, this mesh has 120 cells over the length of a wave (Δz) and 10 cells over the wave height (Δy) with the mesh expanding away from this refined region. Specific details for the mesh of each individual model are given at the beginning of each results section but based upon the mesh selection of mesh 4 as detailed in this chapter.

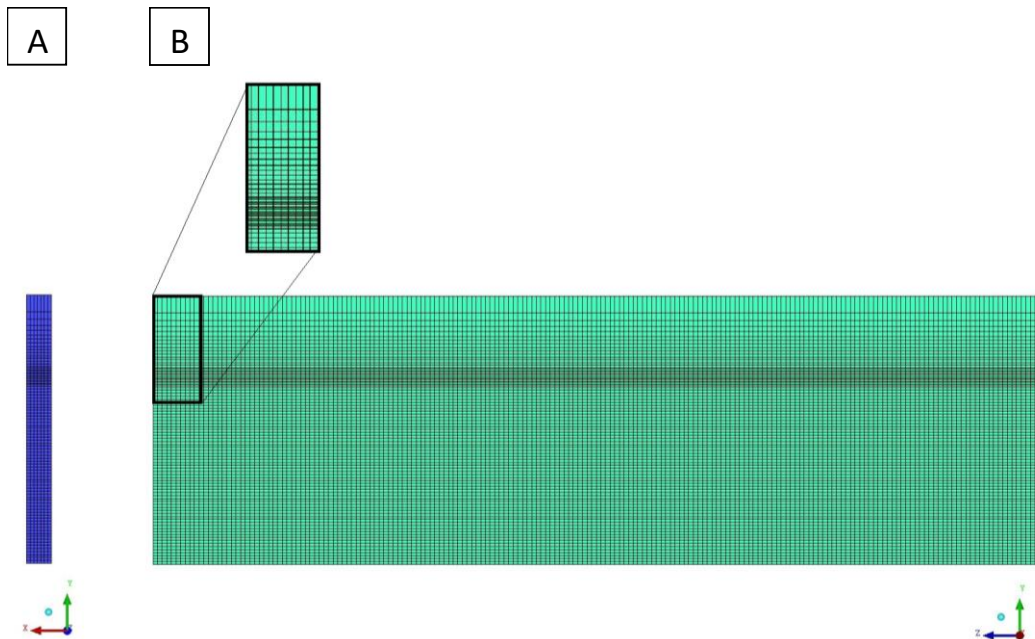


Figure 6.3. Final mesh selection using 120 cells per wavelength and 10 cells over the wave height: A) in the XY plane; B) in the YZ plane.

6.1.2 Turbine model

A mesh optimisation study for the turbine subdomain was carried out using a number of different meshes, detailed in Table 6.3.

TABLE 6.3. A SUMMARY OF EACH MESH SETUP FOR THE TURBINE SUBDOMAIN.

Mesh No.	Element size on each part (m)					Prism Layer Properties			No. Elements (millions)	
	MFR Cylinder	Blade Tip	Blade Middle	Blade Root	Hub	First layer thickness	No. Layers	Growth Rate	MFR Cylinder	Whole domain
1	0.024	0.003	0.005	0.007	0.008	0.002	3	1.0	2.89	7.25
2	0.024	0.003	0.005	0.007	0.008	0.001	3	1.0	2.96	7.30
3	0.024	0.005	0.008	0.011	0.012	0.001	3	1.0	1.47	5.84
4	0.024	0.002	0.004	0.005	0.006	0.001	3	1.0	4.67	9.0
5	0.024	0.003	0.005	0.007	0.008	0.0005	3	1.0	3.03	7.4
6	0.024	0.002	0.004	0.004	0.006	0.00075	6	1.0	3.1	7.4
7	0.024	0.002	0.004	0.004	0.006	-	0	-	2.9	7.3

This study aimed to investigate the effects of mesh refinement on the performance characteristics and loadings of the turbine. The mesh independence study was based upon previous turbine meshing research carried out by the CMERG [71], [89]. The meshes were generated for the rotating sub domain of the MFR cylinder, surrounding the turbine blade and hub surfaces. Each mesh varied in terms of the mesh sizing and distribution over the blade root, middle and tip, as well as considering the effect of inflation layers with the

number of layers and first layer thickness investigated. An explanation of these terms is detailed in Figure 6.4.

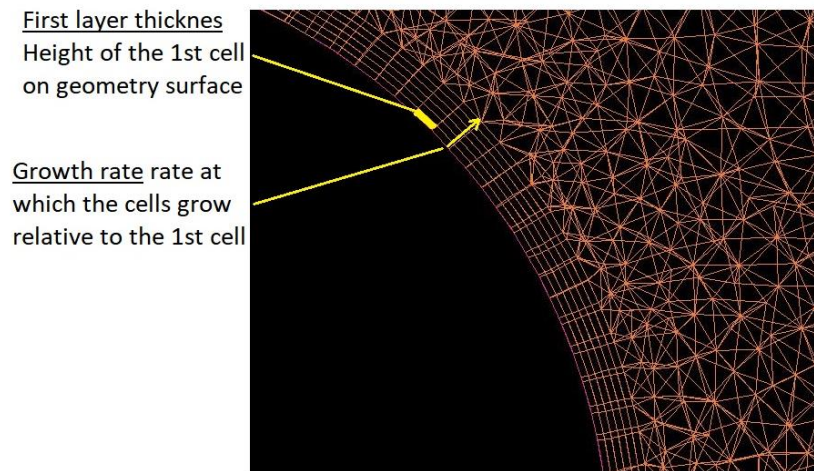


Figure 6.4. Explanation of inflation layer mesh descriptors.

All tests carried out in the mesh study were based upon the conditions used in a test campaign at the IFREMER wave-current flume. A turbine angular velocity of 8.89 rad/s was used which equates to peak power conditions at a TSR ≈ 4 . A TSR of 4 was used as this would be the optimal operating condition used to extract the greatest amount of energy from tidal flows using this specific turbine. The current had a uniform velocity of 1.01 m/s and no waves were present. The torque and thrust on the hub and each blade of the turbine were examined, allowing comparisons to be made between the CFD model and experimental results. Specifically, comparisons between the non-dimensional performance coefficients C_p , C_t , and C_q were used in the development of the turbine mesh, as well as results and methods reported by [68], [86], [110]. The non-dimensional performance coefficients are defined in Chapter 3, using Equations (3.43), (3.44), (3.45). Figure 6.5 shows the comparison for C_p , C_t and C_q between the CFD and experimental results.

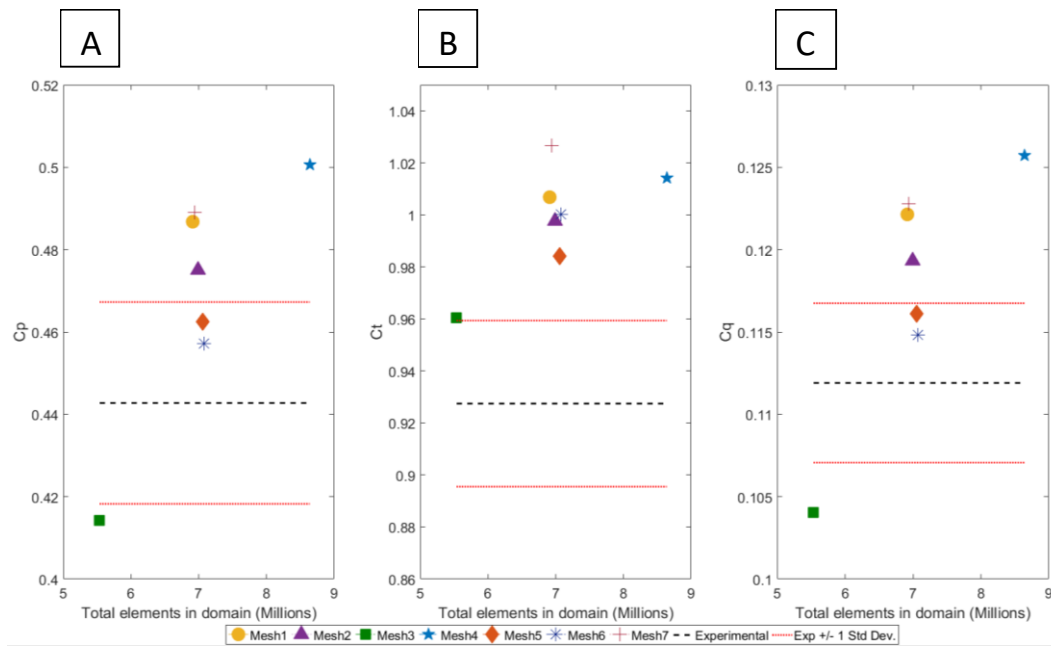


Figure 6.5. Mesh comparison between CFD and experimental results for: A) C_p , B) C_t and; C) C_q . Experimental data supplied by the University of Liverpool [84].

Of the 7 mesh designs, each mesh ranged from 1.5 to 4.7 million elements in the MFR cylinder resulting in 5.8 to 9.0 million elements in total. Mesh 1 was developed as the ‘base’ mesh, upon which other mesh arrangements were established. Mesh 1 was moderately refined over the turbine hub and blade sections with three inflation layers perpendicular to the surface of the turbine. The simulated CFD model results for mesh 1 show that the average C_p , C_t and C_q values were over-predicted in comparison to the experimental results. The difference between experimental and numerical data sets was $\approx 9\%$ for C_p , C_t and C_q . Mesh 2 remained the same as mesh 1 in terms of the overall mesh refinement. However, the first layer thickness of the inflation layers was halved from 0.002m to 0.001m, improving the difference between the CFD and experimental results for each of the performance coefficients by around 2%, resulting in an absolute difference of $\approx 7\%$ for C_p , C_t and C_q . Meshes 3 and 4 both used the same first layer thickness and number of inflation layers as mesh 2, however mesh 3 had a coarser overall mesh and mesh 4 had a finer overall mesh. Mesh 3 under-predicted values of C_p and C_q by about 7% of the experimental values, while only over-predicting C_t by 4%. Refinement of the grid in mesh 4 meant that the CFD results over-predicted the experimental results by 10-13%, showing that the overall grid spacing on the blades and the hub for mesh 2 was better. Figure 6.6 shows the computational time taken for the simulations to reach convergence and complete 60s of simulation time. Mesh 3 completed the simulation in less time than all the other meshes

but at the expense of numerical accuracy, while mesh 4 possessed the longest overall simulation time without any improvement in the performance characteristic results.

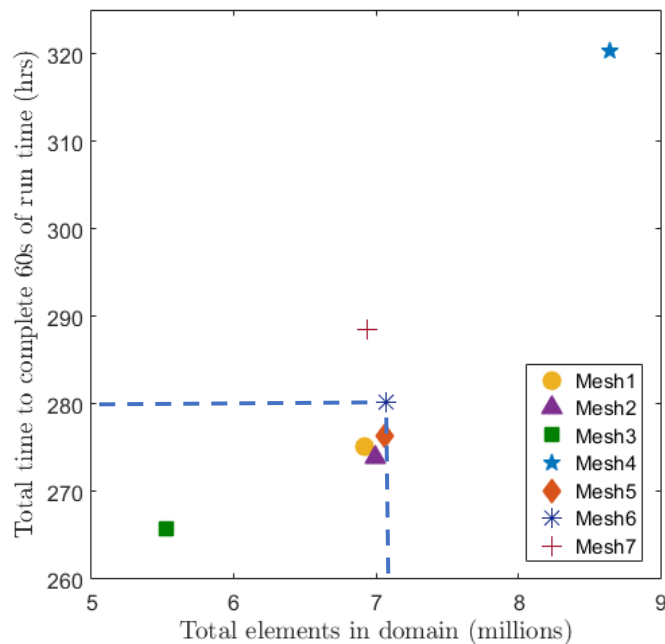


Figure 6.6. Computational time comparison for 60s of run time for meshes 1-7.

Mesh 5 reduced the first layer thickness of the inflation layers at the turbine surface, while using the same overall turbine mesh sizing as mesh 2. The difference between the CFD and experimental results for C_p and C_q reduced to 4% with C_t also seeing a reduction to 6%. Mesh 6 used a first layer thickness of 0.00075m by doubling the number of inflation layers to 6 instead of 3. The overall mesh size was somewhat decreased to enable a smooth transition between the inflation layers and the main mesh sizing over the turbine. These changes saw a smaller difference of 3% between the CFD and experimental results for C_p and C_q , yet an increase to 8% for C_t . To verify the use of inflation layers, the same mesh settings were used in mesh 7 but without any inflation layers. This resulted in a 7% increase for C_p and C_q in comparison to mesh 6, up to a value of 10%, while C_t increased by 3% giving a total difference between CFD and experimental results of 11%. This validated the use of inflation layers on the turbine surface, as not only did the results worsen without the use of inflation layers, but the simulation time also increased as seen in Figure 6.6.

Overall, it was found that mesh 6 gave the best agreement to experimental results at a TSR of 4 and was therefore chosen as the final mesh selection. A TSR of 4 was used as it was found to be the peak value of C_p as shown by turbine characterisation detailed in Chapter 4. The C_p and C_q for mesh 6 differed from the experimental data by < 3%, while the

difference for C_t was 8%. CFD results for C_p and C_q were both within 1 standard deviation of the average experimental results, while all meshes experienced a bigger discrepancy in results for C_t .

It was recommended by [106] to have a mesh with at least 10 nodes in the boundary layer region for accurate representation of these flow effects, giving a $y^+ < 2$ which is found to be excessive and is hard to satisfy for all wall regions. Due to the considerable increase in the number of elements needed to satisfy $y^+ < 2$, the numerical turbine simulations carried out in this thesis used $y^+ = 65 - 220$, dependent on the TSR, which was found to be acceptable, as discussed by [86], [89], [114], with a recommended maximum value of $y^+ < 400-500$. The final mesh layout for the rotating subdomain of the MFR cylinder, surrounding the turbine blade and hub surfaces, can be seen in Figure 6.7.

6.1.2.1 Turbine mesh summary

All numerical modelling carried out with a turbine used the mesh described by mesh 6 as shown in Figure 6.7 and detailed in Table 6.3. This mesh has a mesh sizing of 0.024m in the MFR cylinder, with 0.004m on the blades, except for the tip of the blades which has further refinement to 0.002m. Prism layers are used over the turbine hub and blade surfaces using 6 inflation layers with a growth rate of 1.0.

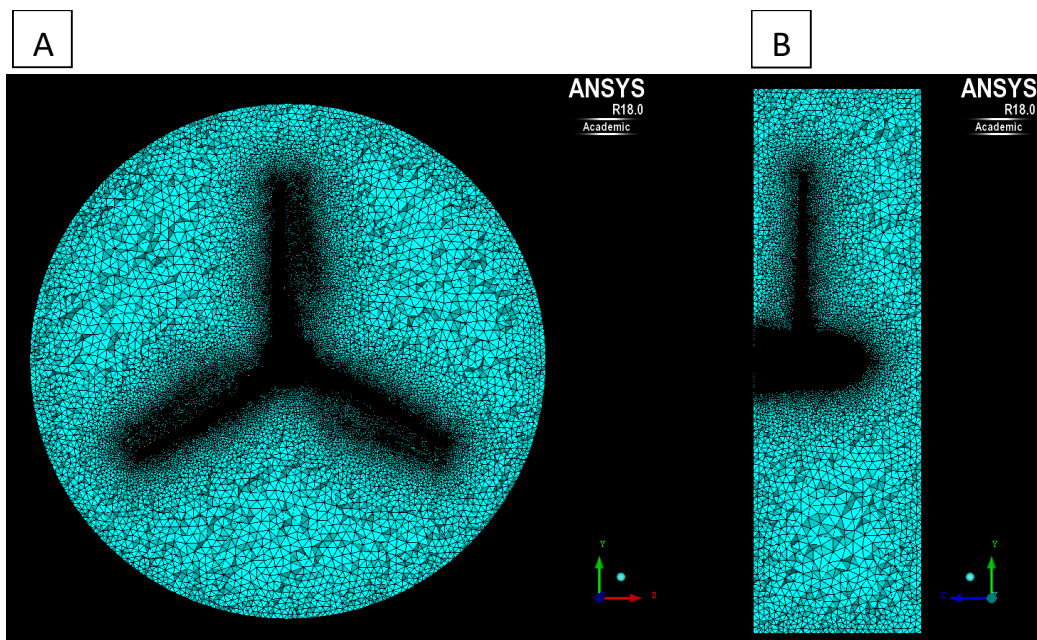


Figure 6.7. Final turbine mesh selection for section 3, the rotating turbine subdomain, using inflation layers and TETRA meshing viewed from the: A) front, and from the; B) side.

6.2 TIME STEP STUDY

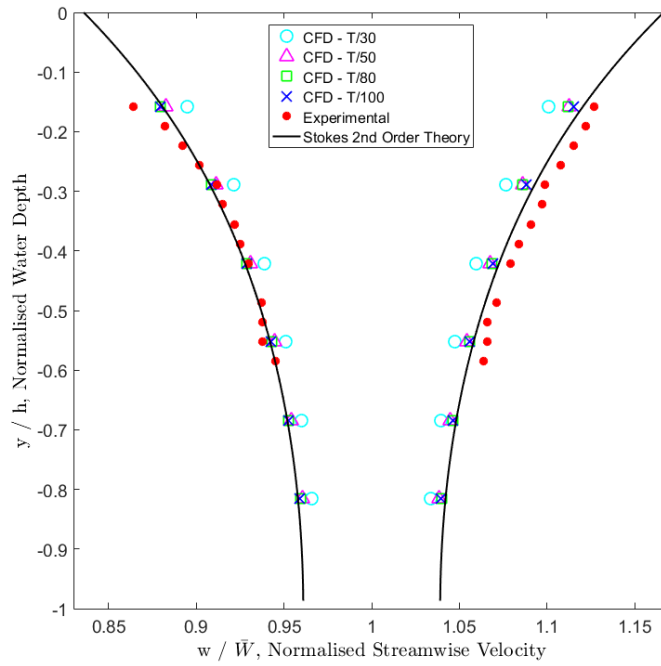
The ANSYS CFX-Solver uses an implicit solution method and therefore requires that the physical timescales in the model are resolved by using a time step to control the simulation [149]. It is not recommended to adopt the Courant number criterion as other CFD software might suggest as this is only advised for explicit solvers [130], [132]. Explicit solution methods exist when a direct computation of the dependent variables can be made in terms of known quantities from previous time steps. Calculations at each timestep are dependent on each other but have the tendency to be unstable and require very small timesteps. The Courant number criterion is therefore adopted to control the solution. Implicit schemes exist when the dependent variables are defined by sets of equations and an iterative technique is required to obtain a solution. This can involve having many iterations per timestep which is more complicated but usually results in a greater stability, allowing for much larger time steps [168]. Therefore, a time step study was carried out to examine the effect it had on the computational time taken to run each simulation, as well as the accuracy between the CFD model results and comparable theoretical and experimental results. The time step was specified in terms of the wave properties, for wave-current simulations, or in terms of the turbine rotation, for simulations using a TST. Both time step calculation methods are detailed in the following sections.

6.2.1 Wave-current CFD simulations

The time step for wave-current CFD simulations, Δt_{wave} , was specified in terms of the wave period and by dividing this into a certain amount of divisions, eg. T/30. Divisions of 30, 50, 80 and 100 were investigated using a wave-current model with the optimum mesh settings described by mesh 4, Section 6.1.1.

The streamwise and vertical velocity components for the CFD model were compared against theory and experimental data as shown in Figure 6.8. For the streamwise velocity results, the models with a time step of T/50, T/80 and T/100 were all <1% different to the experimental and theoretical results and within 0.6% of each other, while T/30 showed bigger differences with a divergence of up to 2% from the experimental and theoretical streamwise velocity. Results for the vertical velocity comparison showed that T/80 gave the best agreement to the experimental and theoretical data, with a maximum difference of 18% while T/30 gave a much bigger difference of up to 33%. Again, T/50, T/80 and T/100 were all within 3% of each other and so there was little difference in accuracy between these selected time steps for the vertical velocity.

A



B

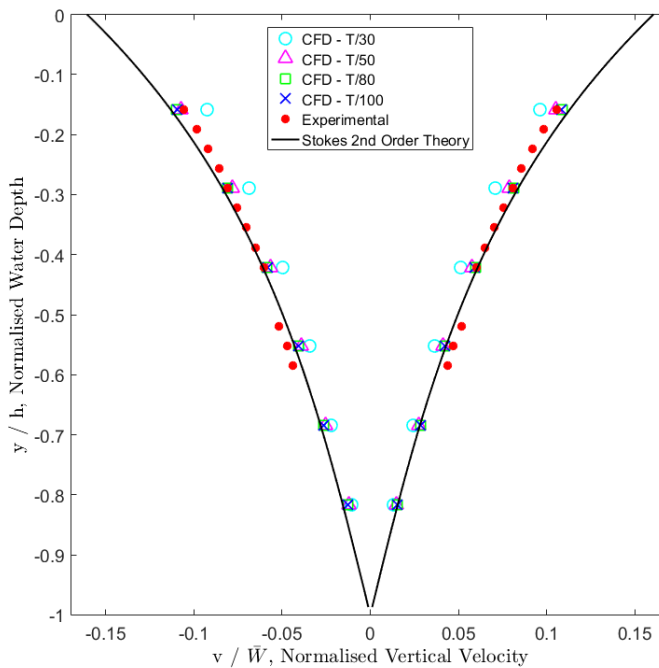


Figure 6.8. Normalised results for the CFD, theoretical and experimental maximum and minimum wave-induced: A) streamwise and; B) vertical velocities for different time steps. Experimental data supplied by the University of Liverpool [84].

Figure 6.9 shows the total time taken for the model to complete 80s of run time for each different time step used. The smaller the time step used, the more computationally expensive the model became. A timestep of T/30 was the quickest to run, however, the

accuracy was not as good as the smaller time steps investigated. $T/50$ gave a 10% increase in time in comparison to $T/30$ but showed better agreement with the experimental and theoretical results. There is a 60% increase in time between using $T/50$ and $T/80$, and 160% increase between $T/50$ and $T/100$. Therefore, a time step size of 50 divisions per wave period ($T/50$) was chosen as there was a negligible increase in accuracy yet a substantial increase in simulation time as the time step was reduced. This agreed with the findings of [128] where a time step of $T/100$ was used, [134] which found $T/40$ was the maximum time step that could be used before numerical instability occurred, and [126] which stated that the optimum time step interval was $\Delta t_{wave} = T/50$.

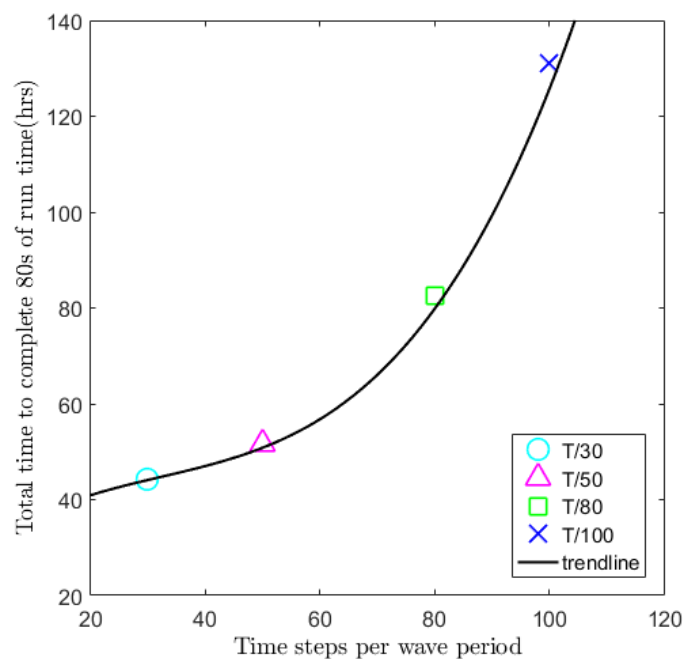


Figure 6.9. Computational speed of numerical model with different time steps.

6.2.2 Turbine CFD simulations

A specific time step study was not carried out for the turbine modelling cases. Instead, recommendations were taken from literature and the time step was defined by the angle (θ) through which the turbine turned per time step (Δt_{turb}). A time step was selected whereby the turbine rotates by $\theta = 5^\circ$ per time step which agreed with the findings of [110] and the recommendation by [169]. The angular frequency of the turbine would change depending on the desired TSR, and therefore the time step for each model would be varied accordingly.

6.2.3 Combined wave-current, turbine CFD simulations

For simulations combining wave-current conditions with turbine modelling, the time step was chosen to be the smallest of the standard time steps used in either the free surface wave-current modelling setup (Δt_{wave}), or in the turbine CFD modelling setup (Δt_{turb}). For example, a CFD model simulating turbine rotation at $\omega = 8.89 \text{ rad/s}$ would have a time step of $\Delta t_{turb} = 0.01s$, equating to 5° of turbine rotation per time step. When wave-current flow conditions are modelled without a turbine, the time step would equal $\Delta t_{wave} = 0.016s$ when a wave is present with an apparent wave period of $T_a = 0.81s$. If the turbine and wave-current conditions were both present in the CFD model then a time step equal to the smaller of the two time steps would be used in order to satisfy the turbine and wave time step requirements. Therefore, in this case the time step would equal $\Delta t = 0.01s$. Equations (6.1) and (6.2) show the method for calculating the time step in wave-current conditions or the presence of a turbine. Equation (6.3) would be used in a CFD model simulating wave-current flow conditions as well as the loadings on a turbine.

$$\Delta t_{wave} = T/50 \quad (6.1)$$

$$\Delta t_{turb} = \frac{\theta}{\omega \cdot \frac{180}{\pi}} \quad (6.2)$$

$$\Delta t = \min(\Delta t_{turb}, \Delta t_{wave}) \quad (6.3)$$

6.3 CFD MODEL SETUP CONFIGURATIONS

The CFD models developed in this thesis were created to replicate various experimental facilities in order to compare between experimental and numerical data sets. Typically, two main CFD model types exist and are widely used for modelling turbine performance in current-only flow conditions. This section investigates the differences between these two model configurations and the implications this has on the generated flow conditions and turbine performance when compared to model scale experimental results.

A ‘free slip’ and a ‘free surface’ CFD model were created and tested using uniform current conditions. The general development of the CFD models for both the main fluid domain and the turbine subdomain is provided in Chapter 5, while specific details are provided in this chapter.

6.3.1 'Free slip' CFD model

General development of the 'free slip' geometry, mesh and setup are given in Chapter 5, however, the following section provides the specific settings used in this 'free slip' CFD model.

6.3.1.1 Geometry, mesh, setup summary

The geometry is representative of typically sized experimental flume dimensions [69] for testing lab scale tidal devices, and the mesh was developed using a mixture of HEXA and TETRA meshing methods with the final mesh shown in Figure 6.10. The simulation was set up as a transient analysis with a uniform current-only flow of 1.0 m/s. The angular velocity of the turbine was controlled using the angular velocities detailed in Table 6.4, while a summary of the specific model settings are detailed in Table 6.5.

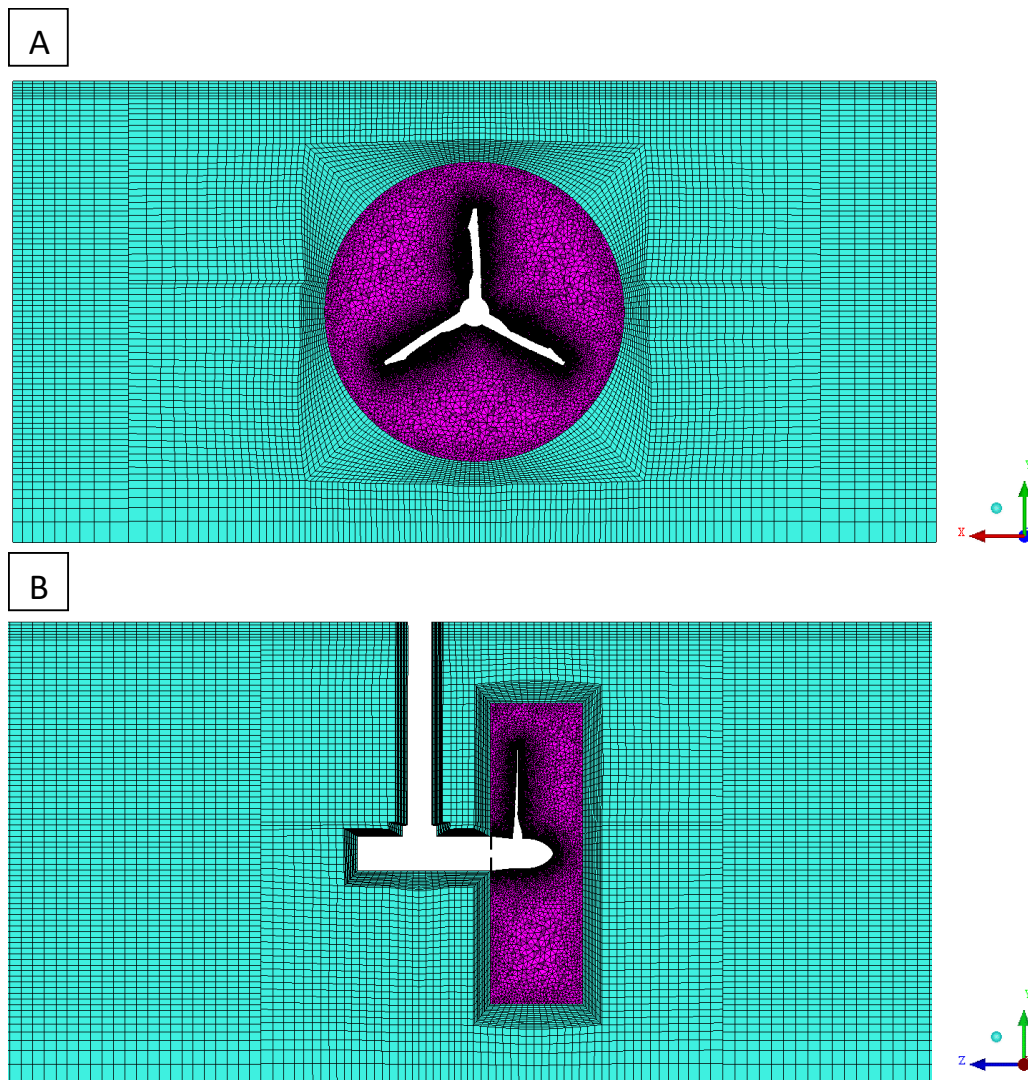


Figure 6.10. The mesh for the 'free slip' model as viewed from: A) the front and; B) the side.

TABLE 6.4. ANGULAR VELOCITIES USED TO CONTROL TURBINE ROTATION.

Turbine Angular Velocity, ω (rad/s)	Approximate TSR, λ
0.0	0
2.22	1
4.44	2
6.67	3
8.89	4
11.11	5
13.33	6
15.55	7

TABLE 6.5. SUMMARY OF THE GEOMETRY, MESH AND SETUP FOR A 'FREE SLIP' UNIFORM FLOW CFD MODEL.

Geometry		
Main domain dimensions	Length x Width x Depth	20 x 4 x 2 m
Subdomain cylinder dimensions	Diameter / Width	1.3 / 0.4 m
Turbine dimensions	Diameter	0.9 m
Mesh		
Main domain element sizing	Mesh expansion from 'top' boundary to 'base' (Δy)	0.02 \rightarrow 0.09 m
	Mesh expansion from centreline to 'side walls' (Δx)	0.02 \rightarrow 0.08 m
	Mesh expansion from 'inlet' boundary to 'outlet' (Δz)	0.05 \rightarrow 0.1 m
Sub domain element sizing	MFR cylinder	0.024 m
	Blade tip	0.002 m
	Blade middle	0.004 m
	Blade root	0.004 m
	Hub	0.006 m
Prism layer properties	First layer thickness	0.00075 m
	Number of layers	6
	Growth rate	1.0
Total number of elements	Main domain	3.3 million
	Turbine subdomain	3.1 million
	Total	6.4 million
Setup		
Time step	Δt_{turb} (see Equation (6.2))	
Fluid Phases present	Water (single phase)	
Buoyancy model	Off	
Boundary conditions	inlet	Velocity-inlet
	Flow type	Uniform current-only flow
	Input velocity components	U: 0 m/s
		V: 0 m/s
		W: 1.0 m/s
	outlet	Pressure-outlet
	Reference pressure	$P_{ref} = 0 Pa$
	Side walls and base	No-slip wall
	Top	Free-slip wall
	Stanchion	No-slip wall
Hub and turbine blades	No-slip wall	

6.3.2 'Free surface' CFD model

General development of the 'free surface' geometry, mesh and setup are given in Chapter 5, however, the following section provides the specific settings used in this 'free surface' CFD model.

6.3.2.1 Geometry, mesh, setup summary

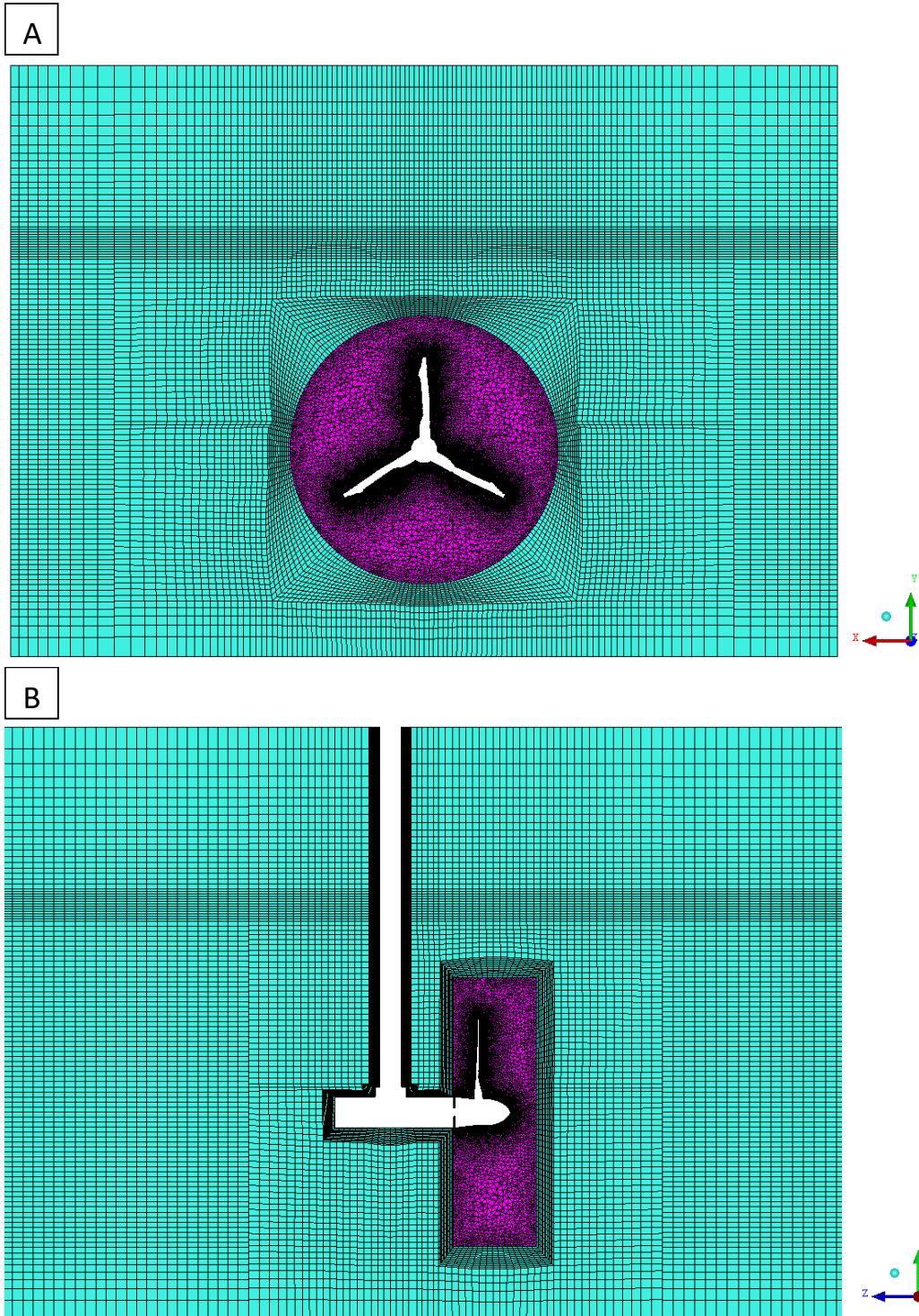


Figure 6.11. The mesh for the 'free surface' model as viewed from: A) the front and; B) the side.

As with the ‘free slip’ model, the geometry for the ‘free surface’ model is representative of experimental flume dimensions [69]. However, the ‘free surface’ model is a multiphase model as opposed to the single phase ‘free slip’ model. The mesh was developed using a mixture of HEXA and TETRA meshing methods with the final mesh shown in Figure 6.11.

The simulation was again set up as a transient analysis with a uniform current-only flow of 1.0 m/s. The angular velocity of the turbine was also controlled using the same angular velocities as the ‘free slip’ model and the experimental testing (Table 6.4). A summary of the specific settings used in this ‘free surface’ model are detailed in Table 6.6.

TABLE 6.6. SUMMARY OF THE GEOMETRY, MESH AND SETUP FOR A ‘FREE SURFACE’ UNIFORM FLOW CFD MODEL.

Geometry		
Main domain dimensions	Length x Width x Depth	20 x 4 x 2.86 m
Subdomain cylinder dimensions	Diameter / Width	1.3 / 0.4 m
Turbine dimensions	Diameter	0.9 m
Mesh		
Main domain element sizing	Air-water interface region	$\Delta y = 0.01$ m $\Delta z = 0.03$ m $\Delta x = 0.025$ m
	Mesh expansion from interface towards the ‘top’ boundary (Δy)	0.01 \rightarrow 0.1 m
	Mesh expansion from interface towards the ‘base’ boundary (Δy)	0.01 \rightarrow 0.09 m
	Mesh expansion from centreline to ‘side walls’ (Δx)	0.02 \rightarrow 0.08 m
	Mesh expansion from ‘inlet’ boundary to ‘outlet’ (Δz)	0.05 \rightarrow 0.1 m
	Sub domain element sizing	MFR cylinder
Blade tip		0.002 m
Blade middle		0.004 m
Blade root		0.004 m
Hub		0.006 m
Prism layer properties	First layer thickness	0.00075 m
	Number of layers	6
	Growth rate	1.0
Total number of elements	Main domain	4.3 million
	Turbine subdomain	3.1 million
	Total	7.4 million
Setup		
Time step	Δt_{turb} (see Equation (6.2))	
Fluid Phases present	Water and air (multiphase)	
Buoyancy model	On	
Boundary conditions	inlet	Velocity-inlet
	Flow type	Uniform current-only flow
	Input velocity components	U: 0 m/s V: 0 m/s

	W: 1.0 m/s
outlet	Pressure-outlet
Reference pressure	$P_{ref} = (\rho_{water} - \rho_{air}) \cdot g \cdot (h - y)$
Side walls and base	No-slip wall
Top	Pressure-opening
Relative pressure	$P_{rel} = 0 Pa$
Stanchion	No-slip wall
Hub and turbine blades	No-slip wall

6.3.3 'Free slip' and 'free surface' CFD model comparison

The difference between the setup of the two CFD models is depicted by Figure 6.12 which shows the streamwise velocity over the whole flow domain for each model type. There is a clear difference in the streamwise velocity through the water depth due to the differences in setup. Figure 6.13 shows the streamwise velocity at different TSRs at a location 2.5m downstream of the model inlet. In the 'free surface' simulation, there is an interaction between the air and water phases at the free surface interface which results in the velocity of the water being slowed towards the top of the water column as well as at the base of the tank due to frictional effects near the walls. The 'free slip' model shows the same frictional effects at the base of the tank however, there is no reduction in velocity near the 'top' boundary surface. This is because the 'top' boundary uses a 'free-slip' boundary condition which is defined with a finite value velocity component parallel to the top boundary.

Even though there are minor differences to the flow characteristics between the CFD models, the volumetrically averaged streamwise velocity over the swept area remains the same for each model at each different TSR between 0 and 7, as shown in Table 6.7. This similarity is because the turbine is situated in the centre of the water column, at a depth of -0.55m to -1.45m, and therefore the flow effects near the surface do not affect the average velocity over the swept area of the turbine. If the turbine was placed nearer to the SWL, this effect would be important and need to be considered.

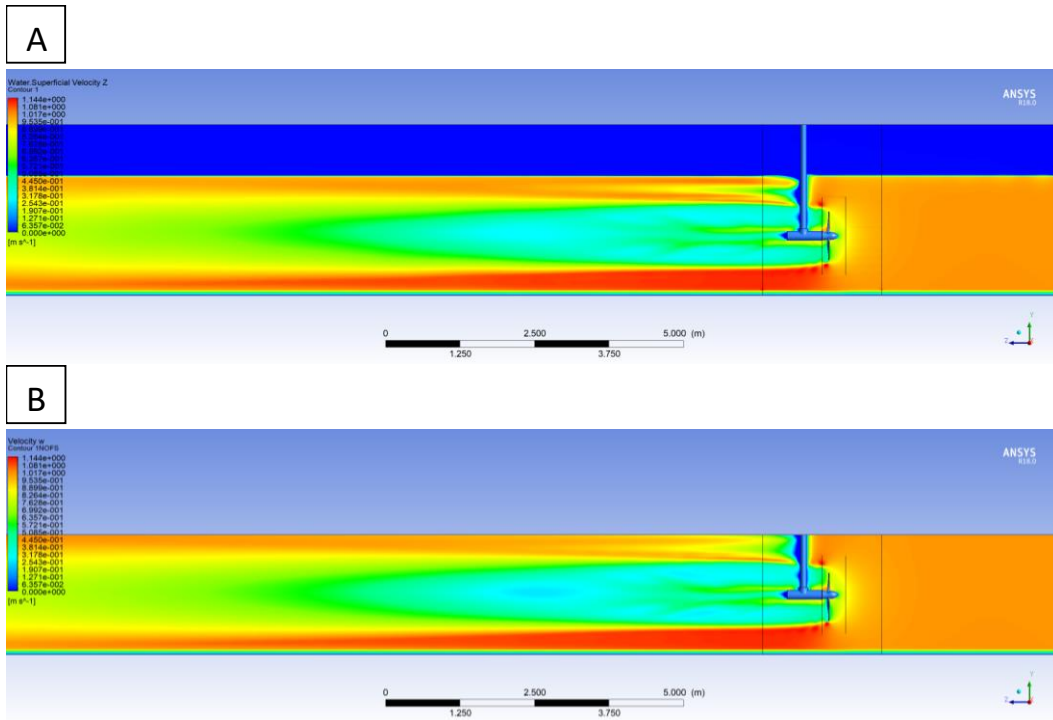


Figure 6.12. The streamwise velocity when the turbine is operating at a TSR of 4 for the: A) the ‘free surface’ and; B) the ‘free slip’ CFD models.

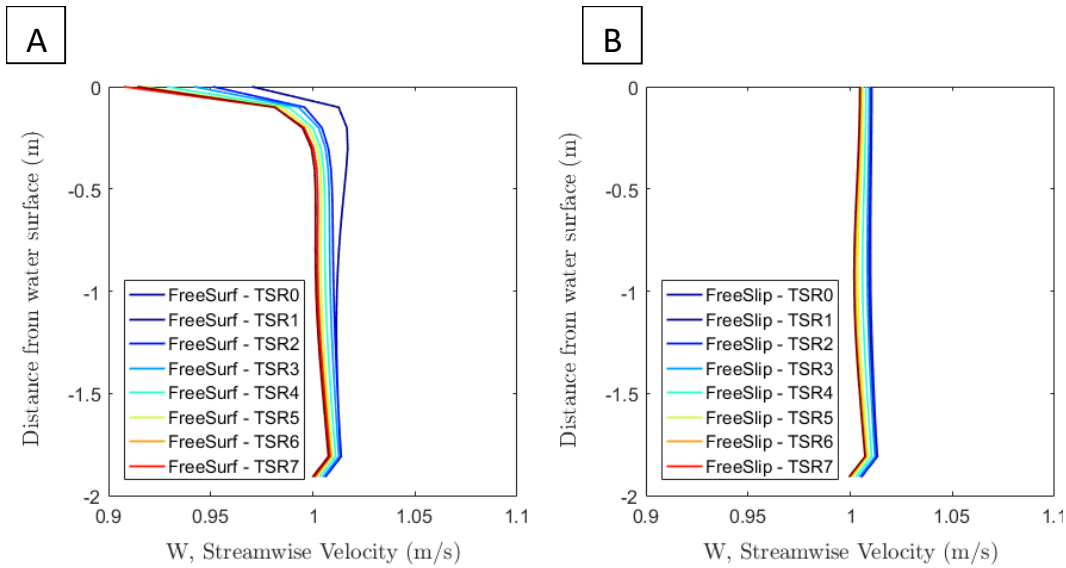


Figure 6.13. The streamwise velocity when the turbine is operating at a TSR of 0 to 7 at a location 2.5m downstream of the inlet for the: A) the ‘free surface’ and; B) the ‘free slip’ CFD models.

TABLE 6.7. VOLUMETRICALLY AVERAGED STREAMWISE VELOCITY OVER THE TURBINE SWEEPED AREA FOR THE 'FREE SURFACE' AND 'FREE SLIP' CFD MODELS.

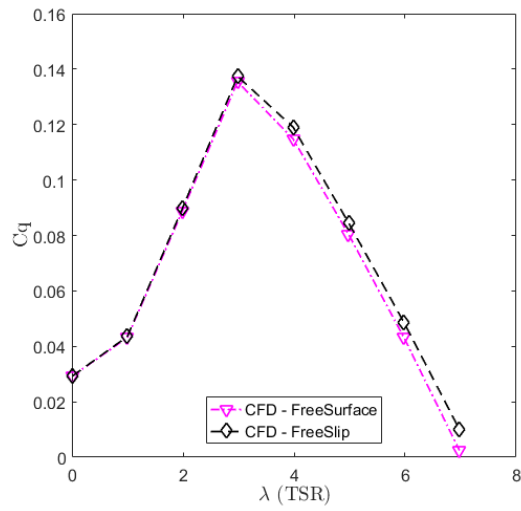
Approx. TSR, λ	Volumetrically averaged streamwise velocity over turbine swept area, \bar{W}_{vol} (m/s)	
	'Free surface' CFD model	'Free slip' CFD model
0	1.01	1.01
1	1.01	1.01
2	1.01	1.01
3	1.01	1.00
4	1.00	1.00
5	1.00	1.00
6	1.00	1.00
7	1.00	1.00

Figure 6.14 shows the average values of C_q , C_t and C_p over a range of TSR values for the 'free surface' and the 'free slip' CFD models. All values for the average performance characteristics show a good agreement between the two types of CFD model over the full range of TSR values. The greatest differences between the two model types for each performance characteristic are 0.008 at TSR 7 for C_q , 0.019 at TSR 4 for C_t , and 0.053 at TSR 7 for C_p . The focal area of this work is $3 < \text{TSR} < 5$ as the peak power for the TST was found to be at a TSR of 4 [156], from experimental work detailed in Section 7.1, and ideally the turbine would be operating around the optimum performance conditions. Therefore, the greatest differences in C_q , C_t and C_p , within the range $3 < \text{TSR} < 5$, is 0.004, 0.019 and 0.021 respectively. These differences are minor and demonstrate that in terms of the average performance characteristics, there is also no clear difference between the two types of model setup.

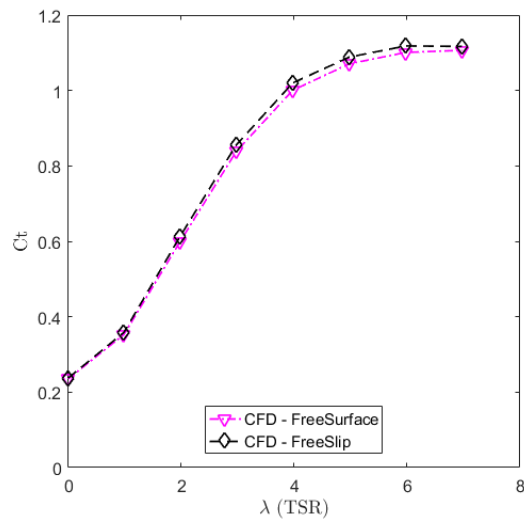
A further investigation into the differences in the results between the two types of CFD model was undertaken by investigating the transient dynamic loadings instead of the average values. Figure 6.15 shows the thrust and torque values obtained on each blade for 5 seconds of converged run time for both the 'free surface' and the 'free slip' models at $3 < \text{TSR} < 5$.

Initially, it is clear to see that the rotational period for both types of model is as expected, giving 0.94s, 0.71s and 0.57s for TSR 3, 4 and 5 respectively. Looking at the variation in the thrust results, there is a significant drop in the thrust every period which is due to a single blade passing the stanchion each rotation and is identical to the rotational frequency of the turbine.

A



B



C

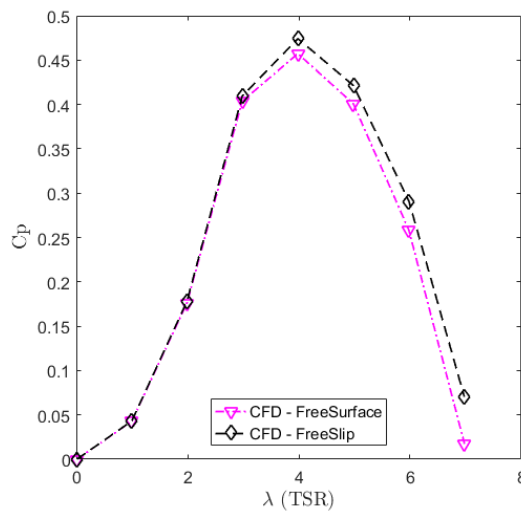


Figure 6.14. The A) C_q , B) C_t and C) C_p over a range of TSRs for the 'free surface' and 'free slip' CFD models in uniform flow conditions.

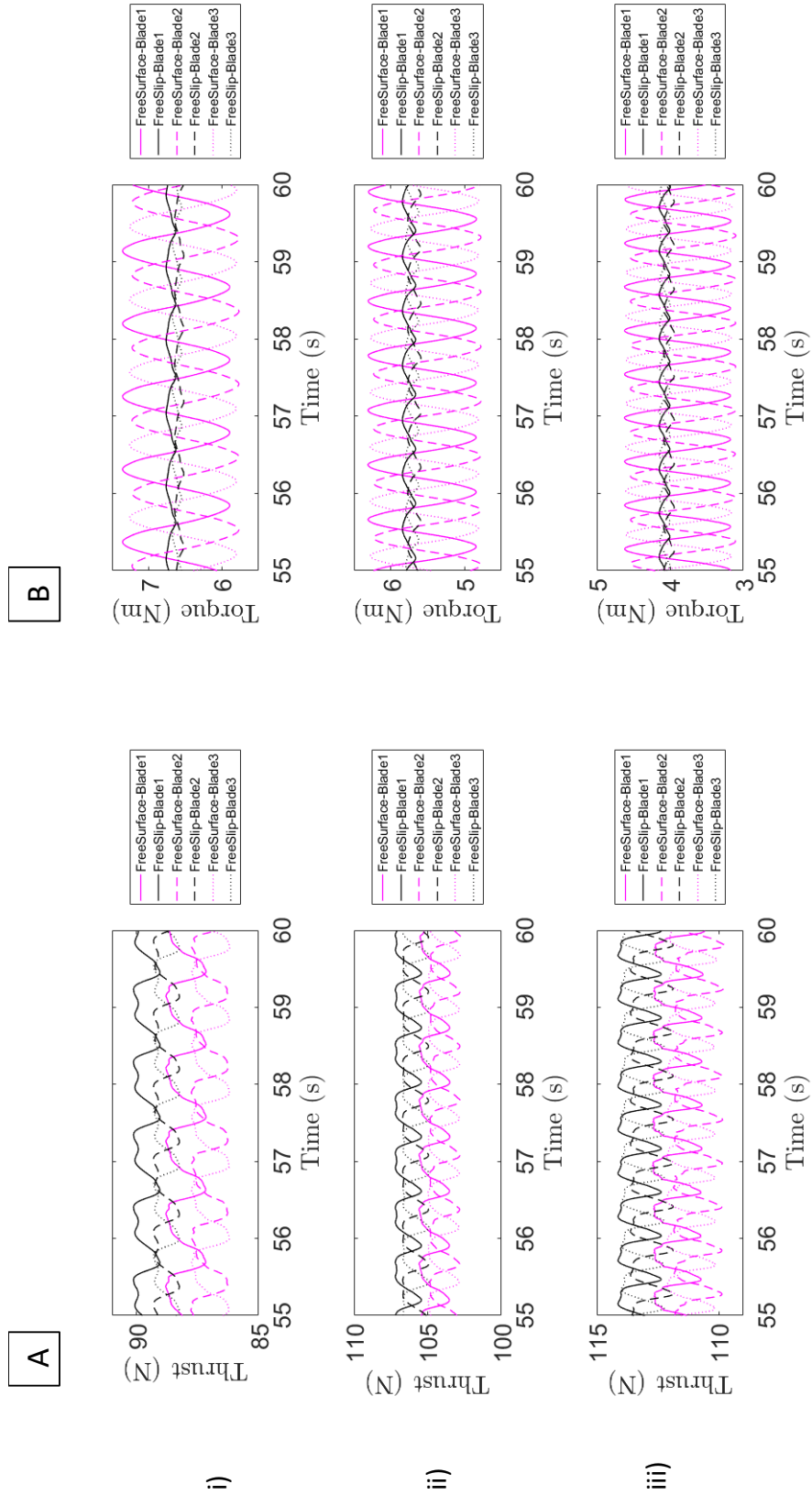


Figure 6.15. Numerical CFD comparison between the 'free surface' and 'free slip' models, for A) thrust and B) torque results on each blade over 5s of converged run time for: i) TSR 3, ii) TSR 4 and; iii) TSR 5.

For both types of model, there are some discrepancies between the results for blade 1 in comparison to blades 2 and 3. Blade 1 has a slightly higher average thrust in comparison to the other blades at all angular velocities investigated. On average, the maximum difference between blade 1 and the other 2 blades is 1 N which has little effect on the overall thrust, however, it was expected that all blades 1-3 would have the same average thrust. Creation of the mesh on the turbine blades was achieved using an automatically generated TETRA mesh in ANSYS ICEM and therefore control over the exact cell sizing is impossible. Therefore, it is hypothesized that due to this factor, marginal differences have the potential to exist between the meshes on each of the blades, and therefore this would account for the small differences seen in the results for blade 1. It is however necessary as manual generation would be extremely time consuming and not necessarily any more accurate. This feature also occurs in the torque results with the torque for blade 1 being on average 0.12 Nm greater than blades 2 and 3.

On average, the 'free slip' models have a higher average thrust and torque for a TSR of 3 to 5 when compared against the 'free surface' results. The difference between the two model types for the thrust on each blade was on average 1.8 N, while the difference in the average torque for each blade was 0.16 Nm. These observations can be seen more clearly in Figure 6.16i which displays the comparison between the 'free surface' and 'free slip' models for the thrust and torque measured at a TSR of 4 on different sections of the turbine over time.

As previously mentioned, the differences between the two model types in average thrust and torque on a single turbine blade are small. The same is true for the differences in average thrust and torque on the hub between the 'free surface' and 'free slip' models, as shown in Figure 6.16ii.

The minor differences in the blade thrust contributions for each model lead to the total turbine thrust of the 'free slip' model being 6 N greater than the 'free surface' model. This is <2% of the total turbine thrust which is inconsequential. The overall average torque results were as expected with the 'free slip' model estimating a marginal 0.6 Nm greater than the 'free surface' model due to small differences in the transient blade torque results.

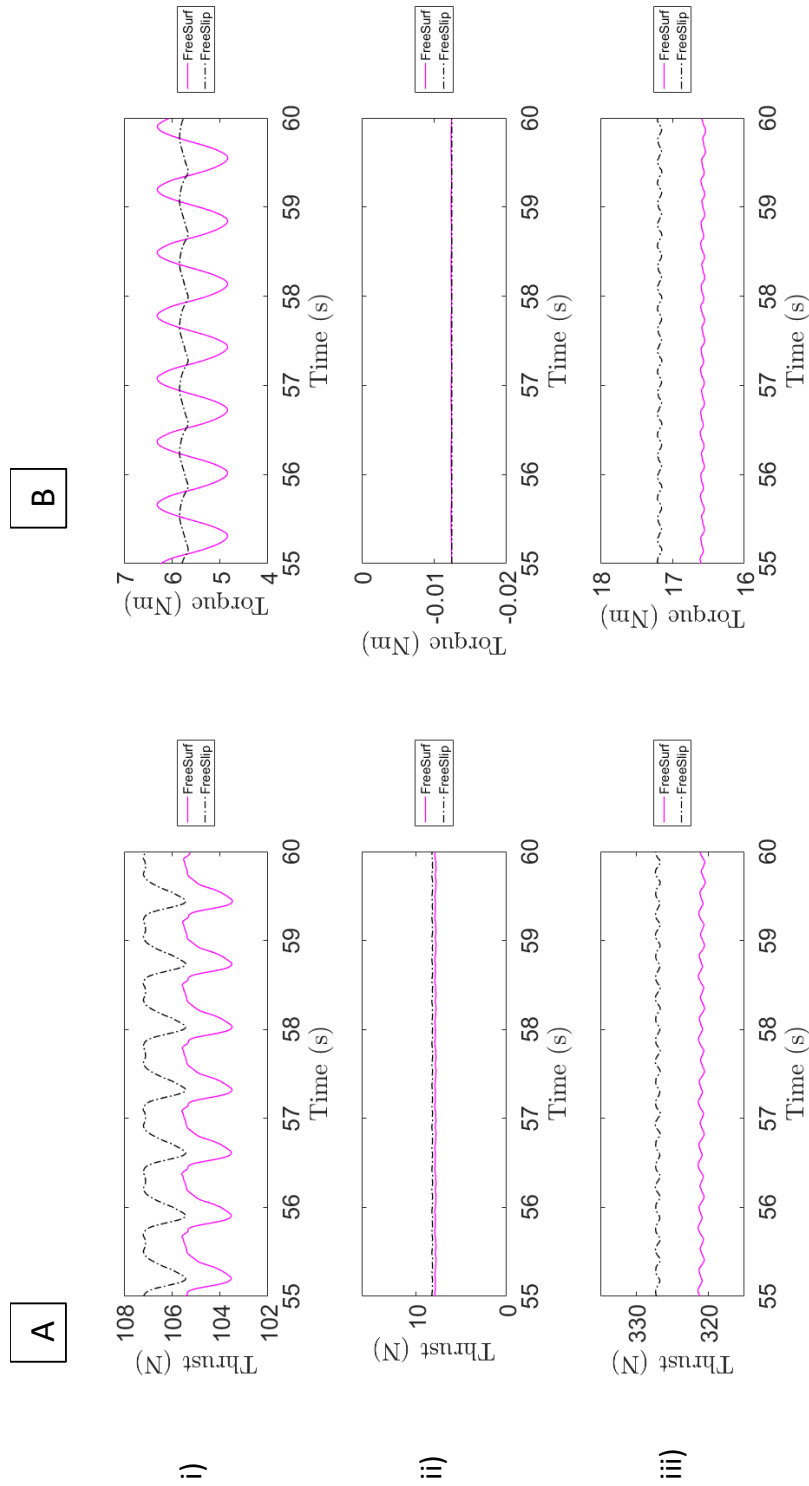


Figure 6.16. Numerical CFD comparison between the 'free surface' and 'free slip' models, for A) thrust and B) torque results at a TSR of 4 relating to: i) blade 1, ii) the hub and; iii) the turbine total (all blades and hub).

The shape of the transient thrust results for each individual blade shows good agreement between the 'free surface' and 'free slip' models. However, the shape of the transient torque results is much more contrasting as the amplitude of fluctuation for each model type is very different. A Fast Fourier Transform (FFT) was carried out to quantify the magnitude of fluctuation in the thrust and torque results. The FFT spectra produced by the 'free surface' and 'free slip' models are shown in Figure 6.17. These results were obtained at a TSR of 4, for a single blade as well as the combined turbine totals. For the single blade thrust and torque cases, Figure 6.17i, it is clear to see there is a dominant peak in amplitude at a frequency of 1.41 Hz which corresponds to the rotational frequency of the turbine and is where each blade crosses the stanchion during each rotation. The cases showing the combined turbine totals, Figure 6.17ii, has a smaller amplitude at a dominant frequency of 4.24 Hz, which corresponds to each turbine blade crossing the stanchion and occurs three times per rotation, hence three times the rotational frequency.

For the full range of TSR values, 1-7, the fluctuation in the thrust measurements for a single blade is marginally higher for the 'free surface' models compared to the 'free slip' models, with an average amplitude of 0.95 +/- 0.067 N and 0.75 +/- 0.137 N respectively. This shows that the magnitude of fluctuation for a single blade remained constant across all angular velocities and showed only minor differences between the amplitude of thrust fluctuation for each model type. This can be seen from looking at the FFT in Figure 6.17Ai or the transient thrust results in Figure 6.16Ai. The same trend is apparent for the thrust results on the hub as well as the combined turbine totals, albeit with different average values.

In comparison, the fluctuation in the torque measurements for a single blade shows a much bigger contrast between the two model types. The average amplitude for the torque fluctuation in the 'free surface' and 'free slip' models over the full range of TSRs are 0.77 +/- 0.012 Nm and 0.06 +/- 0.017 Nm respectively. Again, there is little variation in results over the full range of TSRs but the average difference in fluctuation between the 'free surface' and 'free slip' models is much more significant. The 'free surface' model shows a considerable fluctuation in the results, almost 13 times greater than that of the 'free slip' model, as shown in Figure 6.17Bi and Figure 6.16Bi. Buoyancy forces are present in the 'free surface' model, opposing gravitational forces. When the position of a turbine blade is at TDC or BDC, as shown in Figure 6.18, the buoyancy forces do not contribute to the torque on the blade. However, when the blade is positioned halfway between these locations horizontally, the buoyancy force will have a much greater contribution to the torque on the

blade which results in the oscillations seen in the transient torque results. The 'free slip' model typically neglects any buoyancy forces and therefore the torque results show only the dynamic pressure used to predict the torque around the global axis of rotation. Small dips in these torque results equate to the effect of the blade/stanchion interaction.

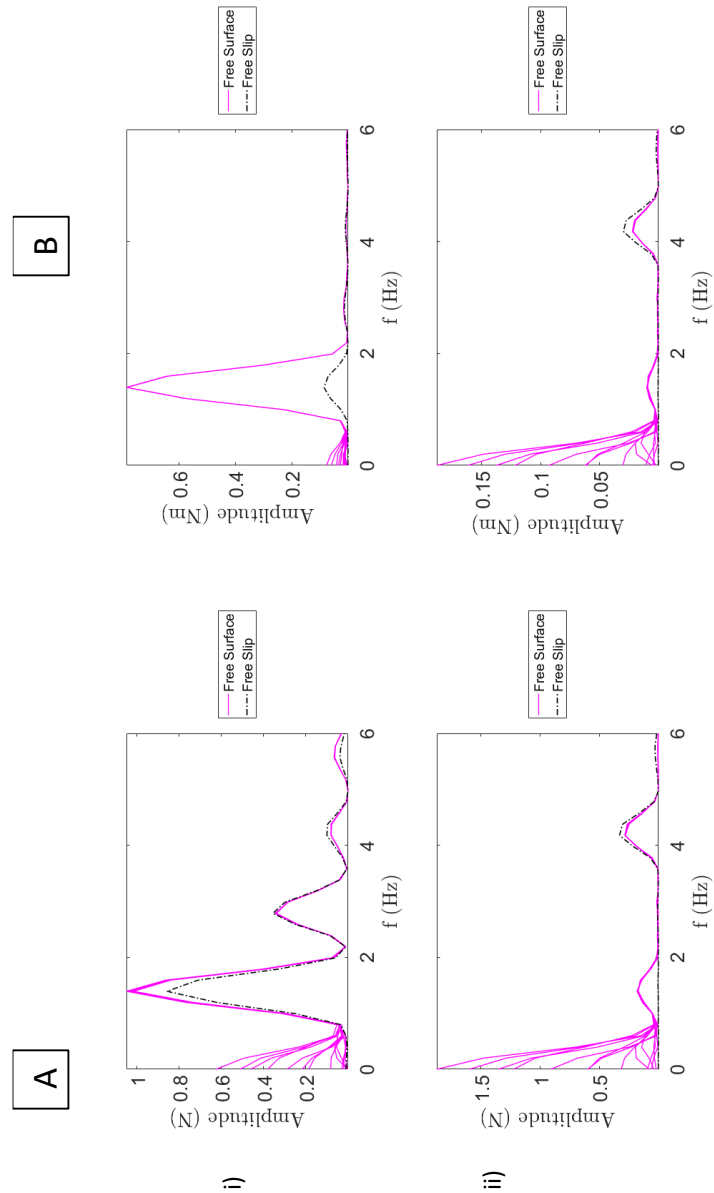


Figure 6.17. FFT analysis for the 'free surface' and 'free slip' CFD models, for A) thrust and B) torque results at a TSR of 4 for: i) blade 1 and; ii) the turbine total (all blades and hub).

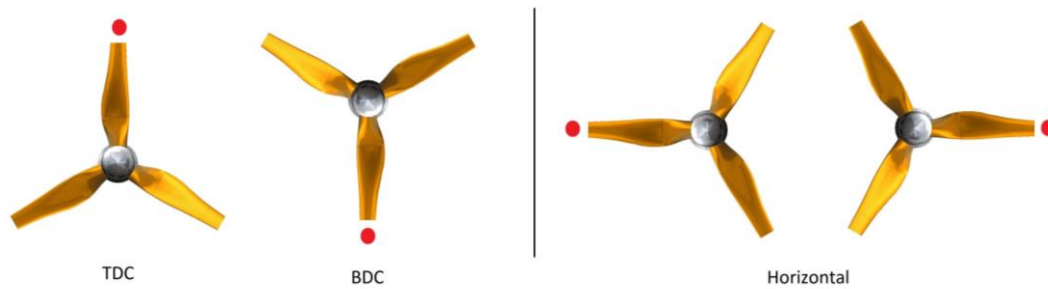


Figure 6.18. The orientation of the turbine when at Top Dead Centre, Bottom Dead Centre, and horizontal.

Even though the individual blade torque results show considerable differences between the model types in terms of fluctuation in the torque results, the results for the total torque over the whole turbine show no difference between the ‘free surface’ and the ‘free slip’ models. Figure 6.17Bi shows the torque fluctuation for a single turbine blade while Figure 6.17Bii accounts for the 3 turbine blades and hub. Each turbine blade is 120° out of phase and so each blade cancels the others out and reduces the amplitude of the frequency overall. Therefore, if only the total turbine torque was investigated and not the individual blade torque, these greater fluctuations would be overlooked and potential design considerations for the turbine blades ignored. This could be crucial for fatigue analysis and survivability of the tidal device [53].

Overall, the average total turbine loadings and performance characteristics are very similar between the two models. However, the transient nature of the individual component loadings show a greater difference. The estimation of the fluctuation in the torque for individual turbine blades was the major difference between the two types of model. If only the overall turbine loadings were considered, vital blade design considerations could have been overlooked. Therefore, if it is the average performance characteristics that are of interest, either model could realistically be used, but if the transient loadings are the focus of the model then it would be necessary to consider the ‘free surface’ type of CFD model. In practice, a velocity profile, surface gravity waves or other complex flow conditions could exist and result in greater variations in the flow velocity, overshadowing those previously stated. Yet, it is still important to accurately analyse the individual component loadings as with more complex flow conditions and even looking at real scale device sizes, these effects will only be enhanced. For these reasons, the ‘free surface’ model is used in all following numerical simulations due to the increased accuracy of the generated flow conditions and individual turbine component loadings.

6.4 SUMMARY

A mesh independence study was carried out to define the optimum mesh settings for engineering applications with the propagation of waves and current, and a rotating subdomain enclosing a TST. The mesh selection is very important to allow a good level of spatial detail to be resolved yet not requiring an excessive amount of computational power to run the simulation. The optimum mesh size for a fluid domain with propagating waves and current was found to have 10 cells over the wave height and 120 cells per wavelength. These settings allow the mesh to accommodate different wave selections making the model more versatile. The mesh settings for the subdomain containing the 0.9m diameter TST used a maximum element mesh size of 0.024m over the whole subdomain, with refinement on the blade root, middle and tip of 0.004m, 0.004m and 0.002m respectively. Six inflation layers were added around the turbine surface using a first layer thickness of 0.00075m with a growth rate of 1.0. This resulted in 3.1 million elements in the turbine subdomain.

A time step study was also carried out to investigate the effect it has on the propagation of waves. It was found that the optimum time step interval in wave-current simulations equated to the wave period divided by 50 ($T/50$). For simulations investigating the loadings on a turbine in current-only flow, a time equal to 5° of turbine rotation per time step was found to be optimal. For combined wave-current and turbine simulations, the smaller of the two time steps was used in order to satisfy both requirements, ie. $\leq 5^\circ$ per time step.

Two different CFD model types are widely used for simulating the TST performance in current-only flow conditions, a 'free slip' and a 'free surface' CFD model. A 3D numerical comparison was carried out to investigate the differences between the two CFD model configurations and how they affect the generated flow conditions and estimated turbine loadings. The thrust and torque of the turbine was measured in a transient analysis at angular velocities corresponding to a TSR of 0-7. The fundamental differences between the two CFD model configurations was in the prediction of the fluctuation in the transient results for the torque on an individual turbine blade. The fluctuation in the torque results for an individual turbine blade was much greater in the 'free surface' model type due to buoyancy forces incorporated into the 'free surface' model. Therefore, it was found that the typical 'free surface' CFD model reproduced the uniform current conditions and transient turbine component loadings better than the typical 'free slip' model. For these reasons, the typical 'free surface' CFD configuration is used in all following numerical simulations.

7 TURBINE PERFORMANCE UNDER CURRENT-ONLY CONDITIONS: UNIFORM AND PROFILED VELOCITY GRADIENTS

Through experimental and numerical investigation, this chapter establishes the performance characteristics of the TST, described in Chapter 4, under uniform and profiled current conditions at a range of angular velocities. The uniform current conditions are the simplest flow conditions presented in this thesis and therefore represent the 'base' case. Increasing levels of complexity are then added to the flow, such as profiled current flows, as well as the generation of regular waves which will be explored later in Chapter 9.

A CFD model comparison is then carried out using the 'free surface' type of model with uniform and profiled current velocity gradients. The differences between the generated uniform and profiled flow conditions are examined, as well as analysing the impact these conditions have on the turbine performance and loadings experienced. Experimental results are used to validate the numerical simulations.

The results are presented for the experimental data as well as the individual CFD model results. Initially the results are displayed for the experimental testing, examining the flow conditions and performance characteristics. Validation of the CFD results are then exhibited in the same way, after which a comparison is drawn between the CFD and experimental data sets, investigating both the flow conditions and the turbine performance characteristics.

7.1 EXPERIMENTAL RESULTS

Experimental results for both the uniform and profiled current flows are obtained from testing carried out at the IFREMER wave-current flume facility, with details on the experimental setup and procedure described in Chapter 4.

7.1.1 Turbine characterisation: uniform current flow

The velocity of the IFREMER flume was set to produce a uniform current velocity of 1.00 m/s as previous testing found that these flow characteristics were independent of Reynolds number above this velocity [156]. The turbine was operated at a range of angular velocities to generate a full set of performance curves for C_p , C_t and C_q . Table 7.1 shows the range of angular velocities used and the approximate corresponding TSRs.

TABLE 7.1. ANGULAR VELOCITIES USED TO CONTROL TURBINE ROTATION.

Turbine Angular Velocity, ω (rad/s)	Approximate TSR, λ
0.0	0
2.22	1
4.44	2
6.67	3
8.89	4
11.11	5
13.33	6
15.55	7

The velocity measurements were taken using 2D LDA situated 1m upstream of the turbine, as described in Chapter 4. Flow measurements were taken point by point through a water depth of 2m at depths of -0.55, -0.68, -0.81, -0.94, -1, -1.13, -1.26, -1.39 and -1.52 m from the SWL. Figure 7.1 shows the measured velocity profile through the water depth for the streamwise and vertical directions. The bars show the variation in the average velocity and represent +/- 1 standard deviation. The biggest difference between the maximum and minimum velocity over the water depth was 0.01 m/s in the streamwise direction and 0.02 m/s in the vertical direction. These magnitudes show how little difference there was in the velocity profile over the water depth and therefore gives the reasonable assumption that the streamwise and vertical velocity showed a uniform current profile. This was aided by flow straighteners placed in the upstream area of the flume. The volumetrically averaged velocity over the swept area of the turbine is 1.01 m/s and -0.03 m/s for the streamwise and vertical velocity, as shown in Table 7.2 using the calculation detailed in Section 3.3.5.

TABLE 7.2. VALUES FOR THE EXPERIMENTAL STREAMWISE AND VERTICAL VELOCITIES UNDER UNIFORM FLOW CONDITIONS.

Direction	Volumetrically averaged velocity over turbine swept area (m/s)
Streamwise (\bar{W}_{vol})	1.01
Vertical (\bar{V}_{vol})	-0.03

7 TURBINE PERFORMANCE UNDER CURRENT-ONLY CONDITIONS: UNIFORM AND PROFILED VELOCITY GRADIENTS

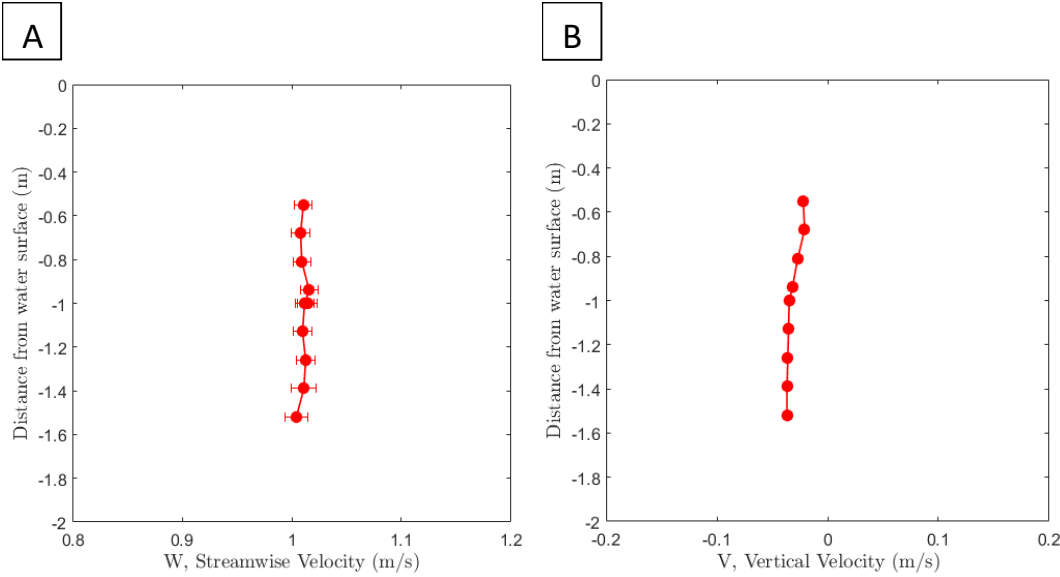


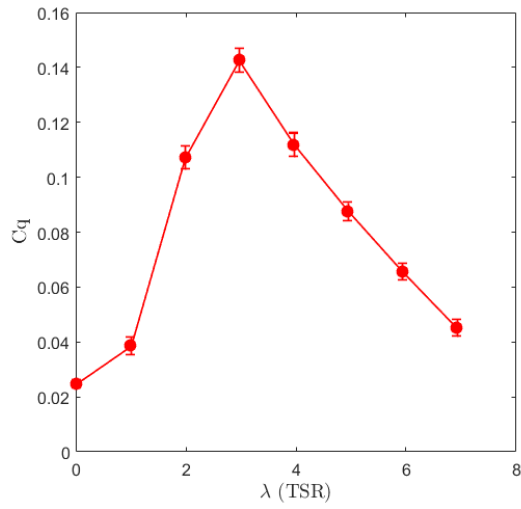
Figure 7.1. The A) streamwise and; B) vertical experimental velocity results through the water depth in uniform flow conditions. Bars show +/- 1 standard deviation.

The rotor thrust and torque were measured and used to calculate the power output by the turbine. The thrust, torque and power were then non-dimensionalised to give C_t , C_q and C_p at different TSRs. The calculations were carried out as detailed in Section 3.3, based upon the volumetrically averaged streamwise velocity over the swept area of the turbine, as recommended by [47]. Given that the LDA measurements were only obtained down the vertical centreline of the flume, it was assumed that the velocity profile through the water depth remained the same across the width of the flume that the turbine occupied. The volumetric flow rate was calculated for each water depth area with a different velocity to account for the difference in velocity over the depth of the turbine. Figure 7.2 shows that a peak C_q of 0.14 was reached at a TSR of 3, while peak C_t of 1.05 was at a TSR of 7, and peak C_p of 0.44 was at a TSR of 4. These values are summarised in Table 7.3.

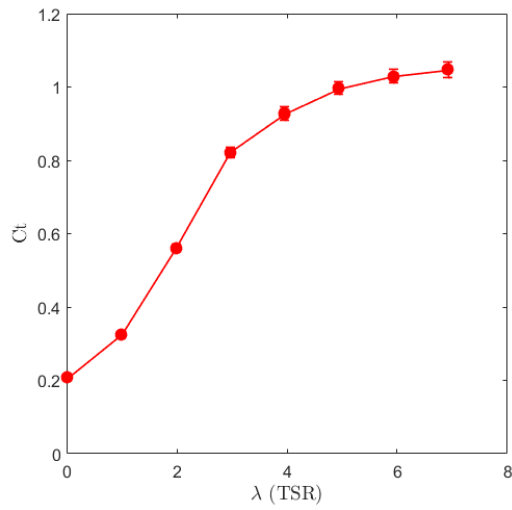
TABLE 7.3. VALUES FOR THE EXPERIMENTAL PEAK PERFORMANCE CHARACTERISTICS UNDER UNIFORM FLOW CONDITIONS.

Performance characteristic	Peak value	TSR
C_q	0.14	3
C_t	1.05	7
C_p	0.44	4

A



B



C

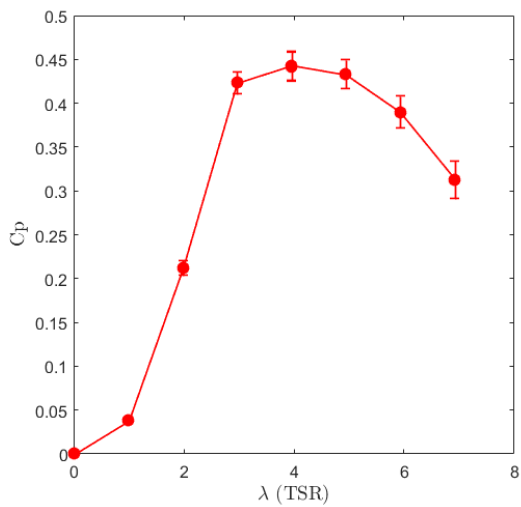


Figure 7.2. The experimental A) C_q , B) C_t and C) C_p over a range of TSRs for the turbine in uniform flow conditions. Bars show +/- 1 standard deviation.

7.1.2 Turbine characterisation: profiled current flow

A velocity profile developed through the water depth when the wave maker paddles were submerged into the top section of the IFREMER flume, producing a blockage. Without installation of the wave maker, the current flow was uniform. This chapter examines current-only flow conditions, and even though the wave maker was sat in the flume it was not operational. The wave maker could be positioned at two different locations which therefore produced two different velocity profiles, as depicted earlier by Figure 4.6. Profile 1 was generated by having the wave maker fully submerged in the top of the water column to a depth of 50cm (WM00), while Profile 2 was generated by raising the wave maker by 20cm so that it was only submerged in the top of the water column by 30cm (WM20). A summary of the wave maker settings and the respective profile names is given in Table 7.4, while further details on this setup is described in Chapter 4.

TABLE 7.4. SUMMARY OF EXPERIMENTAL WAVE MAKER SETTINGS AND THE RESPECTIVE PROFILE NAME.

Profile Name	Wave maker position	Distance wave maker is submerged in top of water column (cm)	Distance wave maker is raised from fully submerged position (cm)
Profile 1	WM00	50	0
Profile 2	WM20	30	20

As with the uniform current flow inlet velocity, the flume was set to produce a target flow velocity of 1.00 m/s before considering the effect of the velocity profile. The turbine angular velocities used for the uniform current flow cases (Table 7.1) were also used in the profiled current flow tests in order to isolate the differences between the two types of test and therefore examine the changes in the turbine performance when under uniform or profiled current conditions.

The LDA was situated 1m upstream of the turbine and measured points through the 2m water depth every 0.2m, between -0.4 and -1.6 m from the SWL. This covered the full diameter of the turbine which occupied a water depth between -0.55m and -1.45m from the SWL. Figure 7.3A shows the measured velocity profiles for Profile 1 and 2 through the water depth in the streamwise direction. The bars represent +/- 1 standard deviation and show the variation in the average velocity as a result of unsteadiness in the water due to vortex shedding in the flow from the stationary wave maker paddles. Both Profile 1 and 2 show a considerable reduction in the flow velocity towards the surface of the water due to the presence of the wave maker. Profile 1 shows a greater reduction in streamwise velocity near the surface when compared to the input flow velocity of 1.00 m/s. Profile 1 displays a

decrease in the streamwise velocity to 0.80 m/s in comparison to Profile 2 which has a reduction to only 0.92 m/s. Near the base of the flume, Profile 1 has an increased streamwise velocity of 1.07 m/s to account for the reduction near the surface, while Profile 2 maintains a velocity of 1.00 m/s near the base of the flume. The greatest difference between the maximum and minimum streamwise velocity over the water depth was 0.27 m/s for Profile 1 and 0.08 m/s for Profile 2. Profile 1 has a greater shear in the velocity through the water depth due to the wave maker being fully submerged in the top of the water column to a depth of 50cm. For Profile 2, the wave maker was raised to a depth of 30cm leading to less of a shearing effect through the water depth. The volumetrically averaged streamwise velocity over the swept area of the turbine is 1.00 m/s for Profile 1 and also 1.00 m/s for Profile 2, even though the shear velocity profiles are different between the two current flows, as shown in Table 7.5.

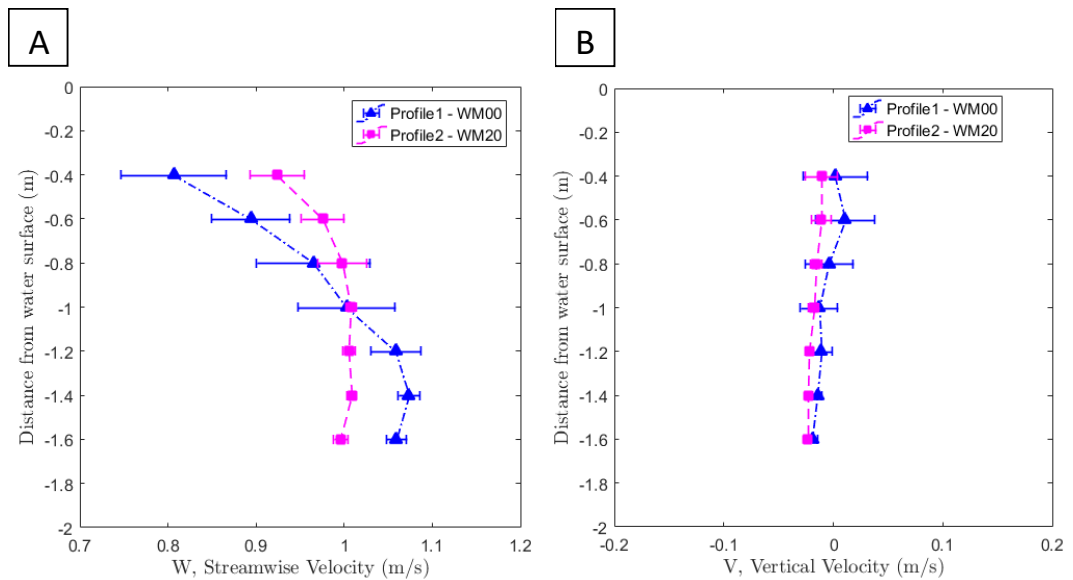


Figure 7.3. The A) streamwise and; B) vertical experimental velocity results through the water depth in 2 different profiled flow conditions. Bars show +/- 1 standard deviation.

TABLE 7.5. VALUES FOR THE EXPERIMENTAL STREAMWISE AND VERTICAL VELOCITIES UNDER PROFILED FLOW CONDITIONS.

	Direction	Volumetrically averaged velocity over turbine swept area (m/s)
Profile 1	Streamwise (\bar{W}_{vol})	1.00
	Vertical (\bar{V}_{vol})	-0.01
Profile 2	Streamwise (\bar{W}_{vol})	1.00
	Vertical (\bar{V}_{vol})	-0.02

Figure 7.3B shows the vertical velocity through the water depth for Profiles 1 and 2. These velocity measurements are comparable to the vertical velocity seen in the uniform

velocity profile. Both Profiles 1 and 2 show a constant velocity through the water depth with minor differences of 0.03 m/s for Profile 1 and 0.01 m/s for Profile 2 between the maximum and minimum velocities over the water depth. The volumetrically averaged vertical velocity over the swept area of the turbine is -0.01 m/s for Profile 1 and -0.02 m/s for Profile 2, which shows a generally uniform vertical velocity exists, as shown in Table 7.5.

The C_q , C_t , and C_p were found using the volumetrically averaged streamwise velocity to account for the differing velocity profiles over the swept area of the turbine. The mean centre line, depth averaged velocities alone would not give an accurate representation of the flow across the turbine due to the shearing effect, as shown in Table 7.6. This underestimation of the streamwise velocity would result in an increase in the performance characteristics and emphasises the importance of accurately estimating the inflow velocity to the TST.

TABLE 7.6. THE DIFFERENCE BETWEEN DEPTH AVERAGED AND VOLUMETRICALLY AVERAGED STREAMWISE VELOCITIES.

	Profile 1	Profile 2
Depth averaged streamwise velocity (m/s)	0.9799	0.9879
Volumetrically averaged streamwise velocity (m/s)	1.004	1.001
Difference (m/s)	0.0241	0.0131
Difference (%)	2.5	1.3

Figure 7.4 shows the C_q of the turbine at different TSRs under the flow conditions presented by Profile 1 (Figure 7.4A) and Profile 2 (Figure 7.4B). Similarly, Figure 7.5 shows the mean values for C_t while Figure 7.6 shows the C_p of the turbine at different TSRs. Repeated tests at a TSR of 4 and 7 are included in the performance characteristic graphs. The peak C_q was reached at a TSR of 3, while peak C_t was reached at a TSR of 7 and the peak C_p was reached at a TSR of 4. The mean values of each performance coefficient shows good agreement between Profiles 1 and 2. The maximum difference between the averaged results for each profile for C_q , C_t and C_p are 0.01, 0.04 and 0.02 respectively, as shown in Table 7.7. These differences are considered small especially as the mean values for each data set are within the limits of the bars of the opposite data set.

However, there is a significant difference in the standard deviation of the data sets for Profiles 1 and 2. Profile 1 has a much bigger standard deviation around the mean in comparison to Profile 2, for all performance characteristics. Profile 1 has an average standard deviation of 0.02, 0.1 and 0.08 for C_q , C_t and C_p respectively, while Profile 2 has an average standard deviation of 0.01, 0.03 and 0.03 respectively. The presence of the

wave maker fully submerged in the top section of the water column causes a high level of disturbance to the current flow. Raising the wave maker by 20cm in the water column reduces the level of unsteadiness in the flow which can clearly be seen in the difference of the standard deviations around the mean for each of the performance characteristics.

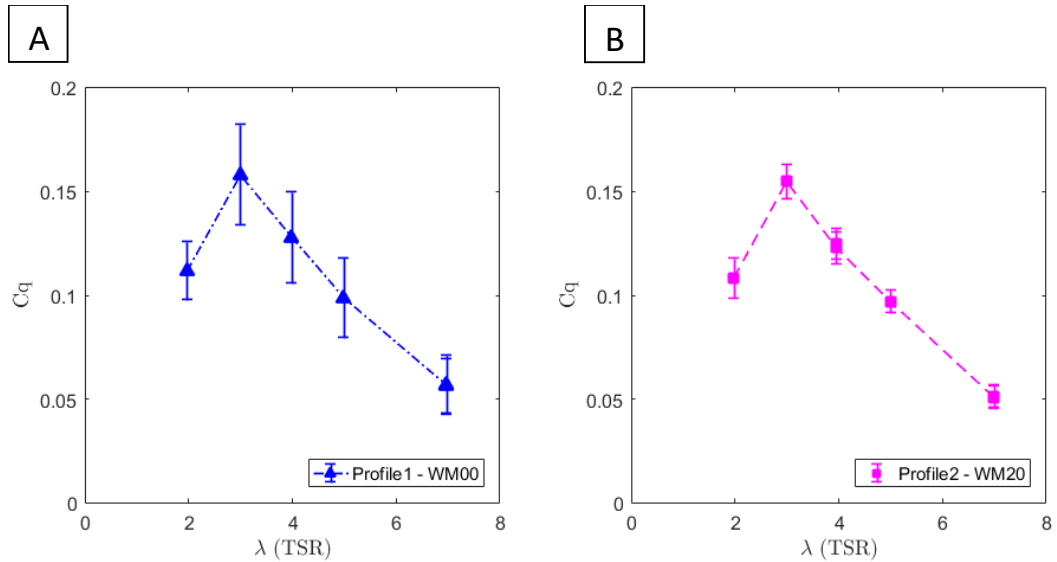


Figure 7.4. The experimental C_q over a range of TSRs for the turbine in flow conditions corresponding to: A) profile 1 and; B) profile 2. Bars show +/- 1 standard deviation.

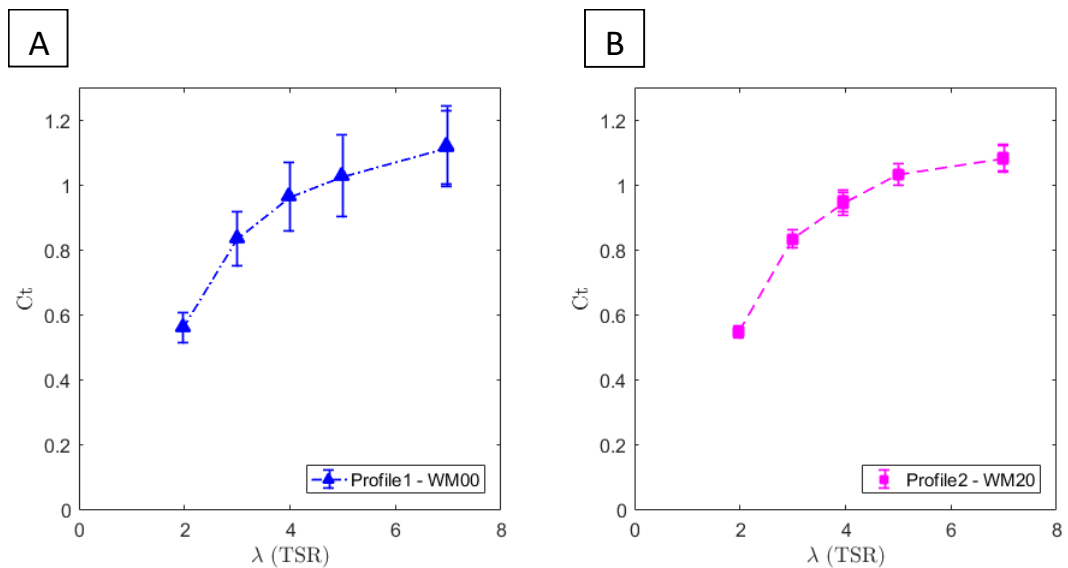


Figure 7.5. The experimental C_t over a range of TSRs for the turbine in flow conditions corresponding to: A) profile 1 and; B) profile 2. Bars show +/- 1 standard deviation.

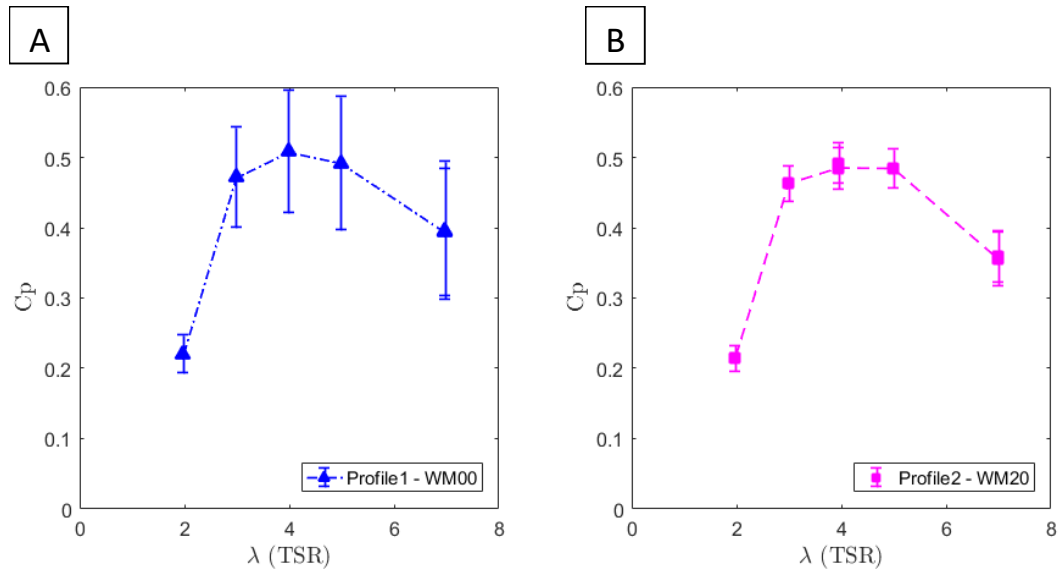


Figure 7.6. The experimental C_p over a range of TSRs for the turbine in flow conditions corresponding to: A) profile 1 and; B) profile 2. Bars show +/- 1 standard deviation.

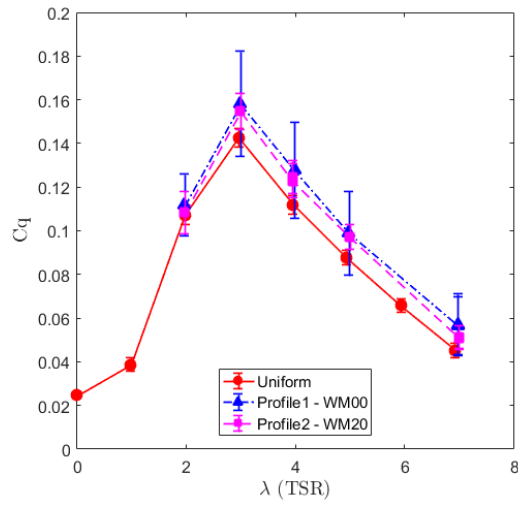
TABLE 7.7. VALUES FOR THE EXPERIMENTAL PEAK PERFORMANCE CHARACTERISTICS UNDER PROFILED FLOW CONDITIONS.

Performance characteristic	Profile 1	Profile 2	Difference
C_q	0.16	0.15	0.01
C_t	1.12	1.08	0.04
C_p	0.51	0.49	0.02

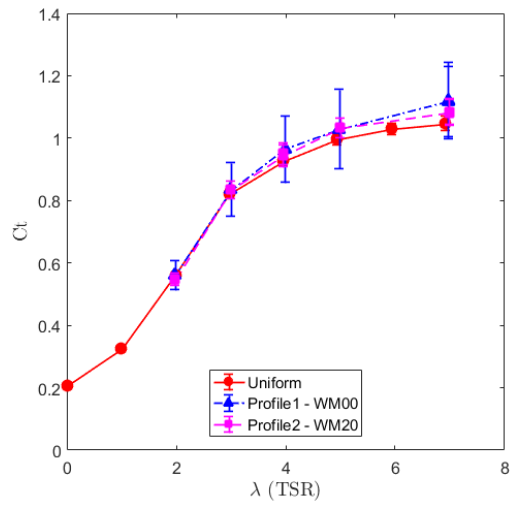
7.1.3 Uniform and profiled comparison

The performance characteristics for Profiles 1 and 2 show good agreement between their experimental average values at all TSRs. When compared to the uniform flow results, as shown in Figure 7.7, the average performance characteristics for the profiled velocity cases show consistently higher values than for the uniform case. There is a greater difference between the uniform and profiled results for C_p and C_q , while C_t shows better agreement between the types of flow condition. Table 7.8 shows the main parameters used to calculate the C_p and C_q at a TSR of 4 as analysis of these parameters can indicate where the larger differences between data sets exist. The \bar{W}_{vol} is a significant term as it is cubed and squared in the calculation for C_p and C_q respectively. The uniform case has the greatest \bar{W}_{vol} while Profiles 1 and 2 are similarly smaller. It would therefore be expected that the torque experienced by the turbine is greatest for the case with the highest \bar{W}_{vol} , however, this is not the case. Profile 1 has the greatest average torque, followed by Profile 2, while the uniform case has the smallest average torque value.

A



B



C

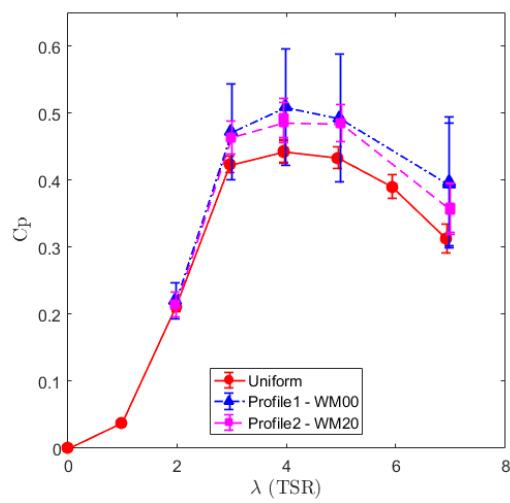


Figure 7.7. The A) C_q , B) C_t and C) C_p for the experimental results in uniform and profiled flow conditions. Bars show +/- 1 standard deviation.

TABLE 7.8. AVERAGE PARAMETERS USED TO CALCULATE THE C_p AND C_q AT TSR 4.

Average parameter	Uniform	Profile 1	Profile 2
Torque, \bar{Q} (Nm)	16.37	18.31	17.63
Angular velocity, $\bar{\omega}$ (rad/s)	8.888	8.887	8.794
Volumetrically averaged streamwise velocity, \bar{W}_{vol} (m/s)	1.011	1.004	1.001

Due to the discrepancies shown in Table 7.8, an investigation into the time series that contribute to the overall volumetrically averaged streamwise velocity was carried out. Figure 7.8 displays histograms of the LDA time series collected at different locations throughout the water depth in each of the 3 types of flow condition. Table 7.9 details the corresponding water depth that each histogram represents. A histogram provides information on the distribution of a data set and displays the shape and spread of the results. If the data is normally distributed, then it appears as a bell curve and is symmetric about the mean, as shown in Figure 7.9. This shows that data near the mean are also more frequent in occurrence, with the value that appears most often known as the mode of the distribution. In a normal distribution, the mean and mode occur at the same value. The histograms for the uniform flow cases are shown in Figure 7.8A. Each histogram shows a normal distribution with the mean and mode values within 0.5% of each other at all water depths.

Figure 7.8B and C show the histograms for Profiles 1 and 2 created using Matlab. Initially looking at Figure 7.8Bi) and Ci), which are positioned at a depth of -0.4m from the SWL, it is clear to see that the data is not normally distributed. In fact, the modal values are 24% and 6% greater than the mean values at these positions nearest the water surface for Profile 1 and 2 respectively. These differences, shown in Table 7.10, are a result of extreme values dragging the mean to the left side of the distribution and exhibiting a negative skew. This signifies that the most frequently occurring streamwise velocity (mode) is not in the same location as the central value of the data set (mean). For the region over which the turbine is present, -0.55m to -1.45m, the difference between the mean and mode is 15% to 0.1% for Profile 1, and 4% to 1% for Profile 2, with the greater differences observed towards the surface in the water column. For Profile 1 the data sets remain negatively skewed most of the way from the SWL to a water depth of -1.4m, as shown in Figure 7.8Biv). At this point, the data seems to be more normally distributed with the mean and mode converging showing a difference of only 0.3%. Profile 2 follows this same trend showing normally distributed data at a depth below -0.8m from the SWL, with the mean and mode values showing a difference < 0.8%.

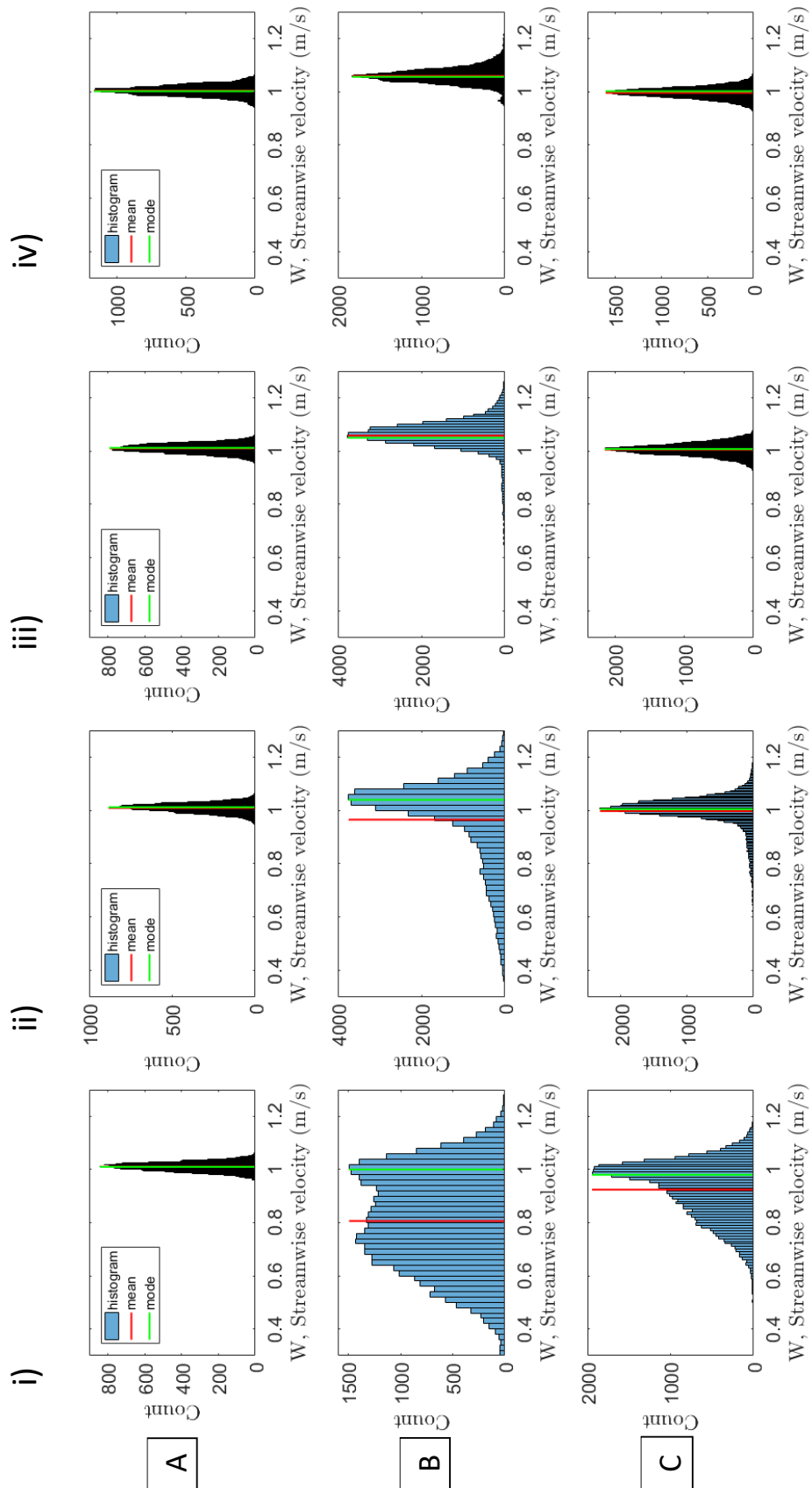


Figure 7.8. Histograms showing the mean and mode of each experimental data set for A) uniform, B) profile 1 and C) profile 2 flow conditions. From i) to iv), each histogram corresponds to LDA data taken at a specific water depth as shown in Table 7.9.

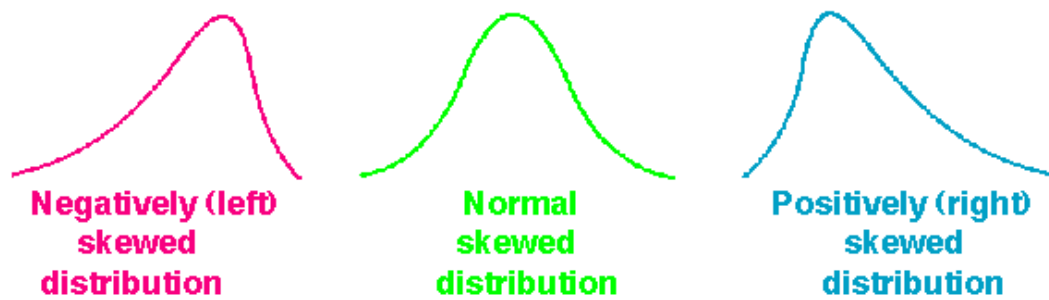


Figure 7.9. Examples of normally distributed and skewed distributions.

TABLE 7.9. CORRESPONDING LDA WATER DEPTH FOR EACH HISTOGRAM.

Position	Corresponding water depth from SWL (m)		
	Uniform	Profile 1	Profile 2
i)	-0.55	-0.4	-0.4
ii)	-0.81	-0.8	-0.8
iii)	-1.13	-1.2	-1.2
iv)	-1.52	-1.6	-1.6

TABLE 7.10. THE MEAN, MODE AND DIFFERENCE OF EACH HISTOGRAM DISPLAYED IN FIGURE 7.8.

Type of flow	Location	Average streamwise velocity, \bar{W}			
		Mean (m/s)	Mode (m/s)	Difference	
				(m/s)	(%)
Uniform	i)	1.011	1.010	0.001	0.1
	ii)	1.009	1.012	0.003	0.3
	iii)	1.010	1.012	0.002	0.2
	iv)	1.004	1.002	0.002	0.2
Profile 1	i)	0.806	1.000	0.194	24
	ii)	0.965	1.040	0.075	8
	iii)	1.058	1.050	0.008	0.8
	iv)	1.059	1.056	0.003	0.3
Profile 2	i)	0.924	0.980	0.056	6
	ii)	0.998	1.005	0.007	0.7
	iii)	1.006	1.008	0.002	0.2
	iv)	0.996	1.002	0.006	0.6

For negatively skewed data, the mean value is not representative of the predominant flow conditions at a specific water depth as it is the mode which is the most frequently occurring streamwise velocity. To account for the differences in the distributions, the volumetrically averaged streamwise velocities were recalculated using the modes instead of the mean values, as shown in Table 7.11. There is little difference for the uniform case due to the fact the data is normally distributed. However, profile 2 gives a 0.3% difference when using the mode to calculate the \bar{W}_{vol} , while profile 1 shows a 4% difference.

TABLE 7.11. THE VOLUMETRICALLY AVERAGED STREAMWISE VELOCITY CALCULATED USING THE MEAN AND MODE.

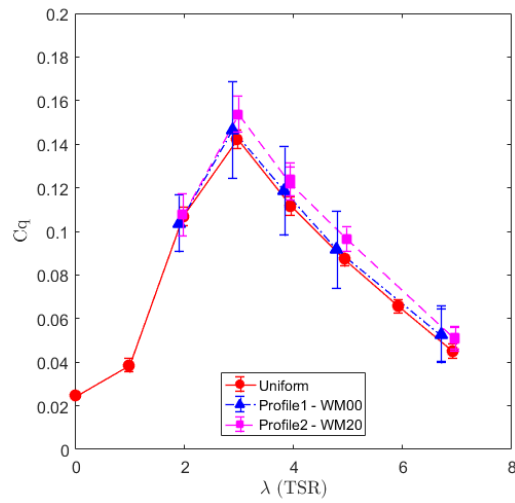
	Volumetrically averaged streamwise velocity over turbine swept area (\bar{W}_{vol}), calculated using...		Difference	
	Mean (m/s)	Mode (m/s)	(m/s)	(%)
Uniform	1.011	1.012	0.001	0.1
Profile 1	1.004	1.042	0.038	4
Profile 2	1.001	1.004	0.003	0.3

The performance characteristics were then also recalculated as shown in Figure 7.10. There is a noticeable change in the performance characteristics for Profile 1 showing between 8-12% difference when using the mean or mode value in the volumetrically averaged streamwise velocity calculation. The results for Profile 1, using the mode, now show good agreement with the uniform flow case which showed a negligible difference of 0.2% between the two different methods used. Profile 2 showed differences < 1% between using the mean and mode in the volumetrically averaged streamwise velocity calculation and remains marginally greater in all performance characteristics than the results for the other flow conditions.

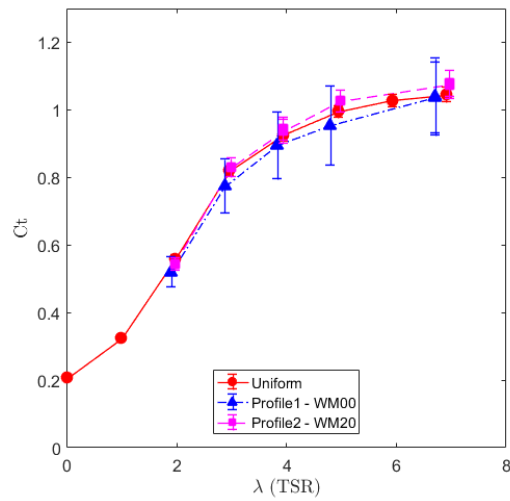
These results show that the distribution of the velocity data sets can have a very significant effect on the calculation of the performance characteristics using the mean value. The mode is the most frequently occurring value in the data set and it is therefore recommended to be used in all following flow analyses as this value is more representative of skewed data sets but remains the same as the mean value in normally distributed data sets.

7 TURBINE PERFORMANCE UNDER CURRENT-ONLY CONDITIONS: UNIFORM AND PROFILED VELOCITY GRADIENTS

A



B



C

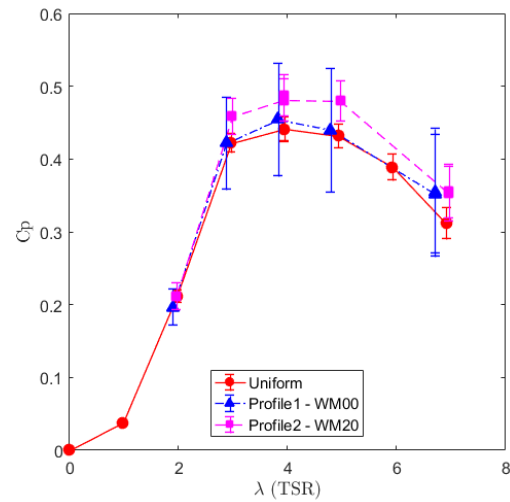


Figure 7.10. The A) C_q , B) C_t and C) C_p for the experimental results in uniform and profiled flow conditions, recalculated using the mode instead of the mean for the \bar{W}_{vol} . Bars show +/- 1 standard deviation.

7.2 CFD MODEL VALIDATION

CFD models were developed to replicate the experimental testing carried out at IFREMER, as mentioned in the previous Section 7.1. Initially, a ‘free surface’ model was created as it was found that the ‘free slip’ model neglects vital components necessary to provide an accurate estimation of the transient turbine loadings, as detailed in Chapter 6, Section 6.3. The ‘free surface’ model was better suited for the engineering applications used in this thesis and so all following CFD models use the ‘free surface’ model configuration. The ‘free surface’ model was used to reproduce the uniform current conditions obtained at the IFREMER flume, progressing to profiled current flows to analyse the difference these conditions have on the loadings and performance of the turbine.

The general development of the CFD models for both the main fluid domain and the turbine subdomain is provided in Chapter 5, while specific details are provided in this chapter.

7.2.1 Uniform flow CFD models

7.2.1.1 *Geometry, mesh, setup summary*

The ‘free surface’ model is based on the IFREMER testing facility to allow comparisons to be made between the numerical CFD and experimental data sets. The mesh was developed using a mixture of HEXA and TETRA meshing methods, with the same final mesh as shown in Table 6.6. A setup summary is also detailed in Chapter 6 but is replicated in Table 7.12 for ease of reading. The simulation was set up as a transient analysis with a uniform current-only flow of 1.00 m/s to replicate the experimental flow velocity. The angular velocity of the turbine was controlled using the same angular velocities as in the experimental testing (Table 7.1). The time step of the simulation was controlled using a time step of Δt_{turb} which equates to 1 time step every 5° of rotation of the turbine, as described in Chapter 6. Stability in the model occurred after 40-50 seconds and so all results reported in this study were taken after this time period. Monitor points were placed in the centre of the domain, 2m upstream of the turbine at locations between $y = -0.1\text{m}$ and $y = -1.9\text{m}$. This enabled a visualisation of the turbine inflow conditions to be achieved.

7 TURBINE PERFORMANCE UNDER CURRENT-ONLY CONDITIONS: UNIFORM AND PROFILED VELOCITY GRADIENTS

TABLE 7.12. SUMMARY OF THE GEOMETRY, MESH AND SETUP FOR A 'FREE SURFACE' UNIFORM FLOW CFD MODEL.

Geometry			
Main domain dimensions	Length x Width x Depth	20 x 4 x 2.86 m	
Subdomain cylinder dimensions	Diameter / Width	1.3 / 0.4 m	
Turbine dimensions	Diameter	0.9 m	
Mesh			
Main domain element sizing	Air-water interface region	$\Delta y = 0.01$ m $\Delta z = 0.03$ m $\Delta x = 0.025$ m	
	Mesh expansion from interface towards the 'top' boundary (Δy)	0.01 \rightarrow 0.1 m	
	Mesh expansion from interface towards the 'base' boundary (Δy)	0.01 \rightarrow 0.09 m	
	Mesh expansion from centreline to 'side walls' (Δx)	0.02 \rightarrow 0.08 m	
	Mesh expansion from 'inlet' boundary to 'outlet' (Δz)	0.05 \rightarrow 0.1 m	
	Sub domain element sizing	MFR cylinder	0.024 m
Prism layer properties	Blade tip	0.002 m	
	Blade middle	0.004 m	
	Blade root	0.004 m	
	Hub	0.006 m	
	First layer thickness	0.00075 m	
Total number of elements	Number of layers	6	
	Growth rate	1.0	
	Total	7.4 million	
Setup			
Time step	Δt_{turb} (see Equation (6.2))		
Fluid Phases present	Water and air (multiphase)		
Buoyancy model	On		
Boundary conditions	inlet	Velocity-inlet	
	Flow type	Uniform current-only flow	
	Input velocity components	U:	0 m/s
		V:	0 m/s
		W:	1.0 m/s
	outlet	Pressure-outlet	
	Reference pressure	$P_{ref} = (\rho_{water} - \rho_{air}) \cdot g \cdot (h - y)$	
	Side walls and base	No-slip wall	
	Top	Pressure-opening	
	Relative pressure	$P_{rel} = 0$ Pa	
Stanchion	No-slip wall		
Hub and turbine blades	No-slip wall		

7.2.1.2 Uniform flow CFD model validation

Figure 7.11 shows a comparison of the performance coefficients between the experimental results and the ‘free surface’ CFD model results. The bars on the experimental data represent +/- 1 standard deviation. Repeats of the CFD model results are included at a TSR of 4 with the performance and flow results presented in Table 7.13.

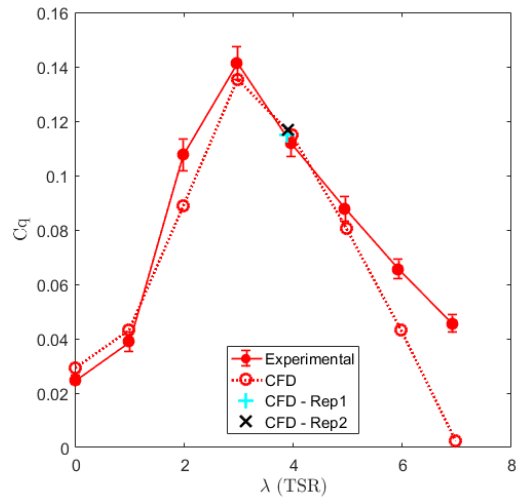
TABLE 7.13. RESULTS FOR THE ‘FREE SURFACE’ UNIFORM FLOW CFD MODELS AND EXPERIMENTAL DATA AT TSR 4.

	Model name			Experimental
	CFD	CFD - Rep1	CFD - Rep2	
Volumetrically averaged streamwise velocity over swept area of turbine, \overline{W}_{vol} (m/s)	1.00	1.02	1.02	1.01
TSRs tested, λ	0-7	4	4	0-7
Angular Velocity at $\lambda \approx 4$, ω (rad/s)	8.888	8.793	8.887	8.888
C_q at $\lambda \approx 4$	0.115	0.115	0.117	0.112
C_t at $\lambda \approx 4$	1.001	0.990	0.982	0.928
C_p at $\lambda \approx 4$	0.457	0.448	0.457	0.443

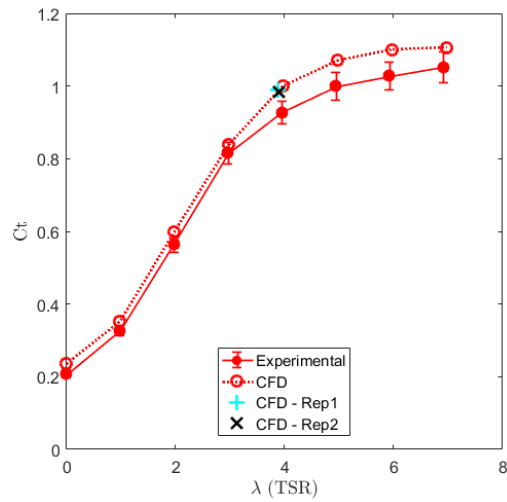
Initially looking at Figure 7.11C, the numerical results for C_p show good agreement with the experimental data up to a TSR of 5, with differences between the data sets of < 0.04. At higher TSRs, the CFD model results drop off a lot quicker than the experimental values, with differences in C_p of < 0.3. Similarly, Figure 7.11A shows a similar pattern with agreement in the results for C_q at TSR < 5 and divergence occurring at TSR > 5. The C_t results of the CFD models are consistently overpredicted in comparison to that of the experimental results. These CFD results are elevated above the experimental results by 0.04 at TSR < 3, increasing to 0.09 at higher TSRs. A possible explanation for this divergence, observed in all the performance coefficients at higher TSRs, is that there are inaccuracies in modelling the boundary layer [110]. As the angular velocity increases at higher TSR values, the flow conditions become more complex and therefore it is possible that flow separation is occurring in a less refined part of the mesh due to the angle of attack changing with the angular velocity. For the purpose of this work, the focus of the CFD-experimental comparison is 3<TSR<5. It has been shown in Section 7.1 that peak power occurs at a TSR of 4 and therefore to achieve optimum operating conditions, the turbine would ideally be operating within this region. Therefore, the CFD models for uniform flow provide a good prediction of the performance characteristics at 3<TSR<5 in comparison to the results obtained experimentally.

7 TURBINE PERFORMANCE UNDER CURRENT-ONLY CONDITIONS: UNIFORM AND PROFILED VELOCITY GRADIENTS

A



B



C

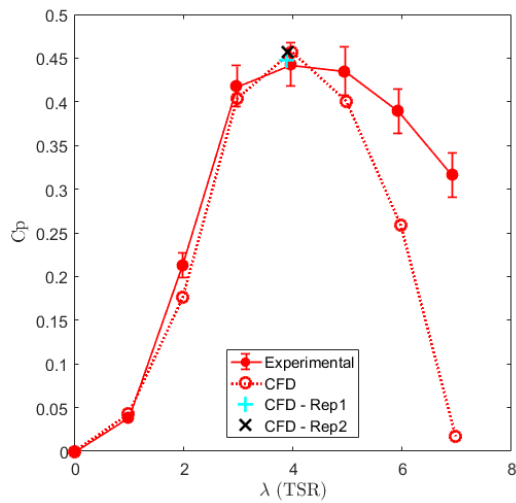


Figure 7.11. The A) C_q , B) C_t and C) C_p over a range of TSRs for the experimental and ‘free surface’ CFD model results in uniform flow conditions. Bars show +/- 1 standard deviation.

7.2.2 Profiled flow CFD models

As described in Section 7.1.2, the experimental facility at IFREMER could create two different velocity profiles dependent on the position of the wave maker. CFD models were developed to replicate these conditions with Profile 1 referring to the wave maker being fully submerged (WM00) and generating the biggest shear velocity profile across the turbine swept area, and Profile 2 referring to the wave maker being raised by 20cm (WM20) resulting in less of a shear velocity profile across the turbine swept area. The general development of the CFD model is detailed in Chapter 6, however, the following section provides the specific settings used in these profiled flow CFD models.

7.2.2.1 *Geometry, mesh, setup summary*

The geometry and mesh of the two ‘free surface’, profiled flow models are the same as those used for the uniform flow model, Section 7.2.1.1, Table 7.12. The only difference is that these models generate a profiled streamwise velocity at the inlet of the fluid domain instead of a uniform streamwise velocity. These profiled flow models use the same volumetrically averaged streamwise velocity as the uniform flow velocity models (1.00 m/s), in order to directly identify the implications, for the loadings and performance of the turbine, of having a uniform or profiled current velocity. Instead of using cartesian velocity components to input the velocity, the profile is input using the ‘Profile Method’ which creates a new boundary condition at the inlet. This method is based upon interpolated values from a data file containing the current profiles obtained from the experimental testing at IFREMER. More details on generating the boundary profile can be found in Section 5.4.3.1.1.

The time step of the simulation was controlled in the same way as the uniform flow velocity models previously discussed. The location of the monitor points in the domain was also replicated from the uniform flow velocity model, and stability in the model again occurred after 40 – 50 seconds. Due to the computational expense of accurately modelling the boundary velocity profile, only a single simulation for each profile could be executed. Therefore, the settings required to achieve peak power at a TSR of 4 were used. A summary of the specific setup conditions are detailed in Table 7.14.

TABLE 7.14. SUMMARY OF THE GEOMETRY, MESH AND SETUP FOR THE 'FREE SURFACE' PROFILED FLOW CFD MODEL.

Geometry		
(see Table 7.12)		
Mesh		
(see Table 7.12)		
Setup		
Time step	Δt_{turb} (see Equation (6.2))	
Fluid Phases present	Water and air (multiphase)	
Buoyancy model	On	
Boundary conditions	inlet	Velocity-inlet (Profile Method)
	Flow type	Profiled current-only flow
	Input velocity components	U: Inlet.Water.Velocity $u(x,y,z)$ V: Inlet.Water.Velocity $v(x,y,z)$ W: Inlet.Water.Velocity $w(x,y,z)$
	outlet	Pressure-outlet
	Reference pressure	$P_{ref} = (\rho_{water} - \rho_{air}) \cdot g \cdot (h - y)$
Side walls and base	No-slip wall	
Top	Pressure-opening	
Relative pressure	$P_{rel} = 0 Pa$	
Stanchion	No-slip wall	
Hub and turbine blades	No-slip wall	

7.2.2.2 Profiled flow CFD model validation

A comparison of the CFD and experimental flow conditions and turbine data was carried out to assess the ability of the CFD model to reproduce the profiled conditions measured during the experimental testing carried out at IFREMER. Figure 7.12 shows the experimental and CFD model results for the streamwise and vertical velocities given by Profiles 1 and 2. The streamwise velocity results show good agreement between the CFD and experimental data sets, confirming that the velocity profile imposed at the inlet has been maintained in the flow, and therefore applying the appropriate boundary conditions at the turbine location. The maximum difference between experimental and CFD results is 0.022 m/s for Profile 1 and 0.018 m/s for Profile 2 at a depth of -0.6 m from the SWL, which are both within 2% of the volumetrically averaged streamwise velocity over the swept area of the turbine for each profile. The difference between the experimental and CFD results for the volumetrically averaged streamwise velocity over the swept area of the turbine is 0.01 m/s for Profile 1 and 0.007 m/s for Profile 2. These values are both < 1% of the volumetrically averaged streamwise velocity over the swept area of the turbine, as shown in Table 7.15.

The vertical velocity results show a maximum difference between the experimental and CFD data sets of 0.02 m/s for Profile 1 and 0.024 m/s for Profile 2, both at a depth of -1.6 m

from the SWL. This is again within 2% of the volumetrically averaged streamwise velocity over the swept area of the turbine for each velocity profile. Even though the differences between the vertical velocity results are small, the CFD model doesn't seem to develop the same profile as the experimental results at all. At each depth the vertical velocity in the CFD model for both profiles is 0.00 m/s while the experimental results fluctuate between -0.02 m/s and 0.01 m/s. The streamwise velocity dominates the flow field and therefore variations in the vertical velocity, input at the inlet, have disappeared by the time the flow is measured 1m upstream of the turbine location. The fluctuations in the experimental vertical velocity could be due to intrinsic flume turbulence as well as particles in the flow interfering with the flow measurement equipment; features which cannot be replicated in the CFD model.

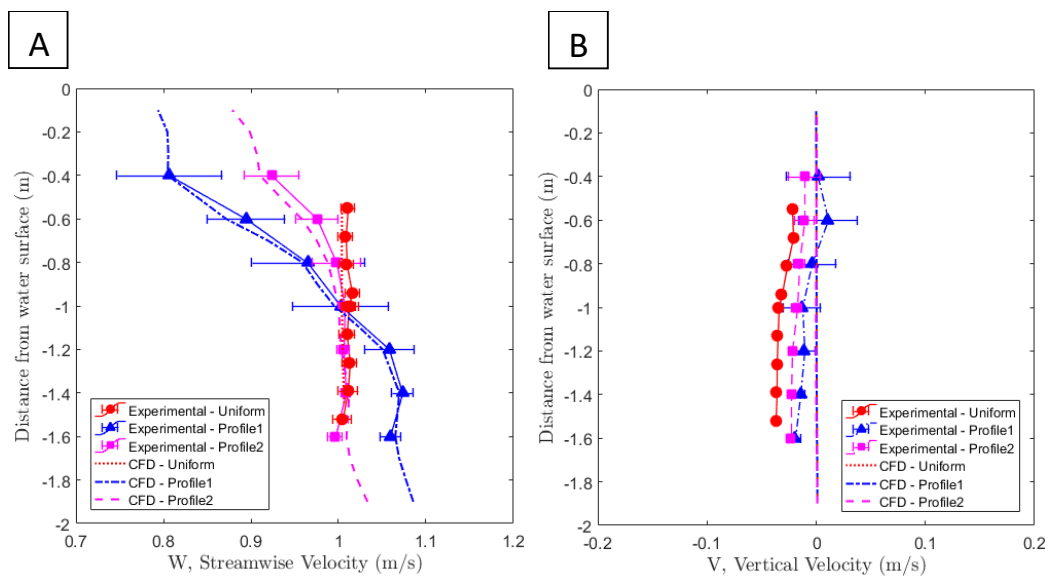


Figure 7.12. The A) streamwise and; B) vertical, CFD and experimental velocity results through the water depth for different flow conditions. Bars show +/- 1 standard deviation.

TABLE 7.15. VOLUMETRICALLY AVERAGED STREAMWISE VELOCITY IN PROFILED FLOW CONDITIONS FOR THE EXPERIMENTAL AND CFD MODEL RESULTS.

Profile	Volumetrically averaged streamwise velocity over swept area of the turbine, \bar{W}_{vol} (m/s)	
	Experimental	CFD
Profile 1	1.04	0.99
Profile 2	1.00	0.99

It is clear to see the different current flow conditions from looking at the streamwise velocities in Figure 7.12A. Figure 7.13 gives a visual representation of the streamwise velocities over the model domain for the conditions generated by uniform, Profile 1 and

7 TURBINE PERFORMANCE UNDER CURRENT-ONLY CONDITIONS: UNIFORM AND PROFILED VELOCITY GRADIENTS

Profile 2. Looking specifically at the top half of the water column, Profile 1 shows the biggest shearing effect for the streamwise velocity while Profile 2 is between that and the uniform flow conditions. The bottom half of the water column still shows Profile 1 as having the greatest shearing effect; however, this is not as severe as it is in the top half of the water column. Profile 2 and the uniform flow case follow the same trend which exhibits steady, uniform behaviour in the bottom half of the water column.

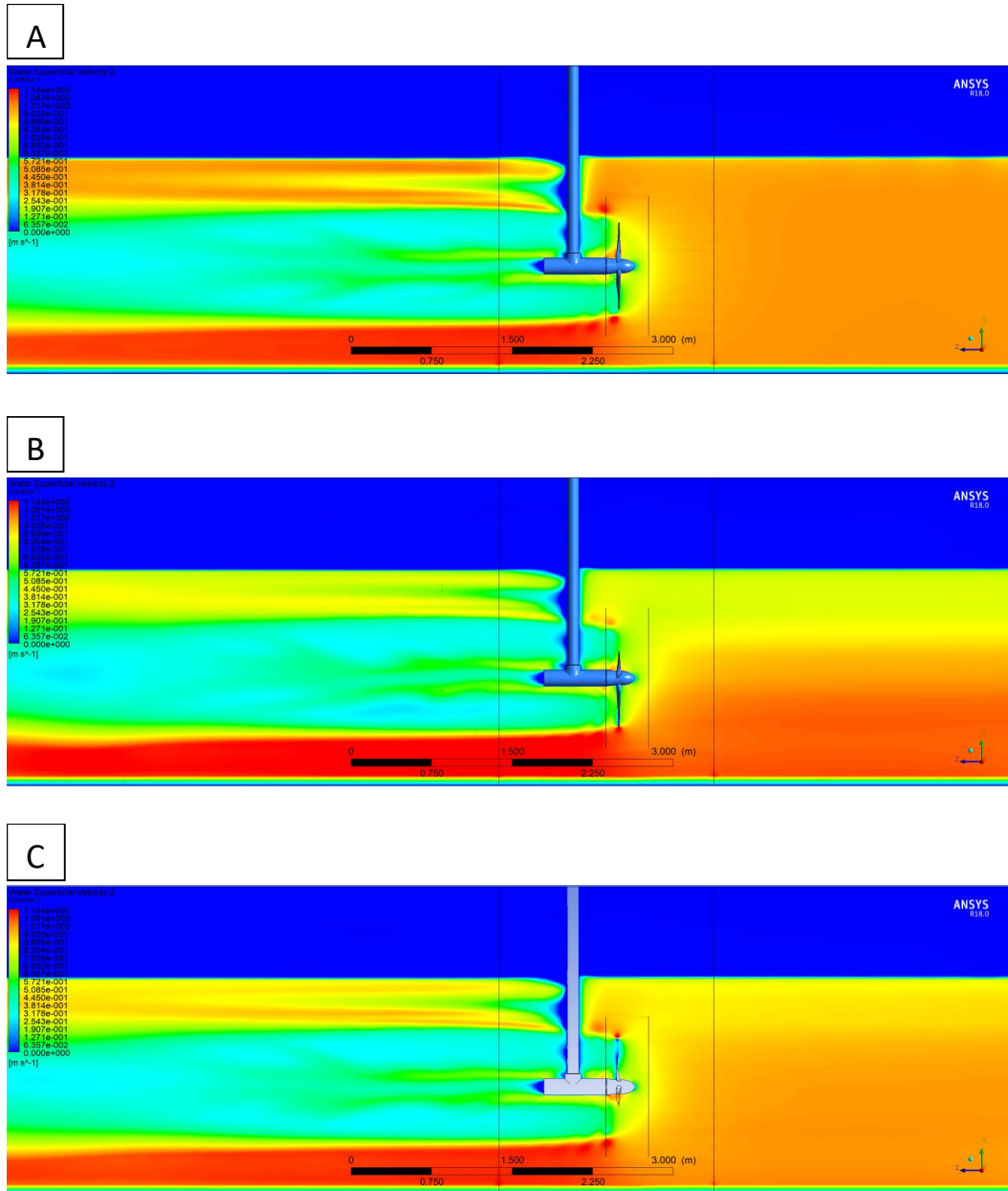


Figure 7.13. The streamwise velocity when the turbine is operating at a TSR of 4 for the inlet current conditions representative of: A) uniform, B) Profile 1, and C) Profile 2.

As well as changes in the average streamwise velocity for each flow condition at different depths through the water column, there are clearly differences in the variance in the data at these locations for each current condition. The bars on the experimental data in Figure 7.12 represent +/- 1 standard deviation which provides 68% confidence that all the data lies within these bounds around the mean value. A high standard deviation indicates a higher amount of variation in the data set.

Experimentally, the uniform current case has an average standard deviation of 0.009 m/s around the mean value. This is consistent throughout the water depth showing that similar conditions are present all the way through the water column. There is a greater standard deviation in the results nearest the surface of the water, with Profiles 1 and 2 showing 0.060 m/s and 0.030 m/s respectively, while the smallest standard deviation was towards the base of the flume, with Profiles 1 and 2 giving 0.012 m/s and 0.008 m/s respectively. This shows that due to the presence of the wave maker, there is more unsteadiness in the flow near the surface and therefore a greater standard deviation in the results. The standard deviation decreases towards the base of the flume where the influence of the wave maker is less prominent. The experimental data gives volumetrically averaged streamwise velocities of 1.01 m/s, 1.04 m/s and 1.00 m/s, while the CFD results give 1.00 m/s, 0.99 m/s and 0.99 m/s for the uniform, Profile 1 and Profile 2 current cases, respectively, to 2 decimal places.

As shown in Figure 7.12B, the vertical velocities show a similar trend with the standard deviations. The uniform current case shows a constant standard deviation throughout the water column while Profiles 1 and 2 show greater variation with a higher standard deviation towards the surface of the water, decreasing towards the base of the flume. However, the average vertical velocity results at each location through the water depth show generally uniform current velocities for the uniform and profiled cases. The experimental data gives a volumetrically averaged vertical velocity of -0.03 m/s, -0.01 m/s and -0.02 m/s, while the CFD results all give 0 m/s for the uniform, Profile 1 and Profile 2 current cases.

Overall, all the differences in velocity are < 2% of the volumetrically averaged streamwise velocity and so the CFD model is therefore capable of reproducing the streamwise and vertical velocity profiles as recorded experimentally at the IFREMER flume to the required accuracy.

The time taken to run a model for a single TSR in profiled flow conditions was 1207 hours for Profile 1 and 852 hours for Profile 2. Due to this extensive simulation time, these profiled flow conditions were only modelled at a TSR of 4, peak power conditions, and other TSRs were not investigated. Therefore, a comparison is made between experimental and CFD model results at a TSR of 4, but the author is aware a wider range of TSRs would provide better reliability in the comparison of results.

Figure 7.14 shows the C_q , C_t and C_p for the experimental results over a range of TSRs and the CFD results at a TSR of 4 for the different flow conditions. The performance characteristics estimated by the CFD models for both profiled flow conditions show good agreement with the experimental results, lying within 1 standard deviation of the mean for all performance characteristics. Table 7.16 shows the average experimental and CFD results for each performance characteristic as well as the difference between them. As previously mentioned, the mode of the streamwise velocity at each water depth was used to calculate the \bar{W}_{vol} instead of the mean due to the negative skew present in the experimental data.

TABLE 7.16. THE EXPERIMENTAL RESULTS, CFD MODEL RESULTS, AND THE DIFFERENCE BETWEEN THEM FOR C_q , C_t AND C_p , IN PROFILED FLOW CONDITIONS.

Profile	C_q			C_t			C_p		
	Exp.	CFD	Dif.	Exp.	CFD	Dif.	Exp.	CFD	Dif.
Profile 1	0.118	0.113	0.006	0.895	1.000	0.105	0.455	0.454	0.001
Profile 2	0.122	0.113	0.009	0.938	0.992	0.054	0.481	0.449	0.032

To further validate the CFD models in uniform and profiled current conditions, the out of plane bending moments (BM x) on the turbine blades were compared as this data was available from the experimental testing at IFREMER. A single turbine blade was analysed as the same trends were present on each of the three individual blades. Figure 7.15 shows the experimental results for the BM x on a single blade in each of the different current conditions, while Figure 7.16 shows the equivalent CFD results. The time series of the experimental results are much more unsteady than the CFD results, due to the presence of unsteady flow features such as turbulence in the flow, as well as unwanted noise interfering with the measurement signal. The greater unsteadiness makes it more difficult to directly compare the experimental and CFD time series. An initial comparison analysing the average BM x showed good agreement between the data sets, as shown in Table 7.17.

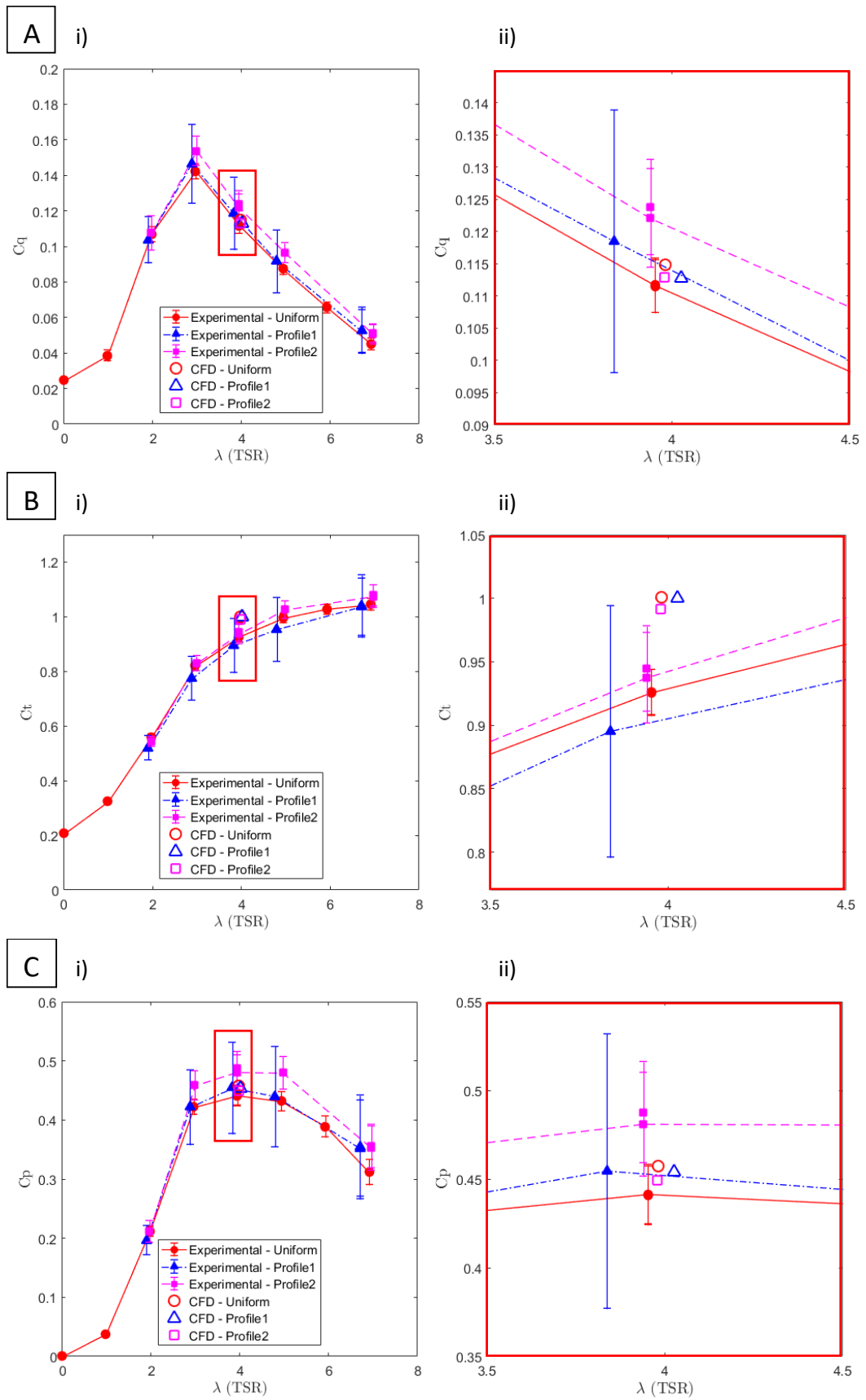


Figure 7.14. The Ai) C_q , Bi) C_t and Ci) C_p for the experimental and CFD results in different flow conditions, with a zoomed in version of TSR 4 in ii). Bars show +/- 1 standard deviation.

7 TURBINE PERFORMANCE UNDER CURRENT-ONLY CONDITIONS: UNIFORM AND PROFILED VELOCITY GRADIENTS

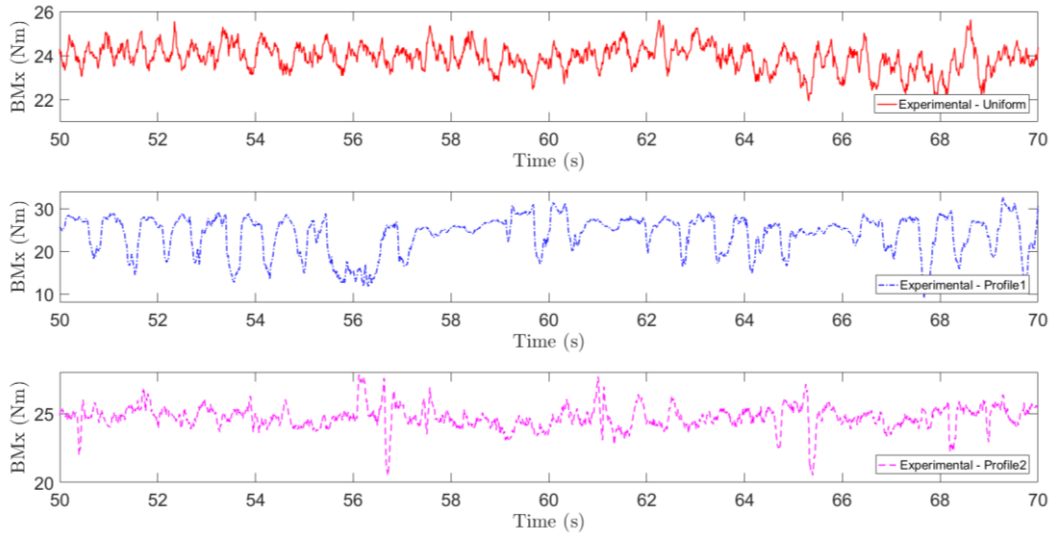


Figure 7.15. The experimental results for the out of plane bending moment on a single blade in uniform, Profile 1 and Profile 2 current conditions.

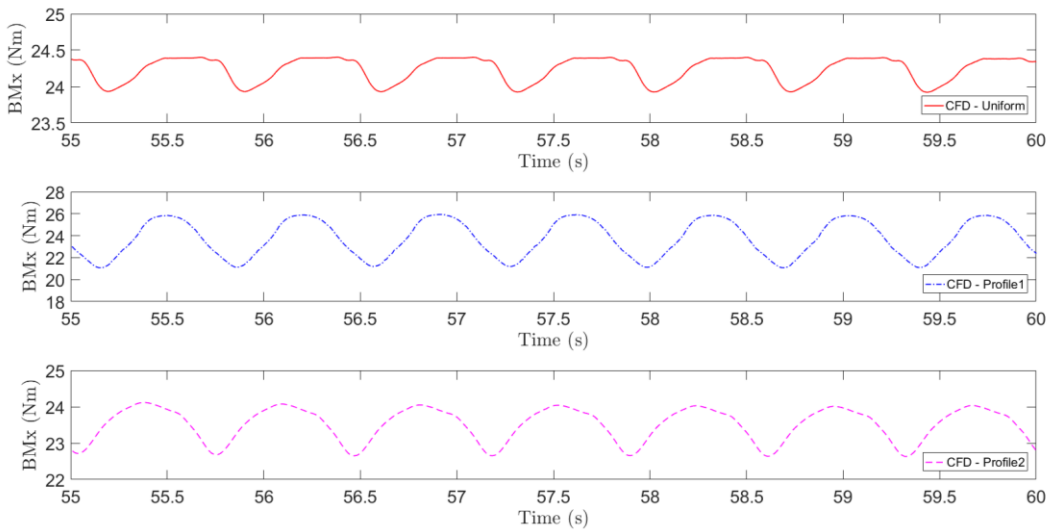


Figure 7.16. The CFD results for the out of plane bending moment on a single blade in uniform, Profile 1 and Profile 2 current conditions.

TABLE 7.17. THE AVERAGE CFD AND EXPERIMENTAL OUT OF PLANE BENDING MOMENT RESULTS IN UNIFORM AND PROFILED FLOW CONDITIONS.

Case	Average out of plane bending moment, BM_x (Nm)		
	Experimental	CFD	Difference
Uniform	23.99	24.24	0.25
Profile 1	25.20	23.73	1.47
Profile 2	24.68	23.53	1.15

A FFT was then carried out to analyse the similarities between the two data sets in the frequency domain. The fluctuation in the CFD results is clear to see from the repeating oscillations in each of the time series. In the uniform current case, these fluctuations have an amplitude of 0.25 Nm, as shown in Table 7.18, and are due to the stanchion interaction with the turbine blade on each rotation. This amplitude of fluctuation in the BM_x increases to 0.67 Nm for Profile 1 and 2.52 Nm for Profile 2 and the increase is directly related to the shear in the velocity profile. Profile 1 has the greatest amount of shear present in the velocity profile and this has the largest effect on the BM_x on a turbine blade. The same trend exists in the experimental data with amplitudes of fluctuation of 0.15 Nm, 0.31 Nm and 0.59 Nm for the uniform, Profile 2 and Profile 1 cases respectively. However, the CFD appears to overpredict these fluctuations by twice the amount for the uniform and profile 2 cases, and 4 times the amount for profile 1. The CFD models reproduced controlled conditions with limited turbulence present in the flow as a result of a high rate of turbulence dissipation in the model. However, higher frequency fluctuations exist in the experimental data which could be affecting the lower frequency fluctuations such as stanchion interaction with the turbine blades. Therefore, an alternate method, known as Time Synchronous Averaging (TSA), was tested to analyse the BM_x fluctuations over the rotational cycle of a turbine blade.

In order to reduce the noise in the signal and emphasise the underlying fluctuations in the time series, the TSA approach was undertaken. The general process of TSA is to use data captured in the time domain, re-sample this data to fixed locations in the displacement domain, and then average over multiple turbine rotations at each sample location, as described by [170]. This averaging method reduces the effect of noise on the signal and highlights the cyclic BM_x fluctuations over a single turbine rotation, as shown in Figure 7.17. This method has been proven to be effective in turbine performance characterisation [170], without adversely affecting the frequency domain representations of the loadings developed.

The relatively steady velocity profile in the uniform flow leads to a low noise content as shown in Figure 7.17A, while the increased noise in Figure 7.17B and Figure 7.17C reflect the unsteadiness seen in the flow due to the presence of the wave maker. The maximum and minimum values of the average BM_x over a single rotation, established using the TSA method, were found and used to calculate the amplitude of fluctuation. This method estimated values of 0.45 Nm, 2.25 Nm and 0.76 Nm for the fluctuation in the signals of the uniform, Profile 1 and Profile 2 flow conditions respectively, as shown in Table 7.18. These

7 TURBINE PERFORMANCE UNDER CURRENT-ONLY CONDITIONS: UNIFORM AND PROFILED VELOCITY GRADIENTS

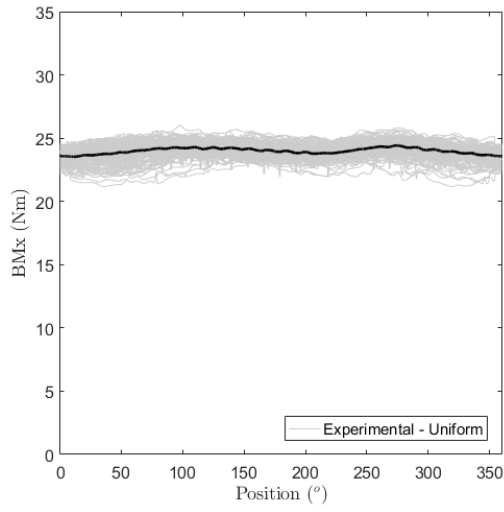
results showed significant improvement over those from the FFT method, as a result of reducing the noise in the signal. The differences between the CFD and experimental fluctuation in the BM_x for uniform, Profile 1 and Profile 2 conditions were 0.2 Nm, 0.27 Nm and 0.09 Nm.

TABLE 7.18. THE AMPLITUDE OF FLUCTUATION IN THE CFD AND EXPERIMENTAL OUT OF PLANE BENDING MOMENT RESULTS CALCULATED USING DIFFERENT METHODS.

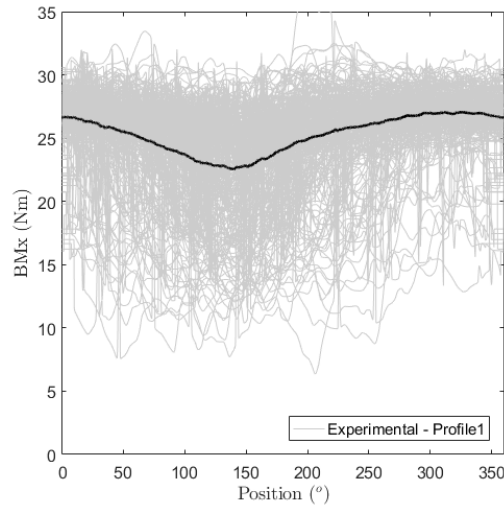
Case	Amplitude of fluctuation in the out of plane bending moment, BM_x (Nm)			Difference between CFD FFT method and experimental TSA method
	CFD	Experimental		
	FFT method	FFT method	TSA method	
Uniform	0.25	0.15	0.45	0.2
Profile 1	2.52	0.59	2.25	0.27
Profile 2	0.67	0.31	0.76	0.09

Validation of the CFD models using uniform and profiled flow conditions has been successfully achieved in the peak power region. The CFD models reflect the experimental conditions to within 1 standard deviation of the experimental data. This validation has been carried out by analysing multiple flow and turbine features, such as the turbine performance characteristics, streamwise and vertical flow velocity data, and individual BM_x blade loadings. Further investigation can now be carried out to analyse the transient loading features as a result of the different flow conditions. The individual turbine component torque and thrust results were not measured during the experimental testing. It is therefore assumed that torque and thrust data presented by the CFD models would be representative of the experimental data as a result of prior validation using alternative parameters.

A



B



C

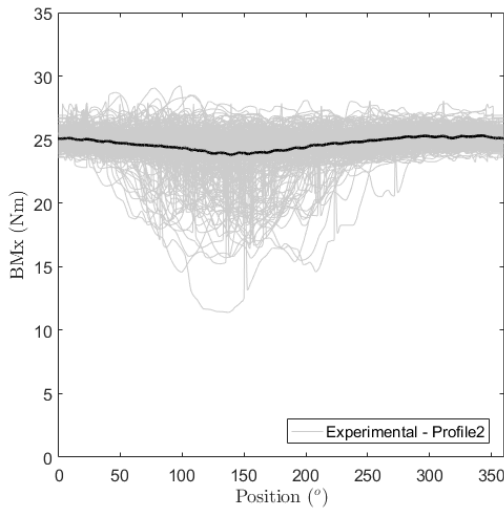


Figure 7.17. The average experimental out of plane bending moment fluctuation on a single blade calculated using TSA for A) uniform, B) Profile 1, and C) Profile 2 current conditions.

7.3 TRANSIENT TURBINE LOADINGS

Section 7.2 examined the ability of the CFD model to reproduce the conditions measured during the experimental testing carried out at IFREMER, which it accomplished. This section carries out a purely CFD comparison of the different profiled flow models to investigate how the generated conditions affect the thrust and torque loadings on the individual turbine components as well as the total loadings.

The average loadings on a single turbine blade under each of the different flow conditions are within 3% and 6% of each other for the thrust and torque respectively. Similarly, the average total turbine thrust and torque measurements for each current flow case are within 3% and 4% of each other, respectively. The hub thrust measurements for each of the model types are within 2.5%, while the hub torque results are the same. Therefore, agreement between the CFD models using uniform, Profile 1 and Profile 2 flow conditions is good with only minor differences in the average loadings, as shown in Table 7.19.

TABLE 7.19. THE INDIVIDUAL AND TOTAL COMPONENT LOADINGS ON THE TURBINE WHEN SUBJECTED TO UNIFORM AND PROFILED FLOW CONDITIONS.

	Average thrust, T (N)			Average torque, Q (Nm)		
	Uniform	Profile 1	Profile 2	Uniform	Profile 1	Profile 2
Blade 1	104.8	102.5	101.7	5.6	5.3	5.4
Hub	7.9	7.7	7.7	0.0	0.0	0.0
Total	321.0	314.0	311.7	16.6	15.9	16.0

The volumetrically averaged streamwise velocity across the swept area of the turbine for the flow conditions created by uniform, Profile 1 and Profile 2 are also very similar, as shown in Table 7.13 and Table 7.15, even though they have different amounts of shear across the water depth. Considering the volumetrically averaged streamwise velocity and the average thrust and torque are very similar, it might be assumed that the operation of the turbine in the conditions presented by the different flow velocities would also be very similar. However, looking at Figure 7.18i, which shows the transient loadings on a turbine blade in the flow conditions given by each profile, it is clear to see that the fluctuation in the thrust and torque loadings on a single turbine blade is very different between each of the types of CFD model.

Figure 7.18Ai shows the transient thrust loadings and shows that the transient cycle of each turbine blade is repeated, with the peak and trough of the results aligned with the rotational frequency of the turbine. The amplitude of fluctuation around the mean thrust is

1.03 N for the uniform flow case, 10.02 N for Profile 1 and 2.65 N for Profile 2. This shows that the fluctuation in the thrust on a single turbine blade in the flow conditions generated by Profile 1 is 3 times that of profile 2, and 10 times that of the uniform flow case. Profile 1 gives a highly sheared velocity profile between 0.81 – 1.07 m/s while Profile 2 produces a less shearing velocity profile between 0.91 – 1.01 m/s, and the uniform case varies between 1.00 – 1.01 m/s. This has a direct effect on the fluctuation of the thrust on the turbine blades but does not affect the average thrust value on a single turbine blade.

This same trend is seen in Figure 7.18Bi, which shows the transient torque loading on the blades, but the difference in the fluctuation around the mean is not as large as in the thrust loadings. The amplitude of fluctuation around the mean torque is 0.79 Nm for the uniform case, 1.39 Nm for Profile 1 and 0.86 Nm for Profile 2. The fluctuation in the torque on a single blade for Profile 1 remains the greatest, while the uniform case and Profile 2 are much more similar. Again, the different flow conditions have a negligible effect on the average torque on a single blade but does affect the fluctuation around the average value.

There is a small discrepancy in the phase of the cyclic loadings between each of the flow conditions. This is due to minor differences in the setting of the angular velocity of the turbine used to reflect the experimental results. These discrepancies in the angular velocity of each of the models resulted in minor changes to the rotational period of the turbine.

Figure 7.18Aii and Figure 7.18Bii show the respective thrust and torque on the hub for each flow condition. For both the thrust and the torque, the loading on the hub is the same in all CFD models. The hub is static in the water depth and at the hub height (-1.0 m from the SWL) both velocity profiles give a streamwise velocity of 1.00 m/s. Therefore, it would be expected that the loadings imparted on the hub for all flow conditions are similar.

The total transient thrust and torque results are given by Figure 7.18Aiii and Figure 7.18Biii respectively. The fluctuation in these results is significantly reduced in comparison to the blade loading results and therefore it is important to analyse each of the turbine loadings individually. This allows analysis of the average and cyclic loadings of each turbine component to be carried out which is critical information used in the design stage of manufacturing a TST to increase the fatigue life of the turbine.

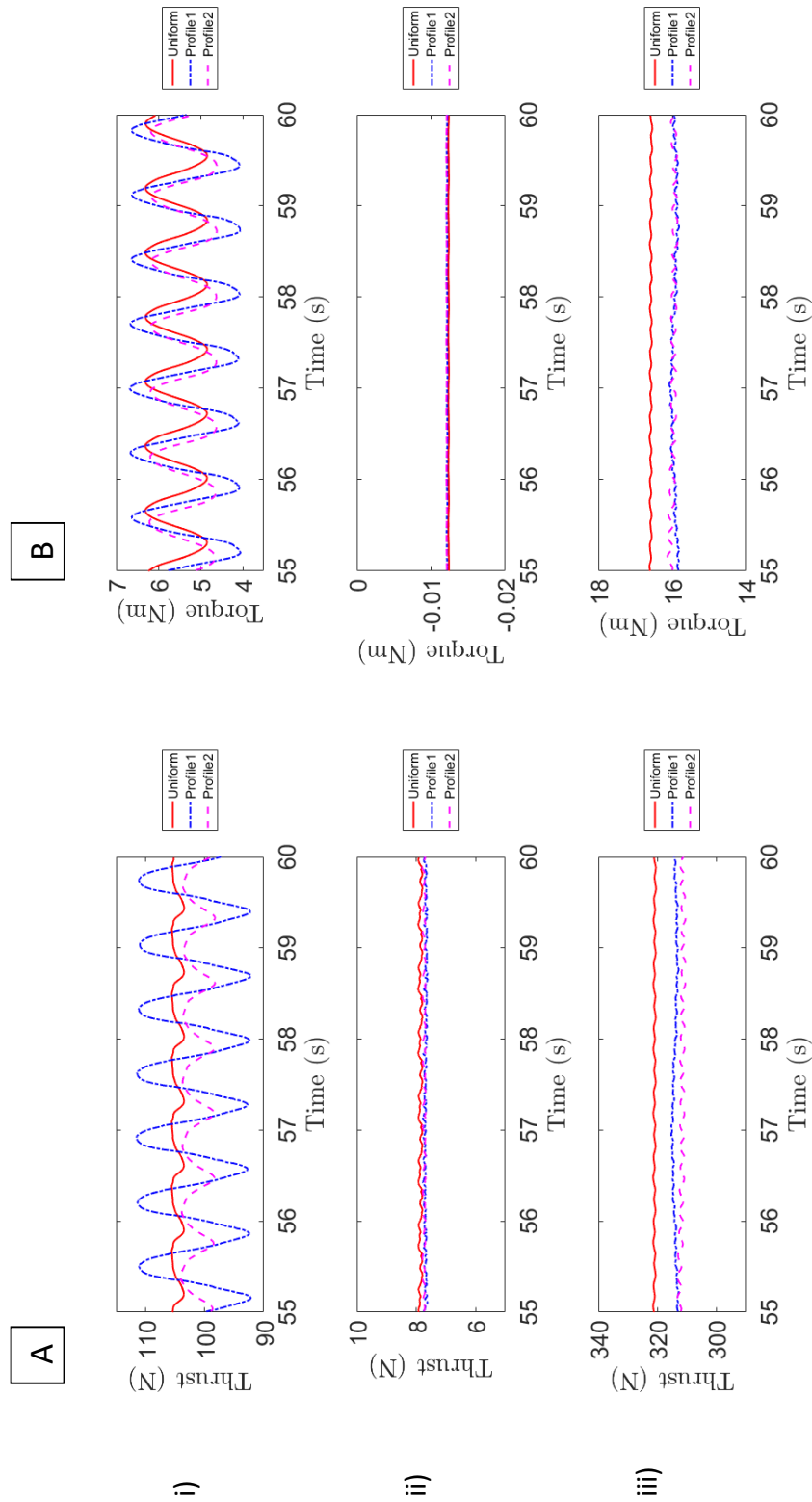


Figure 7.18. Numerical CFD comparison between the uniform, profile 1 and profile 2 models, for A) thrust and B) torque results at a TSR of 4 relating to: i) a single blade, ii) the hub and; iii) the turbine total (all blades and hub).

7.4 SUMMARY

An investigation into the performance of a TST under uniform and profiled flow conditions was carried out, experimentally and numerically. Initially analysing the experimental flow results, the uniform case was found to possess consistently steady flow over the entire water depth, while Profile 2 had a small amount of shear, and Profile 1 had the largest amount of shear across the water depth. It was found that the standard deviation of the flow velocities also had a significant variation between the test cases. The uniform case had a standard deviation of 0.009 m/s throughout the water column while Profile 2 had a larger standard deviation towards the water surface and a smaller variation towards the base with 0.03 m/s and 0.008 m/s respectively. Profile 1 had the biggest change with a standard deviation of 0.06 m/s near the water surface and 0.012 m/s towards the base. The presence of the wave maker submerged in the top of the water column caused a significant disturbance to the flow resulting in high levels of unsteadiness. This caused the variation in the flow measurement to increase, while also having an effect on the variation of the performance characteristics.

The distribution of each time series for the LDA data was investigated as there were clear differences between the performance characteristics displayed by the uniform and profiled flow cases. It was found that the uniform LDA results were normally distributed but Profiles 1 and 2 were negatively skewed. The maximum difference between the mean and mode of the data sets was < 0.5% for the uniform case, 25% for Profile 1 and 6% for Profile 2, which resulted in a difference for \overline{W}_{vol} , depending on the calculation method used, of 0.1%, 4% and 0.3% for the uniform, Profile 1 and Profile 2 cases. This indicates the mean value is not representative of the predominant flow conditions and therefore the \overline{W}_{vol} was recalculated using the modal value instead. This calculation improved the agreement between performance characteristics for each of the flow conditions investigated. It is therefore recommended henceforth that the mode is used to calculate the \overline{W}_{vol} instead of the mean as the mode is more representative of skewed data sets but remains the same as the mean value in normally distributed data sets.

Numerical models were developed to replicate the experimental testing carried out at IFREMER using a 'free surface' type of CFD model. Estimations of the uniform and profiled current flow showed excellent agreement to the experimental data at a TSR of 4. The average performance characteristics also showed good agreement. Further validation of the CFD models, using experimental results, was carried out using the BM x of an individual turbine blade, and agreement was found between the mean values. A TSA method was

used to compare the experimental mean fluctuation of the blade BM_x to the CFD model. This approach reduces the noise in the experimental data to emphasise the underlying fluctuations present in the time series. It was not necessary to use this approach with the CFD data as the experimental flow results possess turbulence, noise and other unsteady features which are not replicated in the CFD analysis. Good agreement was found between the experimental and numerical BM_x results.

Validation of the CFD models in the peak power region was successfully achieved using multiple comparable parameters. The torque and thrust loadings were then examined in a purely CFD comparison. It was found that the transient cyclic thrust loadings on a single blade were significant, with Profile 2 being three times and Profile 1 being ten times the amount of the uniform flow case, directly as a result of the velocity shear increase amongst the flow cases. These differences in the loadings experienced by a single turbine blade are extremely significant and this is before more complex features such as turbulence and surface waves have been considered.

8 DEVELOPMENT OF WAVE-CURRENT NUMERICAL MODEL USING CFD: REGULAR WAVES WITH UNIFORM CURRENT CONDITIONS

This chapter identifies the key factors necessary for developing a CFD model capable of simulating wave and current flow interactions. This chapter expands upon the work of the previous chapter (Chapter 7), aiming to increase the complexity of the flow conditions in the CFD model, enabling analysis of the TST under more complex flow conditions and to investigate how this affects the turbine performance. The work presented in this chapter, however, focusses on the development of the wave-current CFD model, estimating the sub surface velocity fluctuations created by regular waves without a TST. Chapter 9 will explore the effects of combining the wave-current and TST modelling.

Experimental results, independently obtained by the University of Liverpool [84], were used to validate the numerical models. Information on the experimental testing carried out at the University of Liverpool is detailed in Chapter 4. The author took no part in this testing at the University of Liverpool and only uses these experimental results to aid the development and optimisation of the numerical CFD model.

The numerical models discussed here were developed using the simplified ‘thin’ domain model, as described in Chapter 5. This section of work aims to develop a methodology for simulating regular waves superimposed on a uniform current velocity and therefore it is not necessary to have the full width domain when there is no turbine present in the model. Three different regular waves were used to test the model’s versatility and to investigate the effect of wave-current interaction for a variety of wave types. Each wave-current combination was also modelled using two different water depths of 0.76m and 2.5m, producing intermediate and deep-water wave conditions, as defined in Section 3.1.3.

8.1 EXPERIMENTAL RESULTS

All experimental results presented in this chapter were obtained by the University of Liverpool in an independent test campaign carried out at their recirculating water channel [84]. Details of the experimental setup and procedure are provided in Section 4.2. Measurements for both the flow velocity and turbine loadings were collected; however, only the flow velocity measurements were used in this thesis as the turbine data was not required.

8 DEVELOPMENT OF WAVE-CURRENT NUMERICAL MODEL USING CFD: REGULAR WAVES WITH UNIFORM CURRENT CONDITIONS

The current flow of the recirculating water channel was set to a target velocity of 0.93 m/s while a hinged paddle type wave maker generated regular waves propagating in the same direction as the current. A schematic is displayed by Figure 4.3. Table 8.1 shows a summary of the wave and current characteristics used in the experimental testing.

TABLE 8.1. WAVE AND CURRENT CHARACTERISTICS USED IN THE EXPERIMENTAL TESTING.

Wave Name	Depth conditions	Water depth h (m)	H (m)	T_r (s)	Target \bar{W} (m/s)	L (m)	Steepness H/L	Relative depth h/L
Wave 1	Intermediate	0.76	0.058	1.218	0.93	2.25	0.026	0.338
Wave 2	Intermediate	0.76	0.082	1.147	0.93	2.02	0.041	0.377

Velocity measurements were recorded in the streamwise, vertical and cross stream directions using ADV at different water depths down the centre of the recirculating water channel. Measurements were taken at a water depth of -0.12 to -0.445 m from the SWL for Wave 1, and -0.12 to -0.42 from the SWL for Wave 2. The depth-averaged streamwise velocity was 0.931 m/s for Wave 1 and 0.929 m/s for Wave 2, as shown in Figure 8.1. This shows that the target uniform current velocity of 0.93 m/s was achieved.

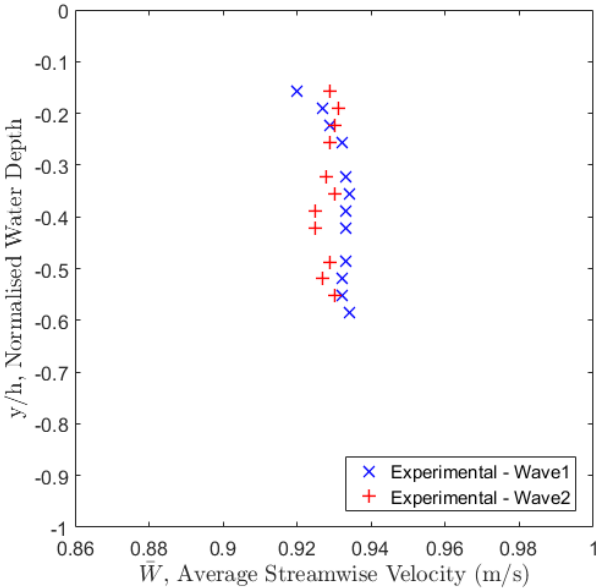


Figure 8.1. Average streamwise velocity at points through the water depth for both Wave 1 and 2. Experimental data taken using an ADV had an estimated error of <1% in the mean velocity and an uncertainty of +/-1%. Data supplied by the University of Liverpool [84].

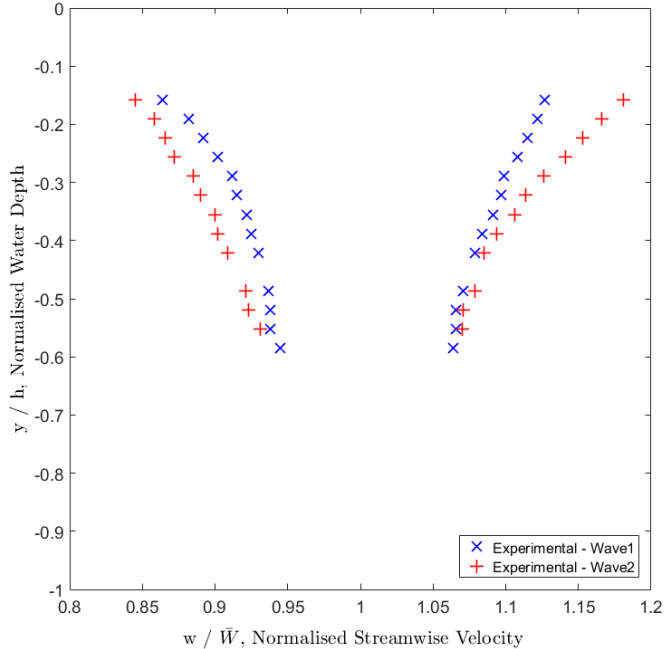
Investigation into the surface elevation of the wave found that the waves produced were essentially regular. However, the wave height did vary by $\pm 5\%$ and the wave period by $\pm 0.5\%$ [84]. The velocity measurements had a good signal to noise ratio above 50 dB so only

a few cases required filtering which used a phase-space threshold despiking method from Goring and Nikora [171]. All data capture and data analysis was carried out by the University of Liverpool [84].

Figure 8.2 shows the wave induced normalised streamwise and vertical velocity components for Waves 1 and 2. This experimental data was pre-processed by the University of Liverpool and therefore no information was provided about the standard deviation of the data sets, hence no error bars are displayed on the figures. Both wave cases show significant oscillatory effects about the mean flow velocity with Wave 2 showing the greatest velocity fluctuations. The maximum streamwise velocity fluctuations nearest the water surface were $< 20\%$ of the mean flow velocity which shows that the flow is dominated by the current.

8 DEVELOPMENT OF WAVE-CURRENT NUMERICAL MODEL USING CFD: REGULAR WAVES WITH UNIFORM CURRENT CONDITIONS

A



B

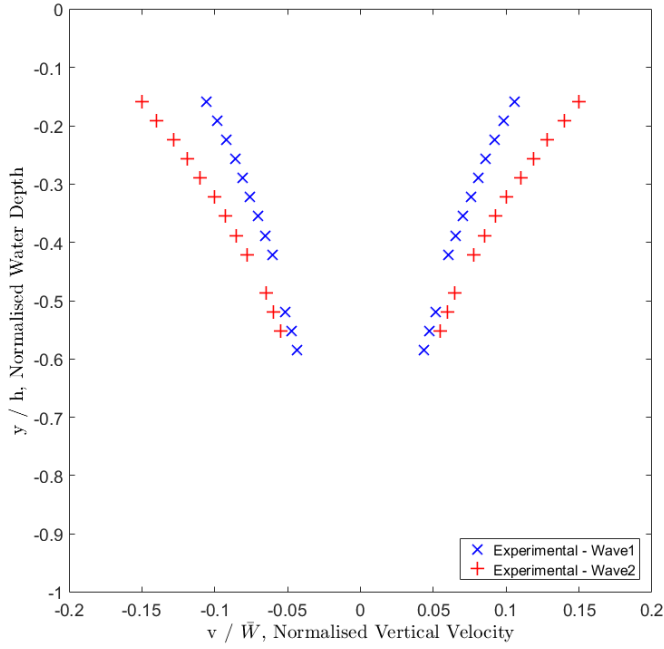


Figure 8.2. Experimental results for Wave 1 and 2 of the normalised A) streamwise and; B) vertical velocities at points through the water depth. Experimental data taken using an ADV had an uncertainty of +/-1%. Data supplied by the University of Liverpool [84].

8.2 CFD RESULTS

A Numerical Wave Tank (NWT) is a numerical representation of a physical experimental testing facility or ocean environment. It can be used to simulate wave-current interactions using various modelling techniques within different available software. This section presents the methodology behind creating a NWT using ANSYS CFX 18.0; all numerical models are based on the testing facility at the University of Liverpool to allow a direct comparison between numerical and experimental data sets. It is necessary to use a 'free surface' model to simulate wave-current interaction as the surface of the water must deflect as the waves propagate through the model. The general development of the 'free surface' model is given in Chapter 5 while the technicalities of the optimisation process for the 'free surface' wave-current model is detailed in the following sections.

8.2.1 Geometry, mesh, setup summary

The development of the wave-current CFD model is based on the University of Liverpool's recirculating water channel facility [84]. However, for computational reasons given in Section 5.2.1, the NWT has a length of 20 m, width of 0.1 m and domain height of 1.09 m in intermediate water wave conditions, and 3.5 m in deep-water wave conditions. This allows for a water depth of 0.76 m and 2.5 m in intermediate and deep-water wave conditions respectively. The aim of developing the NWT is to replicate the flow conditions created when testing at experimental facilities. These settings allow the desired wave-current characteristics to exist in a specific, known region of the model.

The main domain mesh for wave-current modelling was developed as detailed in Section 5.2.2, with a mesh independence carried out and the final mesh for wave-current modelling described in Chapter 6. This mesh had 120 cells over the length of a wave (z -direction) and 10 cells over the wave height (y -direction), with the mesh expanding away from this refined region around the air-water interface. Table 8.2 provides the specific mesh sizings used for the three different flow conditions specified in this chapter.

TABLE 8.2. MESH SIZING PARAMETERS.

Wave Name		Wave 1		Wave 2		Wave 3	
Water depth (m)		0.76	2.5	0.76	2.5	0.76	2.5
Air-water interface region	Δy (m)	0.006	0.006	0.009	0.009	0.001	0.001
	Δz (m)	0.019	0.019	0.017	0.017	0.019	0.019
	Δx (m)	0.014	0.014	0.014	0.014	0.014	0.014
Mesh expansion from interface towards the 'top' boundary	Δy (m)	0.01	0.01	0.01	0.01	0.01	0.01
		→	→	→	→	→	→
Mesh expansion from interface towards the 'base' boundary	Δy (m)	0.07	0.18	0.07	0.12	0.07	0.16
		0.012	→	0.012	→	0.012	→
Mesh expansion in beach region	Δz (m)	0.01	0.01	0.01	0.01	0.01	0.01
		→	→	→	→	→	→
Maximum aspect ratio		0.03	0.03	0.03	0.03	0.03	0.03
Total elements (millions)		0.013	0.013	0.013	0.013	0.013	0.013
		21	22	16	16	127	114
		0.73	1.8	0.75	2.0	1.0	1.7

The simulations were set up as transient runs with a uniform current flow (\bar{W}) and regular wave characteristic as described in Table 8.3. The time step of each simulation is given by $T/50$ as it varies depending on the wave period as described in Chapter 6. The wave and current characteristics were input at the 'inlet' boundary using CEL expressions named "*HorizontalParticleVelocity*" and "*VerticalParticleVelocity*" to specify the velocity components in the streamwise and vertical directions. More information on the setup and boundary conditions used can be found in Section 5.4. The CEL expressions for Wave 1 in intermediate water depth conditions can be found in Appendix A while the equations used in each expression can be found in Chapter 3.

TABLE 8.3. A SUMMARY OF THE WAVE CHARACTERISTICS USED.

Wave Name	Depth condition *	Water depth h (m)	Domain height D (m)	H (m)	T_r (s)	\bar{W} (m/s)	L (m)	Wave Steepness H/L	Relative depth h/L
Wave 1	Int	0.76	1.09	0.058	1.218	0.93	2.250	0.026	0.338
	De	2.5	3.5						
Wave 2	Int	0.76	1.09	0.082	1.147	0.93	2.020	0.041	0.377
	De	2.5	3.5						
Wave 3	Int	0.76	1.09	0.01	1.218	0.1	2.250	0.0044	0.338
	De	2.5	3.5						

* Int – Intermediate, De - Deep

Each of the three wave conditions were run in two different water depths. Waves 1 and 2 are S2OT waves while wave 3 is a LWT wave, as described in Chapter 3. The simulations were initiated with current-only conditions to allow the flow field to stabilise before the wave characteristics were superimposed on top. Stability in the model occurred after 60-70 seconds and so all results reported in this study were taken over a 10 second period after

70 seconds of run time. Monitor points were added into the model, as described in Section 5.4.6, to observe changes through the water depth in the flow velocity and wave period. The deep-water wave cases were monitored every 0.2m between $y = -0.1\text{m}$ and $y = -1.5\text{m}$, while the intermediate water wave cases were monitored every 0.1m between $y = -0.12\text{m}$ and $y = -0.62\text{m}$ at various locations downstream of the inlet. Table 8.4 provides a summary of the settings used in each CFD model.

TABLE 8.4. SUMMARY OF THE GEOMETRY, MESH AND SETUP FOR A 'FREE SURFACE' WAVE-CURRENT CFD MODEL.

Geometry		
Main domain dimensions	Length x Width x Depth	20 x 0.1 x D m (see Table 8.3)
Mesh		
(see Table 8.2)		
Setup		
Time step	Δt_{wave} (see Equation (6.1))*	
Fluid Phases present	Water and air (multiphase)	
Buoyancy model	On	
Boundary conditions	inlet	Velocity-inlet (opening)
	Flow type	Regular wave and uniform current flow
Boundary conditions	Input velocity components	U: 0 m/s V: <i>VerticalParticleVelocity</i> W: <i>HorizontalParticleVelocity</i>
	outlet	Pressure-outlet (opening)
Reference pressure	$P_{ref} = (\rho_{water} - \rho_{air}) \cdot g \cdot (h - y)$	
Side walls	Free-slip wall	
Base	No-slip wall	
Top	Pressure-opening	
Relative pressure	$P_{rel} = 0 Pa$	

8.2.2 Verification of reduced width domain

A restricted width of 0.1 m was used in the CFD model instead of the full width of the recirculating water channel (1.4 m) to simplify the model and increase the speed at which each model would run. This decision needed to be justified by checking that the CFD model could reproduce the current-only conditions observed from the experimental testing. Figure 8.3 shows the average streamwise (\bar{W}) and vertical (\bar{V}) velocities through the water depth over 60 seconds of converged run time, while Figure 8.4 shows the same velocity components but at six different locations, a distance of 2 to 7 m downstream of the inlet, at $t = 80$ seconds. The average streamwise and vertical velocities for the experimental testing results were 0.93 m/s and 0 m/s respectively, so the CFD model was monitored to confirm that these same conditions were being generated. As seen in Figure 8.3, the monitor point nearest the water surface deviates the most in comparison to the other points. This is due

to interaction between the air and water at the free surface interface, reducing the water velocity towards the surface. However, the depth averaged velocity across all the points gave 0.938 m/s in the streamwise direction and 0.0002 m/s in the vertical direction, showing very good agreement with the average experimental results.

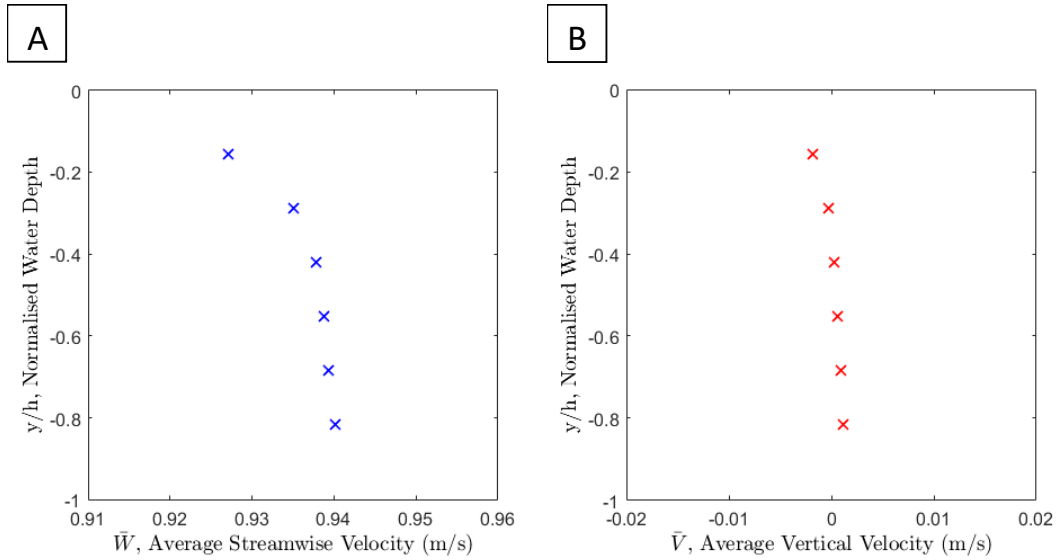


Figure 8.3. Average: A) streamwise and; B) vertical velocities for current-only flow through the water depth over 60s of converged run time.

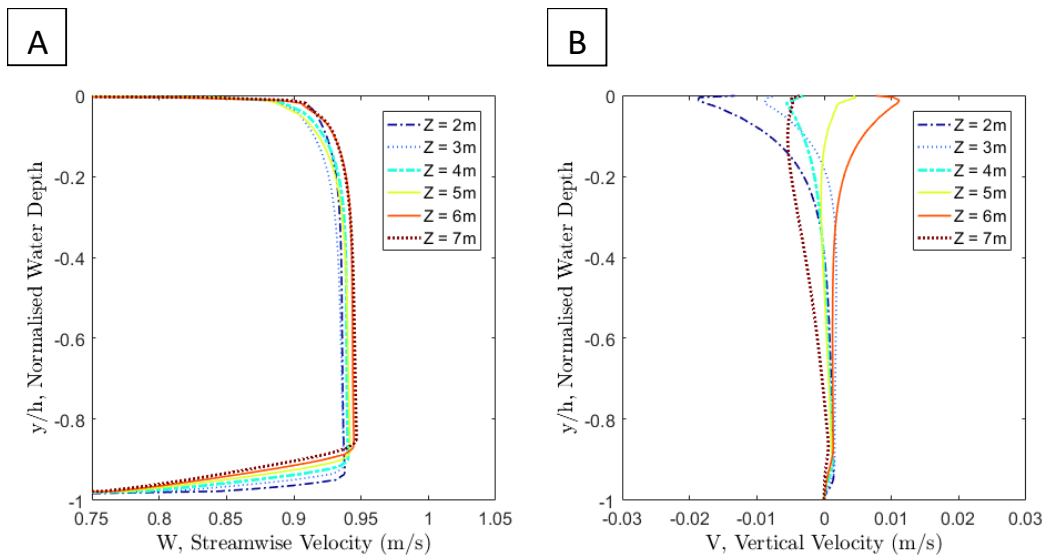


Figure 8.4. Average: A) streamwise and; B) vertical velocities for current-only flow through the water depth at 6 different locations downstream of the inlet on the centreline at $t=80s$.

Figure 8.4 shows the full depth profile of the velocity variation at six different locations downstream of the inlet. A reduction in velocity near the base of the tank and at the water

surface can be seen due to frictional effects. The average streamwise and vertical velocities of the main body of the flow, excluding the top and bottom 10% of the water depth, were found to be 0.938 m/s and -0.0002 m/s respectively. These position averaged results (Figure 8.4) agree with the time averaged results (Figure 8.3) showing that the average velocity was stationary over time, and in the area between 2 and 7 m downstream of the inlet. The average velocities were within the $\pm 1\%$ uncertainty of the experimental results taken using an ADV [84], as detailed in Chapter 4. Therefore, these results verify the decision to use a width of 0.1 m instead of 1.4 m as the computational run time will be reduced without affecting the accuracy of the numerical solution.

8.2.3 Deep-water wave conditions

The following results used a water depth of 2.5m and therefore possess deep-water wave conditions, as described in Table 3.1. Figure 8.5 shows a comparison between the S2OT estimation and the numerical CFD results for the surface elevation of each wave case at a location 4m downstream of the inlet.

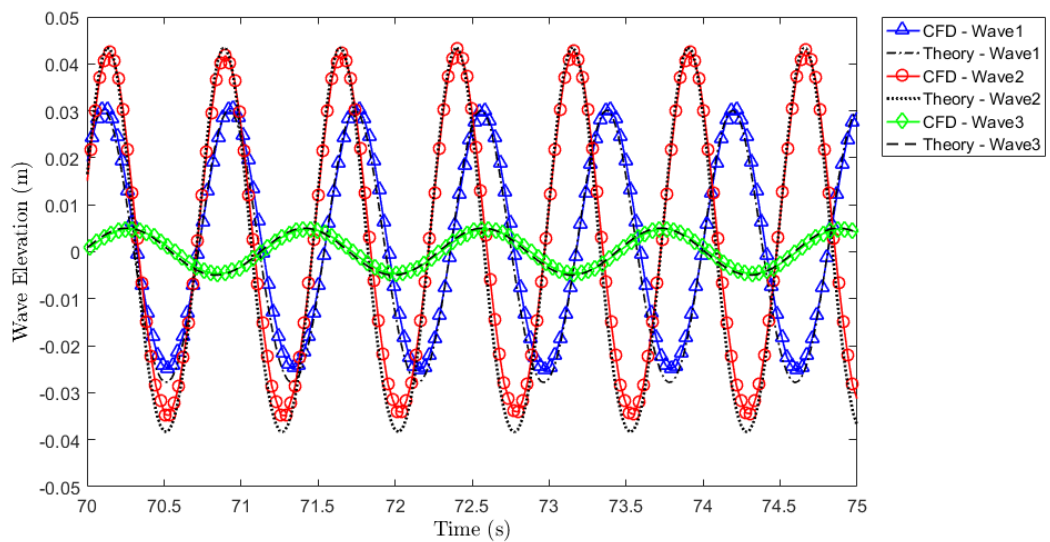


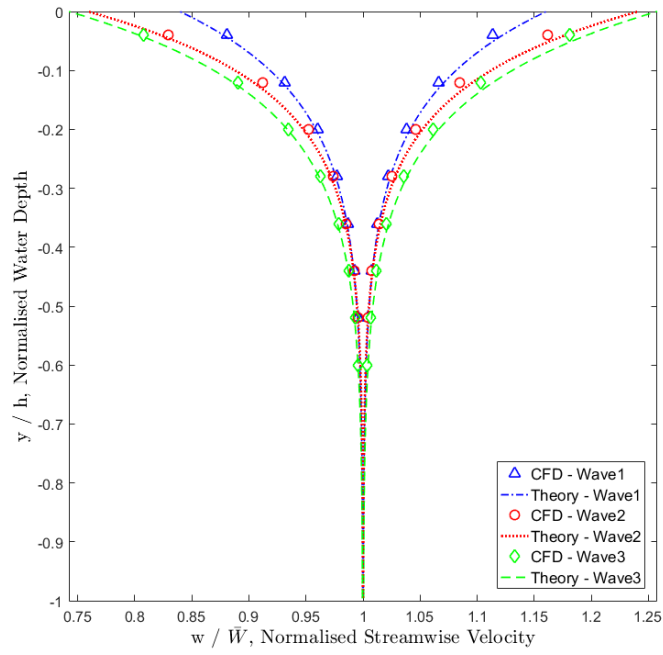
Figure 8.5. A comparison of the CFD and S2OT surface elevation for Wave 1, 2 and 3 in deep-water conditions at a location 4m downstream of the inlet.

There is good agreement in the surface elevation between both data sets for all wave cases, showing that the imposed wave profile at the inlet was maintained downstream. The average wave height is found from the difference between the maximum and minimum surface elevation over time. The difference between the numerical and S2OT results for the wave height is 13%, 6% and 5% for Waves 1, 2 and 3 respectively. There is a greater contrast between the surface elevation results in the trough region compared to the crest

of the wave; however, overall the numerical model provides a good estimate of the surface elevation, and therefore wave height, when compared with the equivalent theory. The average wave period (T_a) of the numerical models are 0.818s, 0.755s and 1.155s for Waves 1, 2 and 3, which agree with the values input to the model using theory, of 0.81s, 0.75s and 1.16s.

The CFD and S2OT results are also compared by examining the normalised streamwise and vertical velocities through the water depth, as shown in Figure 8.6. Looking at the normalised streamwise velocity results, the greatest difference between the CFD model results and theory was 1.3% for the Wave 2 case, present at the monitor points nearest the water surface. Wave 1 shows the smallest differences between the data sets with a difference of 0.8%. The normalised vertical velocities give a higher percentage difference between the numerical and S2OT results with a maximum difference of 41% for Wave 3 at the point nearest the base of the tank. This percentage seems very high in comparison to the differences in the streamwise velocity results. However, the values are very small at -0.0026 m/s for the CFD model and -0.0044 m/s for the theory, resulting in a difference of 0.0018 m/s. The difference between the data sets observed near the water surface is greater with a value of 0.0113 m/s, but as a percentage of the theoretical value is 5.8%, which is much smaller. The difference between the CFD and S2OT vertical velocity is greater at the surface than towards the base of the tank, even though the percentage values suggest otherwise. Therefore, when dealing with values so close to zero, care must be taken when interpreting trends in the data. The biggest differences exist at the point nearest the water surface for Waves 2 and 3, with a difference of 0.01 m/s. Wave 1 shows the smallest differences with a maximum difference of 0.007 m/s. Overall, the NWT produces flow conditions that show good agreement with the S2OT normalised streamwise and vertical velocity results. Therefore, it is acceptable to assume that this NWT is capable of accurately generating deep-water wave conditions and provides a good estimation of the sub surface velocities.

A



B

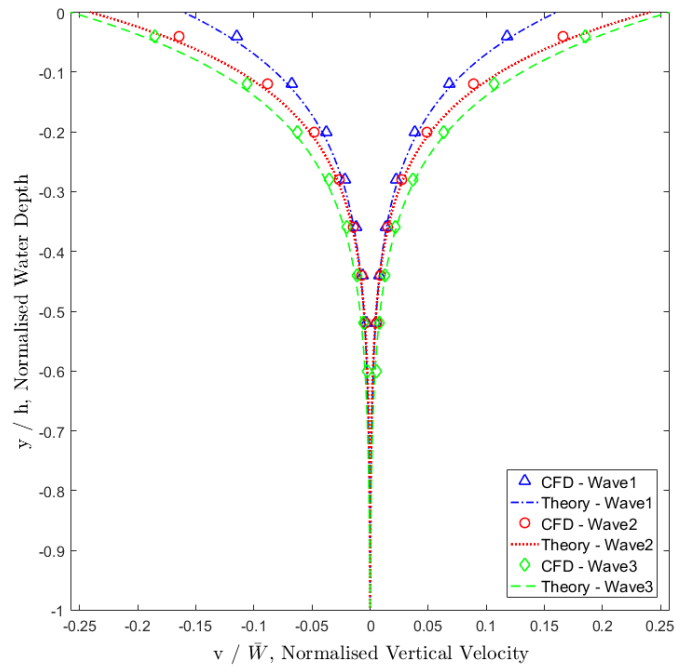


Figure 8.6. The normalised A) streamwise and; B) vertical velocities at monitor points through the water depth at a location 4m downstream of the inlet for numerical results and S2OT.

8.2.4 Intermediate water wave condition

The following results used a water depth of 0.76m and therefore possess intermediate water wave conditions, as described in Table 3.1. Figure 8.7 shows a comparison between the CFD results and S2OT for the surface elevation of each wave case at a location 4m downstream of the inlet. The maximum difference between the numerical and S2OT results for the wave height is 3%, 6% and 2% for Waves 1, 2 and 3 respectively. The overall wave height shows good agreement between the two data sets, however, there is a slight vertical shift in the numerical results for Waves 1 and 2 in comparison to the theory. The average wave period (T_a) of the numerical CFD models are 0.81s, 0.75s and 1.15s for Waves 1, 2 and 3, which agree with the values input to the model using theory.

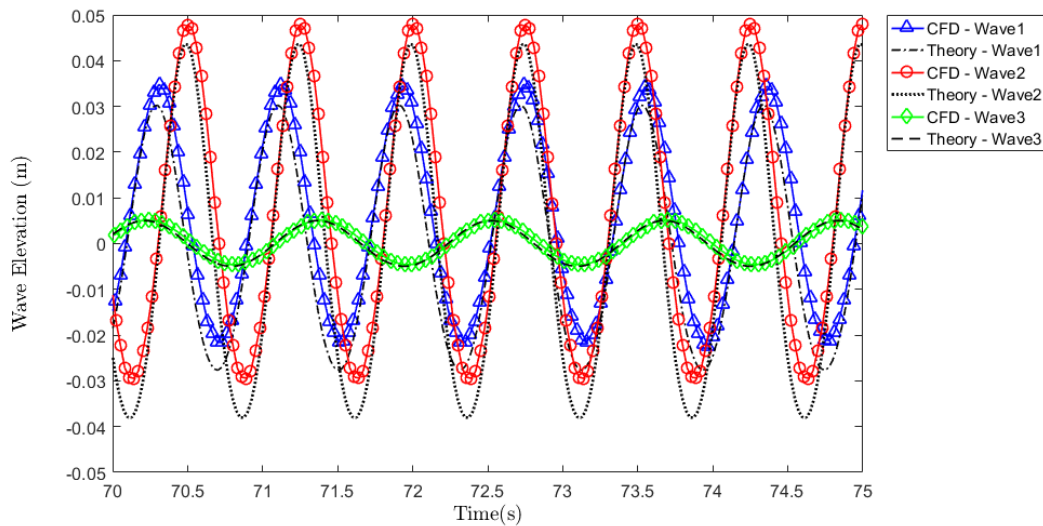
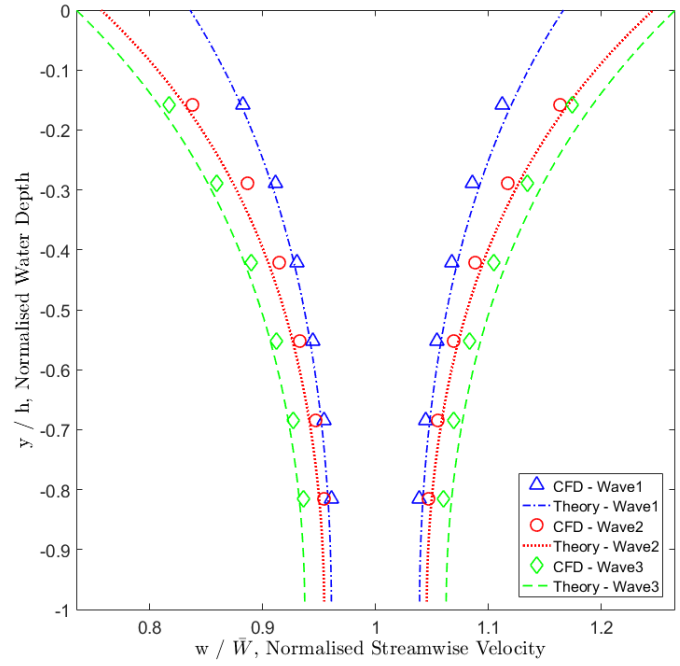


Figure 8.7. A comparison of the CFD and S2OT surface elevation for Wave 1, 2 and 3 in intermediate water conditions at a location 4m downstream of the inlet.

Figure 8.8 shows a comparison of the numerical results and S2OT for the normalised streamwise and vertical velocities at points through the water column in intermediate water wave conditions. The normalised streamwise velocity results show a maximum difference between theory and the CFD results of 1.5%, displayed in the results for Waves 2 and 3. Wave 1 has a maximum difference of 0.7%, showing better agreement between the data sets. In a similar way to the trends seen in the deep-water wave conditions, the biggest discrepancies between the two sets of results for the intermediate water wave conditions are at the points closest to the water surface. This is where the oscillatory motions induced by the surface waves are the greatest. It is hypothesised that the slight disparity in the surface elevation results (Figure 8.7) also contribute to the discrepancies observed between the velocity results near the water surface.

A



B

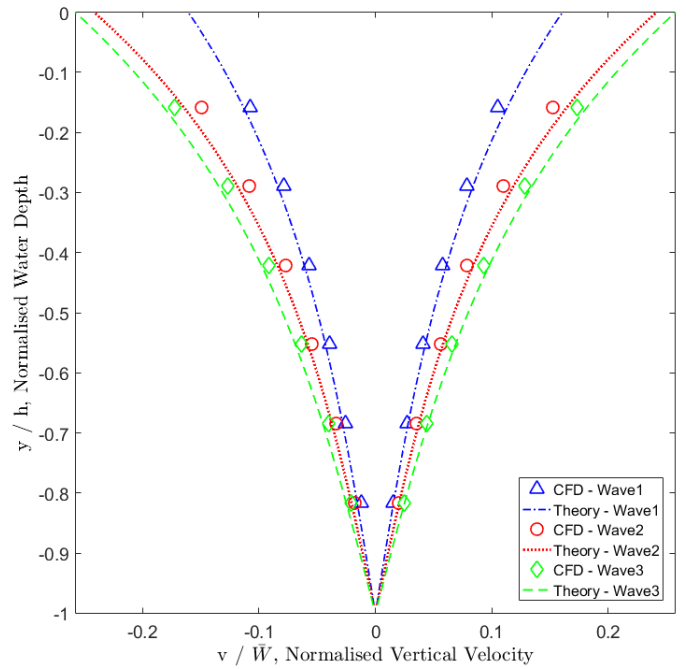


Figure 8.8. The normalised A) streamwise and; B) vertical velocities at monitor points through the water depth at a location 4m downstream of the inlet for numerical results and S2OT.

The maximum difference between the vertical numerical CFD results and the equivalent theory is 0.015 m/s. The biggest divergence observed with these results is again seen near the water surface, following the same trend as the streamwise velocity results. However, the specific settings used to create this NWT are adequate in providing a good representation of the sub surface wave and current interactions for each of the wave cases in intermediate water wave conditions.

8.2.5 Deep and intermediate water wave numerical comparison

Due to the relative depths (h/L) of the conditions created using a water depth of $h = 0.76\text{m}$ and 2.5m , intermediate and deep-water wave conditions were established. As mentioned at the beginning of this chapter, the work presented here focusses on the development of a wave-current CFD model to estimate the sub surface velocity fluctuations created by regular waves. The next chapter will explore the effects of wave-current interactions with a TST, and therefore the wave-current conditions simulated in this chapter need to realistically represent those in an ocean environment at a suitable TST deployment site. The operational water depth range for seabed mounted tidal devices is 25 – 50m [125], while typical sea gravity waves have a wavelength of 1.5 – 150m [124]. Based on these values of h and L , as well as the relative depth requirements stated in Table 3.1, typical TST deployment conditions represent intermediate and deep-water wave conditions. Shallow water wave requirements would need a water depth of $<6\text{m}$ for given values of L which is generally too shallow for turbine deployment and therefore is not assessed in this thesis.

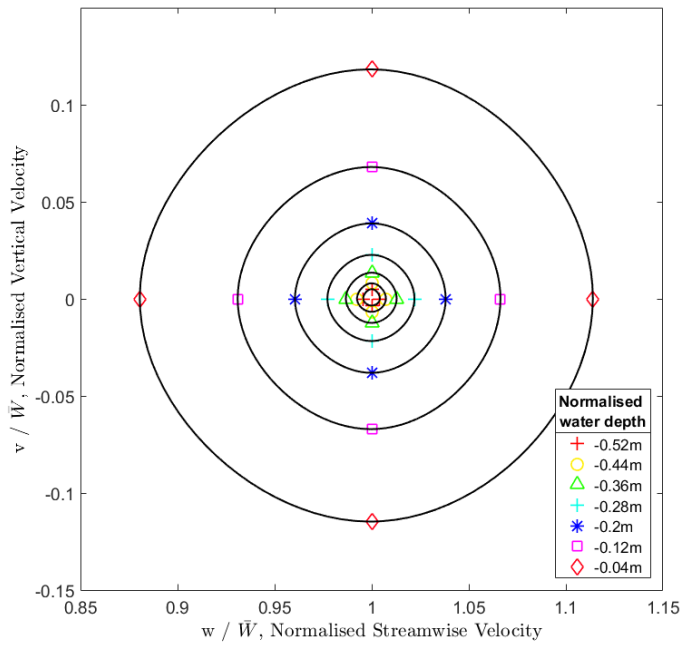
The relative depth of a wave affects its behaviour in terms of propagation through the water depth as well as the shape of the velocity orbital through the water depth. Looking at the streamwise and vertical velocity components through the water depth for both deep and intermediate water wave conditions, shown in Figure 8.6 and Figure 8.8, it is clear to see differences through the water depth. In the case of the deep-water wave conditions, circular velocity orbitals are present through the water column as the streamwise and vertical velocity components are equal. The velocity orbitals remain circular, yet they decay exponentially through the water depth. The streamwise and vertical velocity fluctuations are negligible once they reach a normalised depth of -0.5 , with oscillations decaying completely by the time they reach the base of the tank. The intermediate water wave conditions exhibit a contrasting scenario whereby the streamwise velocity components still have a considerable oscillatory effect at the base of the tank, in comparison to the vertical

velocity component which tends to zero at the base of the tank. Intermediate water wave conditions produce circular velocity orbitals near the water surface, in a similar manner to the deep-water wave conditions. However, as the vertical velocity component decays to zero while the streamwise velocity component remains much greater, the orbitals become elliptical towards the base of the tank. An estimation of the shape and size of the Eulerian velocity history can be seen in Figure 8.9 which shows the normalised maximum and minimum, streamwise and vertical velocities at different water depths through the water column for Wave 1. Figure 8.9A shows the results for the deep-water wave conditions while Figure 8.9B shows the results for the intermediate water wave conditions. Presenting the velocity results in this way displays clear differences between the shape of the orbitals through the water depth. The orbitals are much more circular for the deep-water wave case while the orbitals for the intermediate water wave case become elliptical towards the base of the tank. These results are what would be expected for deep and intermediate water wave conditions.

Examining the impact that these wave conditions would have on a marine device will depend on a variety of factors. If the device was situated in the bottom half of the water depth it would experience minimal velocity variations in deep-water wave conditions. However, in intermediate water wave conditions there would be unequal loadings in the streamwise and vertical directions with a substantial fluctuation in the velocity. Positioning the device further towards the surface would only increase the oscillatory effects encountered by the device in both types of condition; this could be detrimental to the survivability of the device if these variations in loadings on the turbine have not been taken into account and designed for.

8 DEVELOPMENT OF WAVE-CURRENT NUMERICAL MODEL USING CFD: REGULAR WAVES WITH UNIFORM CURRENT CONDITIONS

A



B

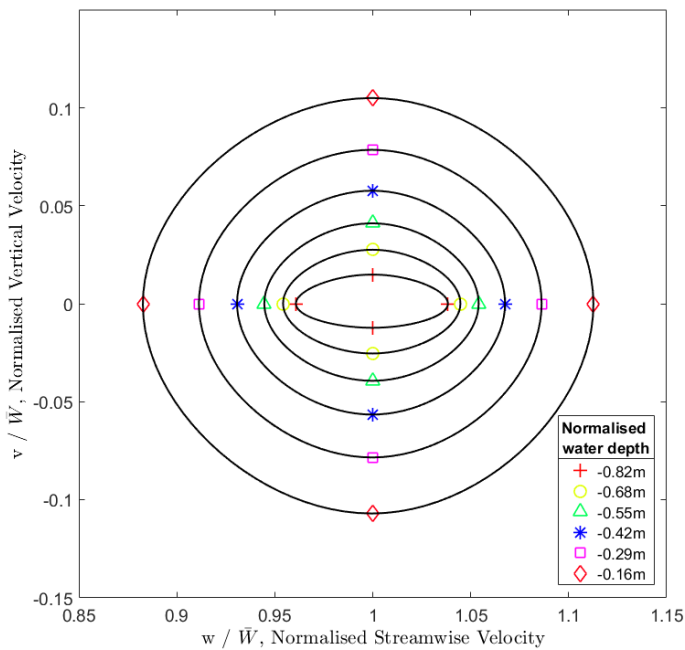


Figure 8.9. The normalised maximum and minimum, streamwise and vertical velocities plotted for the normalised water depth, where the SWL is at 0 and the seabed at -1, to give an idea of the shape and magnitude of the velocity orbitals for A) deep and; B) intermediate water wave conditions for Wave 1.

8.3 NWT VALIDATION USING EXPERIMENTAL DATA

Good agreement for all wave cases between the NWT and S2OT has previously been found as shown in Section 8.2. This following section further validates the NWT developed for simulating wave and current conditions within the S2OT limits, as explained in Section 3.1.3, using experimental data. However, a comparison of the numerical CFD and experimental data was only available for Waves 1 and 2 in the intermediate water wave conditions.

Table 8.5 shows the measured wave heights of Waves 1 and 2 for the experimental and numerical model results under intermediate water wave conditions. The difference between the CFD and experimental values for the wave height are 3% and 6% for Waves 1 and 2 respectively. It was found that the wave height varies by $\pm 5\%$ experimentally and therefore the numerical estimation for Wave 1 is within this margin while Wave 2 is just outside this region. If the purpose of this NWT was to simulate an object floating on the water surface, then the accuracy of the surface elevation would be vital. However, for this study, it is more important that the sub surface flow conditions are accurately simulated as the future focus for this type of numerical modelling is to establish the loadings imparted on a TST situated beneath the water surface. Variation in the loadings will arise from velocity fluctuations in the flow due to wave-current interaction. Therefore, the surface elevation is of a good enough accuracy for the purpose of this CFD model.

TABLE 8.5. A SUMMARY OF THE WAVE HEIGHT FROM EXPERIMENTAL TESTING AND NUMERICAL CFD RESULTS.

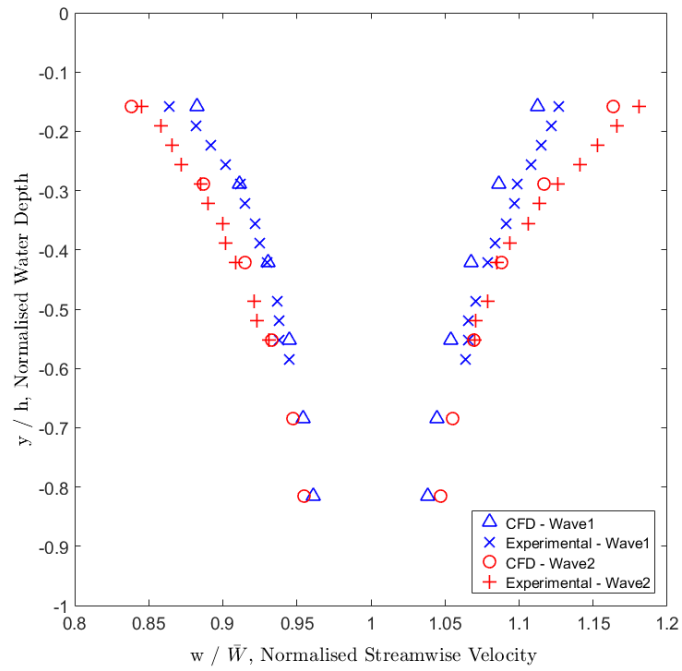
Wave Name	Depth conditions	Wave Height, H (m)	
		Experimental	CFD
Wave 1	Intermediate	0.058	0.056
Wave 2	Intermediate	0.082	0.077

The normalised streamwise and vertical velocities, at points through the water depth, given by the CFD model as well as the experimental testing are shown in Figure 8.10. For Wave 1, the maximum difference between the CFD and experimental normalised streamwise velocity is 2%, while Wave 2 shows a maximum difference of 1.5%. The greatest differences between the two data sets are seen at the water surface where the oscillatory motions induced by the waves have the strongest effect. It is clear to see from Figure 8.10B that the normalised vertical velocity components for Wave 1 and 2 have very good agreement between the numerical CFD and experimental data. The results for Wave 2 sit directly on top of one another while Wave 1 displays the same behaviour most of the way through the water column with a slight divergence seen towards the base of the tank. The

8 DEVELOPMENT OF WAVE-CURRENT NUMERICAL MODEL USING CFD: REGULAR WAVES WITH UNIFORM CURRENT CONDITIONS

biggest discrepancy between the numerical and experimental normalised vertical velocity results for both wave cases is 0.008 m/s. In general, the CFD model gives a very good representation of the experimental results for the streamwise and vertical sub surface velocity components when simulating wave-current interactions in intermediate water depths.

A



B

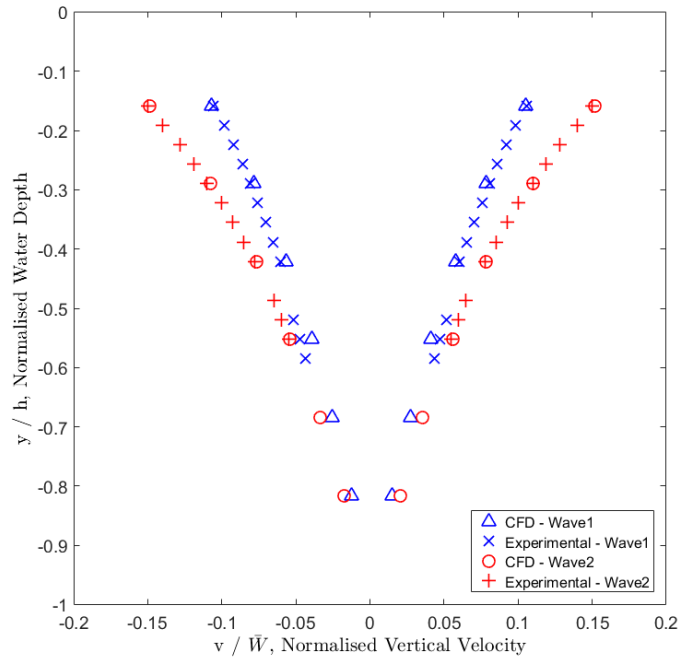


Figure 8.10. Experimental and numerical comparison of Wave 1 and 2 results for the normalised a) streamwise and; b) vertical velocities at points through the water depth.

8.4 SUMMARY

The optimisation of a CFD model to numerically simulate 3D velocity fields of combined wave and current flow has been conducted. The CFD model was designed to replicate the conditions generated at the University of Liverpool's recirculating water channel to enable validation of the CFD models using these results. A reduced width numerical domain was used to simplify the model and increase the run speed of each simulation, while the accuracy of the flow conditions produced were not affected by this decision. Guidelines for the development of an optimised NWT have been established, detailing the importance of mesh sizing/spacing as well as the model setup. Six different simulations were carried out using three different wave characteristics, within the S2OT limits, and two different water depths, $h = 0.76m/2.5m$. Only the CFD models using intermediate water wave conditions for Waves 1 and 2 could be compared to experimental results, while the other simulations were compared to theory. The streamwise and vertical velocity components of the wave, as well as the surface elevation, were the key comparison parameters. Comparisons to experimental and S2OT data highlighted the numerical homogeneity between data sets and showed that CFD models can effectively replicate experimental wave and current results for the conditions shown. Therefore, CFD provides a much cheaper alternative to physical turbine design and experimental flume or tow tank testing.

9 TURBINE PERFORMANCE UNDER WAVE-CURRENT FLOW CONDITIONS: REGULAR WAVES WITH PROFILED VELOCITY GRADIENTS

Following the experimental and numerical investigation into the turbine loadings experienced under current-only conditions (Chapter 7), as well as the development of a CFD model capable of simulating wave and current flow interactions (Chapter 8), this chapter presents the most complex numerical simulations demonstrated in this thesis, consolidating all existing model components into a single type of simulation. The CFD models described in this chapter possess flow conditions with regular surface waves superimposed onto a profiled current velocity. The impact that these flow conditions have on the turbine loadings and performance are examined using the two different profiled velocity gradients discussed in Section 7.1.2, Profile 1 and 2, along with two different wave characteristics, designated Wave 4 and 5.

Experimental results for each wave-current condition were produced over a range of angular velocities in tests carried out at the IFREMER wave-current flume facility. Details of the experimental setup and procedure are described in Chapter 4. These experimental results are used to validate the different numerical wave and profiled current flow models, developed using CFD.

Previously discussed results of the turbine loadings experienced under current-only conditions (Chapter 7) are then compared with the turbine loadings experienced under wave-current flow conditions. The differences in the generated flow conditions are investigated, as well as the subsequent average and transient turbine loadings.

9.1 EXPERIMENTAL RESULTS

The experimental setup and procedure can be found as detailed in Chapter 4.

9.1.1 Turbine characterisation: regular waves and profiled current flow

The velocity of the IFREMER flume was set to produce a target streamwise velocity of 1.00 m/s before considering the effect of the velocity profile induced by the wave maker. As explained in Chapter 7, a paddle type wave maker was used to generate regular waves and could be positioned at two different locations in the flume (WM00 or WM20). This

blockage in the top section of the water column produces a velocity profile, with Profile 1 and 2 referring to the velocity profiles produced by the different wave maker positions, as shown in Table 7.4. These different wave maker positions were used to reduce the standard deviation of the wave elevation, selecting the position depending on the required wave frequency and height. Two different regular wave characteristics were generated by the wave maker as shown in Table 9.1. These waves were both intermediate, S2OT waves and were superimposed upon the profiled current velocity produced by the wave maker position. Wave 4 (W4) was always superimposed upon Profile 1 (P1), and Wave 5 (W5) upon Profile 2 (P2). These waves would be representative of tidal sites with a water depth of between 25 and 40 m by scaling the wave characteristics to match the relative depth and wave steepness criteria, resulting in the following characteristics for W4: $H = 1.1 - 1.8$ m, $T_r = 9.0 - 11.5$ s, $L = 113 - 181$ m, and W5: $H = 1.5 - 2.4$ m, $T_r = 6.8 - 8.6$ s, $L = 70 - 112$ m.

TABLE 9.1. A SUMMARY OF THE WAVE CHARACTERISTICS.

Wave name	Depth condition	Water depth h (m)	H (m)	T_r (s)	L (m)	Wave Steepness H/L	Relative depth h/L
Wave 4	Intermediate	2.0	0.09	2.566	9.07	0.010	0.221
Wave 5	Intermediate	2.0	0.11	1.917	5.61	0.021	0.357

All turbine testing was conducted using speed control, whereby the angular velocity of the turbine was set to a certain value and held constant. A range of angular velocities were tested, equivalent to an average TSR of 2, 3, 4, 5 and 7. The flow velocity measurements were taken using 2D LDA at the same depth intervals described in Chapter 7, while the surface elevation of the water was measured by a wave probe as described in Chapter 4.

The flow conditions in the flume can be presented as shown in Equation (9.1),

$$W(t) = \bar{W} + W' + W_{wave} \quad (9.1)$$

where $W(t)$ is the instantaneous velocity in the streamwise direction, \bar{W} is the time averaged mean value, W' is the fluctuating component, and W_{wave} is the wave orbital component. The addition of surface waves introduces an oscillatory component to the flow which increases the complexity of the flow regime and can have a significant impact on marine devices placed in these regions.

Figure 9.1 and Figure 9.2 show the measured average streamwise and vertical velocities obtained when the flume was operating under current-only, and combined wave and current flow conditions. Figure 9.1 compares the difference between current-only flow

using Profile 1 (WM00) and also Profile 1 with Wave 4, while Figure 9.2 compares the difference between current-only flow using Profile 2 (WM20) and also Profile 2 with Wave 5. The addition of the wave characteristic to each of the existing profiled current flows has a small effect on the average velocity at each water depth. The greatest difference between the current-only and the wave-current cases are < 5% with most water depths showing very good agreement.

The wave characteristic induces an oscillatory component around the mean current flow, referred to as the wave orbital component, as shown in Figure 9.3 and Figure 9.4. The amplitude of oscillation is greater towards the water surface for both the streamwise and vertical wave induced velocities in both P1W4 and P2W5, as shown in Table 9.2. The wave induced fluctuations for the streamwise and vertical velocities in the P2W5 case are greater than the P1W4 case in the top half of the water column. However, the wave induced oscillatory effects decay quicker in the P2W5 case in comparison to the P1W4 case; this is because the oscillatory motions of a wave can penetrate the water column by up to half the wavelength [73] and P1W4 has a greater wavelength of $L = 9.07\text{m}$ in comparison to P2W5 which has $L = 5.61\text{m}$. Both wave cases are intermediate water waves and therefore still have a significant vertical and horizontal velocity component at the base of the flume.

TABLE 9.2. VELOCITY FLUCTUATIONS INDUCED BY THE SURFACE WAVE FOR THE POINTS MEASURED NEAREST THE TOP, MIDDLE AND BOTTOM OF THE FLUME.

Distance from water surface (m)	Amplitude of fluctuation around mean value			
	P1W4		P2W5	
	Streamwise velocity (m/s)	Vertical velocity (m/s)	Streamwise velocity (m/s)	Vertical velocity (m/s)
-0.4	0.09	0.08	0.14	0.1
-1.0	0.06	0.05	0.06	0.04
-1.6	0.05	0.02	0.04	0.02

9 TURBINE PERFORMANCE UNDER WAVE-CURRENT FLOW CONDITIONS: REGULAR WAVES WITH PROFILED VELOCITY GRADIENTS

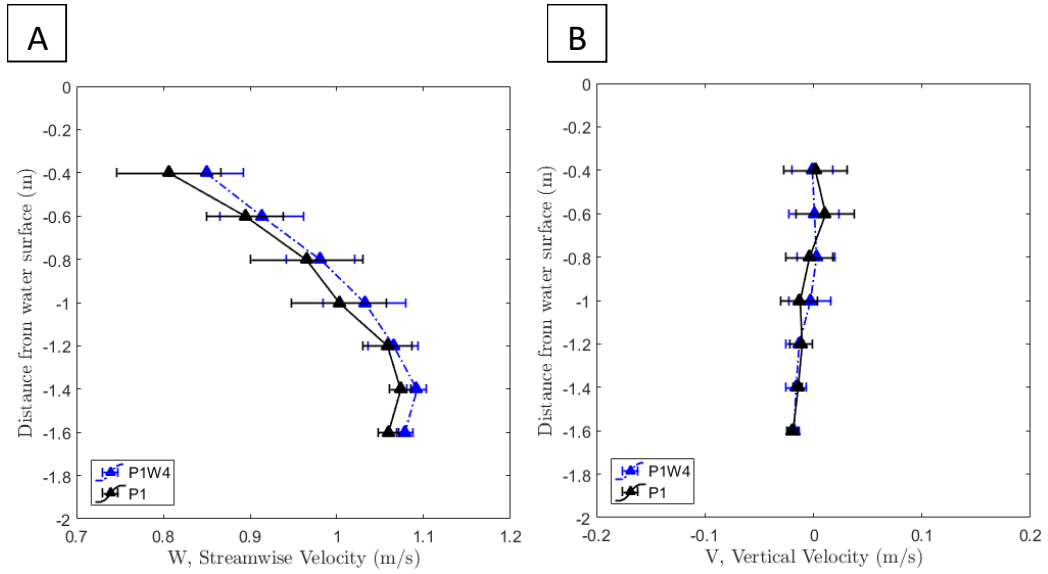


Figure 9.1. The A) streamwise and; B) vertical experimental velocity results through the water depth for conditions representative of Profile 1 (P1), and Profile 1 with Wave 4 (P1W4). Bars show +/- 1 standard deviation.

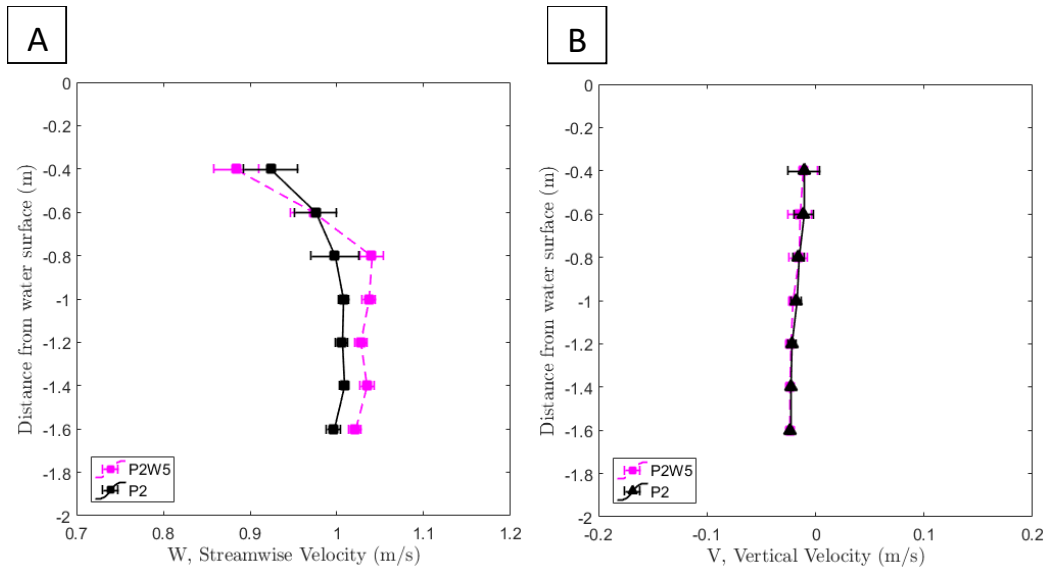


Figure 9.2. The A) streamwise and; B) vertical experimental velocity results through the water depth for conditions representative of Profile 2 (P2), and Profile 2 with Wave 5 (P2W5). Bars show +/- 1 standard deviation.

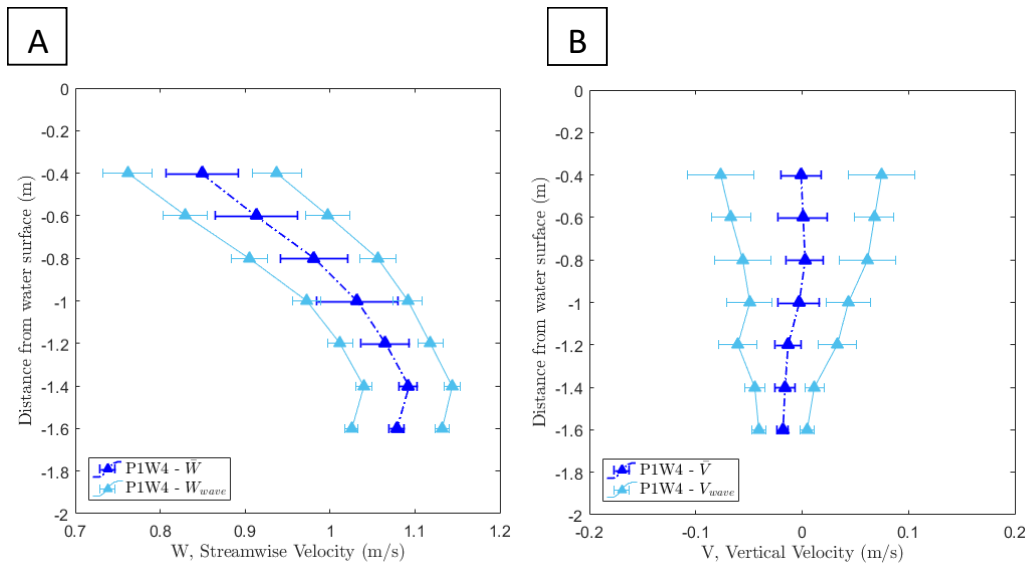


Figure 9.3. The mean and wave orbital components to the A) streamwise and; B) vertical experimental velocity results through the water depth for Profile 1 Wave 4 (P1W4). Bars show +/- 1 standard deviation. [\bar{W} or \bar{V} = average velocity, W_{wave} or V_{wave} = wave orbital velocity component]

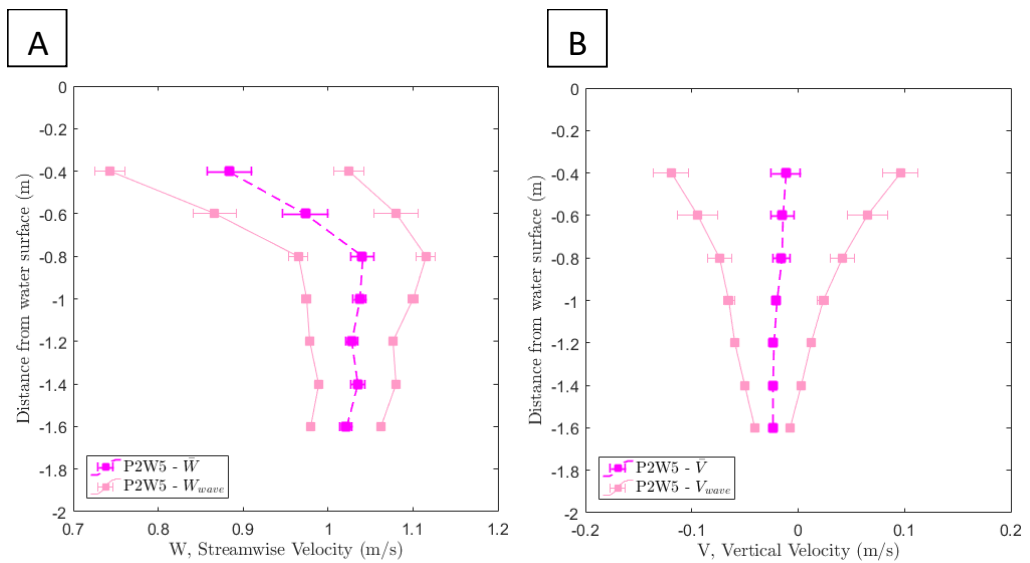


Figure 9.4. The mean and wave orbital components to the A) streamwise and; B) vertical experimental velocity results through the water depth for Profile 2 Wave 5 (P2W5). Bars show +/- 1 standard deviation. [\bar{W} or \bar{V} = average velocity, W_{wave} or V_{wave} = wave orbital velocity component]

The paddle type wave maker was set to produce a target wave frequency and height of 0.5Hz and 0.09m for P1W4, and 0.7Hz and 0.11m for P2W5. Both the wave frequency and wave height were measured over 7 to 10 different tests and an average was obtained across the multiple runs. For P1W4, the measured wave frequency was found to be $0.5 \pm$

0.003 Hz while the wave frequency for P2W5 was 0.7 ± 0.001 Hz. These values show very good agreement with the target values. The measured wave height for P1W4 was 0.082 ± 0.009 m, while for P2W5 the wave height obtained was 0.12 ± 0.008 m. Both mean values are within 9% of the target input value which shows the variability present in the measured wave height. Deflection of the wave probes was observed during the experimental testing which occurred due to the relatively high current velocity along with strong velocity variations induced by the surface waves; this would contribute to the unsteadiness of the readings but is hard to quantify. A summary of the target and measured wave frequency and wave heights are given in Table 9.3. Figure 9.5 shows an example of the surface elevation recorded by the wave probe for a test case using Waves 4 and 5.

TABLE 9.3. A SUMMARY OF THE TARGET AND EXPERIMENTALLY OBTAINED WAVE FREQUENCIES AND WAVE HEIGHTS.

	Mean value \pm 1 standard deviation			
	Target		Measured	
	P1W4	P2W5	P1W4	P2W5
Wave frequency, f (Hz)	0.5	0.7	0.5 ± 0.003	0.7 ± 0.001
Wave height, H (m)	0.09	0.11	0.082 ± 0.009	0.12 ± 0.008

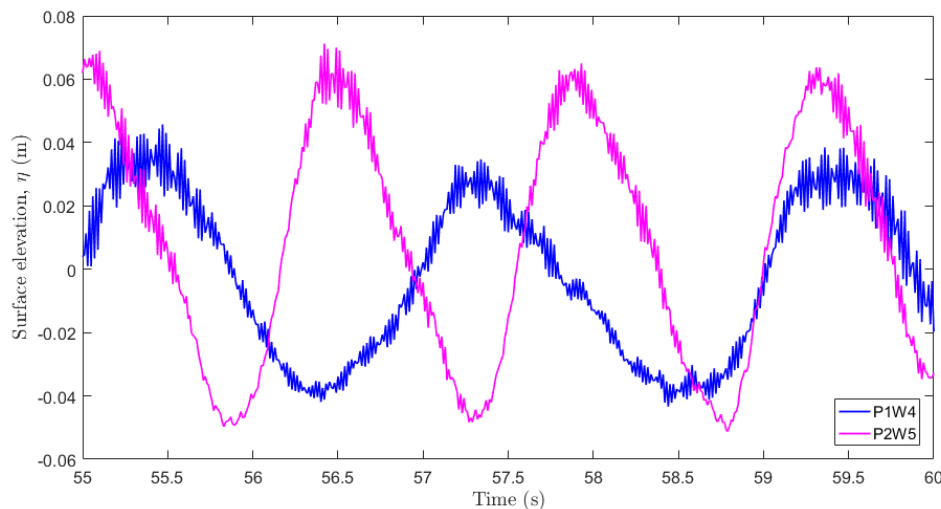


Figure 9.5. The experimental surface elevation results for P1W4 and P2W5.

The values of C_q , C_t , and C_p were found using the volumetrically averaged streamwise velocity to account for the differing velocity profiles over the swept area of the turbine, as shown in Figure 9.6. As discussed in Section 7.1.3, the streamwise velocity data sets at each water depth were examined to check the skewness of the distributions. As previously found, both sets of streamwise velocity data for the conditions using P1 and P2 were negatively skewed. In this study, this is also the case as shown by the modal values for the

streamwise velocity data through the water depth for P1W4 and P2W5 being a maximum of 9% and 4% greater than the mean value respectively. Therefore, the modal value gives a better representation of the predominant flow conditions at each water depth as explained in Section 7.1.3. The volumetrically averaged streamwise velocity over the turbine swept area is therefore calculated using the modal values of each data set. Table 9.4 shows the difference in the calculation of the \bar{W}_{vol} when using the mean and mode values.

TABLE 9.4. THE VOLUMETRICALLY AVERAGED STREAMWISE VELOCITY CALCULATED USING THE MEAN AND MODE.

	Volumetrically averaged streamwise velocity over turbine swept area (\bar{W}_{vol}), calculated using...		Difference	
	Mean (m/s)	Mode (m/s)	(m/s)	(%)
P1W4	1.022	1.046	0.024	2.4
P2W5	1.028	1.052	0.024	2.3

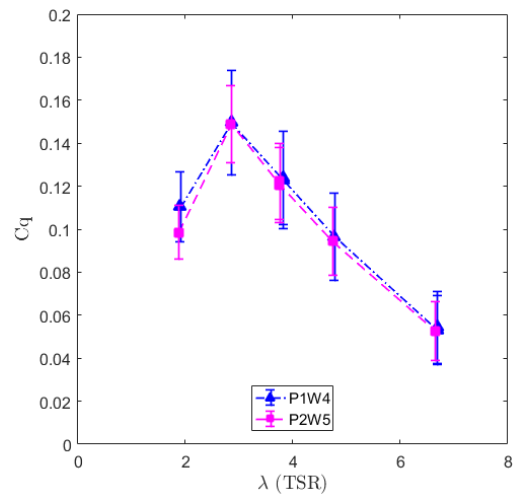
Strong agreement was found between the performance coefficients over the range of TSRs tested for P1W4 and P2W5. Over the peak power region ($3 < \text{TSR} < 5$), the greatest difference between the performance characteristics for P1W4 and P2W5 is 2%, 2% and 4% for C_q , C_t , and C_p respectively. The standard deviation data bars for all the P2W5 cases are marginally smaller than for P1W4 but the results across both cases are very similar. Table 9.5 shows the performance characteristics for each of the wave cases at peak power, TSR 4.

TABLE 9.5. VALUES FOR THE EXPERIMENTAL PERFORMANCE CHARACTERISTICS AT A TSR OF 4.

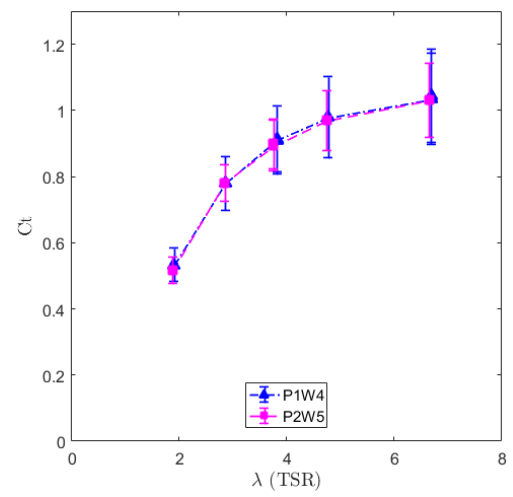
Performance characteristic	P1W4	P2W5	Difference
C_q	0.123	0.121	0.002
C_t	0.909	0.894	0.016
C_p	0.470	0.454	0.016

9 TURBINE PERFORMANCE UNDER WAVE-CURRENT FLOW CONDITIONS: REGULAR WAVES WITH PROFILED VELOCITY GRADIENTS

A



B



C

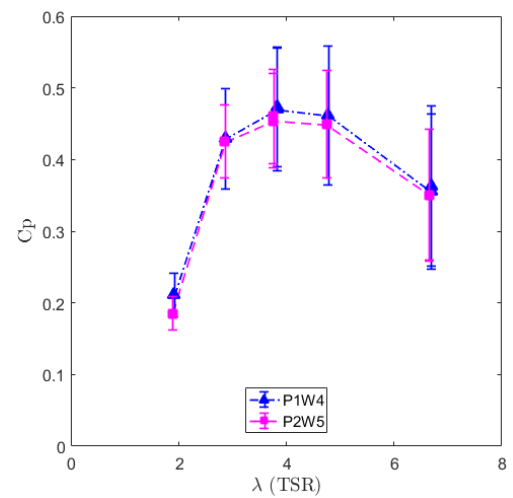


Figure 9.6. The A) C_q , B) C_t and C) C_p for the experimental results in wave and profiled flow conditions - P1W4 and P2W5. Bars show +/- 1 standard deviation.

9.2 CFD MODEL VALIDATION

A CFD model was developed to reproduce the wave-current conditions obtained in the tests carried out at the IFREMER flume. The model compiles previous design iterations which investigated the impact of current-only flow on the performance and loadings of a TST, as well as a model which achieved S2OT wave generation superimposed upon current conditions. A 'free surface' model was used for wave generation to occur with deflection of the water surface. This CFD model examines the effects of combined surface waves and profiled current interaction with a HATT, with particular interest in the performance and loadings obtained when compared to equivalent current velocities without waves. The general development of this CFD model complies with the procedures described in Chapters 7 and 8, while specific settings are detailed in the following section.

9.2.1 Geometry, mesh, setup summary

The 'free surface' model was setup as described in Chapter 6. However, the setup required for wave-current and turbine modelling is a combination of the settings described in Table 7.14 for modelling profiled current conditions with a rotating turbine, and Table 8.1 for simulating wave-current interaction. Table 9.6 provides a summary of the specific settings used when simulating regular waves using the wave characteristics of Wave 4 and 5. It is necessary to extend the length of the model domain when simulating waves to allow a suitable number of waves to propagate before reaching the numerical beach region towards the end of the domain. For this reason, a domain length equating to 8-10 wavelengths was found to be optimum, as discussed in Section 5.2.1, and therefore the length of the domain depends on the wavelength of the wave characteristic. The general mesh development is described in Chapter 5 with an example of the type of mesh used in wave-current and turbine simulations shown in Figure 6.11. The profiled current conditions and wave characteristic were input at the inlet of the domain. Further details on setting up the profiled current conditions, Profile 1 and 2, can be found in Section 5.4.3.1.1, with the general specification of each wave characteristic, Wave 4 and 5, shown in Section 5.4.3.1.2. The CEL expressions used to set up the wave-current and turbine model are given in Appendix A.

The time step of the simulation was controlled using a time step of Δt which satisfied both turbine and wave simulation requirements, as described in Chapter 6. Stability in the model occurred after 40-50 seconds and so all results reported in this study were taken after this time period. Monitor points were placed in the centre of the domain, 2m

upstream of the turbine at locations between $y = -0.1\text{m}$ and $y = -1.9\text{m}$, every 0.1m , enabling a visualisation of the turbine inflow conditions to be achieved.

The types of model discussed in this chapter are highly computationally expensive due to the complex nature of simulating profiled current flows, regular waves and turbine interaction. Therefore, only a single simulation for each type of wave and profiled velocity flow model could be accomplished. The models were setup to simulate the turbine loadings and performance at a TSR of 4 which focusses on peak power operating conditions. The CFD models were run using the Cardiff University supercomputing facilities (HPC cluster ‘Hawk’) using a mixture of 80 – 280 processors in single run periods of 3 days (≈ 72 hours) at a time. The total simulation time taken to run the CFD models for P1W4 and P2W5 was 4855 hours ($\approx 69 \times 3$ days) and 2735 hours ($\approx 39 \times 3$ days), respectively.

TABLE 9.6. SUMMARY OF THE GEOMETRY, MESH AND SETUP FOR ‘FREE SURFACE’ REGULAR WAVE, PROFILED FLOW CFD MODELS USING 2 DIFFERENT WAVE CHARACTERISTICS.

Geometry		Wave 4	Wave 5
Main domain dimensions	Length x Width x Depth	80 x 4 x 2.86 m	50 x 4 x 2.86 m
Subdomain cylinder dimensions	Diameter / Width	1.3 / 0.4 m	1.3 / 0.4 m
Turbine dimensions	Diameter	0.9 m	0.9 m
Mesh			
Main domain element sizing	Air-water interface region	$\Delta y = 0.01$ m	$\Delta y = 0.01$ m
		$\Delta z = 0.03$ m	$\Delta z = 0.03$ m
		$\Delta x = 0.025$ m	$\Delta x = 0.025$ m
	Mesh expansion from interface towards the ‘top’ boundary (Δy)	0.01 \rightarrow 0.1 m	0.01 \rightarrow 0.1 m
	Mesh expansion from interface towards the ‘base’ boundary (Δy)	0.01 \rightarrow 0.09 m	0.01 \rightarrow 0.09 m
	Mesh expansion from centreline to ‘side walls’ (Δx)	0.02 \rightarrow 0.012 m	0.02 \rightarrow 0.08 m
Sub domain element sizing	Mesh expansion from ‘inlet’ boundary to ‘outlet’ (Δz)	0.05 \rightarrow 0.1 m	0.05 \rightarrow 0.1 m
	MFR cylinder	0.024 m	0.024 m
	Blade tip	0.002 m	0.002 m
	Blade middle	0.004 m	0.004 m
	Blade root	0.004 m	0.004 m
Prism layer properties	Hub	0.006 m	0.006 m
	First layer thickness	0.00075 m	0.00075 m
	Number of layers	6	6
	Growth rate	1.0	1.0
Total number of elements	Main domain	12.4 million	8.8 million
	Turbine subdomain	3.1 million	3.1 million
	Total	15.5 million	11.9 million

Setup		
Time step	Δt (see Equation (6.3))	
Fluid Phases present	Water and air (multiphase)	
Buoyancy model	On	
Boundary conditions	inlet	Velocity-inlet (opening) + Profile Method
	Flow type	Regular wave and profiled current flow
	Input velocity components	U: Inlet.Water.Velocity $u(x,y,z)$ V: Inlet.Water.Velocity $v(x,y,z)$ + <i>VerticalParticleVelocity</i> W: Inlet.Water.Velocity $w(x,y,z)$ + <i>HorizontalParticleVelocity</i>
	outlet	Pressure-outlet (opening)
	Reference pressure	$P_{ref} = (\rho_{water} - \rho_{air}) \cdot g \cdot (h - y)$
	Side walls and base	No-slip wall
	Top	Pressure-opening
	Relative pressure	$P_{rel} = 0 Pa$
	Stanchion	No-slip wall
	Hub and turbine blades	No-slip wall

9.2.2 Regular wave and profiled flow CFD model validation

Initially, the flow characteristics produced by the CFD models were compared to the experimental data collected from testing at the IFREMER flume. Figure 9.7 shows the experimental and CFD results for the average streamwise and vertical velocities given by the wave-current conditions of P1W4 and P2W5. The streamwise velocity results show very good agreement between the experimental and the CFD model results. The greatest difference between the two data sets was 0.015 m/s and 0.024 m/s for P1W4 and P2W5 which equates to < 2.5% of the volumetrically averaged streamwise velocities, as shown in Table 9.7. As found previously with the current-only conditions discussed in Chapter 7, the vertical velocity results given by the CFD models do not develop the same profile as the experimental results. Nevertheless, differences between the two data sets were again < 2.5% of the volumetrically averaged streamwise velocities and therefore within an acceptable margin.

TABLE 9.7. VOLUMETRICALLY AVERAGED STREAMWISE VELOCITY FOR THE EXPERIMENTAL AND CFD MODEL RESULTS.

Profile	Volumetrically averaged streamwise velocity over swept area of the turbine, \bar{w}_{vol} (m/s)	
	Experimental	CFD
P1W4	1.046	1.009
P2W5	1.052	1.021

9 TURBINE PERFORMANCE UNDER WAVE-CURRENT FLOW CONDITIONS: REGULAR WAVES WITH PROFILED VELOCITY GRADIENTS

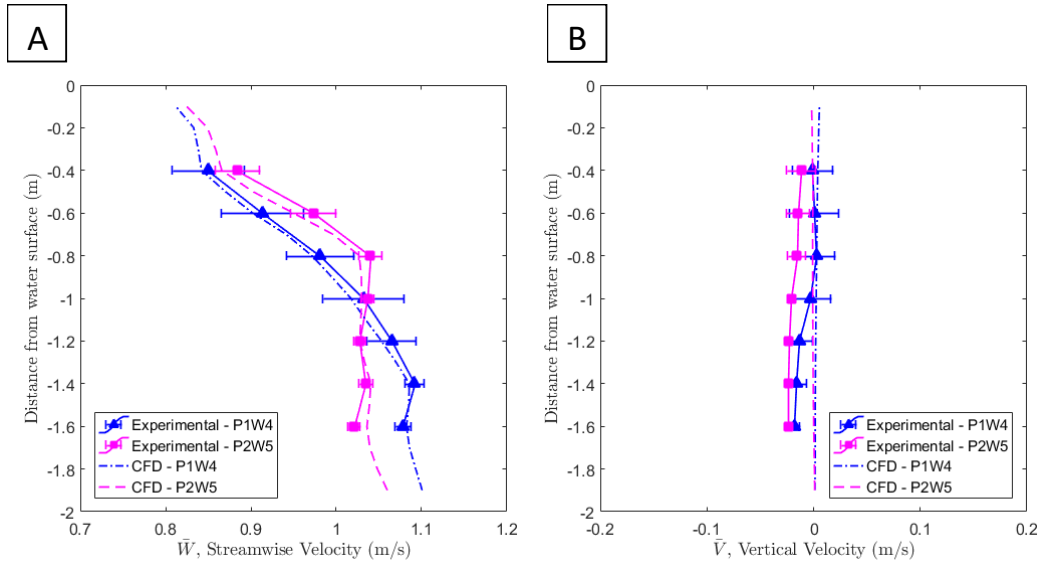


Figure 9.7. The mean A) streamwise and; B) vertical, CFD and experimental velocity results through the water depth for P1W4 and P2W5. Bars show +/- 1 standard deviation.

A time series of the streamwise and vertical velocities at 19 positions through the water depth ($y = -0.1$ to -1.9 m from the SWL) can be seen in Figure 9.8 and Figure 9.9 for the conditions relating to P1W4 and P2W5. Initially looking at the streamwise velocities in Figure 9.8, it can be seen that the wave characteristic induces an oscillatory component to the flow around that of the mean profiled current velocity, as discussed in Section 9.1. The CFD results for P1W4 in Figure 9.8A, show a range of wave orbital velocities between ± 0.05 and ± 0.09 m/s with the greater fluctuations towards the water surface, decaying as the wave motion penetrates through the water depth. The P2W5 case, shown in Figure 9.8B, gives a greater range of wave orbital velocities between ± 0.04 and ± 0.13 m/s. The vertical velocities, as shown in Figure 9.9, oscillate around 0 m/s due to the inability of the CFD to replicate the experimental profiled vertical velocity. However, the magnitude of the vertical wave orbital velocity component is still significant and indicates that the turbine will be subjected to considerable forces in both the horizontal and vertical directions.

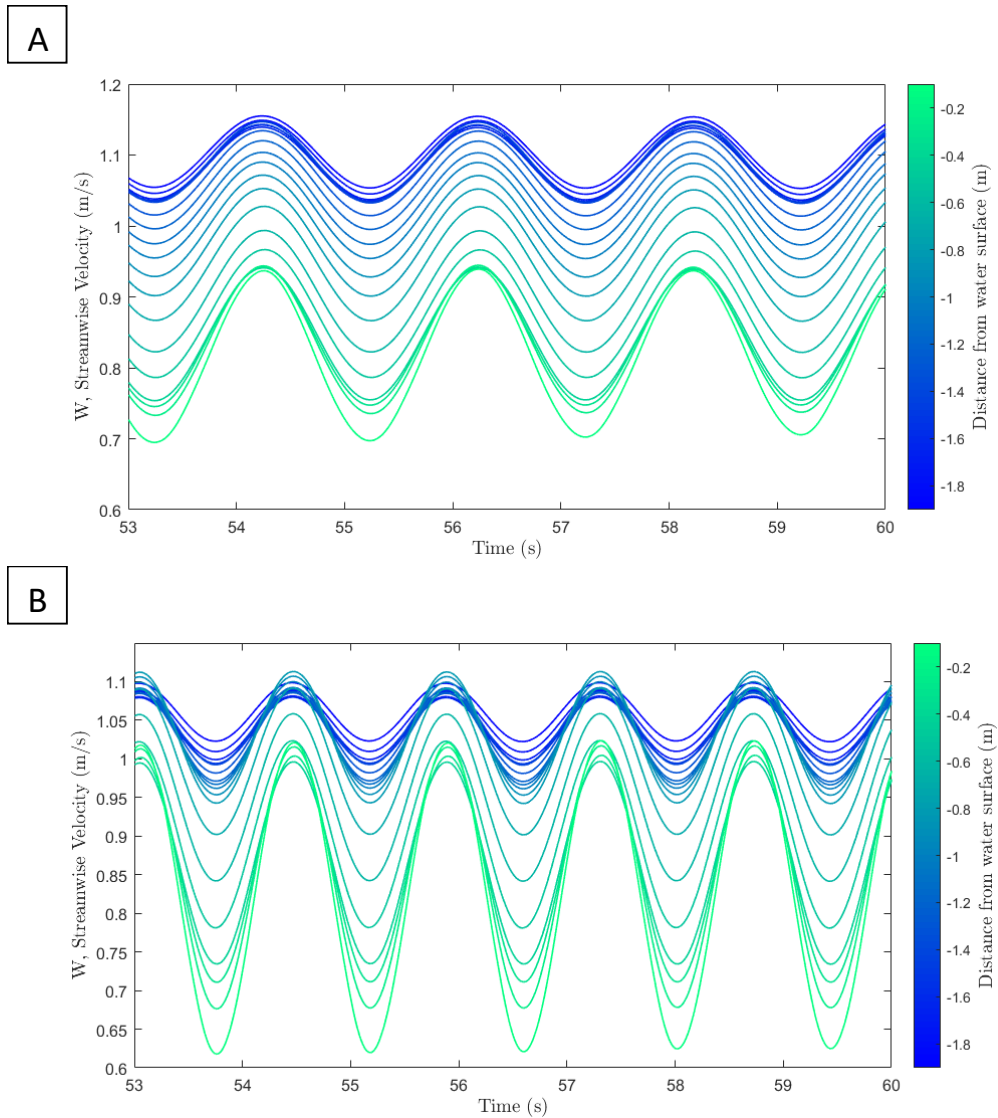


Figure 9.8. A timeseries of the CFD model streamwise velocities taken at 19 positions through the water depth (-0.1 to -1.9m from the SWL) for the conditions given by A) P1W4 and; B) P2W5.

At a water depth of -0.55 to -1.45m from the SWL, the turbine would be present and therefore the flow conditions will have a direct effect on its loadings and performance. For the conditions given by P1W4, the streamwise velocity would reach a minimum of 0.82 m/s towards the water surface at a turbine blade position of TDC and a maximum of 1.14 m/s further down the water column as a single blade passes through the different flow regions and the tip reaches BDC. This is a difference of 0.32 m/s between what a single blade tip will experience at difference stages in the rotational cycle. The streamwise velocity for P2W5 would have a minimum and maximum of 0.85 m/s and 1.09 m/s, respectively, which equates to a difference of 0.24 m/s across the turbine diameter. The current profile that the wave characteristic is superimposed upon will affect the amount of shear across the water depth and consequently the loadings imposed on the turbine. The combination of

9 TURBINE PERFORMANCE UNDER WAVE-CURRENT FLOW CONDITIONS: REGULAR WAVES WITH PROFILED VELOCITY GRADIENTS

wave and current interaction together will have a significantly greater effect across the turbine, as opposed to current or wave only conditions.

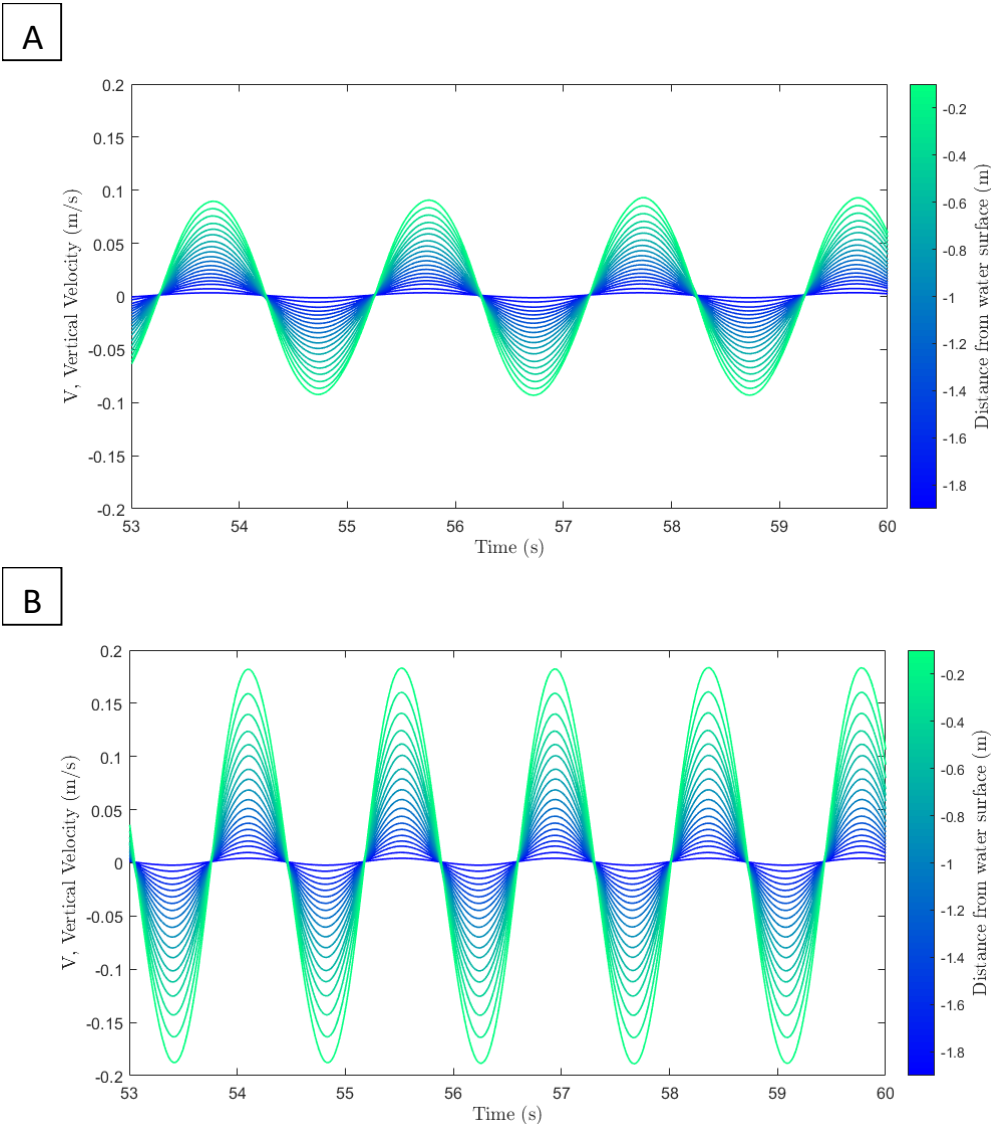


Figure 9.9. A timeseries of the CFD model vertical velocities taken at 19 positions through the water depth (-0.1 to -1.9m from the SWL) for the conditions given by A) P1W4 and; B) P2W5.

Figure 9.10 and Figure 9.11 show a comparison between the experimental and CFD model results for the wave orbital velocity component which is superimposed upon the mean current velocity when operating under the conditions given by P1W4 and P2W5, respectively. The results for the wave induced velocity fluctuation around the average streamwise velocity, as shown in Figure 9.10A and Figure 9.11A, displays very good agreement between the experimental and the CFD model data sets. The greatest difference between the wave orbital component for both data sets and both wave-current characteristics is 0.01 m/s which is 1% of the volumetrically averaged streamwise velocities.

9 TURBINE PERFORMANCE UNDER WAVE-CURRENT FLOW CONDITIONS: REGULAR WAVES WITH PROFILED VELOCITY GRADIENTS

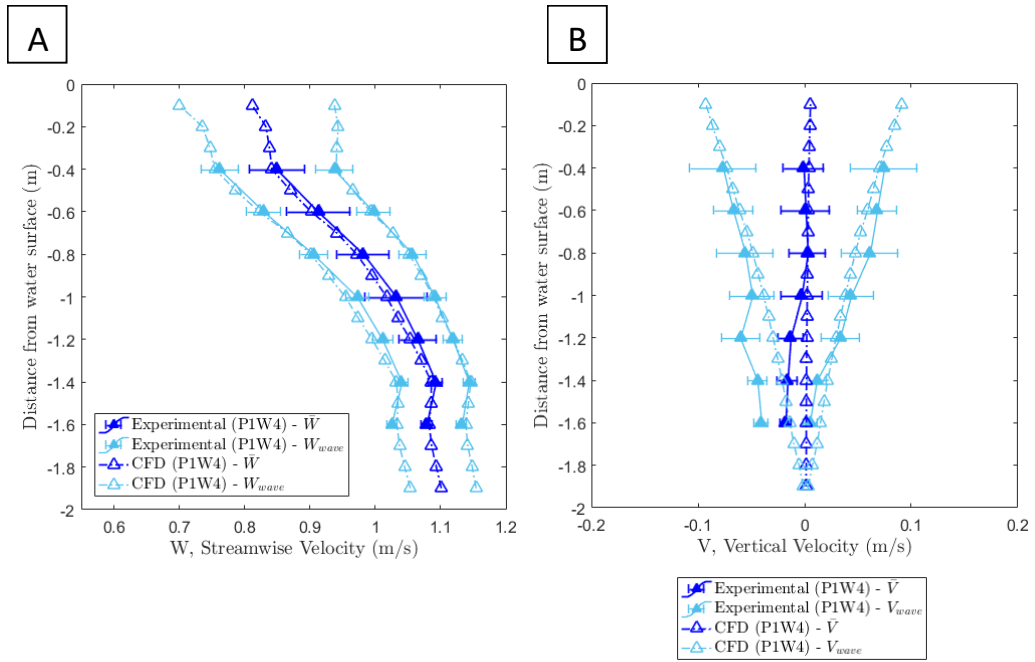


Figure 9.10. The mean and wave orbital components to the A) streamwise and; B) vertical, CFD and experimental velocity results through the water depth for P1W4. Bars show +/- 1 standard deviation. [\bar{W} or \bar{V} = average velocity, W_{wave} or V_{wave} = wave orbital velocity component]

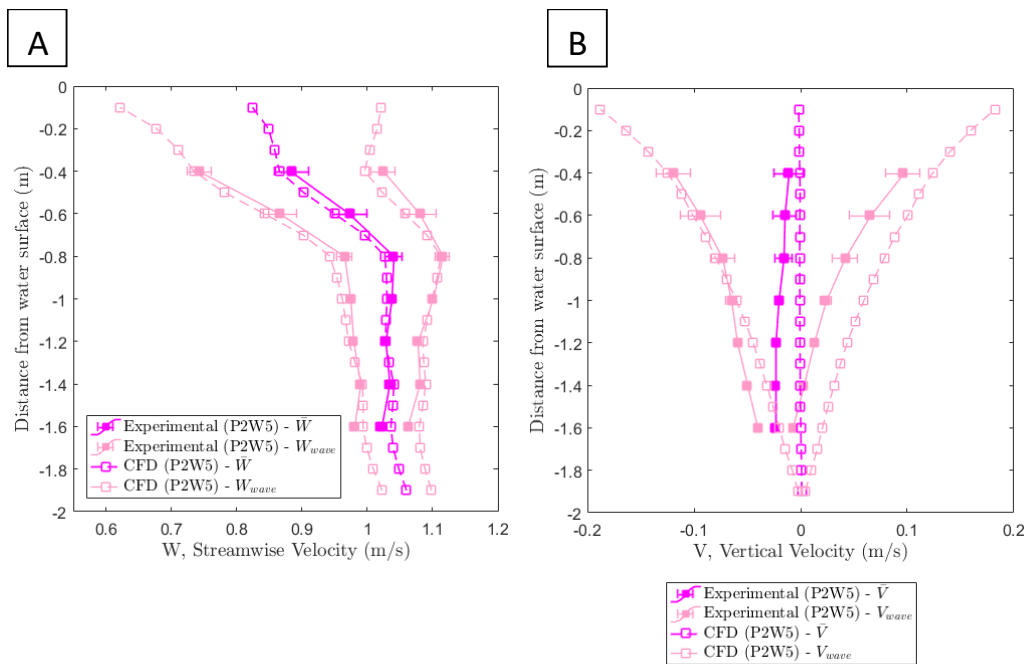


Figure 9.11. The mean and wave orbital components to the A) streamwise and; B) vertical, CFD and experimental velocity results through the water depth for P2W5. Bars show +/- 1 standard deviation. [\bar{W} or \bar{V} = average velocity, W_{wave} or V_{wave} = wave orbital velocity component]

The vertical velocities, Figure 9.10B and Figure 9.11B, have a larger discrepancy between the experimental and CFD results, particularly towards the bottom of the water column. The differences are because the mean velocity values show less agreement between the data sets and therefore the fluctuation induced by the wave around this mean value is also offset by the same amount. Figure 9.12B and Figure 9.13B show the wave orbital components in the vertical direction for P1W4 and P2W5 with their mean values subtracted. This data shows that for the vertical wave orbital components, good agreement is displayed by the experimental and CFD results for both wave-current characteristics. It is the differences in the mean velocities which offsets the wave orbital components and therefore appears to agree less well. All vertical velocity CFD results are within 1 standard deviation of the equivalent experimental values apart from at a distance from the SWL of -0.8 and -1.2m in the P2W5 case. However, at this water depth the greatest difference between the experimental and CFD results is 2% which is still small. The streamwise wave orbital velocity components subtracted from the mean values are shown in Figure 9.12A and Figure 9.13A. Good agreement is generally observed with a maximum difference between the two data sets of < 1% of the volumetrically averaged streamwise velocity.

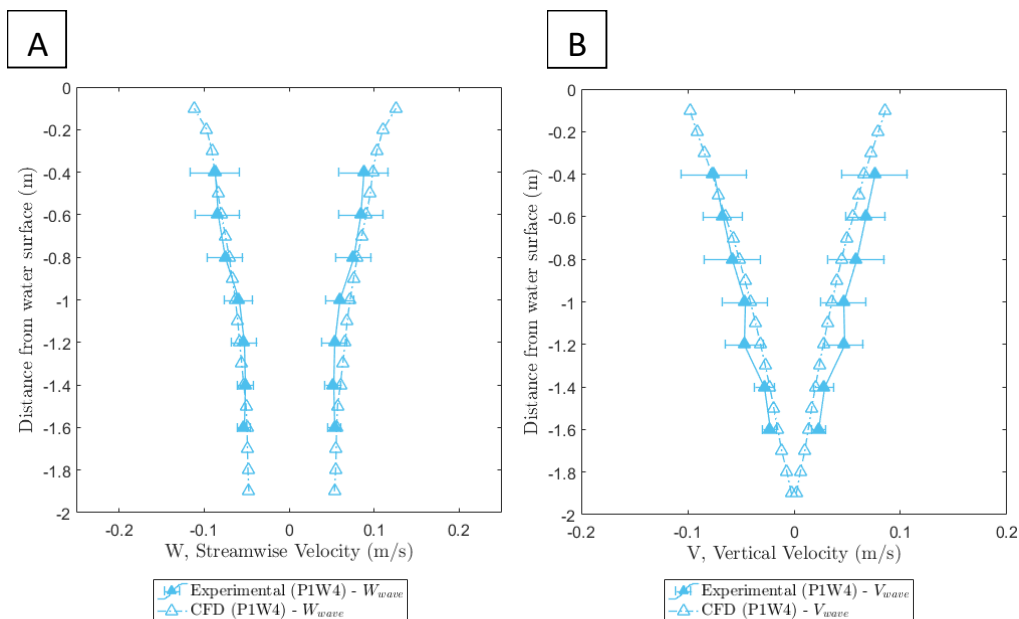


Figure 9.12. The wave orbital components for the A) streamwise and; B) vertical, CFD and experimental velocity results through the water depth for P1W4. Bars show +/- 1 standard deviation. [W_{wave} or V_{wave} = wave orbital velocity component]

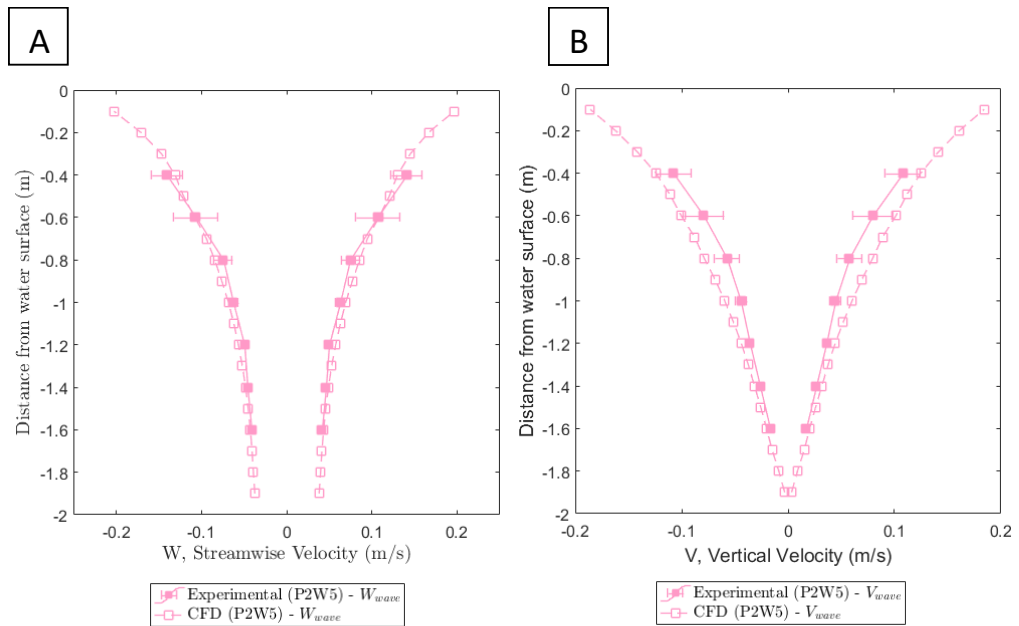


Figure 9.13. The wave orbital components for the A) streamwise and; B) vertical, CFD and experimental velocity results through the water depth for P2W5. Bars show +/- 1 standard deviation. [W_{wave} or V_{wave} = wave orbital velocity component]

The surface elevation of the wave was measured at the same location as the flow velocity monitor points, 2m upstream of the turbine; this gave a good indication of the wave surface profile before interaction of the stanchion and water surface distorted its shape. The CFD models produced a wave height of 0.081m and 0.12m for the conditions represented by P1W4 and P2W5 respectively. These values show good agreement with the experimental results, with only 1.3% difference for P1W4 and no difference in the average value for P2W5. Figure 9.14 and Figure 9.15 show the surface elevation of the wave over a 5 second time period for the experimental and CFD model results of P1W4 and P2W5, respectively. Experimentally Figure 9.14 and Figure 9.15 show a snapshot of the total data set and so an average surface profile is taken over the total time series to get a more representative average of the sample conditions. The CFD results show stability after 40s of run time and therefore show a repeating pattern after this point has been reached.

The average wave frequency given by the CFD models for P1W4 and P2W5 are 0.49 Hz and 0.72 Hz, which shows a minor 2% and 3% difference when compared to the experimental wave frequencies, respectively. Table 9.8 shows a comparison between the experimental and CFD results for the values obtained for the wave height and wave frequency.

9 TURBINE PERFORMANCE UNDER WAVE-CURRENT FLOW CONDITIONS: REGULAR WAVES WITH PROFILED VELOCITY GRADIENTS

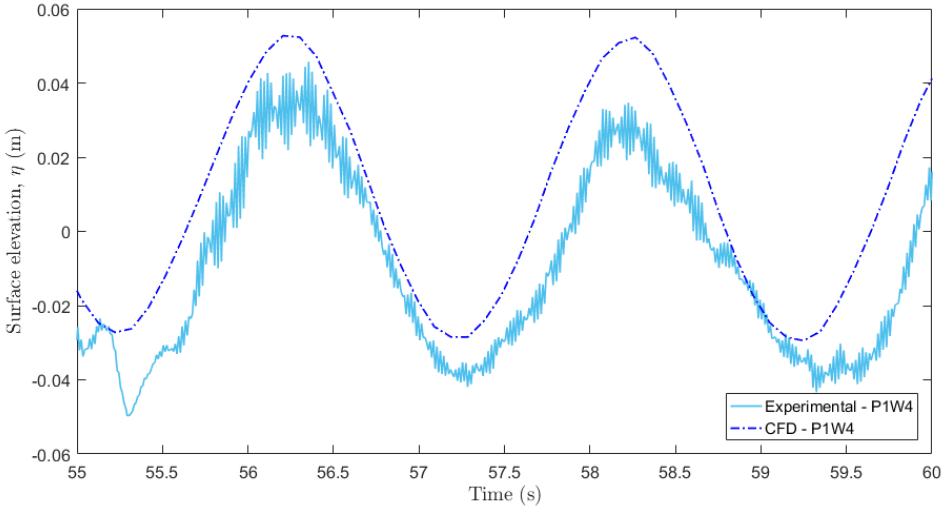


Figure 9.14. The experimental and CFD surface elevation for the conditions given by P1W4.

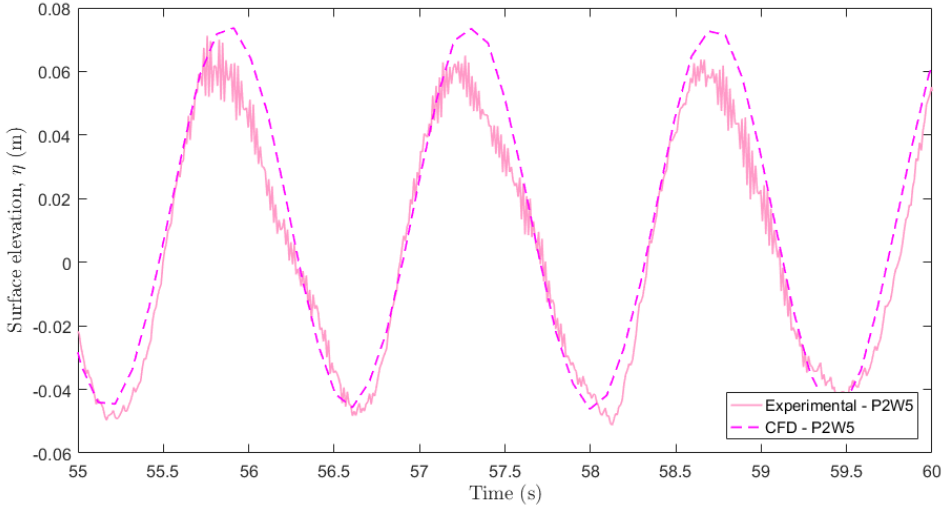


Figure 9.15. The experimental and CFD surface elevation for the conditions given by P2W5.

TABLE 9.8. A SUMMARY OF THE EXPERIMENTAL AND CFD MODEL WAVE FREQUENCIES AND WAVE HEIGHTS.

	Mean value (± 1 standard deviation)			
	P1W4		P2W5	
	Experimental	CFD	Experimental	CFD
Wave frequency, f (Hz)	0.5 ± 0.003	0.49	0.7 ± 0.001	0.72
Wave height, H (m)	0.082 ± 0.009	0.081	0.12 ± 0.008	0.12

Overall, the CFD models reproduce the flow conditions generated by the experimental flume testing very well. The differences between the experimental and CFD model results for the mean velocity and wave orbital velocity components are all < 3% of the volumetrically averaged streamwise velocity. The wave surface elevation produced by the

CFD model is within 2% of the experimental results, and the wave frequencies show < 3% difference. Figure 9.16 shows the flow conditions generated by the CFD models at an instantaneous moment in time for P1W4 and P2W5, as well as indicating the position of the wave crests.

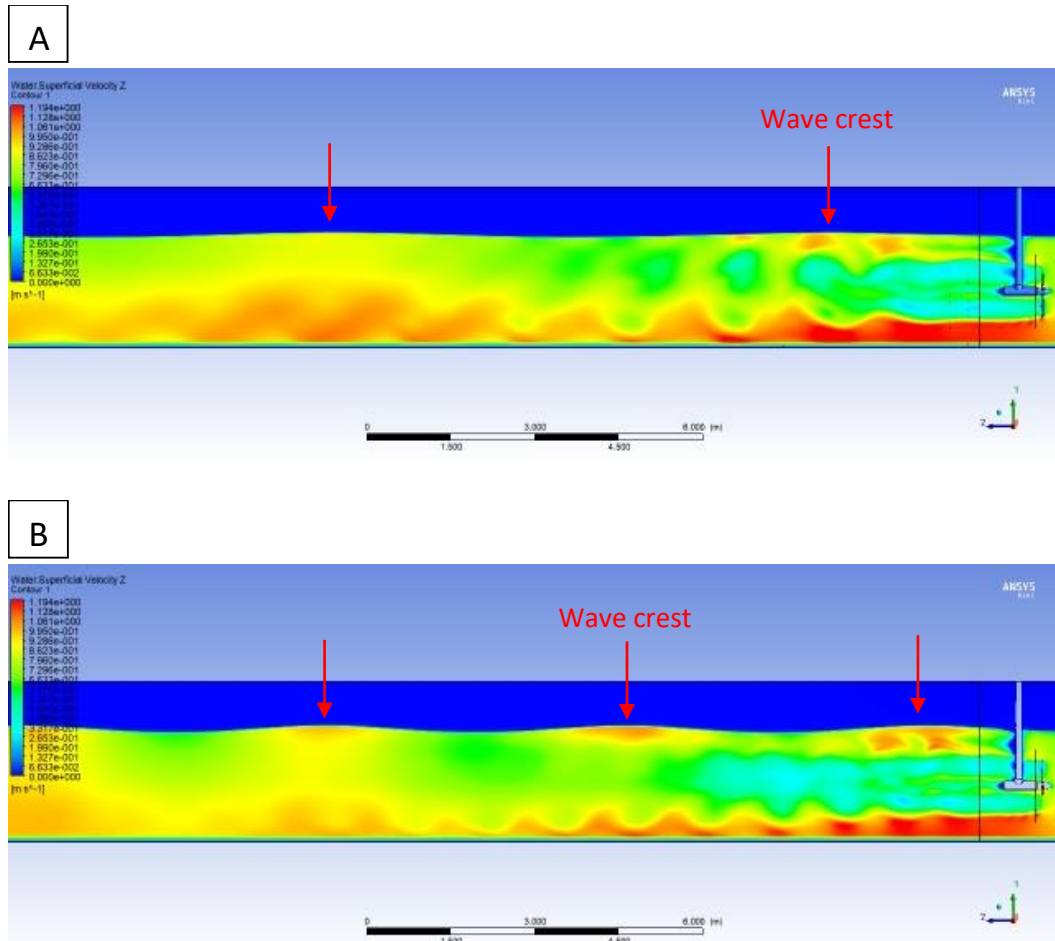


Figure 9.16. The instantaneous streamwise velocity when the turbine is operating at a TSR of 4 for the inlet wave and current conditions representative of: A) P1W4; and B) P2W5.

Figure 9.17 shows the average C_q , C_t and C_p for the experimental results over a range of TSRs while the CFD results exist only at a TSR of 4. The C_q and C_p estimated by the CFD model at a TSR of 4 show good agreement with the experimental results, both lying within 1 standard deviation of the mean value. The agreement between the CFD and experimental data sets for the C_t at a TSR of 4 is still reasonable but lies on the limit of 1 standard deviation from the mean. This is consistent with previous C_t results under current-only conditions (Section 0) which also showed less agreement. Table 9.9 shows a summary of the average experimental and CFD results as well as the differences between them.

9 TURBINE PERFORMANCE UNDER WAVE-CURRENT FLOW CONDITIONS: REGULAR WAVES WITH PROFILED VELOCITY GRADIENTS

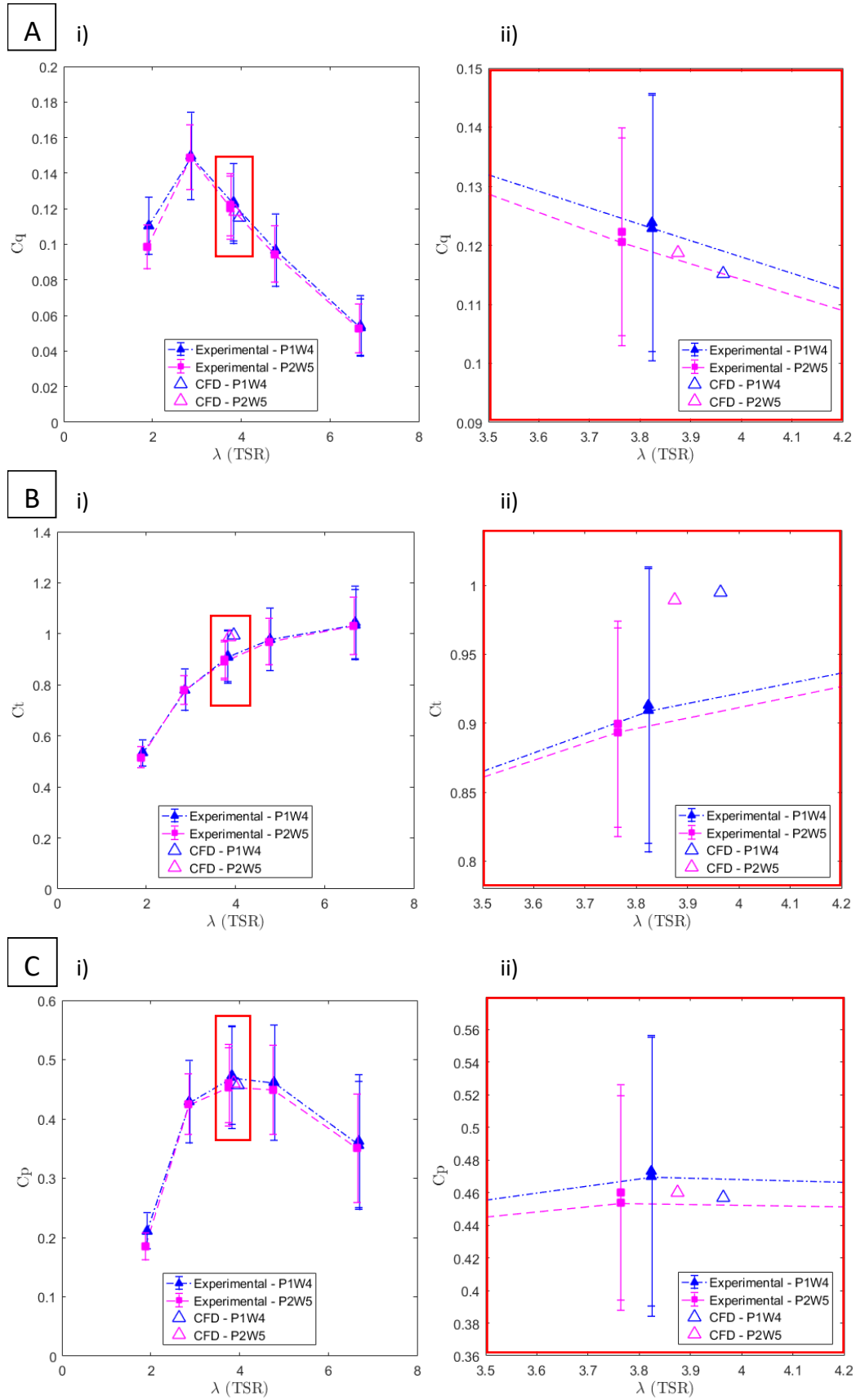


Figure 9.17. The Ai) C_q , Bi) C_t and Ci) C_p for the experimental and CFD results in wave-current conditions, with a zoomed in version of TSR 4 in ii). Bars show +/- 1 standard deviation.

TABLE 9.9. THE EXPERIMENTAL RESULTS, CFD MODEL RESULTS, AND THE DIFFERENCE BETWEEN THEM FOR C_q , C_t AND C_p , IN PROFILED FLOW CONDITIONS.

Case	C_q			C_t			C_p		
	Exp.	CFD	Dif.	Exp.	CFD	Dif.	Exp.	CFD	Dif.
P1W4	0.123	0.115	0.008	0.909	0.995	0.086	0.470	0.457	0.013
P2W5	0.121	0.119	0.002	0.894	0.990	0.096	0.454	0.460	0.006

The out of plane bending moment (BM_x) was compared between the two data sets to further analyse the transient behaviour of the turbine under wave-current conditions. A single turbine blade is presented for each case as the same trends are displayed on each of the three blades. Figure 9.18 shows the CFD results for the BM_x for a single blade in each of the wave-current conditions. Previous studies carried out in current-only conditions, Chapter 7, showed that the dominating fluctuation in the BM_x comes from the stanchion interaction with each turbine blade every rotation. The introduction of waves in this chapter adds an extra component that will affect the loadings on the turbine.

Under P1W4 conditions, the rotational speed was set so that a single blade crossed the stanchion at TDC every 0.7 seconds and the wave period of W4 is 2.0 seconds, so that every 14 seconds, the turbine will rotate 20 times while 7 waves propagate past the turbine. Stanchion rotations are marked with a red arrow and each wave period is marked with a green arrow in Figure 9.18. Due to these two components being out of phase, the transient BM_x will alter over a 14 second window; however, each 14 second window will repeat the same pattern. This 14 second window has been marked on Figure 9.18A and shows the curve of the repeating envelope which will be analysed to assess the average BM_x as well as the fluctuation in the results.

For the conditions represented by P2W5, the time taken for a blade to do a single rotation is 0.7 seconds and the wave period of W5 is 1.43 seconds. The wave period is therefore almost twice the rotational frequency and so both components are essentially in phase with each other. This results in a slight drop in BM_x as a single blade passes the stanchion (marked by the red arrows) but does not affect the transient BM_x as much as in P1W4 as this case is dominated by the wave interaction. Figure 9.18A and B are plotted for different amounts of time in order to clearly observe the features mentioned.

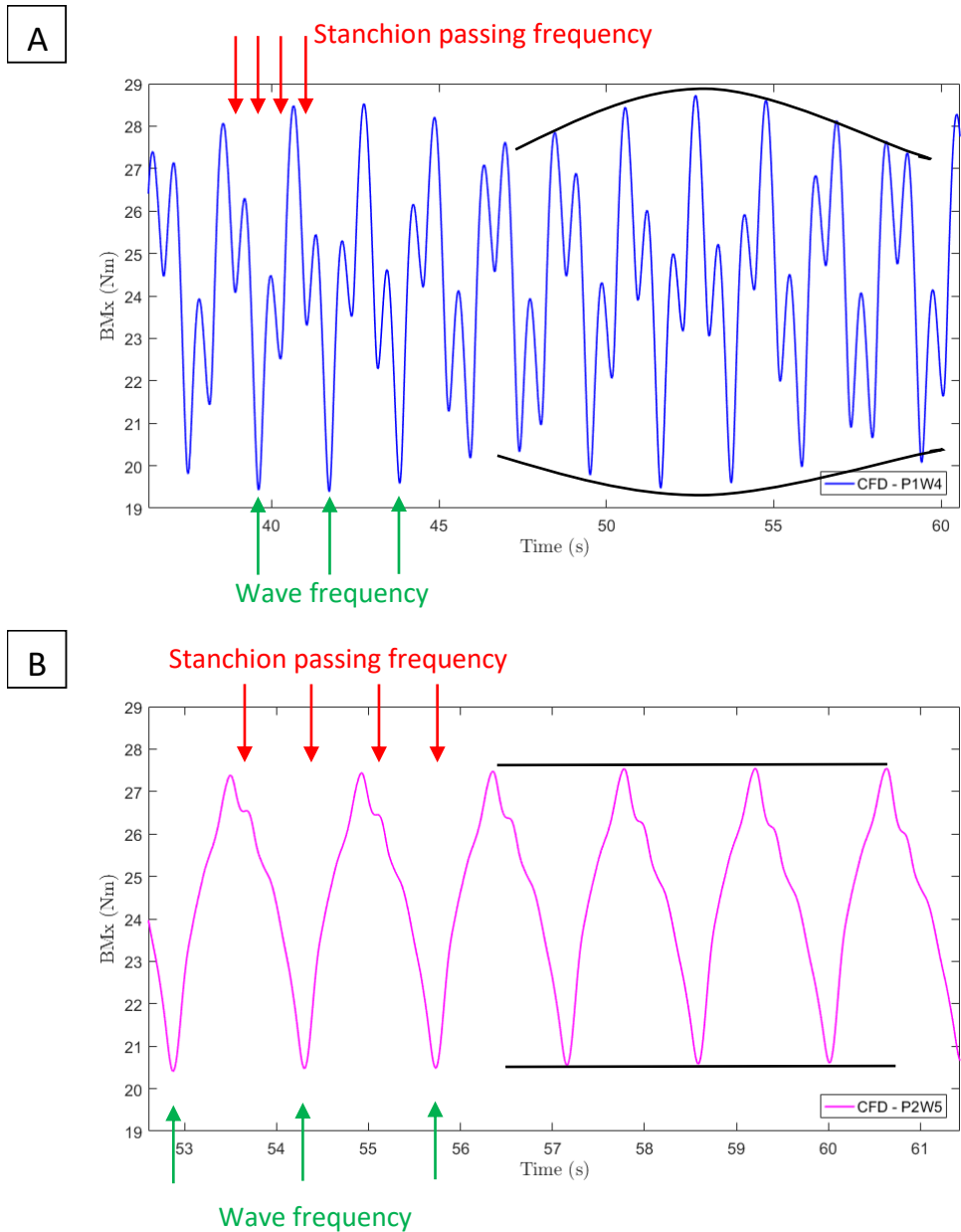


Figure 9.18. The CFD results for the out of plane bending moment on a single blade in wave-current conditions representative of A) P1W4; and B) P2W5.

As previously mentioned in Chapter 7, the TSA method was used to analyse the experimental results by reducing the noise in the signal in order to accentuate the underlying fluctuations in the time series. A comparison of the average BM_x calculated using the TSA method for the experimental and CFD results can be seen in Figure 9.19, while a summary of the average values are displayed in Table 9.10. There is good agreement between the experimental and CFD average values while also showing similarities between the shape of the results fluctuation.

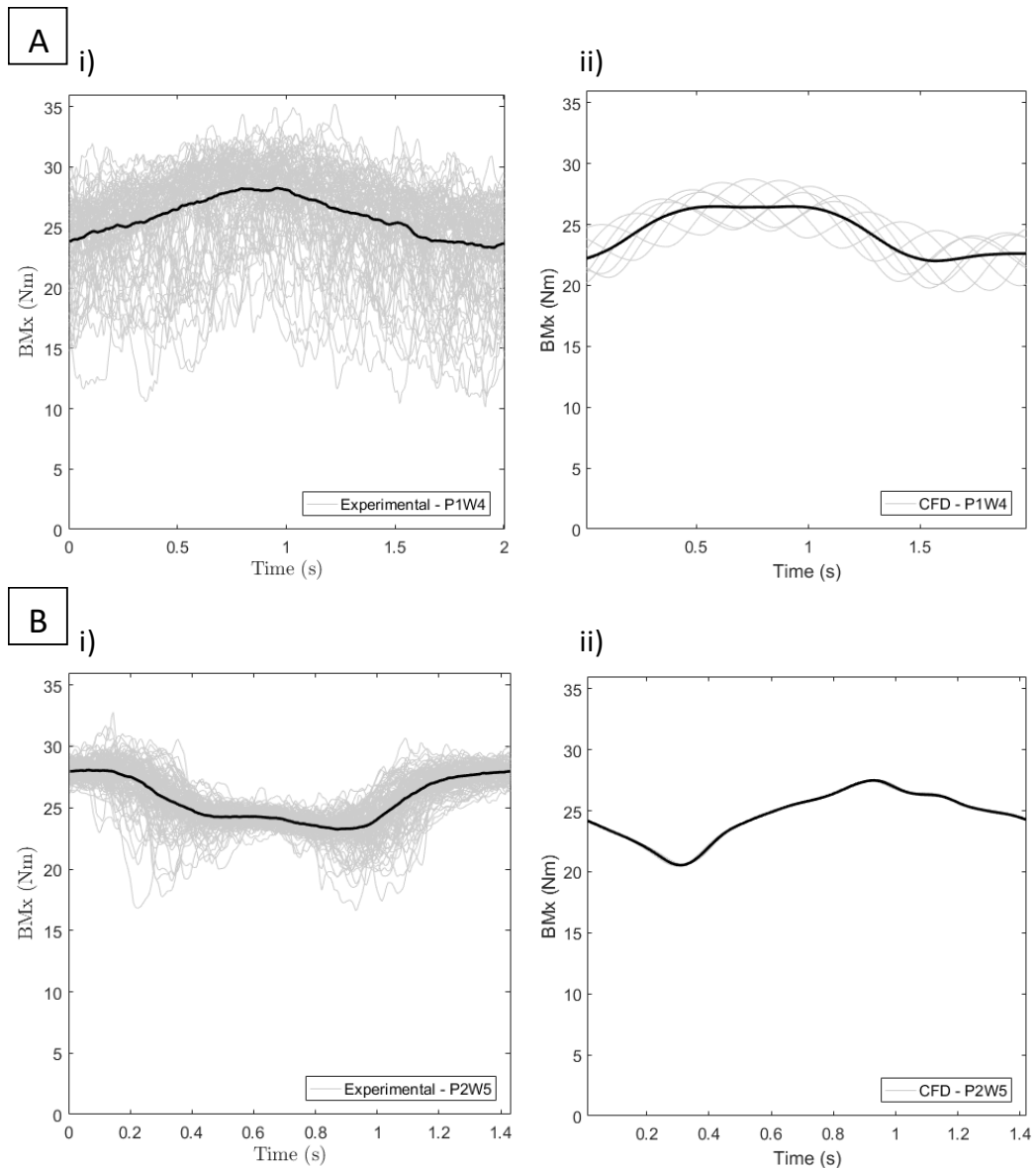


Figure 9.19. The average out of plane bending moment fluctuation on a single blade calculated using TSA for A) P1W4, and B) P2W5 using i) experimental, and ii) CFD results.

Due to the transient results consisting of multiple frequencies, it is difficult to use the maximum and minimum values of the average BM_x over a single turbine rotation to calculate the amplitude of fluctuation in the signal. Instead the FFT method was used to decompose the signal into its dominant frequencies created by stanchion and wave interactions with the turbine.

TABLE 9.10. THE AVERAGE CFD AND EXPERIMENTAL OUT OF PLANE BENDING MOMENT RESULTS FOR WAVE-CURRENT CONDITIONS.

Case	Average out of plane bending moment, BM_x (Nm)		
	Experimental	CFD	Difference
P1W4	25.85	24.45	1.4
P2W5	25.65	24.58	1.07

Figure 9.20 shows a FFT analysis for the experimental and CFD data sets for each wave-current characteristic. Again, the red arrows mark the rotational frequency of the turbine while the green arrows refer to the wave frequency. Looking at the wave-current case of P1W4, Figure 9.20i), there are two clear peaks at a frequency of 0.7 Hz and 1.4 Hz which, respectively, correspond to the wave frequency and rotational frequency at which a blade passes the stanchion. These two dominant peaks are what would be expected with these flow conditions as the wave and stanchion frequencies both contribute to the overall signal but are out of phase. Previous analysis of current-only conditions in Chapter 7 shows a good agreement between the amplitude of the dominant frequency at the stanchion crossing frequency for P1 and P1W4. The amplitude of fluctuation of the BM_x for each component in the experimental and CFD results are shown in Table 9.11.

The FFT analysis for P2W5, shown in Figure 9.20ii), shows a clear peak at the wave frequency of 0.5 Hz with a much smaller peak at the stanchion crossing frequency of 1.4 Hz. The current profile in this case is less shearing across the water depth than in P1W4, resulting in less of a shadow effect from a blade passing the stanchion and therefore a smaller amplitude of fluctuation. This observation agrees with the work previously carried out in Chapter 7 for the current-only conditions of P2. In the combined wave-current case of P2W5, the wave has a much more dominant frequency in comparison to the stanchion crossing frequency, while in P1W4 both components have a similar amplitude of fluctuation.

This analysis shows the considerable effect that a velocity profile across the water column can have on the loading fluctuations of the turbine. The uniform current-only case has a small amplitude of fluctuation in the $BM_x < 0.5$ Nm. Introducing a small amount of shear into the current velocity (P2) through the water column increases this amount of fluctuation to ≈ 0.7 Nm. A large shearing velocity profile (P1) has a significant effect on the amplitude of fluctuation, reaching a magnitude of ≈ 2.4 Nm. Both wave cases induce an amplitude of fluctuation in the BM_x of $\approx 2.2 - 2.7$ Nm, similar to the amplitude of fluctuation caused by P1. Therefore, a velocity profile as severe as P1 can have just as big

an effect as the wave induced loadings (experienced in this study). The phase of the wave in comparison to the position of a turbine blade in its rotational cycle can have a substantial impact on the loading that a single blade experiences. It is important to minimise large loading fluctuations and therefore control strategies can be developed and used to monitor incoming waves and adjust the turbine rotational speed to optimise the blades position in comparison to the waves [53].

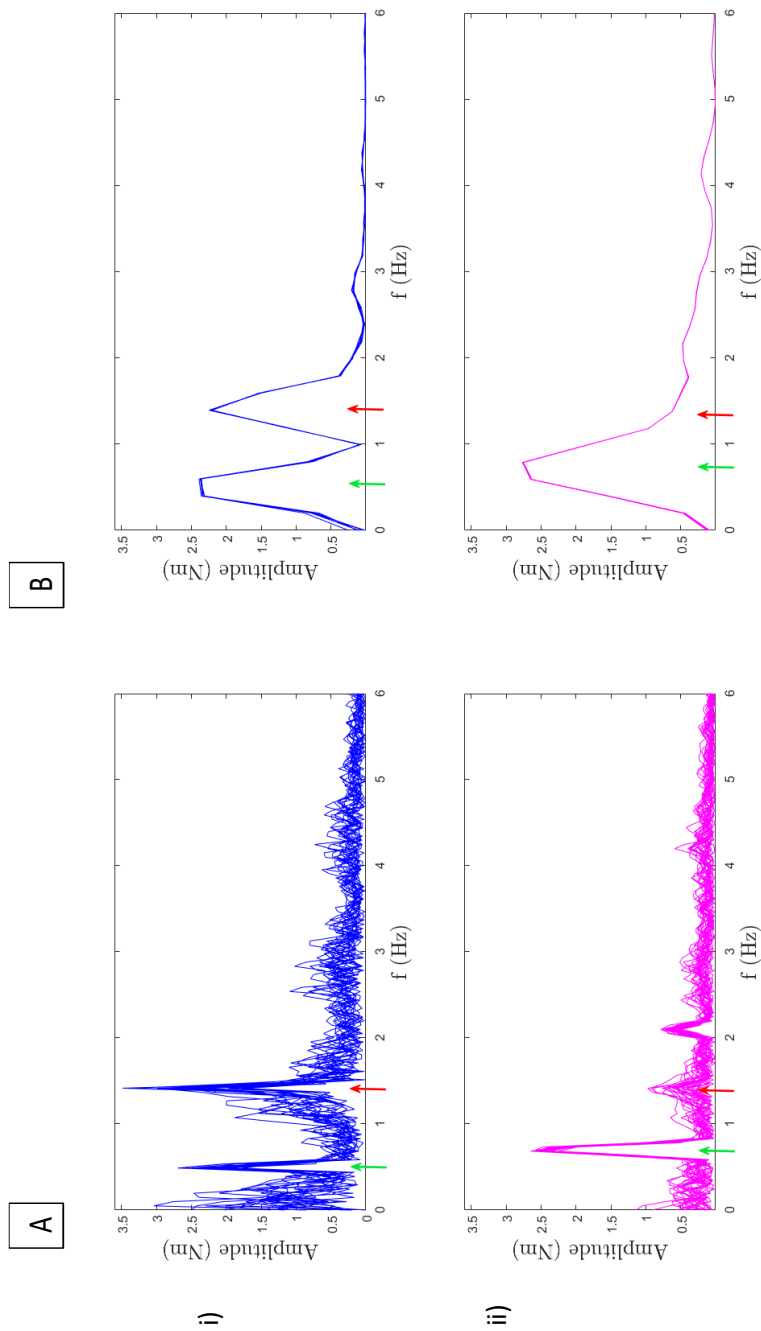


Figure 9.20. FFT analysis for the A) experimental and B) CFD results at a TSR of 4 for: i) P1W4 and; ii) P2W5.

TABLE 9.11. THE AMPLITUDE OF FLUCTUATION IN THE CFD AND EXPERIMENTAL OUT OF PLANE BENDING MOMENT RESULTS.

Case	Amplitude of fluctuation in the out of plane bending moment (± 1 standard deviation), BM_x (Nm)					
	Wave frequency			Stanchion crossing frequency		
	Experimental	CFD	Difference	Experimental	CFD	Difference
P1W4	2.24 ± 0.24	2.37	0.13	2.56 ± 0.49	2.23	0.33
P2W5	2.50 ± 0.10	2.76	0.26	0.55 ± 0.21	0.62	0.07
U	-	-	-	0.45	0.25	0.20
P1	-	-	-	2.25	2.52	0.27
P2	-	-	-	0.76	0.67	0.09

Successful validation of the wave-current CFD models has been obtained in the region of peak power for a $1/20^{\text{th}}$ scale TST in S2OT wave and profiled current conditions. The CFD model was compared to experimental data using the wave flow features, such as average current velocity, wave orbital velocity and wave surface elevation. Furthermore, the turbine loadings and performance characteristics were compared by analysing the average C_q , C_t and C_p as well as the out of plane bending moment. The impact that wave-current conditions can have on the thrust and torque loadings of a TST can now be assessed by comparing CFD results from this study to the previous current-only results.

9.2.3 Transient turbine loadings

As previously discussed with the BM_x loadings, the average thrust and torque on the turbine show good similarity between each of the five test cases for the individual turbine components (blades and hub) as well as the total turbine loadings. Small variations exist between cases, but mainly due to differences in the \overline{W}_{vol} for each case. For example, P2W5 has the greatest \overline{W}_{vol} while P2 has the smallest \overline{W}_{vol} with values of 1.052 m/s and 1.004 m/s, respectively. In turn, the average thrust and torque results reflect these differences as shown in Table 9.12 and Table 9.13.

TABLE 9.12. THE INDIVIDUAL COMPONENT AND TOTAL AVERAGE THRUST LOADINGS ON THE TURBINE WHEN SUBJECTED TO CURRENT-ONLY AND WAVE-CURRENT CONDITIONS.

	Average thrust, T (N)				
	Uniform	Profile 1	Profile 2	P1W4	P2W5
Single blade	104.8	102.5	101.7	105.1	107.0
Hub	7.9	7.7	7.7	7.9	8.2
Total	321.0	314.0	311.7	321.9	327.9

TABLE 9.13. THE INDIVIDUAL COMPONENT AND TOTAL AVERAGE TORQUE LOADINGS ON THE TURBINE WHEN SUBJECTED TO CURRENT-ONLY AND WAVE-CURRENT CONDITIONS.

	Average torque, Q (Nm)				
	Uniform	Profile 1	Profile 2	P1W4	P2W5
Single blade	5.6	5.3	5.4	5.6	6.0
Hub	0.0	0.0	0.0	0.0	0.0
Total	16.6	15.9	16.0	16.8	17.7

Figure 9.21 shows the transient thrust and torque loadings for a single blade, the hub and the turbine total for five different test cases using a variety of current-only and wave-current conditions. The surface elevation of the two wave cases (W4 and W5) is also shown to demonstrate comparisons between the surface elevation and loadings experienced for the wave-current cases. Similar to the single blade BMx results for P1W4 and P2W5, the fluctuation observed in the thrust and torque loadings on a single blade is a complex combination of interactions between the stanchion and propagating surface waves. The frequency of the wave, the amount of shear in the velocity profile and the rotational speed of a blade passing the stanchion, all affect the loading fluctuations experienced by a single turbine blade. In comparison, the current-only cases U, P1 and P2, show fluctuations in the loadings because of a blade passing the stanchion on each rotation, combined with the influence of a uniform or profiled current velocity. These trends can be seen in Figure 9.21i).

The thrust and torque on the hub can be seen in Figure 9.21Aii) and Figure 9.21Bii), respectively, for each of the different flow conditions tested. The presence of a velocity profile is shown to have a negligible effect on the fluctuation of the thrust and torque on the hub. However, the introduction of surface waves increases the fluctuation in the thrust to an amplitude of ≈ 1.2 N while the test cases without waves had an amplitude of fluctuation in the thrust of < 0.05 N. The surface waves did not affect the fluctuation in the torque, however, remaining close to 0 Nm.

9 TURBINE PERFORMANCE UNDER WAVE-CURRENT FLOW CONDITIONS: REGULAR WAVES WITH PROFILED VELOCITY GRADIENTS

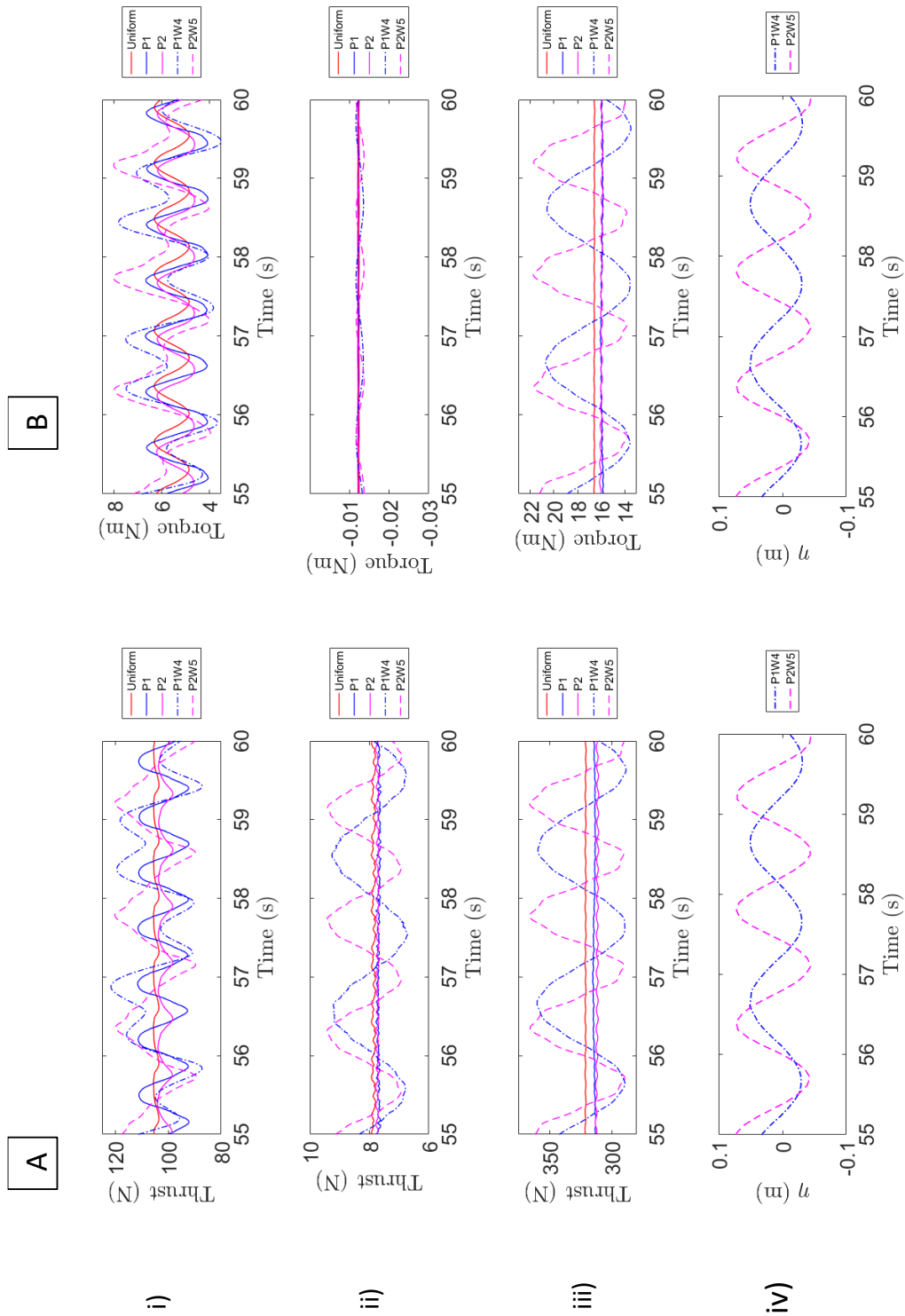


Figure 9.21. Numerical CFD comparison between the uniform, Profile 1, Profile 2, P1W4 and P2W5 models, for A) thrust and B) torque results at a TSR of 4 relating to: i) a single blade, ii) the hub and; iii) the turbine total (all blades and hub). The surface elevation of the waves at the turbine location for P1W4 and P2W5 are shown in iv) in order to compare to the corresponding thrust and torque loadings.

The total turbine thrust and torque fluctuations are where the major differences are observed between the test cases with and without surface waves. Figure 9.21iii) shows the total thrust and torque loadings on the turbine. Combining the loadings on each of the three turbine blades cancels out the fluctuation in the thrust and torque due to a blade passing the stanchion each rotation. This is because each turbine blade is 120° out of phase with one another. It is still important to account for the stanchion effect on the loadings of each single blade, in terms of design and manufacture, however, this fluctuation cannot be seen in the total turbine thrust and torque results. Figure 9.21Aiii) shows the significant difference observed in the transient thrust results for the test cases with and without surface waves. The amplitude of fluctuation around the average total thrust is 0.28 N for the uniform flow case, 0.19 N for P1 and 0.74 N for P2, as shown in Table 9.14. This dramatically increases to a fluctuation of 33.6 N for P1W4 and 37.8 N for P2W5 when surface waves are introduced (≈35 times greater). The maximum and minimum peaks in the transient total thrust results directly coincide with when a crest or trough of the wave propagates past the turbine, as shown in Figure 9.21Aiv).

TABLE 9.14. THE AMPLITUDE OF FLUCTUATION IN THE THRUST LOADING ON THE TURBINE WHEN SUBJECTED TO CURRENT-ONLY AND WAVE-CURRENT CONDITIONS.

Amplitude of fluctuation in the thrust, T (N)					
	Uniform	Profile 1	Profile 2	P1W4	P2W5
Total	0.28	0.19	0.74	33.6	37.8

This same trend is observed in the transient total torque results, as shown in Figure 9.21Biii). The amplitude of fluctuation around the average total torque is 0.02 Nm for the uniform flow case, 0.02 Nm for P1 and 0.07 Nm for P2, as shown in Table 9.15. The amplitude of fluctuation for the cases P1W4 and P2W5 with surface waves are 3.39 Nm and 3.92 Nm respectively (≈35 times greater). Again, the fluctuation in the loading for the cases including waves is significantly greater than without, and peaks in the loading fluctuations align with the crests and troughs of the wave surface elevation, as shown in Figure 9.21Biv). These results show the substantial effect that surface waves can have on the loadings of a turbine. It is the cyclic nature of the wave induced loadings that can critically affect the fatigue life of the turbine components. Numerical analysis of these features allows researchers and developers to investigate these loadings and quantify the impact that certain flow conditions can have on marine devices placed in conditions specific to identified tidal test sites.

TABLE 9.15. THE AMPLITUDE OF FLUCTUATION IN THE TORQUE LOADING ON THE TURBINE WHEN SUBJECTED TO CURRENT-ONLY AND WAVE-CURRENT CONDITIONS.

	Amplitude of fluctuation in the torque, Q (Nm)				
	Uniform	Profile 1	Profile 2	P1W4	P2W5
Total	0.02	0.02	0.07	3.4	3.9

9.3 SUMMARY

The performance of a TST under regular, S2OT waves and profiled current conditions was investigated while also examining the transient loadings experienced by the turbine under these conditions. Initially, an analysis was performed experimentally, using the IFREMER wave-current flume, after which a wave-current CFD model was created to simulate the turbine interaction numerically.

Two regular waves were superimposed upon two profiled current velocities and the flow conditions were compared experimentally against current-only conditions using the same velocity profiles. The average streamwise and vertical velocities showed little difference between the tests using current-only and wave-current conditions, establishing that the superimposed wave characteristic does not affect the dominating current flow. It was also observed that the waves induce a significant oscillatory component to the flow, which decreases as the wave motion penetrates through the water depth.

Numerical CFD models were then developed to replicate the wave-current experimental testing carried out using a 1/20th scale TST. The flow conditions generated by the CFD model showed good agreement to the results obtained experimentally, with differences of < 3% observed for the average current velocity, the oscillating wave orbital velocity and the wave surface elevation. The non-dimensional performance characteristics were compared at a TSR of 4 between the experimental and CFD data sets. It was found that the CFD results were all within 1 standard deviation from the mean of the experimental values, although the results for C_t showed more variation than for C_q or C_p .

Further validation of the wave-current CFD models were achieved by comparing the BM_x of a single turbine blade. Analysis using a FFT found that fluctuations in the BM_x results were produced by interaction of the stanchion and wave motion with the turbine blades. The rotational frequency and wave frequency were out of phase for the conditions presented by P1W4 while for P2W5 the wave period was almost exactly double the rotational period. This meant that in a 14 second window for P1W4 the turbine blade would rotate 20 times while 7 waves propagated past the turbine. This resulted in a changing time

series over each 14 second window which was then continually repeated. The wave-current BM_x results were compared to the current-only test cases, highlighting the similarity between the impact of a profiled current velocity and the influence of surface waves. The introduction of a small amount of shear to the velocity profile increased the BM_x on a single turbine blade from < 0.5 Nm to 0.7 Nm. A greater amount of shear in the velocity profile further increased the BM_x to 2.4 Nm. The introduction of waves gave a BM_x of 2.2 – 2.7 Nm depending on the wave characteristic used. These values are similar to the BM_x caused by a current-only flow with a shearing velocity profile and therefore emphasises the impact of a velocity profile on a TST, which can have a similar impact to that of surface waves. Good agreement was found between experimental and CFD BM_x results for all five test cases. Therefore, validation of the wave-current CFD models was successfully achieved over multiple different parameters.

The thrust and torque loadings were then examined using only the CFD results. The most significant difference was observed between the current-only flow conditions and the wave-current conditions for the total turbine loadings. The greatest amplitude of fluctuation observed in the total turbine thrust for the current-only cases was 0.74 N (P2). The introduction of waves increased this values to ≈ 35 N which is a substantial difference. The total torque results experienced a similar trend where the largest amplitude of fluctuation for the current-only cases was 0.07 Nm (P2) while this increased dramatically to ≈ 3.5 Nm when surface waves were introduced to the model. These loadings experienced under wave-current flow conditions are significant and therefore it is vital that these dynamic characteristics are accounted for when designing marine devices which will be situated in such highly complex regions of flow.

10 CONCLUSIONS AND FUTURE WORK

A summary of the key findings of the work undertaken in this thesis is presented in this chapter. These findings relate to the aims and objectives outlined in Chapter 1. The main conclusions are stated, followed by recommendations for future work.

10.1 CONCLUSIONS

10.1.1 Turbine performance under uniform current conditions

The turbine was fully characterised under uniform current conditions, experimentally and numerically. The flow results, obtained from the IFREMER flume, were consistently steady throughout the water depth and showed a uniformly small standard deviation over the entire depth of the flume. These conditions were successfully replicated using CFD modelling, providing a base case of the simplest flow conditions which could be used for comparisons against the more complex flow investigations.

10.1.2 Turbine performance under profiled current conditions

The volumetrically averaged streamwise velocity over the swept area of the turbine was used in the calculation of the average turbine performance characteristics to account for differences in the upstream flow velocity. Modal values were found to be a more accurate method of calculating the predominant flow conditions at each water depth due to some of the velocity data showing negative skewness.

The performance of the turbine, operating under speed control, was measured using the average performance characteristics, C_q , C_t and C_p . These average values were unaffected by the presence of a profiled current velocity and showed good agreement with the results for the uniform current conditions. The out of plane bending moment, thrust and torque were also examined to evaluate the transient effects of the flow conditions on the turbine. Time synchronous averaging was used to analyse the experimental out of plane bending moment on a single turbine blade over a rotational cycle. The stanchion interaction with a turbine blade was found to induce fluctuations in the out of plane bending moment in all cases. The introduction of shearing velocity profiles resulted in an increasing amplitude of fluctuation with increasing shear. The amplitude of fluctuation in the out of plane bending moment for a high shearing velocity profile showed an increase of five times that seen in the uniform current case. A similar trend was found with the thrust and torque results

taken from the CFD models. The maximum and minimum turbine loadings were aligned with the rotational frequency of the turbine. The magnitude of the stanchion interaction on a single turbine blade loading is minimal for uniform current conditions in comparison to the effect of a profiled current velocity.

The total thrust and torque results, incorporating both the turbine blades and hub, showed a significantly reduced fluctuation in the loadings, due to each turbine blade being 120° out of phase with one another and therefore the fluctuation in the loadings due to the stanchion gets cancelled out. Therefore, it is essential to analyse the individual turbine blade loadings as well as the total turbine loadings in order to fully understand the cyclic loadings on each component. This data can be critical to the design and manufacture of the turbine, and for increasing the fatigue life of the marine device.

10.1.3 Turbine performance under regular wave and profiled current conditions

The addition of a wave characteristic to each of the profiled current cases did not significantly alter the average current flow at each water depth. There was < 5% difference between the average streamwise and vertical current velocities for current-only and wave-current conditions. Whilst the average values of C_q , C_t and C_p were unaffected by the inclusion of regular waves, the presence of a wave induces a significant oscillatory component around the average current flow. This influence is greater towards the water surface and decreases through the water depth, greatly affecting the transient loadings on the turbine.

The fluctuation in the out of plane bending moment for a single turbine blade under wave-current conditions is a result of wave induced loadings as well as interaction with the stanchion over each rotation. There is similarity between the amplitude of fluctuation for a single turbine blade due to stanchion interaction in profiled current-only conditions and the fluctuating amplitude in the wave and profiled current conditions. The main difference with the wave-current cases is the presence of fluctuations in the loadings at an additional frequency due to the wave motion. However, the magnitude of these wave induced loading fluctuations are no greater than those due to stanchion interaction in a high shearing velocity profile. A shearing velocity profile can have an equally significant effect on a turbine blade as that of wave induced loadings. This implies that in profiled current conditions with surface waves, the loadings magnitudes and frequency of fluctuations experienced on the turbine blades could be significantly greater than in uniform current-only conditions. Control strategies could therefore be used to monitor the upstream flow

conditions to optimise the rotational speed of the turbine and minimise large loading fluctuations.

As with the out of plane bending moment on a single turbine blade, the fluctuation observed in the thrust and torque is a combination of stanchion and wave interaction. When combining all the blade and hub loadings to get an overall representation, the fluctuation in the loadings due to stanchion interaction are offset by each of the blades as described for current-only flow; however, the loadings due to the wave motion are amplified. The total amplitude of fluctuation around the average thrust for uniform and profiled current-only flows are < 1.0 N. With the inclusion of waves, the fluctuation in the thrust increased by roughly 35 times showing the difference between stanchion interaction affecting a single blade at a time, while the wave motion affects the whole turbine at the same time. The amplitude of fluctuation in the torque shows a similar trend with the wave cases being around 35 times that for the current-only case. Maximum and minimum peaks in the thrust and torque loadings are aligned with the crest and trough of the wave surface elevation as it passes over the turbine demonstrating the substantial cyclic nature that wave motion induces upon sub surface marine devices. Therefore, it is important that individual tidal sites are examined to find out the predominant flow conditions, and to allow a proposed tidal device design to be adjusted accordingly.

10.1.4 Development of a wave-current CFD model

The development of a numerical model, optimised to simulate combined wave and current interaction, was achieved using the CFD software ANSYS CFX. Three different Stokes 2nd order theory waves were tested in two different water depths relating to intermediate and deep water wave conditions. These comparisons highlighted the congruency between the CFD models and the experimental data sets available showing that, for the conditions tested, the CFD models can replicate the wave and current conditions effectively.

A free surface CFD model was optimised and a set of guidelines were defined which allow any flume geometry and wave characteristic within the Stokes 2nd order theory limits to be simulated. It was found that a reduced width domain of 0.1 m could be used without affecting the flow conditions generated by the model, and it was necessary for the still water level to be at 70% of the overall domain height. The required domain length must allow the propagation of 8-10 waves, and is therefore dependent on the wavelength of the chosen wave characteristic.

A HEXA mesh was favoured to reduce the number of computational points needed while also possessing a high spatial resolution. It was identified that 120 cells over the length of a wave (Δz) and 10 cells over the wave height (Δy) created a mesh with good numerical accuracy and reasonable computational run time. It is necessary to simulate wave-current interaction using a transient analysis to capture the time dependent nature of the flow. The optimum time step interval for wave-current simulations was found to equate to the wave period divided by 50 ($T/50$), thus providing a good temporal resolution.

Numerical wave generation at the inlet was found to be successful but required the use of a numerical beach in a region twice the wavelength upstream of the outlet, to prevent any reflection of the waves from the end of the domain. The solver executable of 'double precision' should be used to permit higher resolution numerical mathematical operations which can improve convergence.

This type of model often requires the use of parallel processing and High Performance Computing facilities. When using parallel processing it is important to restrict the partitioning direction so that the free surface is not aligned with any partition boundaries.

10.1.5 Validation of numerical models using experimental data

The CFD model results were successfully validated using experimental data from two different test facilities, the University of Liverpool's recirculating water channel and the IFREMER wave-current flume.

The University of Liverpool's recirculating water channel test data was used to validate the wave-current model created using Stokes 2nd order theory waves and a uniform current (Chapter 8). The CFD model results showed good agreement to the experimental results with a maximum deviation in wave surface elevation of 6% and < 2% difference between average velocity results.

Validation of simulations investigating flow effects on a model-scale tidal turbine (Chapters 7 and 9) were compared against data sets from the IFREMER wave-current flume. Multiple flow and turbine parameters were considered such as the turbine performance characteristics, streamwise and vertical flow velocity data, and individual out of plane bending moment blade loadings. Good agreement was found for each different model case, showing how valuable numerical modelling can be in this progressive industry. All turbine CFD models were operational in flow conditions independent of Reynolds number and therefore these results can inform researchers and developers of similar outcomes using full-scale tidal devices. This statement highlights the continued requirement for numerical

modelling to be used in the initial stages of device development to reduce the costs associated with device design as well as the operational costs of laboratory testing.

10.2 FUTURE WORK

Further research opportunities were identified throughout this thesis, as detailed below.

- Due to computational limitations and time constraints, the CFD models for profiled current flow and wave-current interaction were limited to a single TSR of 4. Further transient studies over a full range of TSRs would support the findings identified in this thesis.
- Only two types of S2OT, intermediate water waves were investigated in this thesis. This could be expanded to examine the effect of deep-water waves, and even look to use higher order wave theories in the CFD models.
- The relationship between the phase of the wave and the rotational period of the turbine should be investigated to assess the impact of the wave on the turbine loadings when in and out of phase.
- Wave and current combinations were limited to what could be performed in the chosen experimental facilities. More realistic wave and current conditions could be investigated using CFD which is not limited in the same way. Velocity profiles and realistic wave profiles could also be taken from real site data and examined using CFD modelling.
- Regular waves were investigated in this thesis, however, rarely in the ocean environment are these conditions seen. This work could be extended to emulate more realistic ocean flow conditions such as irregular waves, superposition of waves and oblique wave and current combinations.
- The use of the RANS turbulence models in CFD modelling has been found to considerably dissipate the turbulence from the inlet. More complex turbulence models such as LES could be used in order to investigate the effect of waves on a TST and the implications this has to the turbulence in the flow.
- Condition monitoring and signal processing could be investigated to minimise large loading fluctuations on the turbine due to the presence of waves.

REFERENCES

- [1] United Nations, "Climate Change | United Nations," 2020. <https://www.un.org/en/sections/issues-depth/climate-change/> (accessed Jan. 08, 2020).
- [2] Ofgem, "State of the energy market 2019," 2019. <https://www.ofgem.gov.uk/publications-and-updates/state-energy-market-2019> (accessed Oct. 16, 2019).
- [3] Our World in Data, "CO₂ and Greenhouse Gas Emissions - Our World in Data," 2020. <https://ourworldindata.org/co2-and-other-greenhouse-gas-emissions> (accessed Jan. 08, 2020).
- [4] Committee on Climate Change, "Reducing UK emissions: 2019 Progress Report to Parliament," 2019. www.theccc.org.uk/publications (accessed Oct. 16, 2019).
- [5] World Meteorological Organization, "Greenhouse gases | World Meteorological Organization." <https://public.wmo.int/en/our-mandate/focus-areas/environment/greenhouse-gases> (accessed Jan. 16, 2020).
- [6] National Oceanographic and Atmospheric Administration, "Climate Change: Atmospheric Carbon Dioxide | NOAA Climate.gov," 2019. <https://www.climate.gov/news-features/understanding-climate/climate-change-atmospheric-carbon-dioxide> (accessed Jan. 08, 2020).
- [7] National Oceanographic and Atmospheric Administration, "ESRL Global Monitoring Division - Global Greenhouse Gas Reference Network," 2020. <https://www.esrl.noaa.gov/gmd/ccgg/trends/weekly.html> (accessed Jan. 16, 2020).
- [8] U.S Energy Information Administration, "International Energy Outlook 2017," 2017. www.eia.gov/ieo (accessed Dec. 13, 2017).
- [9] UK Department for Business Energy and Industrial Strategy, "Chapter 6 Renewable sources of energy," 2019. www.gov.uk/government/publications/renewable-energy-statistics-data-sources-and-methodologies (accessed Oct. 16, 2019).
- [10] The Carbon Trust, "Cutting Carbon in Europe: The 2020 plans and the future of the EU ETS," 2008. <https://www.carbontrust.com/media/84896/ctc734-cutting-carbon->

REFERENCES

- in-europe-2020-plans.pdf (accessed Dec. 12, 2017).
- [11] UK Department for Business Energy and Industrial Strategy, "UK Energy Statistics, Q1 2019," 2019. www.gov.uk/government/collections/road-transport-consumption-at-regional-and-local-level (accessed Oct. 16, 2019).
- [12] GOV.UK, "UK becomes first major economy to pass net zero emissions law - GOV.UK," 2019. <https://www.gov.uk/government/news/uk-becomes-first-major-economy-to-pass-net-zero-emissions-law> (accessed Jan. 08, 2020).
- [13] "Wind Energy - RenewableUK." <https://www.renewableuk.com/page/WindEnergy> (accessed Oct. 21, 2019).
- [14] Ocean Energy Europe, "Ocean Energy: Key Trends and Statistics 2018," 2018. http://www.oceanenergy-europe.eu/wp-content/uploads/2019/04/Ocean-Energy-Europe-Key-trends-and-statistics-2018_web.pdf.
- [15] M. Lewis, J. McHaughton, C. Marquez-Dominguez, G. Todeschini, M. Togneri, I. Masters, M. Allmark, T. Stallard, S. Neill, A. Goward-Brown, and P. Robins, "Power variability of tidal-stream energy and implications for electricity supply," *Energy*, vol. 183, pp. 1061–1074, Sep. 2019, doi: 10.1016/j.energy.2019.06.181.
- [16] C. Morris, "Influence of Solidity on the Performance, Swirl Characteristics, Wake Recovery and Blade Deflection of a Horizontal Axis Tidal Turbine," PhD Thesis, Cardiff University, 2014.
- [17] Renewable Energy Association, "Marine - Renewable Technologies," *Information on marine*, 2019. <https://www.r-e-a.net/renewable-technologies/marine> (accessed Oct. 18, 2019).
- [18] Ocean Energy Europe, "Ocean energy project spotlight: Investing in tidal and wave energy," 2017. <https://www.oceanenergy-europe.eu/wp-content/uploads/2017/06/170228-Ocean-energy-spotlight-final.pdf> (accessed Jan. 29, 2018).
- [19] European Marine Energy Centre (EMEC), "Wave devices : EMEC: European Marine Energy Centre." <http://www.emec.org.uk/marine-energy/wave-devices/> (accessed Oct. 18, 2019).
- [20] European Commission, "Strategic Energy Technology Plan," 2017. <http://ec.europa.eu/energy/en/topics/technology-and-innovation/strategic-energy->

technology-plan.

- [21] National Tide and Sea Level Facility, “Highest & lowest predicted tides | National Tidal and Sea Level Facility,” 2020. <https://www.ntslf.org/tides/hilo> (accessed Jan. 08, 2020).
- [22] European Technology & Innovation Platform for Ocean Energy, “Powering Homes Today, Powering Nations Tomorrow,” 2019. <https://www.oceanenergy-europe.eu/wp-content/uploads/2019/04/ETIP-Ocean-Integrated-Strategy-2019-LR.pdf>.
- [23] Ocean Energy Europe, “Ocean Energy Europe - Tidal range.” <https://www.oceanenergy-europe.eu/ocean-energy/tidal-lagoons/> (accessed Jan. 29, 2018).
- [24] EDF France, “Tidal Power.” <https://www.edf.fr/en/the-edf-group/industrial-provider/renewable-energies/marine-energy/tidal-power> (accessed Jan. 30, 2018).
- [25] The Crown Estate, “UK Wave and Tidal Key Resource Areas Project: Technical Methodology Report,” 2013. <https://www.thecrownestate.co.uk/media/5478/uk-wave-and-tidal-key-resource-areas-technological-report.pdf> (accessed Dec. 12, 2017).
- [26] J. Harrison and J. Uhomobhi, “Engineering Study of Tidal Stream Renewable Energy,” in *Advanced Visual Interfaces: Supporting Big Data Applications 2016 Workshop*, 2016, pp. 19–34, doi: 10.1007/978-3-319-50070-6.
- [27] Marine Energy Council, “UK Marine Energy 2019: A New Industry,” 2019. https://c.ymcdn.com/sites/renewableuk.site-ym.com/resource/resmgr/publications/OER_inside_track_final_-_onl.pdf (accessed Oct. 17, 2019).
- [28] Sustainable Marine Energy, “Tidal Energy.” <https://sustainablemarine.com/tidal-energy> (accessed Oct. 21, 2019).
- [29] SIMEC Atlantis Energy, “MeyGen | Tidal Projects | SIMEC Atlantis Energy.” <https://simecatlantis.com/projects/meygen/> (accessed Oct. 21, 2019).
- [30] SIMEC Atlantis Energy, “Tidal Turbines | Installation & Procurment | Atlantis Resources.” <https://simecatlantis.com/services/turbines/> (accessed Oct. 22, 2019).

REFERENCES

- [31] MarineSpace and SMRU Consulting, “Decommissioning of the SeaGen tidal turbine in Strangford Lough, Northern Ireland : Environmental Statement,” 2016. <https://tethys.pnnl.gov/sites/default/files/publications/SeaGen-Decommissioning-2016.pdf>.
- [32] C. A. Douglas, G. P. Harrison, and J. P. Chick, “Life cycle assessment of the Seagen marine current turbine,” *Proc. Inst. Mech. Eng. Part M J. Eng. Marit. Environ.*, vol. 222, no. 1, pp. 1–12, 2008, doi: 10.1243/14750902JEME94.
- [33] SIMEC Atlantis Energy, “Strangford Narrows | Tidal Projects | SIMEC Atlantis Energy.” <https://simecatlantis.com/projects/strangford-narrows/> (accessed Oct. 22, 2019).
- [34] MarineEnergy.biz, “Photo of the Day: Atlantis SeaGen Decommissioning | Marine Energy.” <https://marineenergy.biz/2019/03/14/photo-of-the-day-atlantis-seagen-decommissioning/> (accessed Oct. 22, 2019).
- [35] Sustainable Marine Energy, “PLAT-I: Accessible tidal energy for island and coastal communities.” <https://sustainablemarine.com/plat-i> (accessed Oct. 22, 2019).
- [36] Schottel Hydro, “SIT Instream Turbine.” <https://www.schottel.de/schottel-hydro/sit-instream-turbine/> (accessed Oct. 22, 2019).
- [37] Sustainable Marine Energy, “PLAT-O: Tidal energy platforms.” <https://sustainablemarine.com/plat-o> (accessed Oct. 22, 2019).
- [38] S. Eriksson, H. Bernhoff, and M. Leijon, “Evaluation of different turbine concepts for wind power,” *Renew. Sustain. Energy Rev.*, vol. 12, no. 5, pp. 1419–1434, 2008, doi: 10.1016/j.rser.2006.05.017.
- [39] M. J. Khan, G. Bhuyan, M. T. Iqbal, and J. E. Quaiocoe, “Hydrokinetic energy conversion systems and assessment of horizontal and vertical axis turbines for river and tidal applications: A technology status review,” *Appl. Energy*, vol. 86, no. 10, pp. 1823–1835, 2009, doi: 10.1016/j.apenergy.2009.02.017.
- [40] European Marine Energy Centre (EMEC), “Tidal developers : EMEC: European Marine Energy Centre.” <http://www.emec.org.uk/marine-energy/tidal-developers/> (accessed Oct. 23, 2019).
- [41] EEL Energy, “EEL Energy Press Release: 01/06/2018,” 2018. [http://www.eel-energy.fr/article/EEL ENERGY- Communiqué de Presse - June 2018 - ENGLISH.PDF](http://www.eel-energy.fr/article/EEL%20ENERGY-Communique%20de%20Presse-%20June%202018-%20ENGLISH.PDF)

- (accessed Oct. 23, 2019).
- [42] Sciences et Avenir, “Eel energy launches its tidal turbine.” https://www.sciencesetavenir.fr/nature-environnement/eel-energy-lance-son-hydrolienne_131919 (accessed Oct. 23, 2019).
- [43] Minesto, “The future of renewable energy | Minesto.” <https://minesto.com/our-technology> (accessed Oct. 23, 2019).
- [44] Minesto, “DG500 commissioning and testing update | Minesto.” <https://minesto.com/news-media/dg500-commissioning-and-testing-update> (accessed Oct. 23, 2019).
- [45] A. Alberello, A. Chabchoub, O. Gramstad, A. V Babanin, and A. Toffoli, “Non-Gaussian properties of second-order wave orbital velocity,” *Coast. Eng.*, vol. 110, pp. 42–49, 2016, doi: 10.1016/j.coastaleng.2016.01.001.
- [46] European Marine Energy Centre, “Technology Readiness Levels : EMEC: European Marine Energy Centre,” 2019. <http://www.emec.org.uk/services/pathway-to-emec/technology-readiness-levels/> (accessed Nov. 08, 2019).
- [47] A. Mason-Jones, D. M. O'Doherty, C. E. Morris, T. O'Doherty, C. B. Byrne, P. W. Prickett, R. I. Grosvenor, I. Owen, S. Tedds, and R. J. Poole, “Non-dimensional scaling of tidal stream turbines,” *Energy*, pp. 820–829, 2012, doi: 10.1016/j.energy.2012.05.010.
- [48] IMechE, “Changing tide: €47m English Channel tidal stream energy project could boost sector,” 2019. <https://www.imeche.org/news/news-article/changing-tide-47m-english-channel-tidal-stream-energy-project-could-boost-sector> (accessed Nov. 08, 2019).
- [49] Interreg, “Interreg’s biggest ever project approved,” 2019. <https://www.channelmanche.com/en/news-and-media/latest-news/interregs-biggest-ever-project-approved/> (accessed Nov. 08, 2019).
- [50] Verdant Power, “The RITE Project,” 2019. <https://www.verdantpower.com/riteproject> (accessed Nov. 08, 2019).
- [51] G. S. Payne, T. Stallard, R. Martinez, and T. Bruce, “Variation of loads on a three-bladed horizontal axis tidal turbine with frequency and blade position,” *J. Fluids Struct.*, vol. 83, pp. 156–170, Nov. 2018, doi: 10.1016/j.jfluidstructs.2018.08.010.

REFERENCES

- [52] L. E. Myers and A. S. Bahaj, "An experimental investigation simulating flow effects in first generation marine current energy converter arrays," *Renew. Energy*, vol. 37, pp. 28–36, 2012, doi: 10.1016/j.renene.2011.03.043.
- [53] S. Ordonez-Sanchez, K. Porter, C. Frost, M. Allmark, and C. Johnstone, "Effects of Wave-Current Interactions on the Performance of Tidal Stream Turbines," in *Proceedings of the 3rd Asian Wave & Tidal Energy Conference*, 2016, pp. 394–403, Accessed: Aug. 14, 2017. [Online]. Available: https://pure.strath.ac.uk/portal/files/56374602/Ordonez_Sanchez_et_al_AWTEC2016_Effects_of_extreme_wave_current_interactions.pdf.
- [54] B. Gaurier, G. Germain, J. V. Facq, C. M. Johnstone, A. D. Grant, A. H. Day, E. Nixon, F. Di Felice, and M. Costanzo, "Tidal energy 'round Robin' tests comparisons between towing tank and circulating tank results," *Int. J. Mar. Energy*, vol. 12, no. 2015, pp. 87–109, 2015, doi: 10.1016/j.ijome.2015.05.005.
- [55] P. W. Galloway, L. E. Myers, and A. S. Bahaj, "Studies of a scale tidal turbine in close proximity to waves," *3rd Int. Conf. Ocean Energy, Bilbao, Spain, 6 Oct 2010*, no. 1, pp. 3–8, 2010, [Online]. Available: <http://agris.fao.org/agris-search/search.do?f=2013/AV/AV2012083300833.xml;AV2012083398>.
- [56] S. Tedds, R. Poole, I. Owen, G. Natjafian, S. Bode, A. Mason-Jones, C. Morris, T. O'Doherty, and D. O'Doherty, "Experimental investigation of horizontal axis tidal stream turbines," *EWTEC 2011 Proceedings of the 11th European Wave and Tidal Energy Conference, Nantes, France, 2011*, [Online]. Available: http://www.see.ed.ac.uk/~shs/EWTEC_2011_full/EWTEC_CD/default.htm.
- [57] R. Martinez, G. S. Payne, and T. Bruce, "The effects of oblique waves and currents on the loadings and performance of tidal turbines," *Ocean Eng.*, vol. 164, pp. 55–64, 2018, doi: 10.1016/j.oceaneng.2018.05.057.
- [58] J. Schluntz and R. H. J. Willden, "The effect of blockage on tidal turbine rotor design and performance," *Renew. Energy*, 2015, doi: 10.1016/j.renene.2015.02.050.
- [59] FloWave Ocean Energy Research Facility, "Tank Design and Features," 2019. <https://www.flowavett.co.uk/tank-design-and-features> (accessed Nov. 13, 2019).
- [60] M. Allmark, R. Ellis, K. Porter, T. O'Doherty, and C. Johnstone, "The Development and Testing of a Lab-Scale Tidal Stream Turbine for the Study of Dynamic Device

- Loading,” in *Proceedings of the 4th Asian Wave and Tidal Energy Conference*, 2018.
- [61] Tidal Stream Ltd, “Resource,” 2016.
<http://www.tidalstream.co.uk/Resource/resource.html> (accessed Dec. 12, 2017).
- [62] A. S. Bahaj, A. F. Molland, J. R. Chaplin, and W. M. J. Batten, “Power and thrust measurements of marine current turbines under various hydrodynamic flow conditions in a cavitation tunnel and a towing tank,” *Renew. Energy*, vol. 32, no. 3, pp. 407–426, Mar. 2007, doi: 10.1016/j.renene.2006.01.012.
- [63] F. Maganga, G. Germain, J. King, G. Pinon, and E. Rivoalen, “Experimental characterisation of flow effects on marine current turbine behaviour and on its wake properties,” *IET Renew. Power Gener.*, vol. 4, no. 6, p. 498, 2010, doi: 10.1049/iet-rpg.2009.0205.
- [64] P. Evans, A. Mason-Jones, C. Wilson, C. Wooldridge, T. O’Doherty, and D. O’Doherty, “Constraints on extractable power from energetic tidal straits,” *Renew. Energy*, vol. 81, pp. 707–722, Sep. 2015, doi: 10.1016/j.renene.2015.03.085.
- [65] M. Allmark, S. Ordonez-Sanchez, S. Wang, Y. Kang, C. Jo, T. O’Doherty, and C. Johnstone, “An investigation into Reynolds scaling and solidity for a HATT tidal turbine,” in *Proceedings of the 13th European Wave and Tidal Energy Conference 1-6 Sept 2019, Naples, Italy*, 2019.
- [66] E. Hau, *Wind Turbines: Fundamentals, Technologies, Application, Economics*, 2nd Ed. Springer-Verlag, 2006.
- [67] T. Blackmore, L. E. Myers, and A. S. Bahaj, “Effects of turbulence on tidal turbines: Implications to performance, blade loads, and condition monitoring,” *Int. J. Mar. Energy*, vol. 14, pp. 1–26, 2016, doi: 10.1016/j.ijome.2016.04.017.
- [68] T. O’Doherty, A. Mason-Jones, D. M. O, P. S. Evans, C. Wooldridge, and I. Fryett, “Considerations of a horizontal axis tidal turbine,” *Energy*, vol. 163, no. EN3, 2010, doi: 10.1680/ener.2010.163.3.119.
- [69] B. Gaurier, P. Davies, A. Deuff, and G. Germain, “Flume tank characterization of marine current turbine blade behaviour under current and wave loading,” *Renew. Energy*, vol. 59, pp. 1–12, 2013, doi: 10.1016/j.renene.2013.02.026.
- [70] I. A. Milne, A. H. Day, R. N. Sharma, and R. G. J. Flay, “Blade loading on tidal turbines for uniform unsteady flow,” *Renew. Energy*, vol. 77, pp. 338–350, May 2015, doi:

REFERENCES

- 10.1016/j.renene.2014.12.028.
- [71] T. Ebdon, "The impact of turbulence and turbine operating condition on the wakes of tidal turbines," PhD Thesis, Cardiff University, 2019.
- [72] S. C. Tedds, I. Owen, and R. J. Poole, "Near-wake characteristics of a model horizontal axis tidal stream turbine," *Renew. Energy*, vol. 63, pp. 222–235, 2014, doi: 10.1016/j.renene.2013.09.011.
- [73] R. Sorensen, *Basic Coastal Engineering*, 3rd ed. Pennsylvania: John Wiley & Sons, 2006.
- [74] C. Lloyd, T. O'Doherty, and A. Mason-Jones, "Development of a wave-current numerical model using Stokes 2nd Order Theory," *Int. Mar. Energy J.*, vol. 2, no. 1, pp. 1–14, 2019, doi: <https://doi.org/10.36688/imej.2.1-14>.
- [75] J. V Norris and E. Droniou, "Update on EMEC activities, resource description, and characterisation of wave-induced velocities in a tidal flow," in *Proceedings of the 7th European Wave and Tidal Energy Conference, Porto, Portugal, 2007*.
- [76] E. Lust, L. Luznik, K. Flack, J. Walker, and M. Van Benthem, "The influence of surface gravity waves on marine current turbine performance," *Int. J. Mar. Energy*, vol. 3–4, pp. 27–40, 2013, Accessed: Jun. 01, 2017. [Online]. Available: http://ac.els-cdn.com/S2214166913000295/1-s2.0-S2214166913000295-main.pdf?_tid=f45327bc-46b3-11e7-ac83-00000aab0f26&acdnat=1496312617_226571042f43c24d475d07155256db01.
- [77] M. Holst, O. Gunnar Dahlhaug, and C. Faudot, "CFD Analysis of Wave-Induced Loads on Tidal Turbine Blades," *IEEE J. Ocean. Eng.*, vol. 40, no. 3, 2015, Accessed: Oct. 25, 2019. [Online]. Available: <https://ieeexplore.ieee.org/stamp/stamp.jsp?tp=&arnumber=6895177>.
- [78] L. Luznik, K. A. Flack, E. E. Lust, and K. Taylor, "The effect of surface waves on the performance characteristics of a model tidal turbine," *Renew. Energy*, vol. 58, pp. 108–114, 2013, doi: 10.1016/j.renene.2013.02.022.
- [79] N. Barltrop, K. S. Varyani, A. Grant, D. Clelland, and X. P. Pham, "Investigation into wave-current interactions in marine current turbines," *Proc. IMechE, Part A J. Power Energy*, vol. 221, no. 2, pp. 233–242, 2007, doi: 10.1243/09576509JPE315.
- [80] M. Sos, L. Johnston, J. Walker, and M. Rahimian, "The impact of waves and

- immersion depth on HATT performance,” *Proc. 12th Eur. Wave Tidal Energy Conf. 27th Aug -1st Sept 2017, Cork, Irel.*, pp. 1–8, 2017.
- [81] T. A. Henriques, T. S. Hedges, I. Owen, and R. J. Poole, “The effects of wave-current interaction on the performance of a model horizontal axis tidal turbine,” *Int. J. Mar. Energy*, vol. 8, pp. 17–35, 2014, doi: 10.1016/j.ijome.2014.10.002.
- [82] P. W. Galloway, L. E. Myers, and A. S. Bahaj, “Quantifying wave and yaw effects on a scale tidal stream turbine,” *Renew. Energy*, vol. 63, pp. 297–307, 2014, doi: 10.1016/j.renene.2013.09.030.
- [83] B. Gaurier, S. Ordonez-Sanchez, J-V. Facq, G. Germain, C. Johnstone, R. Martinez, I. Santic, and F. Salvatore, “First round of MaRINET 2 Tidal Energy Round Robin Tests : combined wave and current tests,” pp. 1–10, 2019.
- [84] T. A. Henriques, T. S. Hedges, I. Owen, and R. J. Poole, “The influence of blade pitch angle on the performance of a model horizontal axis tidal stream turbine operating under wave-current interaction,” *Energy*, vol. 102, pp. 166–175, 2016, doi: 10.1016/j.energy.2016.02.066.
- [85] S. Draycott, G. Payne, J. Steynor, A. Nambiar, B. Sellar, and V. Venugopal, “An experimental investigation into non-linear wave loading on horizontal axis tidal turbines,” *J. Fluids Struct.*, vol. 84, pp. 199–217, Jan. 2019, doi: 10.1016/j.jfluidstructs.2018.11.004.
- [86] C. Frost, “Flow Direction Effects On Tidal Stream Turbines,” PhD Thesis, Cardiff University, 2016.
- [87] I. Čatipović, N. Hadžić, F. Dias, and H. Kozmar, “Computational model of simultaneous wave and sea current loads on tidal turbines,” *Ocean Eng.*, vol. 184, pp. 323–331, Jul. 2019, doi: 10.1016/j.oceaneng.2019.04.058.
- [88] C. Faudot and O. G. Dahlhaug, “Prediction of Wave Loads on Tidal Turbine Blades,” *Energy Procedia*, vol. 20, pp. 116–133, 2012, doi: 10.1016/j.egypro.2012.03.014.
- [89] A. Mason-Jones, “Performance assessment of a Horizontal Axis Tidal Turbine in a high velocity shear environment,” PhD Thesis, Cardiff University, 2010.
- [90] U. Ahmed, D. D. Apsley, I. Afgan, T. Stallard, and P. K. Stansby, “Fluctuating loads on a tidal turbine due to velocity shear and turbulence: Comparison of CFD with field data,” *Renew. Energy*, vol. 112, pp. 235–246, 2017, doi:

REFERENCES

- 10.1016/j.renene.2017.05.048.
- [91] M. Harrison, W. Batten, L. Myers, and A. Bahaj, "Comparison between CFD simulations and experiments for predicting the far wake of horizontal axis tidal turbines," *IET Renew. Power Gener.*, vol. 4, no. 6, pp. 613–627, 2010, doi: 10.1049/iet-rpg.2009.0193.
- [92] C. Frost, C. E. Morris, A. Mason-Jones, D. M. O'doherty, and T. O'doherty, "The effect of tidal flow directionality on tidal turbine performance characteristics," *Renew. Energy*, vol. 78, pp. 609–620, 2015, doi: 10.1016/j.renene.2015.01.053.
- [93] X. Li, M. Li, S. McLelland, L-B. Jordan, L. Amoudry, Q. Song, and A. Plater, "Modelling impacts of tidal stream turbines on surface waves," *Renew. Energy*, vol. 130, pp. 725–734, Jan. 2019, doi: 10.1016/j.renene.2018.05.098.
- [94] X. Bai, E. J. Avital, A. Munjiza, and J. J. R. Williams, "Numerical simulation of a marine current turbine in free surface flow," *Renew. Energy*, vol. 63, pp. 715–723, 2014, doi: 10.1016/j.renene.2013.09.042.
- [95] X. Su, H. Zhang, G. Zhao, Y. Cao, and Y. Zhao, "Numerical and Experimental Investigations on the Hydrodynamic Performance of a Tidal Current Turbine," *J. Offshore Mech. Arct. Eng.*, vol. 140, 2018, doi: 10.1115/1.4038249.
- [96] T. Burton, N. Jenkins, D. Sharpe, and E. Bossanyi, *Wind Energy Handbook*, 2nd Ed. Wiley, 2011.
- [97] R. Malki, A. Williams, T. Croft, M. Togneri, and I. Masters, "A coupled blade element momentum - Computational fluid dynamics model for evaluating tidal stream turbine performance," *Appl. Math. Model.*, vol. 37, no. 5, pp. 3006–3020, Mar. 2013, doi: 10.1016/j.apm.2012.07.025.
- [98] X. Guo, J. Yang, Z. Gao, T. Moan, and H. Lu, "The surface wave effects on the performance and the loading of a tidal turbine," *Ocean Eng.*, vol. 156, pp. 120–134, May 2018, doi: 10.1016/j.oceaneng.2018.02.033.
- [99] X. Guo, Z. Gao, X. Li, J. Yang, and T. Moan, "Loading and Blade Deflection of a Tidal Turbine in Waves," 2019, doi: 10.1115/1.4041998.
- [100] I. Masters, J. Chapman, M. Willis, and J. Orme, "A robust blade element momentum theory model for tidal stream turbines including tip and hub loss corrections," *J. Mar. Eng. Technol.*, vol. 10, 2011, doi: 10.1080/20464177.2011.11020241.

- [101] R. Ellis, M. Allmark, T. O'Doherty, A. Mason-Jones, S. Ordonez-Sanchez, K. Johannesen, and C. Johnstone, "Design Process for a Scale Horizontal Axis Tidal Turbine Blade .," *Proc. 4th Asian Wave Tidal Energy Conf.*, 2018.
- [102] M. J. Churchfield, Y. Li, and P. J. Moriarty, "A large-eddy simulation study of wake propagation and power production in an array of tidal-current turbines," *Philos. Trans. R. Soc.*, 2013, doi: 10.1098/rsta.2012.0421.
- [103] A. C. W. Creech, A. G. L. Borthwick, and D. Ingram, "Effects of support structures in an LES actuator line model of a tidal turbine with contra-rotating rotors," *Energies*, vol. 10, 2017, doi: 10.3390/en10050726.
- [104] S. Wahono, "Development of Virtual Blade Model for Modelling Helicopter Rotor Downwash in OpenFOAM," *Aust. Gov. Dep. Def. Def. Sci. Technol. Organ.*, 2013.
- [105] S. F. Sufian, M. Li, and B. A. O'Connor, "3D Modeling of Impacts from Waves on Tidal Turbine Wake Characteristics and Energy Output," *Renew. Energy*, pp. 1–15, 2017, doi: 10.1016/j.renene.2017.04.030.
- [106] ANSYS Inc, "ANSYS CFX Modelling Guide." Release 18.0.
- [107] N. Hafeez, S. Badshah, M. Badshah, and Sakhi Jab Khalil, "Effect of velocity shear on the performance and structural response of a small-scale horizontal axis tidal turbine," *Mar. Syst. Ocean Technol.*, 2019, doi: 10.1007/s40868-019-00057-0.
- [108] T. O'Doherty, A. Mason-Jones, D. M. O'Doherty, C. B. Byrne, I. Owen, and Y. X. Wang, "Experimental and Computational Analysis of a Model Horizontal Axis Tidal Turbine," in *Proceedings of the 8th European Wave and Tidal Energy Conference, Uppsala, Sweden, 2009*, pp. 833–841, Accessed: Jan. 30, 2019. [Online]. Available: [http://www.homepages.ed.ac.uk/shs/Wave Energy/EWTEC 2009/EWTEC 2009 \(D\)/papers/263.pdf](http://www.homepages.ed.ac.uk/shs/Wave Energy/EWTEC 2009/EWTEC 2009 (D)/papers/263.pdf).
- [109] A. Mason-Jones, D. M. O'Doherty, C. E. Morris, and T. O'Doherty, "Influence of a velocity profile & support structure on tidal stream turbine performance," *Renew. Energy*, vol. 52, pp. 23–30, 2013, doi: 10.1016/j.renene.2012.10.022.
- [110] R. McSherry, J. Grimwade, I. Jones, S. Mathias, A. Wells, and A. Mateus, "3D CFD modelling of tidal turbine performance with validation against laboratory experiments," *Proc. 9th EWTEC Southampton, UK*, 2011.
- [111] J. Yan, X. Deng, A. Korobenko, and Y. Bazilevs, "Free-surface flow modeling and

REFERENCES

- simulation of horizontal-axis tidal-stream turbines,” *Comput. Fluids*, vol. 158, pp. 157–166, Nov. 2017, doi: 10.1016/j.compfluid.2016.06.016.
- [112] T. G. Thomas and J. J. R. Williams, “Development of a parallel code to simulate skewed flow over a bluff body,” *J. Wind Eng. Ind. Aerodyn.*, pp. 155–167, 1997, Accessed: Jan. 31, 2019. [Online]. Available: https://ac.els-cdn.com/S0167610597000706/1-s2.0-S0167610597000706-main.pdf?_tid=dd6d2d49-a545-4f87-a006-41b6417ac903&acdnat=1548928742_ad2390c85ab2af24cbe3ee484a5ff1f2.
- [113] X. Sun, J. P. Chick, and I. G. Bryden, “Laboratory-scale simulation of energy extraction from tidal currents,” *Renew. Energy*, vol. 33, pp. 1267–1274, 2008, doi: 10.1016/j.renene.2007.06.018.
- [114] W. M. H.K.Versteeg, *An Introduction to Computational Fluid Dynamics*, vol. M. 2007.
- [115] S. Kang, I. Borazjani, J. A. Colby, and F. Sotiropoulos, “Numerical simulation of 3D flow past a real-life marine hydrokinetic turbine,” *Adv. Water Resour.*, vol. 39, pp. 33–43, 2012, doi: 10.1016/j.advwatres.2011.12.012.
- [116] T. Ebdon, D. O’Doherty, T. O’Doherty, and A. Mason-Jones, “Simulating Marine Current Turbine Wakes Using Advanced Turbulence Models,” in *Proc. of 3rd Asian Wave & Tidal Energy Conference (AWTEC)*, 2016.
- [117] G. Mccann, “Implications of Site-Specific Conditions on the Prediction of Loading and Power Performance of a Tidal Stream Device,” in *2nd International Conference on Ocean Energy (ICOE 2008)*, 2008, Accessed: Dec. 19, 2018. [Online]. Available: <https://www.researchgate.net/publication/228402190>.
- [118] R. E. Murray, S. Ordonez-Sanchez, K. E. Porter, D. A. Doman, M. J. Pegg, and C. M. Johnstone, “Towing tank testing of passively adaptive composite tidal turbine blades and comparison to design tool,” *Renew. Energy*, vol. 116, pp. 202–214, 2018, doi: 10.1016/j.renene.2017.09.062.
- [119] K. Porter, S. Ordonez-Sanchez, R. Murray, M. Allmark, C. Johnstone, T. O’Doherty, A. Mason-Jones, D. Doman, and M. Pegg, “Flume testing of passively adaptive composite tidal turbine blades under combined wave and current loading,” 2020.
- [120] Edinburgh Designs, “Wave Generators,” 2019. <http://www4.edesign.co.uk/waves/some-wave-1/> (accessed Nov. 18, 2019).

- [121] X.-F. Liang, J.-M. Yang, J. Li, X. Long-Fei, and L. Xin, "Numerical Simulation of Irregular Wave - Simulating Irregular Wave Train," *J. Hydrodyn.*, vol. 22, no. 4, pp. 537–545, 2010, doi: 10.1016/S1001-6058(09)60086-X.
- [122] P. Higuera, J. L. Lara, and I. J. Losada, "Realistic wave generation and active wave absorption for Navier-Stokes models Application to OpenFOAM®," *Coastal Eng.*, vol. 71, pp. 102–118, 2013, doi: 10.1016/j.coastaleng.2012.07.002.
- [123] A. Lal and M. Elangovan, "CFD Simulation and Validation of Flap Type Wave-Maker," *Int. J. Math. Comput. Sci.*, vol. 2, no. 10, pp. 708–714, 2008, Accessed: Jan. 22, 2018. [Online]. Available: <https://www.waset.org/publications/3457/cfd-simulation-and-validation-of-flap-type-wave-maker>.
- [124] A. Toffoli and E. M. Bitner-Gregersen, "Types of Ocean Surface Waves, Wave Classification," *Encycl. Marit. Offshore Eng.*, pp. 1–8, 2017, doi: 10.1002/9781118476406.emoe077.
- [125] A. S. Iyer, S. J. Couch, G. P. Harrison, and A. R. Wallace, "Variability and phasing of tidal current energy around the United Kingdom," *Renew. Energy*, 2013, doi: 10.1016/j.renene.2012.09.017.
- [126] W. Finnegan and J. Goggins, "Numerical simulation of linear water waves and wave-structure interaction," *Ocean Eng.*, vol. 43, pp. 23–31, 2012, doi: 10.1016/j.oceaneng.2012.01.002.
- [127] R. J. Lambert, "Development of a numerical wave tank using OpenFOAM," PhD Thesis, University of Coimbra, 2012.
- [128] M. C. Silva, M. A. Vitola, P. T. T. Esperanca, S. H. Sphaier, and C. A. Levi, "Numerical simulations of wave-current flow in an ocean basin," *Appl. Ocean Res.*, vol. 61, pp. 32–41, 2016, doi: 10.1016/j.apor.2016.10.005.
- [129] F. M. Marques Machado, A. M. Gameiro Lopes, and A. D. Ferreira, "Numerical simulation of regular waves: Optimization of a numerical wave tank," *Ocean Eng.*, vol. 170, pp. 89–99, Dec. 2018, doi: 10.1016/j.oceaneng.2018.10.002.
- [130] N. Jacobsen, D. Fuhrman, and J. Fredsøe, "A wave generation toolbox for the open-source CFD library: OpenFoam," *Int. J. Numer. Methods Fluids*, vol. 70, no. 9, pp. 1073–1088, 2012, doi: 10.1002/flid.2726.
- [131] X. Tian, Q. Wang, G. Liu, W. Deng, and Z. Gao, "Numerical and experimental studies

REFERENCES

- on a three-dimensional numerical wave tank," *IEEE Access*, 2018, doi: 10.1109/ACCESS.2018.2794064.
- [132] H. Bihs, A. Kamath, A. Chella, A. Aggarwal, and Ø. A. Arntsen, "A new level set numerical wave tank with improved density interpolation for complex wave hydrodynamics," *Comput. Fluids*, vol. 140, pp. 191–208, 2016, doi: 10.1016/j.compfluid.2016.09.012.
- [133] S.-Y. Kim, K.-M. Kim, J.-C. Park, G.-M. Jeon, and H.-H. Chun, "Numerical simulation of wave and current interaction with a fixed offshore substructure," *Int. J. Nav. Archit. Ocean Eng.*, vol. 8, pp. 188–197, 2016, doi: 10.1016/j.ijnaoe.2016.02.002/pISSN.
- [134] D. Ning and B. Teng, "Numerical simulation of fully nonlinear irregular wave tank in three dimension," *Int. J. Numer. Methods Fluids*, no. 53, pp. 1847–1862, 2007, doi: 10.1002/fld.138.
- [135] W. Finnegan and J. Goggins, "Linear irregular wave generation in a numerical wave tank," *Appl. Ocean Res.*, vol. 52, pp. 188–200, 2015, doi: 10.1016/j.apor.2015.06.006.
- [136] S. C. Tatum, C. H. Frost, M. Allmark, D. M. O'Doherty, A. Mason-Jones, P. W. Prickett, R. I. Grosvenor, C. B. Byrne, and T. O'Doherty, "Wave-current interaction effects on tidal stream turbine performance and loading characteristics," *Int. J. Mar. Energy*, vol. 14, pp. 161–179, 2016, doi: 10.1016/j.ijome.2015.09.002.
- [137] G. B. Airy, "Tides and Waves," *Encycl. Metrop.*, vol. 5, pp. 341–396, 1845.
- [138] G. G. Stokes, "On the theory of oscillatory waves," *Trans. Cambridge Philos. Soc.*, vol. 8, pp. 441–455, 1847.
- [139] V. Sundar, *Ocean Wave Mechanics: Applications in Marine Structures*. London: Wiley, 2016.
- [140] C. M. Linton and P. McIver, *Handbook of mathematical techniques for wave/structure interactions*. CRC Press, 2001.
- [141] B. Le Mehaute, *An Introduction to Hydrodynamics and Water Waves*. New York: Springer-Verlag, 1976.
- [142] J. S. Mani, *Coastal Hydrodynamics*. New Delhi: PHI Learning Private Limited, 2012.
- [143] R. Dean and R. Dalrymple, *Water wave mechanics for engineers and scientists*.

- World Scientific Publishing Co. Pte. Ltd, 2010.
- [144] G. Crapper, *Introduction to Water Waves*. Chichester: John Wiley & Sons, 1984.
- [145] R. Salmon, *Introduction to Ocean Waves*. University of California, San Diego, 2004.
- [146] M. Rahman, "Fundamentals concerning Stokes waves," *Trans. Eng. Sci.*, vol. 9, 1996, Accessed: Sep. 12, 2019. [Online]. Available: www.witpress.com,
- [147] T. S. Hedges, "Regions of validity of analytical wave theories," *Proc. Inst. Civ. Eng. - Water Marit. Eng.*, vol. 112, no. 2, pp. 111–114, 1995, Accessed: Mar. 28, 2017. [Online]. Available: <http://www.icevirtuallibrary.com/doi/pdf/10.1680/iwtme.1995.27656>.
- [148] R. Miche, *Movements ondulatoires des mers en profondeur constante ou décroissante*. Annales des Ponts et Chaussées, 1944.
- [149] ANSYS Inc, "ANSYS CFX." Release 18.0.
- [150] ANSYS Inc, "ANSYS CFX Theory Guide." Release 18.0.
- [151] D. C. Wilcox, *Turbulence Modeling for CFD*, 3rd Editio. DCW Industries, 2006.
- [152] F. R. Menter, "A Comparison of Some Recent Eddy-Viscosity Turbulence Models," *J. Fluids Eng.*, vol. 118, pp. 514–519, 1996, Accessed: Jan. 18, 2019. [Online]. Available: <https://fluidsengineering.asmedigitalcollection.asme.org>.
- [153] F. Menter, M. Kuntz, and R. Langtry, "Ten Years of Industrial Experience with the SST Turbulence Model," in *Proceedings of the 4th International Symposium on Turbulence, Heat and Mass Transfer, 12-17 October 2003, Antalya, Turkey, 2003*, Accessed: Jan. 18, 2019. [Online]. Available: <http://aaac.larc.nasa.gov/tsab/cfdlarc/aiaa-dpw/>.
- [154] J. Manwell, J. McGowan, and A. Rogers, *Wind Energy Explained: Theory, Design and Application*, 2nd Editio. Wiley, 2009.
- [155] Wolfram MathWorld, "Circular Segment -- from Wolfram MathWorld." <http://mathworld.wolfram.com/CircularSegment.html> (accessed Jan. 15, 2020).
- [156] M. Allmark, R. Ellis, C. Lloyd, S. Ordonez-Sanchez, K. Johannesen, C. Byrne, C. Johnstone, T. O'Doherty, and A. Mason-Jones, "The development, design and characterisation of a scale model Horizontal Axis Tidal Turbine for Dynamic Load

REFERENCES

- Quantification," *Renew. Energy*, 2020.
- [157] Applied Measurements Ltd, "Engineering Notes on Pressure Measurement," 2019. <https://appmeas.co.uk/resources/pressure-measurement-notes/> (accessed Dec. 10, 2019).
- [158] British Standards Institution, "BS 8422:2003 - Force measurement: Strain gauge load cell systems- Calibration method 696 697 BSI," 2003. doi: 0 580 42746 3.
- [159] Specialist committee on modelling environmental conditions of 25th ITTC, "Recommended Procedures and Guidelines: Guide to the Expression of Uncertainty in Experimental Hydrodynamics," 2008. Accessed: Oct. 08, 2018. [Online]. Available: <https://ittc.info/media/1213/75-02-01-01.pdf>.
- [160] R. Poole, "Private communication." 2018.
- [161] R. Howell, N. Qin, J. Edwards, and N. Durrani, "Wind tunnel and numerical study of a small vertical axis wind turbine," *Renew. Energy*, vol. 35, pp. 412–422, 2009, doi: 10.1016/j.renene.2009.07.025.
- [162] ANSYS Inc., "ANSYS Fluent Advanced Workshop: Simulation of Small Floating Objects in Wavy Environment with ANSYS Fluent," 2016.
- [163] A. Raval, "Numerical Simulation of Water Waves using Navier-Stokes Equations," PhD Thesis, University of Leeds, 2008.
- [164] ANSYS Inc, "ANSYS ICEM Help Manual." Release 18.0.
- [165] M. O. L. Hansen, J. N. Sørensen, S. Voutsinas, N. Sørensen, and H. A. Madsen, "State of the art in wind turbine aerodynamics and aeroelasticity," *Prog. Aerosp. Sci.*, vol. 42, pp. 285–330, 2006, doi: 10.1016/j.paerosci.2006.10.002.
- [166] A. Alberello, C. Pakodzi, F. Nelli, E. M. Bitner-Gregersen, and A. Toffoli, "Three Dimensional Velocity Field Underneath a Breaking Rogue Wave," *Proc. ASME 36th Int. Conf. Ocean. Offshore Arct. Eng. June 25-30th 2017, Trondheim, Norw.*, no. June, p. V03AT02A009, 2017, doi: 10.1115/OMAE2017-61237.
- [167] ANSYS Inc, "Innovative Turbulence Modeling: SST Model in ANSYS CFX," 2004. Accessed: Apr. 20, 2018. [Online]. Available: <http://fluid.itcmp.pwr.wroc.pl/~pblasiak/CFD/UsefullInformation/sst.pdf>.
- [168] T. Hirt, "Implicit vs Explicit Numerical Methods," *CFD-101*, 2019.

- <https://www.flow3d.com/resources/cfd-101/numerical-issues/implicit-versus-explicit-numerical-methods/> (accessed Nov. 22, 2019).
- [169] ANSYS Inc, "ANSYS CFX Reference Guide." Release 18.0.
- [170] M. Allmark, R. Grosvenor, and P. Prickett, "An approach to the characterisation of the performance of a tidal stream turbine," *Renew. Energy*, vol. 111, pp. 849–860, 2017, doi: 10.1016/j.renene.2017.05.010.
- [171] D. G. Goring and V. I. Nikora, "Despiking Acoustic Doppler Velocimeter Data," *J. Hydraul. Eng.*, 2002, doi: 10.1061/ASCE0733-94292002128:1117.
- [172] M. Allmark, "Condition Monitoring and Fault Diagnosis of Tidal Stream Turbines Subjected to Rotor Imbalance Faults," PhD Thesis, Cardiff University, 2016.
- [173] C. Morice, J. Kennedy, N. Rayner, and P. Jones, "Quantifying uncertainties in global and regional temperature change using an ensemble of observational estimates: The HadCRUT4 dataset," *J. Geophys. Res.*, vol. 117, no. D08101, 2012, doi: 10.1029/2011JD017187.
- [174] A. H. Hammerfest, "Tidal Turbines – ANDRITZ HYDRO Hammerfest," 2019. <http://www.andritzhydrohammerfest.co.uk/tidal-turbines/> (accessed Dec. 16, 2019).
- [175] SABELLA, "SABELLA's tidal turbines: tidal stream power to trigger the energy transition," 2019. <https://www.sabella.bzh/en> (accessed Dec. 16, 2019).
- [176] Renovables Magallanes, "Proyecto Magallanes," 2019. <http://www.magallanesrenovables.com/en/proyecto> (accessed Dec. 16, 2019).
- [177] Nautricity, "Nautricity," 2019. <https://www.nautricity.com/> (accessed Dec. 16, 2019).
- [178] Orbital Marine Power, "Orbital Marine Power - the world leader in the development of floating tidal stream and run-of-river turbines.," 2019. <https://orbitalmarine.com/> (accessed Dec. 16, 2019).
- [179] Marine Energy, "Tides wash away OpenHydro | Marine Energy," 2019. <https://marineenergy.biz/2018/07/26/tides-wash-away-openhydro/> (accessed Dec. 16, 2019).
- [180] European Marine Energy Centre, "Alstom (formerly TGL) : EMEC: European Marine

REFERENCES

- Energy Centre,” 2019. <http://www.emec.org.uk/about-us/our-tidal-clients/alstom/> (accessed Dec. 16, 2019).
- [181] Tocardo, “Tocado | tidal, river and ocean energy power turbines.” <https://www.tocado.com/> (accessed Dec. 16, 2019).
- [182] Voith Hydro, “Voith,” 2019. <http://voith.com/corp-en/index.html> (accessed Dec. 16, 2019).
- [183] FloWave Ocean Energy Research Facility, “Welcome to the FloWave Ocean Energy Research Facility | FloWave Ocean Energy Research Facility,” 2019. <https://www.flowavett.co.uk/> (accessed Dec. 16, 2019).
- [184] T. Ebdon, D. M. O. Doherty, and T. O. Doherty, “Modelling the Effect of Turbulence Length Scale on Tidal Turbine Wakes using Advanced Turbulence Models,” in *Proceedings of the 12th European Wave and Tidal Energy Conference, 27th Aug -1st Sept 2017, Cork, Ireland, 2017*, pp. 1–10.

APPENDIX

A. CFX EXPRESSION LANGUAGE (CEL) EXPRESSIONS

CEL is a language that has been developed to enable CFX users to enhance their simulations without linking separate external Fortran routines. CEL expressions can be used anywhere that a value is required for input in ANSYS CFX, and can be used to define material properties, specify complex boundary conditions, add terms to solved equations, and monitor the value of an expression during the solution using monitor points. Further information can be found in [169].

The following section details the CEL expressions used in specific simulations, as described in Table 5.7, with conditions specific to:

- uniform current only conditions with a TST: [CFD_UC3_Turb](#)
- profiled current only conditions with a TST: [CFD_PC1_Turb](#)
- uniform current and wave conditions: [CFD_UC1_W1_Int](#)
- profiled current and wave conditions with a TST: [CFD_PC1_W4_Turb](#)

CEL for [CFD_UC3_Turb](#)

```
# State file created: 2020/01/21 09:32:13
# Build 18.0 2016-12-02T23:56:05.472000
```

LIBRARY:

CEL:

EXPRESSIONS:

```
AirDensity = 1.185 [kg m^-3]
AngularFreqTurbine = 8.8878 [rad/s]
AvailPower = 0.5*WaterDensity*SweptArea*(FluidVelocity^3)
AvailThrust = 0.5*WaterDensity*SweptArea*(FluidVelocity^2)
Cpower = OutputPower/AvailPower
Cq = (torque_z_Rot Axis()@Blade1+torque_z_Rot Axis()@Blade2+torque_z_Rot
Axis()@Blade3+torque_z_Rot Axis()@Hub)/(AvailThrust*turbrad)
Cthrust = OutputThrust/AvailThrust
DSHydrostaticPressure = ((WaterDensity-ReferenceDensity)*g*(DownStreamHeight-
y))*DownStreamVolFractWater
DownStreamHeight = Seabed+WaterDepth
DownStreamPressure = ((WaterDensity-ReferenceDensity)*g*(DownStreamHeight-
y))*DownStreamVolFractWater
DownStreamVolFractAir = step((y-DownStreamHeight)/1[m])
DownStreamVolFractWater = 1-DownStreamVolFractAir
FluidVelocity = 1.0107 [m/s]
FluidVelocityInit = 1.0107 [m/s]*DownStreamVolFractWater
```

APPENDIX

```
OutputPower = (torque_z_Rot Axis()@Blade1+torque_z_Rot Axis()@Blade2+
torque_z_Rot Axis()@Blade3+torque_z_Rot Axis()@Hub)*AngularFreqTurbine
OutputThrust = force_z_Rot Axis()@Blade1+force_z_Rot Axis()@Blade2+force_z_Rot
Axis()@Blade3+force_z_Rot Axis()@Hub
ReferenceDensity = AirDensity
Seabed = 0.0 [m]
SweptArea = pi*(turbrad^2)
TimeStep = 1/((AngularFreqTurbine*(180/pi[rad]))/5)
UpStreamHeight = Seabed+WaterDepth
UpStreamPressure = ((WaterDensity-ReferenceDensity)*g*(UpStreamHeight-
y))*UpStreamVolFractWater
UpStreamVolFractAir = step((y-UpStreamHeight)/1[m])
UpStreamVolFractWater = 1-UpStreamVolFractAir
WaterDensity = 997 [kg m^-3]
WaterDepth = 2 [m]
lambda = (AngularFreqTurbine*turbrad)/FluidVelocity
turbrad = 0.45 [m]
END
END
END
COMMAND FILE:
Version = 18.0
END
```

CEL for [CFD_PC1_Turb](#)

```
# State file created: 2020/01/21 09:34:57
# Build 18.0 2016-12-02T23:56:05.472000
```

LIBRARY:

CEL:

EXPRESSIONS:

```
AirDensity = 1.185 [kg m^-3]
AngularFreqTurbine = 8.8874 [rad/s]
AvailPower = 0.5*WaterDensity*SweptArea*(FV^3)
AvailThrust = 0.5*WaterDensity*SweptArea*(FV^2)
Cpower = OutputPower/AvailPower
Cq = (torque_z_Rot Axis()@Blade1+torque_z_Rot Axis()@Blade2+torque_z_Rot
Axis()@Blade3+torque_z_Rot Axis()@Hub)/(AvailThrust*turbrad)
Cthrust = OutputThrust/AvailThrust
DSHydrostaticPressure = ((WaterDensity-ReferenceDensity)*g*(DownStreamHeight-
y))*DownStreamVolFractWater
DownStreamHeight = Seabed+WaterDepth
DownStreamPressure = ((WaterDensity-ReferenceDensity)*g*(DownStreamHeight-
y))*DownStreamVolFractWater
DownStreamVolFractAir = step((y-DownStreamHeight)/1[m])
DownStreamVolFractWater = 1-DownStreamVolFractAir
FV = 1.0 [m/s]
FluidVelocity = 1.0 [m/s]
FluidVelocityInit = 1.0 [m/s]*DownStreamVolFractWater
```

```

OutputPower = (torque_z_Rot Axis()@Blade1+torque_z_Rot Axis()@Blade2+
torque_z_Rot Axis()@Blade3+torque_z_Rot Axis()@Hub)*AngularFreqTurbine
OutputThrust = (torque_z_Rot Axis()@Blade1+torque_z_Rot Axis()@Blade2+
torque_z_Rot Axis()@Blade3+torque_z_Rot Axis()@Hub)*AngularFreqTurbine
ReferenceDensity = AirDensity
Seabed = 0.0 [m]
SweptArea = pi*(turbrad^2)
TimeStep = TimeStepTurb
TimeStepTurb = 1/((AngularFreqTurbine*(180/pi[rad]))/5)
UpStreamHeight = Seabed+WaterDepth
UpStreamPressure = ((WaterDensity-ReferenceDensity)*g*(UpStreamHeight-
y))*UpStreamVolFractWater
UpStreamVolFractAir = step((y-UpStreamHeight)/1[m])
UpStreamVolFractWater = 1-UpStreamVolFractAir
WaterDensity = 997 [kg m^-3]
WaterDepth = 2 [m]
lambda = (AngularFreqTurbine*turbrad)/FV
turbrad = 0.45 [m]
END
END
END
COMMAND FILE:
Version = 18.0
END

```

CEL for [CFD_UC1_W1_Int](#)

```

# State file created: 2020/01/21 09:32:58
# Build 18.0 2016-12-02T23:56:05.472000

```

LIBRARY:

CEL:

EXPRESSIONS:

```

AirDensity = 1.185 [kg m^-3]
AngularFreqTurbine = 8.89 [rad/s]
BeachLinCoeff = WaterDensity*g/(8*MeanVelocity)*BeachRamp
BeachQuadCoeff = WaterDensity*g/(8*MeanSquareVelocity)*BeachRamp
BeachRamp = min( max(0, 1+ (z-zOutlet)/BeachSourceWidth), 1)
BeachSourceWidth = 2*Wavelength
DSHydrostaticPressure = (((WaterDensity-ReferenceDensity)*g*(DownStreamHeight-
y))+3/8*(WaterDensity-ReferenceDensity)*g*(pi*(WaveHeight^2)/Wavelength)*
(tanh(WaveNumber*WaterDepth)/((sinh(WaveNumber*WaterDepth))^2))*((cosh(2*
WaveNumber*y)/((sinh(WaveNumber*WaterDepth))^2))-1/3*(cos(2*WavePhase)))-
(1/8*(WaterDensity-ReferenceDensity)*g*(pi*(WaveHeight^2)/Wavelength)*
(tanh(WaveNumber*WaterDepth)/((sinh(WaveNumber*WaterDepth))^2))*(cosh(2*
WaveNumber*y)-1)))*DownStreamVolFractWater
DownStreamHeight = Seabed+WaterDepth
DownStreamPressure = (((WaterDensity-ReferenceDensity)*g*WaveElevation*
(cosh(WaveNumber*y)/cosh(WaveNumber*WaterDepth)))+(WaterDensity-
ReferenceDensity)*g*(DownStreamHeight-y))+3/8*(WaterDensity-ReferenceDensity)*
g*(pi*(WaveHeight^2)/Wavelength)*(tanh(WaveNumber*WaterDepth)/((sinh(Wave

```

```

Number*WaterDepth))^2))*((cosh(2*WaveNumber*y)/((sinh(WaveNumber*WaterDepth)
^2))-1/3)*(cos(2*WavePhase)))-(1/8*(WaterDensity-ReferenceDensity)*g*(pi*(WaveHeight
^2)/Wavelength)*(tanh(WaveNumber*WaterDepth)/((sinh(WaveNumber*WaterDepth)
^2))*(cosh(2*WaveNumber*y)-1))) *DownStreamVolFractWater
  DownStreamVolFractAir = step((y-DownStreamHeight)/1[m])
  DownStreamVolFractWater = 1-DownStreamVolFractAir
  FluidVelocity = 0.93 [m/s]
  FluidVelocityInit = 0.93 [m/s]*DownStreamVolFractWater
  GroupVelocity = (rWaveCelerity/2)*(1+((2*WaveNumber*WaterDepth)/(sinh(2*
WaveNumber*WaterDepth))))
  HorizontalParticleVelocity = if(t<aTimePeriod, FluidVelocity*UpStreamVolFractWater,
(FluidVelocity*UpStreamVolFractWater)+(rAngularFreqWave*WaveAmplitude*cosh(Wave
Number*y)/sinh(WaveNumber*WaterDepth)*cos(WavePhase)+(0.75*(((pi*WaveHeight)/
Wavelength)^2)*rWaveCelerity*(cosh(2*WaveNumber*y)/((sinh(WaveNumber*WaterDept
h))^4))*cos(2*WavePhase))))*UpStreamVolFractWater
  MaxVelocity = rAngularFreqWave*WaveAmplitude
  MeanSquareVelocity = 0.5*(rAngularFreqWave*WaveAmplitude)^2
  MeanVelocity = rAngularFreqWave*WaveAmplitude/pi
  MomSourceCoeff = 10000 [kg m^-3 s^-1]*BeachRamp
  MomSourceZ = (MomSourceCoeff* (FluidVelocity - Velocity w))
*UpStreamVolFractWater
  NonDimDepth = WaterDepth/(g*rTimePeriod^2)
  NonDimHeight = WaveHeight/(g*rTimePeriod^2)
  ReferenceDensity = AirDensity
  Seabed = 0.0 [m]
  TimeStep = aTimePeriod/50
  UpStreamHeight = if(t<aTimePeriod, Seabed+WaterDepth,Seabed+
WaterDepth+WaveElevation)
  UpStreamPressure = (((WaterDensity-ReferenceDensity)*g*WaveElevation*(cosh(Wave
Number*y)/cosh(WaveNumber*WaterDepth)))+(WaterDensity-ReferenceDensity)*g*
(UpStreamHeight-y)+(3/8*(WaterDensity-ReferenceDensity)*g*(pi*(WaveHeight^2)/
Wavelength)*(tanh(WaveNumber*WaterDepth)/(sinh(WaveNumber*WaterDepth)^2))*
((cosh(2*WaveNumber*y)/(sinh(WaveNumber*WaterDepth)^2))-1/3)*(cos(2*Wave
Phase)))-(1/8*(WaterDensity-ReferenceDensity)*g*(pi*(WaveHeight^2)/Wavelength)
*(tanh(WaveNumber*WaterDepth)/(sinh(WaveNumber*WaterDepth)^2))*(cosh(2*
WaveNumber*y)-1))) *UpStreamVolFractWater
  UpStreamVolFractAir = step((y-UpStreamHeight)/1[m])
  UpStreamVolFractWater = 1-UpStreamVolFractAir
  VerticalParticleVelocity = if(t<aTimePeriod, 0 [m/s],(rAngularFreqWave*
WaveAmplitude*sinh(WaveNumber*y)/sinh(WaveNumber*WaterDepth)*sin(WavePhase)
+(0.75*(((pi*WaveHeight)/Wavelength)^2)*rWaveCelerity*(sinh(2*WaveNumber*y)/
((sinh(WaveNumber*WaterDepth))^4))*sin(2*WavePhase))))*UpStreamVolFractWater)
  WaterDensity = 997 [kg m^-3]
  WaterDepth = 0.76 [m]
  WaveAmplitude = WaveHeight/2
  WaveElevation = if(t<aTimePeriod, 0[m], WaveAmplitude*cos(WavePhase)+
(((pi*(WaveHeight^2))/(8*Wavelength))*((cosh(WaveNumber*WaterDepth))/(sinh(
WaveNumber*WaterDepth)^3))*(2+cosh(2*WaveNumber*WaterDepth))*(cos(2*
WavePhase))))
  WaveHeight = 0.058[m]
  WaveNumber = InvXTanhX(rAngularFreqWave^2*WaterDepth/g)/WaterDepth
  WavePhase = (WaveNumber*z)-(aAngularFreqWave*t)

```

```

WavePower = EnergyDensityAv*GroupVelocity*Width
Wavelength = 2*pi/WaveNumber
aAngularFreqWave = rAngularFreqWave+(WaveNumber*FluidVelocity)
aTimePeriod = 1/((1/rTimePeriod)+(FluidVelocity/Wavelength))
aWaveCelerity = rWaveCelerity+FluidVelocity
rAngularFreqWave = (2*pi)/rTimePeriod
rTimePeriod = 1.217735 [s]
rWaveCelerity = rAngularFreqWave/WaveNumber
zOutlet = 20[m]
END
END
END
COMMAND FILE:
Version = 18.0
END

```

CEL for *CFD_PC1_W4_Turb*

```

# State file created: 2020/01/21 09:33:52
# Build 18.0 2016-12-02T23:56:05.472000

```

LIBRARY:

CEL:

EXPRESSIONS:

```

AirDensity = 1.185 [kg m^-3]
AngularFreqTurbine = 8.8874 [rad/s]
AvailPower = 0.5*WaterDensity*SweptArea*(FV^3)
AvailThrust = 0.5*WaterDensity*SweptArea*(FV^2)
BeachLinCoeff = WaterDensity*g/(8*MeanVelocity)*BeachRamp
BeachQuadCoeff = WaterDensity*g/(8*MeanSquareVelocity)*BeachRamp
BeachRamp = min( max(0, 1+ (z-zOutlet)/BeachSourceWidth), 1)
BeachSourceWidth = 2*Wavelength
Cpower = OutputPower/AvailPower
Cq = (torque_z_Rot Axis()@Blade1+torque_z_Rot Axis()@Blade2+torque_z_Rot
Axis()@Blade3+torque_z_Rot Axis()@Hub)/(AvailThrust*turbrad)
Cthrust = OutputThrust/AvailThrust
DSHydrostaticPressure = (((WaterDensity-ReferenceDensity)*g*(DownStreamHeight-
y))+3/8*(WaterDensity-ReferenceDensity)*g*(pi*(WaveHeight^2)/Wavelength)*
(tanh(WaveNumber*WaterDepth)/((sinh(WaveNumber*WaterDepth))^2))*((cosh(2*
WaveNumber*y)/((sinh(WaveNumber*WaterDepth))^2))-1/3)*(cos(2*WavePhase)))-
(1/8*(WaterDensity-ReferenceDensity)*g*(pi*(WaveHeight^2)/Wavelength)*
(tanh(WaveNumber*WaterDepth)/((sinh(WaveNumber*WaterDepth))^2))*((cosh(2*
WaveNumber*y)-1)))*DownStreamVolFractWater
DownStreamHeight = Seabed+WaterDepth
DownStreamPressure = (((WaterDensity-
ReferenceDensity)*g*WaveElevation*(cosh(WaveNumber*y)/cosh(WaveNumber*WaterDe
pth))+((WaterDensity-ReferenceDensity)*g*(DownStreamHeight-y))+3/8*(WaterDensity-
ReferenceDensity)*g*(pi*(WaveHeight^2)/Wavelength)*(tanh(WaveNumber*WaterDepth)
/((sinh(WaveNumber*WaterDepth))^2))*((cosh(2*WaveNumber*y)/((sinh(WaveNumber*
WaterDepth))^2))-1/3)*(cos(2*WavePhase)))-1/8*(WaterDensity-ReferenceDensity)*g*

```

```

(pi*(WaveHeight^2)/Wavelength)*(tanh(WaveNumber*WaterDepth)/((sinh(WaveNumber*
WaterDepth))^2))*(cosh(2*WaveNumber*y)-1))*DownStreamVolFractWater
DownStreamVolFractAir = step((y-DownStreamHeight)/1[m])
DownStreamVolFractWater = 1-DownStreamVolFractAir
FV = 1.0175 [m/s]
FluidVelocity = Inlet.Water.Velocity w(x,y,z)
FluidVelocityInit = Inlet.Water.Velocity w(x,y,z)*DownStreamVolFractWater
GroupVelocity = (rWaveCelerity/2)*(1+((2*WaveNumber*WaterDepth)/
(sinh(2*WaveNumber*WaterDepth))))
HorizontalParticleVelocity = if(t<TP, 0[m/s],(rAngularFreqWave*WaveAmplitude*
cosh(WaveNumber*y)/sinh(WaveNumber*WaterDepth)*cos(WavePhase)+(0.75*
((pi*WaveHeight)/Wavelength)^2)*rWaveCelerity*(cosh(2*WaveNumber*y)/((sinh(
WaveNumber*WaterDepth))^4))*(cos(2*WavePhase))))*UpStreamVolFractWater
MaxVelocity = rAngularFreqWave*WaveAmplitude
MeanSquareVelocity = 0.5*(rAngularFreqWave*WaveAmplitude)^2
MeanVelocity = rAngularFreqWave*WaveAmplitude/pi
MomSourceCoeff = 10000 [kg m^-3 s^-1]*BeachRamp
MomSourceZ = (MomSourceCoeff*(FluidVelocityInit - Water.Velocity w))
*UpStreamVolFractWater
NonDimDepth = WaterDepth/(g*rTimePeriod^2)
NonDimHeight = WaveHeight/(g*rTimePeriod^2)
OutputPower = (torque_z_Rot Axis()@Blade1+torque_z_Rot Axis()@Blade2+
torque_z_Rot Axis()@Blade3+torque_z_Rot Axis()@Hub)*AngularFreqTurbine
OutputThrust = (torque_z_Rot Axis()@Blade1+torque_z_Rot Axis()@Blade2+
torque_z_Rot Axis()@Blade3+torque_z_Rot Axis()@Hub)*AngularFreqTurbine
ReferenceDensity = AirDensity
Seabed = 0.0 [m]
SweptArea = pi*(turbrad^2)
TP = 2 [s]
TargetFluidVel = FV
TimeStep = if(TimeStepWave>TimeStepTurb,TimeStepTurb,TimeStepWave)
TimeStepTurb = 1/((AngularFreqTurbine*(180/pi[rad]))/5)
TimeStepWave = aTimePeriod/50
UpStreamHeight = if(t<TP, Seabed+WaterDepth,Seabed+WaterDepth+WaveElevation)
UpStreamPressure = (((WaterDensity-ReferenceDensity)*g*WaveElevation*
(cosh(WaveNumber*y)/cosh(WaveNumber*WaterDepth)))+(WaterDensity-
ReferenceDensity)*g*(UpStreamHeight-y)+(3/8*(WaterDensity-ReferenceDensity)*g*
(pi*(WaveHeight^2)/Wavelength)*(tanh(WaveNumber*WaterDepth)/(sinh(WaveNumber*
WaterDepth)^2))*((cosh(2*WaveNumber*y)/(sinh(WaveNumber*WaterDepth)^2))-
1/3)*(cos(2*WavePhase)))-(1/8*(WaterDensity-ReferenceDensity)*g*(pi*(WaveHeight^2)
/Wavelength)*(tanh(WaveNumber*WaterDepth)/(sinh(WaveNumber*WaterDepth)^2))*
(cosh(2*WaveNumber*y)-1))*UpStreamVolFractWater
UpStreamVolFractAir = step((y-UpStreamHeight)/1[m])
UpStreamVolFractWater = 1-UpStreamVolFractAir
VerticalParticleVelocity = if(t<TP, 0 [m/s],(rAngularFreqWave*WaveAmplitude*
sinh(WaveNumber*y)/sinh(WaveNumber*WaterDepth)*sin(WavePhase)+(0.75*
((pi*WaveHeight)/Wavelength)^2)*rWaveCelerity*(sinh(2*WaveNumber*y)/((sinh(
WaveNumber*WaterDepth))^4))*(sin(2*WavePhase))))*UpStreamVolFractWater
WaterDensity = 997 [kg m^-3]
WaterDepth = 2 [m]
WaveAmplitude = WaveHeight/2

```

```

WaveElevation = if(t<TP, 0[m], WaveAmplitude*cos(WavePhase)+
(((pi*(WaveHeight^2))/(8*Wavelength))*((cosh(WaveNumber*WaterDepth))/(sinh(
WaveNumber*WaterDepth)^3))*(2+cosh(2*WaveNumber*WaterDepth))*(cos(2*
WavePhase))))
WaveHeight = 0.082[m]
WaveNumber = InvXTanhX(rAngularFreqWave^2*WaterDepth/g)/WaterDepth
WavePhase = (WaveNumber*z)-(aAngularFreqWave*t)
WavePower = EnergyDensityAv*GroupVelocity*Width
Wavelength = 2*pi/WaveNumber
aAngularFreqWave = rAngularFreqWave+(WaveNumber*TargetFluidVel)
aTimePeriod = 1/((1/rTimePeriod)+(TargetFluidVel/Wavelength))
aWaveCelerity = rWaveCelerity+TargetFluidVel
lambda = (AngularFreqTurbine*turbrad)/FV
rAngularFreqWave = (2*pi)/rTimePeriod
rTimePeriod = 2.565882925 [s]
rWaveCelerity = rAngularFreqWave/WaveNumber
turbrad = 0.45 [m]
zOutlet = 80[m]
END
END
END
COMMAND FILE:
Version = 18.0
END

```

B. MATLAB: RESULTS PROCESSING SCRIPTS

Matlab was used to process both the experimental and CFD model results. Examples of the scripts created for various experimental and CFD data processing are shown in the following section. These scripts detail the methods used in importing the data to Matlab, processing the imported data using various functions and outputting information on the flow conditions and turbine performance characteristics.

Matlab scripts used for CFD data processing:

Data import

Script name: ImportData_Force_Torque_Velocity_BMx_Prof_WAVES.m

```

% Extract Force, Torque, w_Velocity, v_Velocity and Out of plane bending
% moment (BMx) from CFD

Limit_ts_bottom = [55]; % Import
start time
Limit_ts_top = [60.01]; % Import
end time
run_names={'w22_Prof2_WAVES'; 'w21R_Prof1_WAVES'}; % Run
names
runs = length(run_names);
Num_Depth_Points = [-1.9:0.1:-0.1]'; % Depth of

```

```

monitor points placed through the water column at Z=2m downstream of inlet
                                                                    % Used
only for W and V Velocity results
% FORCE CFD Results:
for n=1:runs

    step = sprintf('Select force files - %s',run_names{n})           % Details
which run file to select

    [filenames, pathname, filterindex] = uigetfile('*..*',...       % Use GUI
to multiple-select all the files that should be read in
    'Pick data files to process','MultiSelect','on');
    cd(pathname);                                                    % Change
directory to pathname where the results came from - easier to pick up files later on

    filename = char(filenames);                                       % Set
filename for import, convert to char array. filenames = array of filenames, filename
= single files, at a certain position of(i)in filenames array
    A = xlsread(filename);                                           % Import
data
    A_time = A(:,1);
    A_force = A(:,2);

    p=1;
    for q=1:4                                                         % q=1,2,3
are blades 1,2,3 and q=4 is the hub data
        j=0;
        for p=p:length(A)                                           % Position
of the values starting at 1 and finishing at the last position of the length of the
data
            if isnan(A_time(p))                                       % if - is
the cell a NaN? If true then...
                break                                               % ...
break the for loop - exits for loop
            end
            if isnumeric(A_time(p))                                    % if - is
the cell numerical? If true then...
                j=j+1;
                ALLtime.(sprintf('Time%d',q))(j,:)=A_time(p);       % Stores
the time value for the force data
                ALLforce.(sprintf('Force%d',q))(j,:)=A_force(p);   % Stores
the force value
            end
            p=p+1;
        end
        p=p+7;                                                       % Skips to
p+7 as there are 7 header lines between data sets
    end

    for q=1:4                                                         % Creates
a structure with all FORCE data for each blade and the hub included for the import
start and end times specified initially
        Force.(sprintf('%s',run_names{n})).(sprintf('blade_%d_ALL',q))=...
        [ALLtime.(sprintf('Time%d',q)),ALLforce.(sprintf('Force%d',q))];
        Force.(sprintf('%s',run_names{n})).(sprintf('blade_%d',q))=...
        [ALLtime.(sprintf('Time%d',q)),ALLforce.(sprintf('Force%d',q))];
        Force.(sprintf('%s',run_names{n})).(sprintf('blade_%d',q))=...
        Force.(sprintf('%s',run_names{n})).(sprintf('blade_%d',q))...

```

```

        (Force.(sprintf('%s',run_names{n})).(sprintf('blade_%d',q))(:,1)...
        >= Limit_ts_bottom, :); %
A=A(A(:,1) >= 55, :) Keeps all values above Limit_ts_bottom
        Force.(sprintf('%s',run_names{n})).(sprintf('blade_%d',q))=...
        Force.(sprintf('%s',run_names{n})).(sprintf('blade_%d',q))...
        (Force.(sprintf('%s',run_names{n})).(sprintf('blade_%d',q))(:,1)...
        <= Limit_ts_top, :); %
A=A(A(:,1) <= 60.01, :) Keeps all values below Limit_ts_top
        Force.(sprintf('%s',run_names{n})).(sprintf('Total_blade_%d_mean',q))...
        =mean(Force.(sprintf('%s',run_names{n})).(sprintf('blade_%d',q))(:,2));
end

        Force.(sprintf('%s',run_names{n})).Total_Force=... % Adds
total forces into structure
        sum(Force.(sprintf('%s',run_names{n})).(sprintf('Total_blade_1_mean'))...
        +Force.(sprintf('%s',run_names{n})).(sprintf('Total_blade_2_mean'))...
        +Force.(sprintf('%s',run_names{n})).(sprintf('Total_blade_3_mean'))...
        +Force.(sprintf('%s',run_names{n})).(sprintf('Total_blade_4_mean')));
        Force.(sprintf('%s',run_names{n})).ALL_blades(:,1)...
        =Force.(sprintf('%s',run_names{n})).(sprintf('blade_%d_ALL',1))(:,1);
        Force.(sprintf('%s',run_names{n})).ALL_blades(:,2)...
        =(Force.(sprintf('%s',run_names{n})).(sprintf('blade_%d_ALL',1))(:,2)...
        +Force.(sprintf('%s',run_names{n})).(sprintf('blade_%d_ALL',2))(:,2)...
        +Force.(sprintf('%s',run_names{n})).(sprintf('blade_%d_ALL',3))(:,2)...
        +Force.(sprintf('%s',run_names{n})).(sprintf('blade_%d_ALL',4))(:,2));
        Force.(sprintf('%s',run_names{n})).ALL_blades_20s(:,1)=...
        Force.(sprintf('%s',run_names{n})).(sprintf('blade_%d',1))(:,1);
        Force.(sprintf('%s',run_names{n})).ALL_blades_20s(:,2)=...
        (Force.(sprintf('%s',run_names{n})).(sprintf('blade_%d',1))(:,2)...
        +Force.(sprintf('%s',run_names{n})).(sprintf('blade_%d',2))(:,2)...
        +Force.(sprintf('%s',run_names{n})).(sprintf('blade_%d',3))(:,2)...
        +Force.(sprintf('%s',run_names{n})).(sprintf('blade_%d',4))(:,2));
        Force.(sprintf('%s',run_names{n})).ALL_blades_20s_mean=...
        mean(Force.(sprintf('%s',run_names{n})).ALL_blades_20s(:,2));

        clearvars -except Limit_ts_bottom Limit_ts_top run_names Perf_names ... % Clears
variables except those specified
        runs filenames filterindex n num_files pathname Force
end

% Identical procedure is used to import the Torque, w_Velocity, v_Velocity
% and the out of plane bending moment (BMx)

```

[Published with MATLAB® R2016b](#)

Process imported data

Script name: Turbine_CFD_Data_P2W5_P1W4_Prof_WAVES.m

```

% Processes FORCE data imported from CFD
% Specific script uses cases P1W4 and P2W5 but can be used for any CFD case
% and any variable - Force, Torque, Velocity etc

RouteDirectory = cd; % Name
current_directory "RouteDirectory"
StudyName = 'Waves_w22_w21R_PROF_Num'; % Set up

```

APPENDIX

```

study folder
StudyDir = strcat(RouteDirectory, '\', StudyName);           % Create
study directory

run_names={'W22_Prof2_WAVES'; 'W21R_Prof1_WAVES'};         % Names of
files to process
runs = length(run_names);

% Load in Force, Torque and Velocity data along with the angular frequency
% of the turbine input to the CFD models
load('K:\Drive_2\Matlab\IFREMER\April 2018 Data\Numerical Data
Processing\Uni_Prof_Waves_Turb\Force_Torque_Vel_W22_W21R_Prof_WAVES.mat')
load('K:\Drive_2\Matlab\IFREMER\April 2018
Data\Raw_Data_Week2\Ang_Freq_W22_W21R_Num.mat')

sec_per_1rot=1./((Ang_Freq.*(180/pi))./360);               % Defines
the time taken for the turbine to do 1 full rotation at input angular frequencies
wavefreq = [0.7;0.5];                                     % Defines
the wave frequencies used
samps = [3.5;2.5];                                       % Defines
the number of waves per sample size used

R = 0.45;                                                 % Rotor
diameter in meters
FlumeHeight = 2.0;                                       % Flume
height in metres
Flumewidth = 4.0;                                        % Flume
width in metre

for n=1:runs                                             % Sets up
'for' loop for the number of CFD cases being processed

    % Defines file path for folders to put results figures in
    TS = strcat(StudyDir, '\Figures\', sprintf('%s', run_names{n}), '\TimeSeries');
    Thrust_folder =
strcat(StudyDir, '\Figures\', sprintf('%s', run_names{n}), '\Thrust');
    Torque_folder =
strcat(StudyDir, '\Figures\', sprintf('%s', run_names{n}), '\Torque');

    % Make and change directory
    mkdir(strcat(TS, '\', sprintf('%s', run_names{n})));
    cd(strcat(TS, '\', sprintf('%s', run_names{n})));

    % CHANGE HUB FORCE TO EXCLUDE HYDROSTATIC PRESSURE COMPONENT (HSP)
                                                                    % Hub
force includes hydrostatic pressure which must be removed to isolate the thrust force
component
    water_HSP = 12.2355;                                     %
Hydrostatic pressure at hub depth to be subtracted from total force
    Force.(sprintf('%s', run_names{n})).(sprintf('blade_%d_ALL', 4))(:,2)=...% blade 4
= hub
        Force.(sprintf('%s', run_names{n})).(sprintf('blade_%d_ALL', 4))(:,2)-
water_HSP;
        Force.(sprintf('%s', run_names{n})).(sprintf('blade_%d', 4))(:,2)=...
        Force.(sprintf('%s', run_names{n})).(sprintf('blade_%d', 4))(:,2)-water_HSP;
        Force.(sprintf('%s', run_names{n})).(sprintf('Total_blade_%d_mean', 4))=...
        Force.(sprintf('%s', run_names{n})).(sprintf('Total_blade_%d_mean', 4))-
water_HSP;

```

```

Force.(sprintf('%s',run_names{n})).Total_Force=...
    Force.(sprintf('%s',run_names{n})).Total_Force-Water_HSP;
Force.(sprintf('%s',run_names{n})).ALL_blades(:,2)=...
    Force.(sprintf('%s',run_names{n})).ALL_blades(:,2)-Water_HSP;
Force.(sprintf('%s',run_names{n})).ALL_blades_20s(:,2)=...
    Force.(sprintf('%s',run_names{n})).ALL_blades_20s(:,2)-Water_HSP;
Force.(sprintf('%s',run_names{n})).ALL_blades_20s_mean=...
    Force.(sprintf('%s',run_names{n})).ALL_blades_20s_mean-Water_HSP;
% HSP removed from hub force component

% Plots figures for each time series
% FORCE
figure % Opens
figure window % Creates
subplot(4,1,1) % Creates
4 x 1 subplot and selects top left corner of subplot
plot(Force.(sprintf('%s',run_names{n})).(sprintf('blade_%d_ALL',1))... % Plots
figure
(:,1),Force.(sprintf('%s',run_names{n})).(sprintf('blade_%d_ALL',1))(:,2))
title('Thrust - Blade 1') % Inputs
title
xlabel('Time (s)'); % Set x
axis label
ylabel('Thrust (N)'); % Set y
axis label
axis([55 60 85 125]) % Set x
and y axis limits

subplot(4,1,2)
plot(Force.(sprintf('%s',run_names{n})).(sprintf('blade_%d_ALL',2))...
(:,1),Force.(sprintf('%s',run_names{n})).(sprintf('blade_%d_ALL',2))(:,2))
title('Thrust - Blade 2')
xlabel('Time (s)');
ylabel('Thrust (N)');
axis([55 60 85 125])

subplot(4,1,3)
plot(Force.(sprintf('%s',run_names{n})).(sprintf('blade_%d_ALL',3))...
(:,1),Force.(sprintf('%s',run_names{n})).(sprintf('blade_%d_ALL',3))(:,2))
title('Thrust - Blade 3')
xlabel('Time (s)');
ylabel('Thrust (N)');
axis([55 60 85 125])

subplot(4,1,4)
plot(Force.(sprintf('%s',run_names{n})).ALL_blades(:,1),...
Force.(sprintf('%s',run_names{n})).ALL_blades(:,2))
title('All Thrust - All Blades')
xlabel('Time (s)');
ylabel('Thrust (N)');
axis([55 60 280 375])

print('Subplot - Thrust','-dpng','-r0') % Saves
subplot figure as a picture file
savefig(gcf,'Subplot - Thrust') % Saves
subplot figure as a matlab figure file

% Previous steps are repeated for torque figures

```

```

% Calculations

% THRUST Processing
% Blades 1,2,3 + hub - the 'for' loop cycles through each blade and hub data for
all calculations detailed below

for q=1:4 % q=1,2,3
are blades 1,2,3 and q=4 is the hub data
    Min_Ts = min(diff(Force.(sprintf('%s',run_names{n})).(sprintf... % Min
timestep (s)
    ('blade_%d',q))(:,1)));
    Min_Fs = 1/Min_Ts; % Min
sampling frequency (Hz) (1/s)
    mintime = Force.(sprintf('%s',run_names{n})).(sprintf... % Min time
(s)
    ('blade_%d',q))(1,1);
    maxtime = Force.(sprintf('%s',run_names{n})).(sprintf... % Max time
(s)
    ('blade_%d',q))(end,1);

    Mean_Thrust = mean(Force.(sprintf('%s',run_names{n})).(sprintf... % Mean
thrust calculated using 'mean' function
    ('blade_%d',q))(:,2));
    Area_Trapz_Thrust = trapz(Force.(sprintf('%s',run_names{n})).... % Mean
thrust calculated using the trapezium rule
    ).(sprintf('blade_%d',q))(:,1),Force.(sprintf('%s',...
run_names{n})).(sprintf('blade_%d',q))(:,2));
    Mean_Trapz_Thrust = Area_Trapz_Thrust/(maxtime-mintime);
    Std_Thrust = std(Force.(sprintf('%s',run_names{n})).(sprintf... % Standard
deviation of thrust
    ('blade_%d',q))(:,2));

% Creates a structure with processed thrust data for each blade and the hub

Thrust_Results.(sprintf('%s',run_names{n})).(sprintf('blade_%d',q)).Mean_Thrust =
Mean_Trapz_Thrust;

Thrust_Results.(sprintf('%s',run_names{n})).(sprintf('blade_%d',q)).Std_Thrust =
Std_Thrust;
    Thrust_Results.(sprintf('%s',run_names{n})).(sprintf('blade_%d',q)).Time =
Force.(sprintf('%s',run_names{n})).(sprintf('blade_%d',q))(:,1);
    Thrust_Results.(sprintf('%s',run_names{n})).(sprintf('blade_%d',q)).Thrust =
Force.(sprintf('%s',run_names{n})).(sprintf('blade_%d',q))(:,2);

%%%%%%%%%%%% Carries out Fast Fourier Transform (FFT) using Script - *CFD_FFT.m*
%%%%%%%%%%%%

%%%%%%%%%%%% Calculation of running mean - split into 100 windows - *CFD_RunningMean.m*
%%%%%%%%%%%%

clearvars -except RouteDirectory StudyName Force Torque Performance...
Velocity surf_names StudyDir TS Thrust_folder Torque_folder R...
FlumeHeight Flumewidth fieldnames_force fieldnames_torque ...
fieldnames_performance fieldnames_velocity n i g q Perf_names ...
Thrust_Results Torque_Results sec_per_1rot Ang_Freq runs ...
run_names wavefreq samps

```

```

%% Calculation of max/min peaks using 'findpeaks' - *CFD_findpeaks.m*
%%

%% Calculation of wave period - *CFD_waveperiod.m*
%%

end % End of
'for' loop for blades 1,2,3 and hub

% Save Total Thrust results
Thrust_Results.(sprintf('%s',run_names{n})).Tot_running_Thrust(:,1)=...
    Force.(sprintf('%s',run_names{n})).(sprintf('blade_%d',1))(:,1);
Thrust_Results.(sprintf('%s',run_names{n})).Tot_running_Thrust(:,2)=...
    Force.(sprintf('%s',run_names{n})).(sprintf('blade_%d',1))(:,2)+...
    Force.(sprintf('%s',run_names{n})).(sprintf('blade_%d',2))(:,2)+...
    Force.(sprintf('%s',run_names{n})).(sprintf('blade_%d',3))(:,2)+...
    Force.(sprintf('%s',run_names{n})).(sprintf('blade_%d',4))(:,2);
Thrust_Results.(sprintf('%s',run_names{n})).Tot_running_Thrust_Mean=...
    mean(Thrust_Results.(sprintf('%s',run_names{n})).Tot_running_Thrust(:,2));

% FOR ALL BLADES AND HUB
% Same procedure is carried out for the total thrust (blades 1,2,3 and
% hub) instead of individual blade and hub results

% for example:
Min_Ts = min(diff(Force.(sprintf('%s',run_names{n})).ALL_blades_20s(:,1)));
% instead of
Min_Ts =
min(diff(Force.(sprintf('%s',run_names{n})).(sprintf('blade_%d',q))(:,1)));

% TORQUE Processing
% Blades 1,2,3 + hub - the 'for' loop cycles through each blade and hub data for
all calculations
% Exactly the same procedure as detailed for 'THRUST' processing

end % Ends
'for' loop for the number of CFD cases being processed

% Collates all results for running mean, mean FFT amplitude, max/min peaks
% for the Thrust results into a structure

for n=1:runs

    % Thrust 1:number, 2,3,4,5,6:Running Means, 7,8,9,10,11:Mean FFT amp,
12,13,14,15,16:Av Max Peak, 17,18,19,20,21:Av Min Peak
    Thrust_Indiv_Blades.(sprintf('%s',run_names{n}))(1,1)=0;
    Thrust_Totals.(sprintf('%s',run_names{n}))(1,1)=0;

    Thrust_Indiv_Blades.(sprintf('%s',run_names{n}))(1,2)=Thrust_Results.(sprintf('%s',ru
n_names{n})).(sprintf('blade_%d',1)).RunningMean;

    Thrust_Indiv_Blades.(sprintf('%s',run_names{n}))(1,3)=Thrust_Results.(sprintf('%s',ru
n_names{n})).(sprintf('blade_%d',2)).RunningMean;

    Thrust_Indiv_Blades.(sprintf('%s',run_names{n}))(1,4)=Thrust_Results.(sprintf('%s',ru
n_names{n})).(sprintf('blade_%d',3)).RunningMean;

```

```

Thrust_Indiv_Blades.(sprintf('%s',run_names{n}))(1,5)=Thrust_Results.(sprintf('%s',run_names{n})).(sprintf('blade_%d',4)).RunningMean;

Thrust_Indiv_Blades.(sprintf('%s',run_names{n}))(1,6)=Thrust_Results.(sprintf('%s',run_names{n})).ALL_blades_20s.RunningMean;

Thrust_Indiv_Blades.(sprintf('%s',run_names{n}))(1,7)=Thrust_Results.(sprintf('%s',run_names{n})).(sprintf('blade_%d',1)).Mean_FFTamplitude;

Thrust_Indiv_Blades.(sprintf('%s',run_names{n}))(1,8)=Thrust_Results.(sprintf('%s',run_names{n})).(sprintf('blade_%d',2)).Mean_FFTamplitude;

Thrust_Indiv_Blades.(sprintf('%s',run_names{n}))(1,9)=Thrust_Results.(sprintf('%s',run_names{n})).(sprintf('blade_%d',3)).Mean_FFTamplitude;

Thrust_Indiv_Blades.(sprintf('%s',run_names{n}))(1,10)=Thrust_Results.(sprintf('%s',run_names{n})).(sprintf('blade_%d',4)).Mean_FFTamplitude;

Thrust_Indiv_Blades.(sprintf('%s',run_names{n}))(1,11)=Thrust_Results.(sprintf('%s',run_names{n})).ALL_blades_20s.Mean_FFTamplitude;

Thrust_Indiv_Blades.(sprintf('%s',run_names{n}))(1,12)=Thrust_Results.(sprintf('%s',run_names{n})).(sprintf('blade_%d',1)).AvMaxPeak;

Thrust_Indiv_Blades.(sprintf('%s',run_names{n}))(1,13)=Thrust_Results.(sprintf('%s',run_names{n})).(sprintf('blade_%d',2)).AvMaxPeak;

Thrust_Indiv_Blades.(sprintf('%s',run_names{n}))(1,14)=Thrust_Results.(sprintf('%s',run_names{n})).(sprintf('blade_%d',3)).AvMaxPeak;

Thrust_Indiv_Blades.(sprintf('%s',run_names{n}))(1,15)=Thrust_Results.(sprintf('%s',run_names{n})).(sprintf('blade_%d',4)).AvMaxPeak;

Thrust_Indiv_Blades.(sprintf('%s',run_names{n}))(1,16)=Thrust_Results.(sprintf('%s',run_names{n})).ALL_blades_20s.AvMaxPeak;

Thrust_Indiv_Blades.(sprintf('%s',run_names{n}))(1,17)=Thrust_Results.(sprintf('%s',run_names{n})).(sprintf('blade_%d',1)).AvMinPeak;

Thrust_Indiv_Blades.(sprintf('%s',run_names{n}))(1,18)=Thrust_Results.(sprintf('%s',run_names{n})).(sprintf('blade_%d',2)).AvMinPeak;

Thrust_Indiv_Blades.(sprintf('%s',run_names{n}))(1,19)=Thrust_Results.(sprintf('%s',run_names{n})).(sprintf('blade_%d',3)).AvMinPeak;

Thrust_Indiv_Blades.(sprintf('%s',run_names{n}))(1,20)=Thrust_Results.(sprintf('%s',run_names{n})).(sprintf('blade_%d',4)).AvMinPeak;

Thrust_Indiv_Blades.(sprintf('%s',run_names{n}))(1,21)=Thrust_Results.(sprintf('%s',run_names{n})).ALL_blades_20s.AvMinPeak;

Thrust_Totals.(sprintf('%s',run_names{n}))(1,2)=Thrust_Results.(sprintf('%s',run_names{n})).Tot_running_Thrust_Mean;

```

% Torque results are processed in exactly the same way

```
end
```

[Published with MATLAB® R2016b](#)

Fast Fourier Transform (FFT) used to identify dominant frequency in time series

Script name: CFD_FFT.m

```
% Carries out Fast Fourier Transform (FFT) for CFD results
% Can be used to identify the dominant frequency in a time series
% Used for variables: Force, Torque, Velocity, BMX, Wave surface elevation
% The following example uses the variable Force

for n=1:runs % Sets up
'for' loop for the number of CFD cases being processed

    for q=1:4 % q=1,2,3
are blades 1,2,3 and q=4 is the hub data

        fs = Min_Fs; % Sampling
frequency (Hz) (1/s)
        test_length = maxtime-mintime; % Sample
length (s)

        N = length(Force.(sprintf('%s',run_names{n})).(sprintf('blade_%d',q))(:,1));
% Length of data set
        nsc = floor(N/(test_length/((1/wavefreq(n,1))*2))); % Number
of samples per window
        nov = floor(nsc/2); % Overlap
between windows (1 = total overlap, 2 = 50% overlap)
        nff = max(256,2^nextpow2(nsc)); % Number
of Discrete Fourier Transform points

        [s,f,t] = spectrogram(Force.(sprintf('%s',run_names{n})).(sprintf... %
Spectrogram using short-time Fourier transform
('blade_%d',q))(:,2)-Mean_Trapz_Thrust,hamming(nsc),nov,nff,fs);
        sAmps =(2*abs(s))/(nsc/2); %
Adjustment of scale

        mkdir(strcat(Thrust_folder,'\FFT_',sprintf('%s',run_names{n}))); % Make
folder to save FFT Figures in
        cd(strcat(Thrust_folder,'\FFT_',sprintf('%s',run_names{n})));

        figure % Plots
FFT frequency against FFT magnitude in figures for each blade and hub
        subplot(4,1,q)
        plot(f,sAmps,'b-')
        xlabel('f (Hz)');
        ylabel('s, short time Fourier transform');
        title(['FFT freq against FFT magnitude - Blade ',{q}])
        axis([0 10 -inf inf])
        hold all

        print('FFT','-dpng','-r0') % Saves
figure as a picture file
```

```

        savefig(gcf,'FFT') % Saves
figure as a matlab figure file

        % Finds the amplitude of the dominant wave frequency from the FFT figures eg.
wavefreq = 0.5 or 0.7
        [Diff, freq_index] = min(abs(f-wavefreq(n,1)));
        AllFFT_amps = sAmps(freq_index,:);

        Mean_FF Tamp = nanmean(AllFFT_amps); % Mean
amplitude of dominant frequency
        Std_FF Tamp = nanstd(AllFFT_amps); % Standard
deviation of the dominant frequency

Thrust_Results.(sprintf('%s',run_names{n})).(sprintf('blade_%d',q)).Mean_FF Tamp
= Mean_FF Tamp;

Thrust_Results.(sprintf('%s',run_names{n})).(sprintf('blade_%d',q)).Std_FF Tamp
= Std_FF Tamp;

        end % End of
'for' loop for blades 1,2,3 and hub
end % Ends
'for' loop for the number of CFD cases being processed

```

[*Published with MATLAB® R2016b*](#)

Running mean calculation

Script name: CFD_RunningMean.m

```

% Calculates the running mean of the time series split into 100 windows
% for the CFD results
% Can be used for variables: Force, Torque, Velocity, BMx and
% Wave surface elevation
% The following example uses the variable Force

for n=1:runs % Sets up
'for' loop for the number of CFD cases being processed

        for q=1:4 % q=1,2,3
are blades 1,2,3 and q=4 is the hub data

                N=length(Force.(sprintf('%s',run_names{n})).(sprintf('blade_%d',q))...
                (:,2));
                Samps_window = samps(n,1)/3; %
Propagation of 3 waves per 'window'
                Overlap = floor(0.5*Samps_window); % Overlap
of 'windows'

                loops=1; % Starting
loop = 1
                start_res = 1; % Starting
index of data
                end_res = floor(Samps_window*loops); % No
samps in first loop

```

```

run_means(1,:)=mean(Force.(sprintf('%s',run_names{n})).(sprintf... % Creates
running mean variable
('blade_%d',q))(start_res:end_res,2));

while end_res < N+1 %
Continues looping until reach end of data length
loops=loops+1;
start_res=floor((end_res)-Overlap);
end_res=floor(start_res+Samps_Window);
if end_res > N
break
end
run_means(loops,:)=mean(Force.(sprintf('%s',run_names{n})...
). (sprintf('blade_%d',q))(start_res:end_res,2));
end

run_mean=mean(run_means);
run_std=std(run_means);

Thrust_Results.(sprintf('%s',run_names{n})).(sprintf('blade_%d',q))...
.Running_Means = run_means;
Thrust_Results.(sprintf('%s',run_names{n})).(sprintf('blade_%d',q))...
.RunningMean = run_mean;
Thrust_Results.(sprintf('%s',run_names{n})).(sprintf('blade_%d',q))...
.RunningMean_std = run_std;

end % End of
'for' loop for blades 1,2,3 and hub
end % Ends
'for' loop for the number of CFD cases being processed

```

[Published with MATLAB® R2016b](#)

'findpeaks' Matlab function used to find max/min peaks in time series

Script name: CFD_findpeaks.m

```

% Uses 'findpeaks' function to find max and min peaks in data for
% the CFD results
% Can be used for variables: Force, Torque, Velocity, BMx and
% Wave surface elevation
% The following example uses the variable Force

for n=1:runs % Sets up
'for' loop for the number of CFD cases being processed

    for q=1:4 % q=1,2,3
are blades 1,2,3 and q=4 is the hub data

        timestep = 1/((Ang_Freq(1,n)*(180/pi))/5); % Timestep
equals the time taken for the turbine to rotate 5 degrees
        no_steps = floor(1/wavefreq(n,1)/timestep); % Number
of time steps in a single wave period
        [max_pks,max_locs] = findpeaks(Force.(sprintf('%s',run_names{n})).... % Finds
the max peaks and the index they occur at
        .(sprintf('blade_%d',q))(:,2), 'MinPeakDistance', no_steps*0.9);

```

```

        upsidedown = -(Force.(sprintf('%s',run_names{n})).(sprintf... % Flips
time series up side down to find the minimum peaks using same function
        ('blade_%d',q))(:,2));
        [min_pks,min_locs] = findpeaks(upsidedown, 'MinPeakDistance',... % Finds
the min peaks and the index they occur at
        no_steps*0.9);
        min_pks_adj = min_pks*-1; % Flip the
time series back to original orientation

        Max_Time_locs = Force.(sprintf('%s',run_names{n})).(sprintf... % Stores
the max and min time locations
        ('blade_%d',q))(max_locs,1);
        Min_Time_locs = Force.(sprintf('%s',run_names{n})).(sprintf...
        ('blade_%d',q))(min_locs,1);

        Av_Max = mean(max_pks); % Finds
the average max and min peaks
        Av_Min = mean(min_pks_adj);

        Thrust_Results.(sprintf('%s',run_names{n})).(sprintf('blade_%d',q))...
        .MaxPeaks(:,1) = [Max_Time_locs]';
        Thrust_Results.(sprintf('%s',run_names{n})).(sprintf('blade_%d',q))...
        .MaxPeaks(:,2) =[max_pks]';
        Thrust_Results.(sprintf('%s',run_names{n})).(sprintf('blade_%d',q))...
        .AvMaxPeak = [Av_Max];
        Thrust_Results.(sprintf('%s',run_names{n})).(sprintf('blade_%d',q))...
        .StdMaxPeak = std(max_pks);
        Thrust_Results.(sprintf('%s',run_names{n})).(sprintf('blade_%d',q))...
        .MinPeaks(:,1) = [Min_Time_locs]';
        Thrust_Results.(sprintf('%s',run_names{n})).(sprintf('blade_%d',q))...
        .MinPeaks(:,2) =[min_pks_adj]';
        Thrust_Results.(sprintf('%s',run_names{n})).(sprintf('blade_%d',q))...
        .AvMinPeak = [Av_Min];
        Thrust_Results.(sprintf('%s',run_names{n})).(sprintf('blade_%d',q))...
        .StdMinPeak = std(min_pks_adj);

    end % End of
'for' loop for blades 1,2,3 and hub
end % Ends
'for' loop for the number of CFD cases being processed

```

[Published with MATLAB® R2016b](#)

Wave period/stanchion rotational period calculation

Script name: CFD_waveperiod.m

```

% Calculated the wave period/stanchion rotational period of the
% time series for the CFD results
% Can be used for variables: Force, Torque, Velocity, BMx and
% Wave surface elevation
% The following example uses the variable Force

for n=1:runs % Sets up
'for' loop for the number of CFD cases being processed

```

```

    for q=1:4                                     % q=1,2,3
are blades 1,2,3 and q=4 is the hub data

        Diffs_Max=diff(Thrust_Results.(sprintf('%s',run_names{n})).... % Finds
the time difference between each of the max peaks (peak of the wave)
            .(sprintf('blade_%d',q)).MaxPeaks(:,1));
        Av_rot_period_Max = mean(Diffs_Max);           % Average
of all the time differences between the max peaks
        Std_rot_period_Max = std(Diffs_Max);          % Standard
deviation of the max peaks
        Thrust_Results.(sprintf('%s',run_names{n})).(sprintf...
            ('blade_%d',q)).Av_rot_period_Max = [Av_rot_period_Max];
        Thrust_Results.(sprintf('%s',run_names{n})).(sprintf...
            ('blade_%d',q)).Std_rot_period_Max = [Std_rot_period_Max];

        Diffs_Min=diff(Thrust_Results.(sprintf('%s',run_names{n})).... % Finds
the time difference between each of the min peaks (trough of the wave)
            .(sprintf('blade_%d',q)).MinPeaks(:,1));
        Av_rot_period_Min = mean(Diffs_Min);           % Average
of all the time differences between the min peaks
        Std_rot_period_Min = std(Diffs_Min);          % Standard
deviation of the min peaks
        Thrust_Results.(sprintf('%s',run_names{n})).(sprintf...
            ('blade_%d',q)).Av_rot_period_Min = [Av_rot_period_Min];
        Thrust_Results.(sprintf('%s',run_names{n})).(sprintf...
            ('blade_%d',q)).Std_rot_period_Min = [Std_rot_period_Min];

    end                                           % End of
'for' loop for blades 1,2,3 and hub
end                                             % Ends
'for' loop for the number of CFD cases being processed

```

[Published with MATLAB® R2016b](#)

Volumetrically averaged streamwise velocity over turbine swept area calculation

Script name: CFD_Wvol.m

```

% Volumetrically averaged velocity over turbine swept area
% Uses CFD data through the water depth to find the volumetrically
% averaged velocity over the turbine swept area
% The following example uses the variable w velocity (streamwise)

% Load in velocity data along with the angular frequency of the
% turbine input to the CFD models
load('K:\Drive_2\Matlab\IFREMER\April 2018
Data\Raw_Data_Week2\Waves_w22_w21R_PROF_Num\AngVel_Thrust_Torque_Results_w22_w21R_Prof_WAVES_HSCorr.mat')

run_names={'w21R_Prof1_WAVES';'w22_Prof2_WAVES'}; % Names of
files to process
runs = length(run_names);
Num_Depth_Points = [-1.9:0.1:-0.1]; % Depth of
monitor points placed through the water column at Z=2m downstream of inlet

```

```

% w velocity
for n=1:length(run_names) % Extract
    average values for the velocity at each water depth
    w_vel.(sprintf('%s',run_names{n}))(:,1) = Num_Depth_Points;
    for i=1:19
        w_vel.(sprintf('%s',run_names{n}))(i,2) = ... % Create
    structure to store all mean velocity values
        Velocity_w22_w21R_Prof_WAVES.W.(sprintf('%s',run_names{n}))....
        .(sprintf('ve1%d_mean',i));
    end
end

% Volumetric averaged flow rate
% Area of horizontal strips
r = 0.45; % Radius
of turbine
h = 0.01:0.01:0.45; % Height
of horizontal sections used to split up the turbine swept area
d = 0.45-h; % Height
of triangle created by removing horizontal sections from circle area
Total_Area = pi*(r^2); % Turbine
swept area

for i = 1:length(h) % Creates
    a 'for' loop for the number of horizontal sections that the swept area has been
    divided into

    c = sqrt((r-(h(i)/2))*(8*h(i))); %
    Calculation of the chord length
    half_c = c/2;
    half_centre_angle = atand(half_c/d(i));
    centre_angle = half_centre_angle*2; % Angle
    created at circle centre when connecting segment ends to the circle centre of length
    (r)

    Sector_Area = (centre_angle/360)*pi*(r^2); % Area of
    sector created
    Triangle_Area = 0.5*c*d(i); % Area of
    triangle created
    Segment_Area(i) = Sector_Area - Triangle_Area; % Area of
    segment created

    if i==1 %
        Calculation of each individual horizontal area rather than getting each total segment
        area
        Strip_Area(i) = Segment_Area(i);
    else
        Strip_Area(i) = Segment_Area(i)-Segment_Area(i-1);
    end
end

horiz_area = [Strip_Area';flip(Strip_Area')]; % Summary
of all individual horizontal section areas

% Analyse velocity profile over turbine swept area
for n=1:runs
    LinDepth = [linspace(Num_Depth_Points(1,:),Num_Depth_Points(end,:),... % Creates
    a water depth spacing for every 0.01m

```

```

181)]';
InterpLDA1 = interp1(Num_Depth_Points,W_Vel.(sprintf...           % Linear
interpolation of average velocity results over evenly spaced water depth points
previously created
('%s',run_names{n}))(:,2),LinDepth);
InterpLDA1(:,2) = LinDepth;

Reduced_InterpLDA1 = InterpLDA1;                               % Velocity
data between a water depth of 0.55m - 1.45m (over turbine diameter) to only show
results within the turbine swept area
Reduced_InterpLDA1=Reduced_InterpLDA1(Reduced_InterpLDA1(:,2) <= -0.55, :); %
Cuts off depth points above turbine swept area
Reduced_InterpLDA1=Reduced_InterpLDA1(Reduced_InterpLDA1(:,2) >= -1.451, :); %
Cuts off depth points below turbine swept area

% Volumetric Flowrate (Q=AU)
for i = 1:length(horiz_area)                                   % Creates
'for' loop the length of the number of horizontal sections
    Q(i,:) = horiz_area(i)*Reduced_InterpLDA1(i+1,1);         %
Calculates the individual volumetric flow rates over each horizontal section area
end

Q_total = sum(Q);                                           %
Calculates the total volumetric flow rate over the turbine swept area
Mean_VolAv_W_Vel = Q_total/Total_Area;                       %
Calculates the volumetrically averaged streamwise velocity over the turbine swept
area

end

% The same methodology is used in calculating the volumetrically averaged
% vertical velocity over the turbine swept area

```

[Published with MATLAB® R2016b](#)

Non dimensional performance characteristics

Script name: CFD_NDV_PerfChar.m

```

% Creates a Non Dimensional Values (NDV) structure for all the
% variables needed to calculate the Cq, Ct and Cp

% Load in Force, Torque and Velocity data along with the angular frequency
% of the turbine input to the CFD models
load('K:\Drive_2\Matlab\IFREMER\April 2018 Data\Numerical Data
Processing\Uni_Prof_Waves_Turb\Force_Torque_Vel_w22_w21R_Prof_WAVES.mat')
load('K:\Drive_2\Matlab\IFREMER\April 2018
Data\Raw_Data_Week2\Ang_Freq_w22_w21R_Num.mat')

water_Density = 999.7;                                       % Water
density
R = 0.45;                                                     % Turbine
radius
Swept_Area = pi*(R^2);                                       % Turbine
swept area

```

```

NDV_Prof_WAVES.names = {'w21R_Prof1_WAVES', 'w22_Prof1_WAVES'}; % Creates
structure (NDV_Prof_WAVES) to store all performance characteristics and related
variables

NDV_Prof_WAVES.HorizFluidVel(1,n) = Mean_VolAv_W_Vel; %
Volumetrically averaged streamwise velocity over turbine swept area

NDV_Prof_WAVES.U2 = NDV_Prof_WAVES.HorizFluidVel.^2; % squared
velocity term
NDV_Prof_WAVES.U3 = NDV_Prof_WAVES.HorizFluidVel.^3; % cubed
velocity term

% Average velocity between 0.55m - 1.45m (over turbine diameter)
for i=1:runs

    NDV_Prof_WAVES.AngVel(1,i) = Ang_Freq_w22_w21R_Prof_WAVES(1,3-i); % Angular
velocity
    NDV_Prof_WAVES.TSR(1,i) = (NDV_Prof_WAVES.AngVel(1,i).*R)./... % Tip
Speed Ratio
    NDV_Prof_WAVES.HorizFluidVel(1,i);

    % Cp
    Var_Prof_WAVES(i).Average_Output_Power(:,i) = ... % Average
output power
    Torque_Results_w22_w21R_Prof_WAVES.(sprintf('%s', run_names{i}))....
.ALL_blades_20s.Torque.*NDV_Prof_WAVES.AngVel(1,i);
    NDV_Prof_WAVES.Average_Available_Power(1,i) = ... % Average
available power
    0.5*Water_Density*Swept_Area*NDV_Prof_WAVES.U3(1,i);
    Var_Prof_WAVES(i).All_Cp(:,i) = ... %
Calculated Cp over whole time series
    (Var_Prof_WAVES(i).Average_Output_Power(:,i))./...
    NDV_Prof_WAVES.Average_Available_Power(1,i);
    NDV_Prof_WAVES.Cp(1,i) = mean(Var_Prof_WAVES(i).All_Cp(:,i)); % Average
Cp
    NDV_Prof_WAVES.Cp(2,i) = std(Var_Prof_WAVES(i).All_Cp(:,i)); % Cp
standard deviation

    % Ct
    Var_Prof_WAVES(i).All_Thrust_Total(:,i) = ... % Total
thrust
    Thrust_Results_w22_w21R_Prof_WAVES.(sprintf('%s', run_names{i}))....
.ALL_blades_20s.Thrust;
    NDV_Prof_WAVES.Thrust_Total(1,i) = ... % Average
thrust total
    Thrust_Results_w22_w21R_Prof_WAVES.(sprintf('%s', run_names{i}))....
.ALL_blades_20s.RunningMean;
    NDV_Prof_WAVES.Thrust_Total(2,i) = ... % Thrust
standard deviation
    Thrust_Results_w22_w21R_Prof_WAVES.(sprintf('%s', run_names{i}))....
.ALL_blades_20s.RunningMean_std;
    NDV_Prof_WAVES.Average_Available_Thrust(1,i) = ... % Average
available thrust
    0.5*Water_Density*Swept_Area*NDV_Prof_WAVES.U2(1,i);
    Var_Prof_WAVES(i).All_Ct(:,i) = ...
%Calculated Ct over whole time series
    (Var_Prof_WAVES(i).All_Thrust_Total(:,i))./...
    NDV_Prof_WAVES.Average_Available_Thrust(1,i);

```

```

    NDV_Prof_WAVES.Ct(1,i) = mean(Var_Prof_WAVES(i).All_Ct(:,i));           % Average
Ct
    NDV_Prof_WAVES.Ct(2,i) = std(Var_Prof_WAVES(i).All_Ct(:,i));         % Ct
standard deviation

    % Cq
    Var_Prof_WAVES(i).All_Torque_Total(:,i) = ...                       % Total
torque
    Torque_Results_W22_W21R_Prof_WAVES.(sprintf('%s',run_names{i}))....
    .ALL_blades_20s.Torque;
    NDV_Prof_WAVES.Torque_Total(1,i) = ...                               % Average
total torque
    Torque_Results_W22_W21R_Prof_WAVES.(sprintf('%s',run_names{i}))....
    .ALL_blades_20s.RunningMean;
    NDV_Prof_WAVES.Torque_Total(2,i) = ...                               % Torque
standard deviation
    Torque_Results_W22_W21R_Prof_WAVES.(sprintf('%s',run_names{i}))....
    .ALL_blades_20s.RunningMean_std;
    Var_Prof_WAVES(i).All_Cq(:,i) = ...                                  %
Calculated Cq over whole time series
    (Var_Prof_WAVES(i).All_Torque_Total(:,i))./...
    (NDV_Prof_WAVES.Average_Available_Thrust(1,i)*R);
    NDV_Prof_WAVES.Cq(1,i) = mean(Var_Prof_WAVES(i).All_Cq(:,i));       % Average
Cq
    NDV_Prof_WAVES.Cq(2,i) = std(Var_Prof_WAVES(i).All_Cq(:,i));       % Cq
standard deviation

end

```

[Published with MATLAB® R2016b](#)

Wave surface elevation at specific location downstream of the inlet

Script name: CFD_SurfElevation.m

```

% Calculates the wave surface elevation from the CFD data at a specific
% location at z = 2m downstream of the inlet
% The following example calculates the surface elevation and wave period
% for the wave case P2W5

% TimeSteps saved:
% P2W5 = 5534 to 6054

wavefreq=0.7; % Wave
frequency
waterD = 2.0; % Water
depth
C2 = 2; % Location
downstream of the inlet on the z-axis (2m)
waves = 1; % Number
of wave cases loaded
fieldmeshes=[1:waves];

AngularFreqTurb = 8.7934; % Angular
frequency of turbine
ts=1/((AngularFreqTurb*(180/pi))/5); % Time

```

```

step used in CFD model

ST=round(((1/ts)*55)/2)*2; % timestep
required to equal 55s
FIN=round(((1/ts)*60)/2)*2; % timestep
required to equal 60s
st=5534; % First
time step downloaded from CFD model
fin=6054; % Last
time step downloaded from CFD model

for b=1:waves

    step = sprintf('Select timesteps from %d to %d...',st,fin) % Details
which run files to select

    [filenames, pathname, filterindex] = uigetfile('*..*',... % Use GUI
to multiple-select all the files that should be read in
    'Pick data files to process','MultiSelect','on');
    num_files = length(filenames); % Find
number of files present
    cd(pathname); % Change
directory to pathname where the results came from - easier to pick up files later on

    n=0;
    a = waitbar(0,'Total progress...'); % Creates
waitbar - shows the time taken to process data
    for i=1:num_files;
        waitbar((i)/(num_files)) % Update
waitbar time

    n=n+1;
    timestep = [st:10:fin];

    filename = char(filenames(i)); % Set
filename for import and convert to char array. filenames = array of filenames,
filename = single files, at a certain position of (i)in filenames array
    A = importdata(filename,',',6); % Import
file, (filename, comma delimited, 6 lines of header. Imports all data in file.
    Ycoord = A.data(:,strcmp(A.colheaders,' Y [ m ]')); % Set
variable to be analysed. colheaders = column headers
    Zcoord = A.data(:,strcmp(A.colheaders,' Z [ m ]')); % Set z-
coordinate (all rows, column wanted - strcmp:look in col headers and look for name x
coord)

    AllData.(sprintf('ts_%d',timestep(n))) = [Zcoord,Ycoord(:,1)]; % New
structure called AllData has results for each timestep of variables Zcoord and
Ycoord. %d puts in value of n per timestep

    %Finds the SE at location C2
    [dif index] = min(abs(Zcoord-C2)); % Finds
the minimum difference between the Z coordinates input and the specified desired
location (Z=2m)
    Zval(n,:)=Zcoord(index); % Saves
the Z and Y coordinates from the desired location (Z=2m) as well as the relevant time
step and equivalent time value
    Yval(n,:)=Ycoord(index);
    TS(n,:)=timestep(n);

```

```

        Time(n,:)=timestep(n)*ts;

        SE = [Zval,Yval,Time,TS];

        end
        delete(a) % Remove
waitbar indicator
end

%%%%%%%%%% Calculation of max/min peaks using 'findpeaks' - *CFD_findpeaks.m*
%%%%%%%%%%

SE_Results.MaxPeaks(:,1) = [Max_Time_locs]';
SE_Results.MaxPeaks(:,2) =[max_pks]';
SE_Results.MinPeaks(:,1) = [Min_Time_locs]';
SE_Results.MinPeaks(:,2) =[min_pks_adj]';
SE_Results.AvMaxPeak = [Av_Max];
SE_Results.StdMaxPeak = std(max_pks);
SE_Results.AvMinPeak = [Av_Min];
SE_Results.StdMinPeak = std(min_pks_adj);
SE_Results.Wave_Height = SE_Results.AvMaxPeak-SE_Results.AvMinPeak;
SE_Results.Wave_Height_Std =
sqrt((SE_Results.StdMaxPeak^2)+(SE_Results.StdMinPeak^2));

%%%%%%%%%% Calculation of wave period - *CFD_waveperiod.m*
%%%%%%%%%%

```

[Published with MATLAB® R2016b](#)

Matlab scripts used for experimental data processing:

The methods used for the experimental data processing are mostly the same as used for the CFD results. There is, however, a different method for importing the data as well as the approach used for Time Synchronous Averaging (TSA). These additional methods are shown below.

Data import

Script name: Turbine_Motor_Analog_DataImport_P1W4.m (adapted from [172])

```

% Imports and processes data from turbine instrumentation & flow measurements:
% thrust, torque, blade BMx, time, encoder position,encoder speed and LDA
% Specific script uses case P1W4 but can be used for any experimental
% data case

RouteDirectory = cd; % Name
current directory "RouteDirectory"
StudyName = 'waves2_1R_1ms_SpeedControl'; % Set up
study folder
load('FilestoProcess_waves2_1R.mat') % Loads
names of files to import and process
StudyDir = strcat(RouteDirectory,'\',StudyName); % Create
study directory

```

APPENDIX

```

% Defines file path for folders to put results figures in
TS = strcat(StudyDir,'\Figures\TimeSeries');
Thrust_folder = strcat(StudyDir,'\Figures\Thrust');
Torque_folder = strcat(StudyDir,'\Figures\Torque');

wavefreq = 0.5; % Defines
the wave frequency used
R = 0.45; % Rotor
diameter in meters
FlumeHeight = 2.0; % Flume
height in metres
Flumewidth = 4.0; % Flume
width in metres

% Calibration Information
% Thrust/Torque Transducer
ThrustGradient = 0.00534888;
ThrustZero = 0.01224;
TorqueGradient = 0.0801019;
TorqueZero = 0.012006;

% Blade root bending moment (BMx)- blade 2 only
Blade2MxGradient = 0.16248;
Blade2MxZero = 0.0084862;

% Measurement Uncertainties
ThrustUncertainty = 9.24;
TorqueUncertainty = 0.64;
BladeRootBendingMomentUncertainty = 0.61;
DensityUncertainty = 2.0;
RadiusUncertainty = 0.005;
EncoderUncertainty = 0.028;
FluidVelUncertainty = 0.02;

for i = 1:size(FilestoProcess,1) % Sets up
'for' loop for the number of experimental cases being imported/processed

    % DataImport
    % Analog data
    RouteAnalog = strcat(RouteDirectory,'\AnalogData'); %
Specifies file containing all the Analog Data
    cd (RouteAnalog) % Changes
directory
    [DATA(i).AnalogData] = IFREMERAnalogImport(strcat(FilestoProcess... % Imports
Analog Data from specified file using function *IFREMERAnalogImport.m*
    {i},'.txt'));

    % Motor data
    RouteMotor = strcat(RouteDirectory,'\MotorData'); %
Specifies file containing all the Motor Data
    cd (RouteMotor) % Changes
directory
    [DATA(i).MotorData] = IFREMERMotorDataImport(strcat(FilestoProcess... % Imports
Motor Data from specified file using function *IFREMERMotorImport.m*
    {i},'.txt'));

    % LDA data
    RouteLDA = strcat(RouteDirectory,'\LDADData'); %

```

```

Specifies file containing all the LDA Data
    cd (RouteLDA) % Changes
directory
    [DATA(i).LDAData] = IFREMERLDAImport(strcat(FilestoProcess{i},'.txt'));% Imports
LDA Data from specified file using function *IFREMERLDAImport.m*

    % Create structure for all data after applying calibration adjustments
    DATA(i).AnalogData.Thrust = (DATA(i).AnalogData.Thrust - ... % Apply
thrust calibration
        ThrustZero)*1000/ThrustGradient;
    DATA(i).AnalogData.Torque = (DATA(i).AnalogData.Torque- ... % Apply
torque calibration
        TorqueZero)*1000 /TorqueGradient;
    DATA(i).AnalogData.Blade2Mx = (DATA(i).AnalogData.Blade2Mx- ... % Apply
blade 2 BMx calibration
        Blade2MxZero)*1000 /Blade2MxGradient;

    % Interpolate data to create uniform time axis
    % Thrust/torque transducer
    MaxTime = min([max(DATA(i).AnalogData.Time) max(DATA(i).MotorData... % Create
global time axis using shortest file length
        .Time)]);
    Time = linspace(0,MaxTime,MaxTime*200); % Create
time variable at 200Hz

    % LDA data
    MaxTime = min([max(DATA(i).LDAData.Time1) max(DATA(i).LDAData.Time2)]);
    Time = linspace(0,MaxTime,MaxTime*200)';

%Analog data interpolate
DATA(i).AnalogData.Thrust = interp1(DATA(i).AnalogData.Time,DATA(i)...
    .AnalogData.Thrust,Time,'pchip');
DATA(i).AnalogData.Torque = interp1(DATA(i).AnalogData.Time,DATA(i)...
    .AnalogData.Torque,Time,'pchip');
DATA(i).AnalogData.Blade2Mx = interp1(DATA(i).AnalogData.Time,DATA...
    (i).AnalogData.Blade2Mx,Time,'pchip');
DATA(i).AnalogData.Time = Time;

%Motor data interpolate
DATA(i).MotorData.VelocityRPM = interp1(DATA(i).MotorData.Time,DATA...
    (i).MotorData.VelocityRPM,Time,'pchip');
DATA(i).MotorData.PositionDeg = interp1(DATA(i).MotorData.Time,DATA...
    (i).MotorData.PositionDeg,Time,'pchip');
DATA(i).MotorData.Time = Time;

%LDA data interpolate
DATA(i).LDAData.LinLDA1ms = interp1(DATA(i).LDAData.Time1,DATA(i)...
    .LDAData.LDA1ms,Time,'pchip');
DATA(i).LDAData.LinLDA2ms = interp1(DATA(i).LDAData.Time2,DATA(i)...
    .LDAData.LDA2ms,Time,'pchip');
DATA(i).LDAData.LinTime1= Time;
DATA(i).LDAData.LinTime2= Time;

% Cut first 10 seconds (2000 pieces of data) from Analog data sets
DATA_CUT(i).AnalogData.Thrust = DATA(i).AnalogData.Thrust(2000:end);
DATA_CUT(i).AnalogData.Torque = DATA(i).AnalogData.Torque(2000:end);
DATA_CUT(i).AnalogData.Time = DATA(i).AnalogData.Time(1:end-1999);

%Cut first 10 seconds (2000 pieces of data) from Motor data sets

```

```

DATA_CUT(i).MotorData.AngularVelocity = DATA(i).MotorData...           % Also
adjusts angular velocity from RPM to rad/s
    .VelocityRPM(2000:end)*0.1047;
DATA_CUT(i).MotorData.Time = DATA(i).MotorData.Time(1:end-1999);

%Cut first 10 seconds (2000 pieces of data) from LDA data sets
DATA_CUT(i).LDADData.LinTime1 = DATA(i).LDADData.LinTime1(1:end-1999);
DATA_CUT(i).LDADData.LinLDA1ms = DATA(i).LDADData.LinLDA1ms(2000:end);
DATA_CUT(i).LDADData.LinTime2 = DATA(i).LDADData.LinTime2(1:end-1999);
DATA_CUT(i).LDADData.LinLDA2ms = DATA(i).LDADData.LinLDA2ms(2000:end);
maxTime = DATA_CUT(i).LDADData.LinTime1(end);

mkdir(strcat(TS, '\',sprintf('%d',i)));                                 % Make a
folder to save Figures in
cd(strcat(TS, '\',sprintf('%d',i)));

% Plots figures for each time series: thrust, torque, angular velocity
% FORCE
figure                                                                    % Opens
figure window                                                                % Creates
subplot(3,1,1)
3 x 1 subplot and selects top left corner of subplot
plot(DATA_CUT(i).AnalogData.Time,DATA_CUT(i).AnalogData.Thrust)         % Plots
figure
title('Thrust')                                                            % Inputs
title
xlabel('Time (s)');                                                         % Set x
axis label
ylabel('Thrust (N)');                                                       % Set y
axis label
axis([0 200 -inf inf])                                                     % Set x
and y axis limits

subplot(3,1,2)
plot(DATA_CUT(i).AnalogData.Time,DATA_CUT(i).AnalogData.Torque)
title('Torque')
xlabel('Time (s)');
ylabel('Torque (Nm)');
axis([0 200 -inf inf])

subplot(3,1,3)
plot(DATA_CUT(i).MotorData.Time,DATA_CUT(i).MotorData.AngularVelocity)
title('Angular velocity')
xlabel('Time (s)');
ylabel('Angular velocity (rad/s)');
axis([0 200 -inf inf])

print('Subplot','-dpng','-r0')                                             % Saves
subplot figure as a picture file
savefig(gcf,'Subplot')                                                    % Saves
subplot figure as a matlab figure file

% Calculations

% THRUST Processing
Min_Ts = min(diff(DATA_CUT(i).AnalogData.Time));                          % Min
timestep (s)
Min_Fs = 1/Min_Ts;                                                         % Min

```

```

sampling frequency (Hz) (1/s)
    mintime = DATA_CUT(i).AnalogData.Time(1); % Min time
(s)
    maxtime = DATA_CUT(i).AnalogData.Time(end); % Max time
(s)

    Mean_Thrust = mean(DATA_CUT(i).AnalogData.Thrust); % Mean
thrust calculated using 'mean' function
    Area_Trapz_Thrust = trapz(DATA_CUT(i).AnalogData.Time,DATA_CUT(i)... % Mean
thrust calculated using the trapezium rule
    .AnalogData.Thrust);
    Mean_Trapz_Thrust = Area_Trapz_Thrust/maxtime;
    Std_Thrust = std(DATA_CUT(i).AnalogData.Thrust); % Standard
deviation of thrust

    % Creates a structure with processed thrust data for each blade and the hub
    Thrust_Results.(sprintf('Run_%d',i)).Mean_Thrust = Mean_Trapz_Thrust;
    Thrust_Results.(sprintf('Run_%d',i)).Std_Thrust = Std_Thrust;
    Thrust_Results.(sprintf('Run_%d',i)).Time = DATA_CUT(i).AnalogData.Time';
    Thrust_Results.(sprintf('Run_%d',i)).Thrust = DATA_CUT(i).AnalogData.Thrust';

%% Carries out Fast Fourier Transform (FFT) using similar method to -
*CFD_FFT.m*

%% Calculation of running mean using similar method to - *CFD_RunningMean.m*
%%

%% Calculation of max/min peaks using 'findpeaks' similar method to -
*CFD_findpeaks.m*

%% Calculation of wave period similar method to - *CFD_waveperiod.m*
%%

% Torque, Angular velocity and LDA processing can be carried out in exactly
% the same way as the thrust

end % Ends
'for' loop for the number of experimental cases being processed

% Collates all results for running mean, mean FFT amplitude, max/min peaks
% for the Thrust results into a structure

Thrust(:,1)=g;
for i=1:size(FilestoProcess,1)
    Thrust(i,2)=Thrust_Results.(sprintf('Run_%d',i)).RunningMean;
    Thrust(i,3)=Thrust_Results.(sprintf('Run_%d',i)).RunningMean_std;
    Thrust(i,4)=Thrust_Results.(sprintf('Run_%d',i)).Mean_FFtamplitude;
    Thrust(i,5)=Thrust_Results.(sprintf('Run_%d',i)).Std_FFtamplitude;
    Thrust(i,6)=Thrust_Results.(sprintf('Run_%d',i)).AvMaxPeak;
    Thrust(i,7)=Thrust_Results.(sprintf('Run_%d',i)).StdMaxPeak;
    Thrust(i,8)=Thrust_Results.(sprintf('Run_%d',i)).AvMinPeak;
    Thrust(i,9)=Thrust_Results.(sprintf('Run_%d',i)).StdMinPeak;
    Thrust(i,10)=Thrust_Results.(sprintf('Run_%d',i)).Av_wave_period_Max;
    Thrust(i,11)=Thrust_Results.(sprintf('Run_%d',i)).Std_wave_period_Max;
    Thrust(i,12)=Thrust_Results.(sprintf('Run_%d',i)).Av_wave_period_Min;
    Thrust(i,13)=Thrust_Results.(sprintf('Run_%d',i)).Std_wave_period_Min;

```

```
% Torque, Angular velocity and LDA results are processed in exactly the same way
end
```

[Published with MATLAB® R2016b](#)

Analog data import function

Function name: IFREMERAnalogImport (reproduced from [170])

```
function [AnalogData] = IFREMERAnalogImport(filename, startRow, endRow)
%IMPORTFILE Import numeric data from a text file as column vectors.
% [TORQUE,BLADE1,BLADE2,BLADE3,MOISTURE,TIME,THRUST] =
% IMPORTFILE(FILENAME) Reads data from text file FILENAME for the default
% selection.
%
% [TORQUE,BLADE1,BLADE2,BLADE3,MOISTURE,TIME,THRUST] =
% IMPORTFILE(FILENAME, STARTROW, ENDROW) Reads data from rows STARTROW
% through ENDROW of text file FILENAME.
%
% Example:
% [Torque,Blade1,Blade2,Blade3,Moisture,Time,Thrust] =
importfile('IFREMER_090418_Turbine4-0_7-5m_Zero1.txt',1, 4098);
%
% See also TEXTSCAN.

% Auto-generated by MATLAB on 2018/04/10 06:45:32

% Initialize variables.
delimiter = '\t';
if nargin<=2
    startRow = 1;
    endRow = inf;
end

% Format for each line of text:
% column2: double (%f)
% column3: double (%f)
% column4: double (%f)
% column5: double (%f)
% column6: double (%f)
% column7: double (%f)
% column8: double (%f)
% For more information, see the TEXTSCAN documentation.
formatSpec = '%*s%f%f%f%f%f%f%[\n\r]';

% Open the text file.
fileID = fopen(filename,'r');

% Read columns of data according to the format.
% This call is based on the structure of the file used to generate this
% code. If an error occurs for a different file, try regenerating the code
% from the Import Tool.
dataArray = textscan(fileID, formatSpec, endRow(1)-startRow(1)+1, 'Delimiter',
delimiter, 'TextType', 'string', 'EmptyValue', NaN, 'HeaderLines', startRow(1)-1,
'ReturnOnError', false, 'EndOfLine', '\r\n');
for block=2:length(startRow)
```

```

frewind(fileID);
dataArrayBlock = textscan(fileID, formatSpec, endRow(block)-startRow(block)+1,
'Delimiter', delimiter, 'TextType', 'string', 'EmptyValue', NaN, 'HeaderLines',
startRow(block)-1, 'ReturnOnError', false, 'EndOfLine', '\r\n');
for col=1:length(dataArray)
    dataArray{col} = [dataArray{col};dataArrayBlock{col}];
end
end

% Close the text file.
fclose(fileID);

% Post processing for unimportable data.
% No unimportable data rules were applied during the import, so no post
% processing code is included. To generate code which works for
% unimportable data, select unimportable cells in a file and regenerate the
% script.

% Allocate imported array to column variable names
AnalogData.Thrust = dataArray{:, 1};
AnalogData.Blade1Mx = dataArray{:, 2};
AnalogData.Blade2Mx = dataArray{:, 3};
AnalogData.Blade3Mx = dataArray{:, 4};
AnalogData.Moisture = dataArray{:, 5};
AnalogData.Time = dataArray{:, 6};
AnalogData.Time = AnalogData.Time-min(AnalogData.Time);
AnalogData.Torque = dataArray{:, 7};
end

```

[Published with MATLAB® R2016b](#)

Motor data import function

Function name: IFREMERMotorDataImport (reproduced from [170])

```

function [MotorData] = IFREMERMotorDataImport(filename, startRow, endRow)
%IMPORTFILE Import numeric data from a text file as column vectors.
% [TMS,VELOCITYRPM,DCBUSPOWERWATTS,MOTORPOWERWATTS,TGCAMPS,POSITIONDEG] =
% IMPORTFILE(FILENAME) Reads data from text file FILENAME for the default
% selection.
%
% [TMS,VELOCITYRPM,DCBUSPOWERWATTS,MOTORPOWERWATTS,TGCAMPS,POSITIONDEG] =
% IMPORTFILE(FILENAME, STARTROW, ENDROW) Reads data from rows STARTROW
% through ENDROW of text file FILENAME.
%
% Example:
% [tms,velocityRPM,DCBusPowerWatts,MotorPowerWatts,TGCamps,PositionDeg] =
importfile('IFREMER_090418_Turbine4-0_7-5m_C_Nm_10-00_T3-0_3.6.txt',2, 6001);
%
% See also TEXTSCAN.

% Auto-generated by MATLAB on 2018/07/11 14:46:38

% Initialize variables.
delimiter = ',';
if nargin<=2

```

```

    startRow = 2;
    endRow = inf;
end

% Format for each line of text:
% column1: double (%f)
% column2: double (%f)
% column3: double (%f)
% column4: double (%f)
% column5: double (%f)
% column6: double (%f)
% For more information, see the TEXTSCAN documentation.
formatSpec = '%f%f%f%f%f%f%[\n\r]';

% Open the text file.
fileID = fopen(filename, 'r');

% Read columns of data according to the format.
% This call is based on the structure of the file used to generate this
% code. If an error occurs for a different file, try regenerating the code
% from the Import Tool.
dataArray = textscan(fileID, formatSpec, endRow(1)-startRow(1)+1, 'Delimiter',
delimiter, 'TextType', 'string', 'EmptyValue', NaN, 'HeaderLines', startRow(1)-1,
'ReturnOnError', false, 'EndOfLine', '\r\n');
for block=2:length(startRow)
    frewind(fileID);
    dataArrayBlock = textscan(fileID, formatSpec, endRow(block)-startRow(block)+1,
'Delimiter', delimiter, 'TextType', 'string', 'EmptyValue', NaN, 'HeaderLines',
startRow(block)-1, 'ReturnOnError', false, 'EndOfLine', '\r\n');
    for col=1:length(dataArray)
        dataArray{col} = [dataArray{col}; dataArrayBlock{col}];
    end
end

% Close the text file.
fclose(fileID);

% Post processing for unimportable data.
% No unimportable data rules were applied during the import, so no post
% processing code is included. To generate code which works for
% unimportable data, select unimportable cells in a file and regenerate the
% script.

% Allocate imported array to column variable names
MotorData.Time = dataArray{:, 1}/1000;
MotorData.VelocityRPM = dataArray{:, 2};
MotorData.DCBusPowerWatts = dataArray{:, 3};
MotorData.MotorPowerWatts = dataArray{:, 4};
MotorData.TGCamps = dataArray{:, 5};
MotorData.PositionDeg = dataArray{:, 6};
end

```

[Published with MATLAB® R2016b](#)

LDA data import function

Function name: IFREMERLDAImport (reproduced from [170])

```

function [LDVData] = IFREMERLDAImport(filename, startRow, endRow)
%IMPORTFILE1 Import numeric data from a text file as column vectors.
% [ROW,ATMS,TTUS,LDA1MS,AT2MS,TT2US,LDA22MS] = IMPORTFILE1(FILENAME)
% Reads data from text file FILENAME for the default selection.
%
% [ROW,ATMS,TTUS,LDA1MS,AT2MS,TT2US,LDA22MS] = IMPORTFILE1(FILENAME,
% STARTROW, ENDROW) Reads data from rows STARTROW through ENDROW of text
% file FILENAME.
%
% Example:
% [Row,ATms,TTus,LDA1ms,AT2ms,TT2us,LDA2ms] = importfile1('IFREMER_110418_Turbine4-
% 0_4-0m_TSR_0-0_U_1-00_LDV055.txt',7, 52042);
%
% See also TEXTSCAN.

% Auto-generated by MATLAB on 2018/07/11 16:51:38

% Initialize variables.
delimiter = '\t';
if nargin<=2
    startRow = 7;
    endRow = inf;
end

% Format for each line of text:
% column1: double (%f)
% column2: double (%f)
% column3: double (%f)
% column4: double (%f)
% column5: double (%f)
% column6: double (%f)
% column7: double (%f)
% For more information, see the TEXTSCAN documentation.
formatSpec = '%f%f%f%f%f%f%f%[\n\r]';

% Open the text file.
fileID = fopen(filename,'r');

% Read columns of data according to the format.
% This call is based on the structure of the file used to generate this
% code. If an error occurs for a different file, try regenerating the code
% from the Import Tool.
dataArray = textscan(fileID, formatSpec, endRow(1)-startRow(1)+1, 'Delimiter',
delimiter, 'TextType', 'string', 'EmptyValue', NaN, 'HeaderLines', startRow(1)-1,
'ReturnOnError', false, 'EndOfLine', '\r\n');
for block=2:length(startRow)
    frewind(fileID);
    dataArrayBlock = textscan(fileID, formatSpec, endRow(block)-startRow(block)+1,
'Delimiter', delimiter, 'TextType', 'string', 'EmptyValue', NaN, 'HeaderLines',
startRow(block)-1, 'ReturnOnError', false, 'EndOfLine', '\r\n');
    for col=1:length(dataArray)
        dataArray{col} = [dataArray{col};dataArrayBlock{col}];
    end
end

% Close the text file.
fclose(fileID);

```

```

% Post processing for unimportable data.
% No unimportable data rules were applied during the import, so no post
% processing code is included. To generate code which works for
% unimportable data, select unimportable cells in a file and regenerate the
% script.

% Allocate imported array to column variable names
%LDVData.Row = dataArray{:, 1};
LDVData.Time1 = dataArray{:, 2}/1000;
%LDVData.TTus = dataArray{:, 3};
LDVData.LDA1ms = dataArray{:, 4};
LDVData.Time2 = dataArray{:, 5}/1000;
%LDVData.TT2us = dataArray{:, 6};
LDVData.LDA2ms = dataArray{:, 7};
LDVData.LDA2ms(LDVData.Time2==0)=[];
LDVData.Time2(LDVData.Time2==0)=[];

end

```

[Published with MATLAB® R2016b](#)

Time Synchronous Averaging (TSA) calculation

Function name: TSA2019 (reproduced from [170])

```

function [TSA] = TSA2019(Position,Measurement)
%UNTITLED7 Summary of this function goes here
% Detailed explanation goes here

%Find the indexes where the encoder jumps from 360 to 0 degrees.
Indexes = find(diff(Position)<0);
Indexes = Indexes(diff(Indexes)>1);

%Create a consistent position index
TSA.PosIndex = linspace(0,360,360*5);

%loop through each rotational and interpolate onto the consistent position
%index
for i = 2:max(size(Indexes))
posloop = (Position(Indexes(i-1):Indexes(i)));
TSA.Data(i-1,:) = interp1(posloop,Measurement(Indexes(i-1):Indexes(i)),TSA.PosIndex, 'PCHIP',mean([Measurement(Indexes(i-1))
Measurement(Indexes(i))])));
end
TSA.MeanValue = mean(TSA.Data,1);
% figure;
% polarplot(deg2rad(TSA.PosIndex),TSA.Data,'color',[0.5 0.5 0.5]);
% hold on;
% polarplot(deg2rad(TSA.PosIndex),TSA.MeanValue,'color',[0 0 0]);
% A = gca;
% A.ThetaZeroLocation = 'top';

end

```

[Published with MATLAB® R2016b](#)

C. PUBLICATIONS

Journal publications

- M. Allmark, R. Ellis, C. Lloyd, S. Ordonez-Sanchez, K. Porter, C. Byrne, C. Johnstone, T. O’Doherty, and A. Mason-Jones, “The development, design and characterisation of a scale model Horizontal Axis Tidal Turbine for Dynamic Load Quantification,” *Renewable Energy*, 2020.
- R. Martinez, S. Ordonez-Sanchez, M. Allmark, C. Lloyd, T. O’Doherty, G. Germain, B. Gaurier, and C. Johnstone, “Analysis of the effects of control strategies and wave climates on the loading and performance of a laboratory scale horizontal axis tidal turbine,” under review April 2020: *Ocean Engineering*.
- C. Lloyd, T. O’Doherty, and A. Mason-Jones, “Development of a wave-current numerical model using Stokes 2nd Order Theory,” *International Marine Energy Journal*, vol. 2, no. 1, pp. 1–14, 2019.
- S. Ordonez-Sanchez, M. Allmark, K. Porter, R. Ellis, C. Lloyd, I. Santic, T. O’Doherty, and C. Johnstone, “Analysis of a Horizontal-Axis Tidal Turbine Performance in the Presence of Regular and Irregular Waves Using Two Control Strategies,” *Energies*, vol. 12, no. 3, p. 367, 2019.

Conference publications

- C. Lloyd, M. Allmark, R. Ellis, S. Ordonez-Sanchez, A. Mason-Jones, T. O’Doherty, G. Germain, and B. Gaurier, “CFD surface effects on flow conditions and tidal stream turbine performance,” in *Proceedings of the 13th European Wave and Tidal Energy Conference 1st – 6th Sep 2019, Naples, Italy*, 2019.
- R. Martinez, S. Ordonez-Sanchez, M. Allmark, C. Johnstone, T. O’Doherty, C. Lloyd, G. Germain, and B. Gaurier, “Effects on the loading of horizontal axis turbines when operating under wave and currents,” in *Proceedings of the 13th European Wave and Tidal Energy Conference 1st – 6th Sep 2019, Naples, Italy*, 2019.
- C. Lloyd, T. O’Doherty, and A. Mason-Jones, “Development of a wave-current numerical model using Stokes 2nd order theory,” in *Proceedings of the 4th Asian Wave and Tidal Energy Conference 9th -13th Sept 2018, Taipei, Taiwan*, 2018.
- K. Porter, S. Ordonez-Sanchez, M. Allmark, R. Ellis, C. Lloyd, T. O’Doherty, and C. Johnstone, “Laboratory study of tidal turbine performance in irregular waves,” in

APPENDIX

*Proceedings of the 4th Asian Wave and Tidal Energy Conference 9th -13th Sept 2018,
Taipei, Taiwan, 2018.*